UNIVERSITY OF CAMBRIDGE

ZnSe Quantum Dots as a platform for solar fuels synthesis

Constantin Dominik Sahm

St. John's College

A dissertation submitted for the degree of

Doctor of Philosophy

Department of Chemistry

University of Cambridge

March 2021

Declaration of Authorship

I hereby declare that this dissertation is the result of my own work and includes nothing which is the outcome of work done in collaboration except as declared in the preface and specified in the text. It is not substantially the same as any work that I have submitted, or, is being concurrently submitted for a degree, diploma or other qualification at the University of Cambridge or any other University or similar institution. I further state that no substantial part of my dissertation has already been submitted, or, is being concurrently submitted for any such degree, diploma or other qualification at the University of Cambridge or any other University or similar institution. This dissertation does not exceed the prescribed word limit of 60 000 words.

Constantin D. Sahm
Cambridge, March 3, 2021

Abstract

ZnSe Quantum Dots as a platform for solar fuels synthesis

by Constantin Dominik Sahm

This work studied the generation of solar fuels (CO_2 to CO reduction and H_2 evolution) on photocatalysts comprised of nanoparticulate ZnSe Quantum Dots (QDs) in aqueous (ascorbate) solution.

A continuous-flow setup for photocatalysis was successfully developed which enables in-line gas chromatography of multiple samples in parallel with high sensitivity and operates in an automated fashion. This setup formed a robust experimental protocol for photocatalytic light experiments throughout this dissertation.

First, ligand-free ZnSe-BF_4 QDs were examined as light absorbers in combination with a range of molecular catalysts (co-catalysts) based on earth-abundant metal complexes. After an initial co-catalyst screening, three co-catalysts were studied in-depth comprising a phosphonated Ni(cyclam), a Co(quarterpyridine) and a Co(tetraphenylporphyrin) functionalised with three sulfonate groups and one amine group. The latter hybrid photocatalyst exhibited the highest photocatalytic activity (18.6 μmol CO, 27.8 μmol H_2) reaching an unprecedented TON_{Co} (CO) of 619 after 1000 min of irradiation with a CO (vs. H_2) selectivity of $> 40\%$. This hybrid photocatalyst showed a distinct induction period which was assigned to slow initial Co^{III} to Co^{II} reduction and can be accelerated by priming the catalyst in ascorbic acid solution. The insights demonstrate that the photocatalytic activity is not limited to one type of molecular catalyst and that ZnSe QDs are a particularly versatile light-absorber platform to drive a range of molecular co-catalysts based on different catalyst classes and anchoring strategies.

Subsequently, the QDs were used for CO_2 reduction in the absence of a molecular co-catalyst by employing an organic surface modification strategy: The chemical environment of the QD surface was modified through design of a capping ligand, which incorporates an imidazolium motif and binds to the QD surface via a thiol group. The ligand capping suppressed H_2 evolution and promoted photocatalytic CO_2 reduction. The ligand-QD interactions were characterised quantitatively using ^{1}H-NMR spectroscopy

and isothermal titration calorimetry which quantified the number of strongly interacting ligands with the QD surface (12 to 17 ligands). Transient absorption spectroscopy and DFT calculations were used to propose a mechanism for the QD-surface promoted reaction in which the imidazolium ligand plays a key role in stabilising a surface-adsorbed $^{*}CO_2^{\delta-}$ intermediate. Thus, for the first time QDs have been rendered active towards CO_2 reduction by means of an organic surface-modification strategy and the results establish capping ligands as a powerful tool to modify the secondary coordination sphere and therefore the product selectivity of colloidal photocatalysts.

Furthermore, dithiols, a class of capping ligands not examined in the context of CO_2 reduction previously, were found to enhance CO_2 reduction on ZnSe QDs as well. A length dependence of the dithiols was found in which shorter dithiols ($\sim$ 4 Å) promote CO_2 reduction on the QD surface, whereas longer dithiols (6-8 Å) enhance CO_2 reduction in the presence of an additional molecular co-catalyst. The QD-dithiol interactions were studied with ^{1}H-NMR spectroscopy which revealed a solvation sphere dominated by hydrophobic interactions. Additional control experiments and DFT simulations point towards an influence through non-covalent interactions in the secondary coordination sphere to explain the enhanced CO_2 reduction.

Finally, the ZnSe QDs operated in a photoelectrochemical setup by deposition on a p-type semiconductor $CuCrO_2$, forming a QD-sensitised photocathode. The $CuCrO_2$-ZnSe photocathode exhibited photocurrents of up to 15 μA cm^{-2} and was active in controlled potential photoelectrolysis for the reduction of aqueous protons to evolve H_2 (38 nmol H_2 after 4 h irradiation).

Overall, this work examined ZnSe QDs in aqueous solution as a versatile and efficient platform free of precious metals for photocatalytic CO_2 reduction alongside H_2 evolution. This work also unveiled organic ligand capping to modify the chemical environment on colloidal photocatalysts, thus enabling control over the product selectivity (H_2 vs. CO).

Acknowledgements

I would first like to thank my supervisor Erwin Reisner of the Department of Chemistry at the University of Cambridge for the opportunity to work in his laboratory and continuous support and guidance throughout this dissertation.

Financial support by the *Christian Doppler Research Association*, the *Austrian Federal Ministry for Digital and Economic Affairs, the National Foundation for Research, Technology and Development*, *the OMV Group*, an *ERC Consolidator Grant "MatEnSAP" (682833)* and *St. John's College, Cambridge* is greatly acknowledged. This generous financial support has made this PhD Thesis possible.

My sincere thanks goes to Moritz Kühnel, who was my mentor during the first year. His support, motivation and deep knowledge helped me to start this project and guided me into conducting thorough research.

There are number of collaborators from both within the University of Cambridge and externally who I had the opportunity to work with. Some special thanks goes to Eric Mates-Torres, Anna Ciotti and Max García-Melchor from Trinity College Dublin for the fruitful collaboration and conducting DFT simulations. The theoretical insights and stimulating discussions pushed this research substantially forward. It would like to thank Nora Eliasson and Leif Hammarström from Uppsala University for performing transient absorption (TA) spectroscopy which gave a much deeper understanding of the capping ligand project. In addition, I thank Kamil Sokołowski, Zehuan Huang and Oren Scherman for help with NMR and ITC experiments. I am very grateful to Kamil Sokołowski for his support and uplifting words, jokes and discussions, which made this collaboration very enjoyable. I would like to kindly acknowledge Alex Cowan and his co-workers from the University of Liverpool for providing cyclam catalysts. Matt Castle is acknowledged for being extremely helpful with questions regarding statistics and help with programming the data evaluation scripts. A big thanks goes to Heather Greer for operating the TEM.

There are many fantastic colleagues, labmates and friends from the Reisner Group that I would like to acknowledge. Especially, I would like to thank Andreas Wagner for the many collaborations, including developing the continuous-flow system, the review of the local chemical environment and convincing me to use the programming language *R* to evaluate the datasets. Charles Creissen is greatly acknowledged for the collaboration on QD-photocathodes and for preparing and providing delafossite $CuCrO_2$ electrodes. My sincere thanks goes to Kristian Dalle, who helped me countless times with synthetic problems, and additionally provided and screened the Fe(tpp$(TMA)_4$) catalyst

and started the synthesis of the capping ligand MEMI. A big thanks goes to Daniel Antón-García for endless support in the lab and help with photoluminescence studies. Another big thanks goes to Carla Casadevall Serrano for more help regarding synthesising and purifying Co porphyrins. Sam Cobb is kindly acknowledged for help in acquiring SEM images and EDX spectra. Further, I would like to thank Souvik Roy and Geani Ucoski for providing and screening molecular catalysts (Co(pcN4), Co(pcS4), Co(qpy) and Co(ttpS3N1).

Furthermore, I would like to thank all current members of the Reisner Group for the great atmosphere and many laughs we could share over the years, which have made this a truly enjoyable place to work. I would also like to thank former members of the Reisner Group, Khoa, Nick, Nina, Jane, Julien, Annika and Bertrand for the support and help which really made a difference.

I would also like to thank my friends in Cambridge, Anja, Andi, Marisa, Esther, Dan, Charlie, Mark, Kristian, Vivek, Arjun, Carla and Annika for making this such a great journey. I look back on years of memories with countless pub nights, formal dinners, punting and the many trips/concerts/festivals (in particular Glastonbury, Esther!) which have made my time in Cambridge unforgettable.

I am also extremely grateful to my family for the unconditional support throughout the years. Lastly, I thank my wonderful partner Franziska for the sustained support that carried me through all the highs and lows of the PhD.

List of publications

The results presented in this dissertation have been (in parts) published in the following peer-reviewed journals:

1. M. F. Kuehnel*, C. D. Sahm*, G. Neri, J. R. Lee, K. L. Orchard, A. J. Cowan, E. Reisner, ZnSe quantum dots modified with a Ni(cyclam) catalyst for efficient visible-light driven CO_2 reduction in water. *Chemical Science* **2018**, 9, 2501–2509. (* denotes equal contribution)

2. M. F. Kuehnel*, C. E. Creissen*, C. D. Sahm*, D. Wielend, A. Schlosser, K. L. Orchard, E. Reisner, ZnSe Nanorods as Visible-Light Absorbers for Photocatalytic and Photoelectrochemical H_2 Evolution in Water. *Angewandte Chemie International Edition* **2019**, 58, 5059–5063. (* denotes equal contribution)

3. A. Wagner*, C. D. Sahm*, E. Reisner, Towards molecular understanding of local chemical environment effects in photo- and electrocatalytic CO_2 reduction. *Nature Catalysis* **2020**, 3, 775–786. (* denotes equal contribution)

4. C. D. Sahm, E. Mates-Torres, N. Eliasson, K. Sokołowski, A. Wagner, K. E. Dalle, Z. Huang, O. A. Scherman, L. Hammarström, M. García-Melchor, E. Reisner, Imidazolium-modification enhances photocatalytic CO_2 reduction on ZnSe quantum dots. *Chemical Science* **2021**, DOI: 10.1039/d1sc01310f.

5. C. D. Sahm, E. Mates-Torres, A. Ciotti, K. Sokołowski, G. Neri, A. J. Cowan, M. García-Melchor, E. Reisner, Tuning the local chemical environment of ZnSe QDs with dithiols towards photocatalytic CO_2 reduction. **2021**, *in preparation.*

6. C. D. Sahm, G. M. Ucoski, S. Roy, E. Reisner, Automated and continuous-flow platform to analyze photocatalytic semiconductor-metal complex hybrid systems for CO_2 reduction, **2021**, *submitted manuscript.*

Other contributions have been made to the following publications but were not included in this dissertation:

1. S. Roy, M. Miller, J. Warnan, J. J. Leung, C. D. Sahm, E. Reisner, Electrocatalytic and Solar-Driven Reduction of Aqueous CO_2 with Molecular Cobalt Phthalocyanine–Metal Oxide Hybrid Materials. *ACS Catalysis* **2021**, 11, 1868-1876.

2. Q. Wang, S. Kalathil, C. Pornrungroj, C. D. Sahm, E. Reisner, Bacteria photocatalyst sheet for selective carbon dioxide conversion into acetate. **2021**, *submitted manuscript.*

Contents

Chapter 1

Introduction

Our modern society demands increasing amounts of energy which has been largely met by fossil fuels (coal, natural gas, oil) as the main energy source in the last centuries [1]. Their combustion has led to an exponential increase in atmospheric carbon dioxide (CO_2) concentration, starting from 280 ppm (pre-industrial revolution) to more than 400 ppm to date (Figure 1.1-A) [2]. CO_2 acts as a greenhouse gas by absorbing infrared radiation (reflected from the earth's surface) in the atmosphere leading to a temperature increase [3]. While the short-term atmospheric temperature fluctuates naturally, the median global average temperature has risen by approximately 1.1 °C in the last 150 years (Figure 1.1-B) [4]. It is arguably difficult to predict the exact temperature increase with rising CO_2 concentrations and even more complicated to model its consequences on the climate, however, there is a large consensus amongst climate scientists that global warming can have disastrous consequences for the earth's climate and consequently for human society [5, 6]. As a result, there is an urgent need for humankind to transition to a sustainable energy supply.

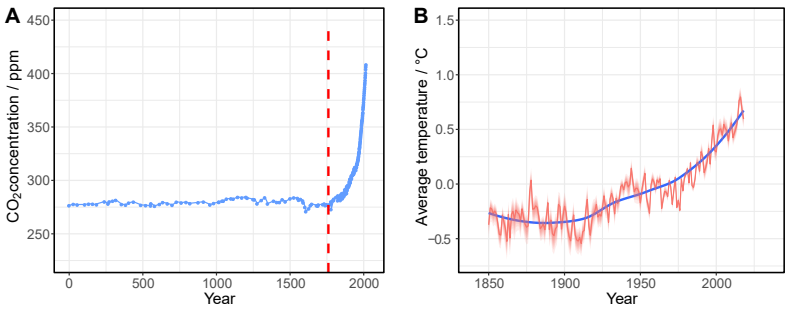

FIGURE 1.1: (A) Global average atmospheric CO_2 concentration. The dashed line indicates the approximate start of the industrial revolution (1760). (B) Global average land-sea temperature relative to the average temperature from 1961-1990. The shaded area (red) represents the upper and lower 95% confidence intervals, whereas the trend is represented by the blue line based on a polynomial regression. Data based on references [4, 7] retrieved from *ourworldindata.org*

Sustainable/renewable energy encompasses a range of energy sources including wind, solar, hydro, tidal, biomass and geothermal. Without doubt, solar energy provides the largest source of energy amongst other renewables; for example, the energy irradiated to earth within one hour surpasses the world's total energy consumption in one year [8]. Ultimately, except for nuclear, tidal and geothermal, most energy sources originate back to solar in some way. Utilising this virtually unlimited supply of energy remains the major challenge in our response to climate change.

The current energy landscape is depicted in Figure 1.2. Even though renewables such as photovoltaics and wind power are growing rapidly, the global primary energy consumption is still largely dominated by fossil fuels such as oil, natural gas and coal, which together account for 85% (as of 2019) [9]. This large share of fossil energy sources is reflected in the prevalence of fuels (81%) as a method of energy distribution, whereas electricity only accounts for 19% [10]. Most commercially viable renewable options (photovoltaics (PV) and wind) generate electricity which has led to an electrification of parts of the energy sector [10]. While this strategy is successful in some applications and prices of photovoltaics have declined drastically [11], the electrification of the whole energy landscape may remain extremely challenging with some end-uses requiring high energy density fuels in the future. Furthermore, the generation of electricity through renewable sources is highly intermittent and dependent on short-term weather conditions and long-term seasonal changes, thus creating a need to store energy in order to match the energy consumption period. Therefore, a sustainable alternative to fuels derived from fossil energy carriers is required. Batteries are an established way for the storage of electricity but are relatively expensive and not ideally suited for large scale transportation applications due to their low specific energy density [8]. Chemical fuels, however, are extremely attractive due to their high specific energy density and their easy transportation/distribution which has made them the predominant energy vector in most industrial and transport applications.

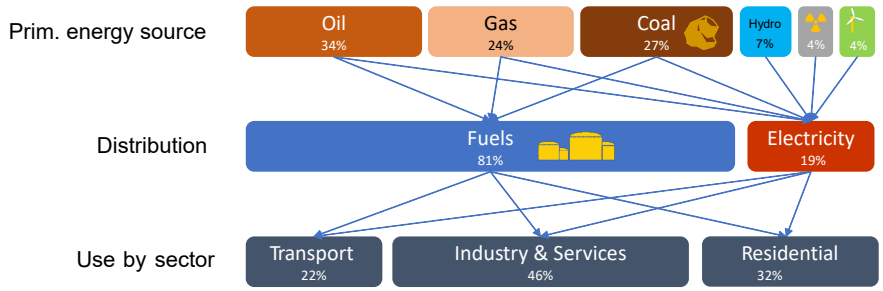

FIGURE 1.2: Overview of the global energy landscape (as of 2018). Data acquired from references [1, 9, 10].

Consequently, generating chemical fuels from solar energy has attracted scientists from many disciplines and has grown into a widely recognised and active research field [12–14]. These so-called *solar fuels* will be reviewed in the next section.

1.1 Solar Fuels

Solar fuels can be classified by their method of generation (Figure 1.3).

1. PV + electrolyser: a PV cell is combined with an electrolysis cell that drives a light-independent electrochemical reaction.
2. Photoelectrochemical (PEC): a PEC cell is composed of two electrodes immersed into a solution containing electrolytes and are often separated by a membrane. At least one of the electrodes absorbs light to drive the reaction.
3. Photochemical: Light absorber, oxidation and reduction catalysts operate in solution or suspension in the same compartment.
4. Thermochemical: concentrated solar thermal energy drives a chemical reaction.

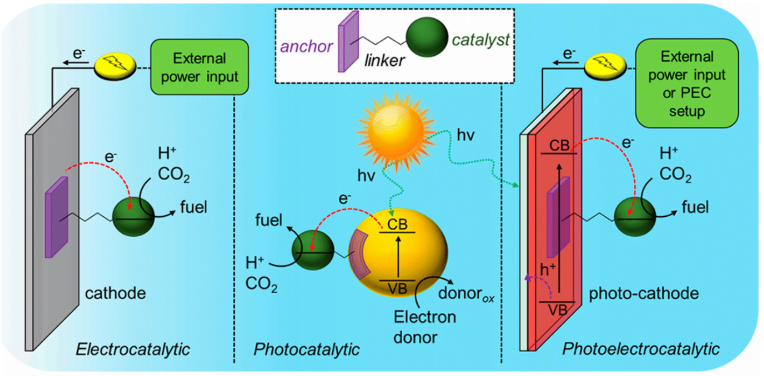

FIGURE 1.3: Overview of the different configurations for the production of solar fuels. (Thermochemical approaches have been excluded). Figure from reprinted from reference [13] under CC-BY.

It is yet unclear which method will be the most economically viable [12, 15] and will likely depend on the specific application. Thermochemical approaches are beyond the scope of this dissertation and will not be further reviewed herein.

PV + electrolysis combines two established technologies. A PV cell absorbs photons and provides the electrical potential in order to drive a (light-independent) electrolyser [16]. This technology is mature for the electrolysis of hydrogen (H_2) and increasingly moving towards commercial applications. However, the configuration requires a sophisticated

set of electrical system components (membranes, separator plates, electrodes) and often expensive catalysts [17].

PEC and photochemical approaches directly transform solar energy into chemicals, similar to natural photosynthesis; therefore they are also referred to as *artificial photosynthesis*. The main difference lies in the incorporation of both steps, generation of photogenerated charges and subsequent conversion into chemical energy, into a single device. In a PEC cell, the light-absorbing functionality is directly incorporated into an electrode which can operate with or without external bias. The (photo)-anode and (photo)-cathode are electrically coupled and can be placed in separate compartments for each oxidation and reduction reaction [18, 19]. This approach is controversially debated in the literature, especially if it can benefit overall cost and efficiencies compared to a conventional PV + electrolysis configuration [14, 19–21]. Next to the reduced device complexity, a benefit is the separation of both oxidation and reduction half-reaction (in comparison to photochemical, see below) so products can be separated easily and the reactions can be optimised individually.

In photochemical solar fuel production, instead of an external bias, a light absorber (also referred to as *photosensitiser* if a molecule is used as light absorber) is employed in combination with oxidation and reduction catalysts [22]. The system usually operates in one compartment, either homogeneously in solution [22] or "heterogenised" [23] by immobilising a molecular catalyst on a colloidal light absorber. Having both reduction and oxidation catalysts in one compartment requires high specificity and compatibility of both catalysts. For example, during full water splitting to O_2 and H_2, the O_2 reduction reaction is thermodynamically favourable to proton reduction which requires the reduction catalyst to be very specific towards the desired reduction reaction. Additionally, the reaction products need to be separated when they are generated in one compartment. On the other hand, this simple ("one-pot") approach would presumably enable scalability in the long-term at low costs [24].

Solar fuels can be further categorised by the feedstock that is being converted. One approach is to split water into its elements H_2 and O_2 [25, 26]. H_2 is considered a promising energy carrier and is moving rapidly towards large-scale adoption but nonetheless, some challenges in the handling of H_2 still remain, for example storage and safety [17]. Moreover, a H_2 economy requires a newly developed infrastructure which is likely to come at high costs. An alternative approach consists of converting CO_2 into carbon-based fuels such as formic acid, carbon monoxide (CO), methanol, methane and multicarbon products [12, 27–29]. Such fuels may be used in the established energy infrastructure with little adjustments [30]. CO, not a fuel in the conventional sense, is a highly versatile intermediate product in large scale industrial applications and can be readily converted

into chemical fuels via Fischer-Tropsch chemistry [31]. Additionally, carbon-based chemical fuels excel due to their high specific and volumetric energy density which renders them particularly suitable for transport applications. Ultimately, a sustainable carbon-neutral cycle is required, whether the energy vector will be H_2 or carbon-based fuels is subject to many variables and both are likely to coexist in a future economy relying on clean energy.

One key objective of this dissertation is to develop novel photocatalysts for the generation of H_2 and carbon-based fuels through the photocatalytic reduction of aqueous protons and CO_2. On a fundamental level, the process consists of two main functions - 1) light absorption to generate photoexcited electrons and 2) the reduction reaction using the photogenerated electrons - as depicted in Figure 1.4. Both functions will be reviewed in the next two sections.

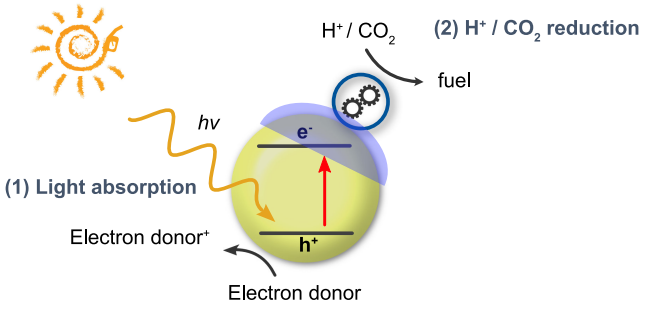

FIGURE 1.4: Illustration of a photocatalytic system for solar fuel generation. The yellow sphere represents a colloidal light absorber. The blue overlay/gear represents a surface modification strategy that is typically required in order to utilise colloidal light absorbers for CO_2 reduction.

1.2 Light absorption

This section summarises the light absorption functionality within photocatalytic CO_2 reduction and H_2 evolution. After a brief overview of reported material classes, the fundamental principles of semiconductor photocatalysis are explained. This is followed by an overview of Quantum Dots, the material class studied herein, their photophysical properties and preparation, followed by a review of their surface chemistry.

1.2.1 Overview of light absorbers

In principle, light absorbers are either (metal)-organic molecules or solid-state semiconductors which absorb electromagnetic radiation in the visible or ultra-violet spectrum and induce an electron transfer to another molecular entity such as a catalyst [32].

The former are usually referred to as *photosensitisers* in this context [33]. There is a vast breadth of molecular photosensitisers [34] and the most common ones are based on Ruthenium [35, 36] and Iridium [37, 38]. Examples for solid state semiconductors include metal oxides, most prominently TiO_2 [39–41] but also Ta_2O_5 [42, 43], (oxy)nitrides [44] as well as (oxy)sulfides [45] and many more are known [46, 47]. Compared to organic molecules, these solid-state materials posses typically a higher stability during reaction conditions [48]. However, many metal oxides feature a very large bandgap which requires UV-irradiation in order to generate excited charges limiting the use of the solar spectrum. This is often circumvented by immobilising molecular dyes (*i.e. sensitise*) on the materials [40, 48]. Metal-free light absorbers based on graphitic carbon nitride (C_3N_4) [49–51] and carbon dots [52, 53] have emerged recently within the search for ultra-low costs alternatives to traditional light absorbers and have gained considerable attention.

With the advent of nanotechnology, semiconducting nanoparticles, so-called *Quantum Dots*, mostly based on chalcogenides, have likewise gained considerable attention due to their high tunability and photocatalytic activity [54]. This novel class of material bridges the discrete energy levels of molecular photosensiters with the continuous band structure of bulk semiconductors and will be reviewed in more detail in the section 1.2.3.

1.2.2 Semiconductor photocatalysis

The general scheme of photocatalytic process is briefly summarised in the following section based on reference [18].

Upon irradiation of a semiconductor, the absorption of a photon with energy above the band gap leads to the promotion of an electron from the valence band (VB) to the conduction band (CB) and the formation of an electron-hole pair (*exciton*). Effectively, the Fermi level of the electrons is elevated. The exciton may separate into individually moving electrons and holes upon overcoming the exciton dissociation energy. A prerequisite for a catalytic reaction is that the charges migrate separately to their distinct reaction sites for the reduction and oxidation respectively. Excited electrons can transfer from the semiconductor CB to an electron acceptor (A), for example a co-catalyst (reduction half reaction). Likewise, photogenerated holes in the VB can be quenched by an electron donor (D) (oxidation reaction) (Figure 1.5).

The Fermi levels of both photogenerated electrons and holes can be approximated with the semiconductor conduction and valence band edge positions. For a desired reaction to occur, the semiconductor CB needs to be above (more negative) than the reduction potential $E(A/A^-)$ of the reduction reaction. Similarly, the VB needs to be lower (more

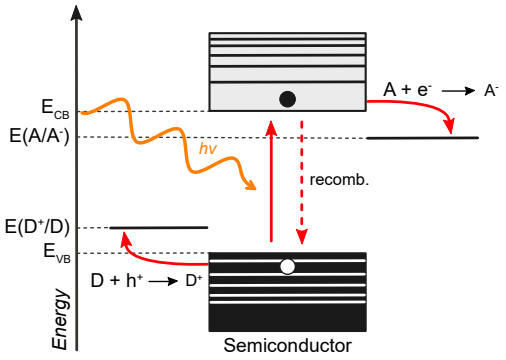

FIGURE 1.5: Mechanism and energy level diagram for a photocatalytic reaction; A: Electron Acceptor; D: Electron Donor; Figure adapted from reference [55] with permission from *John Wiley and Sons*.

positive) than the oxidation potential $E(D^+/D)$ for the oxidation reaction to occur. Furthermore, the semiconductor junction has to provide an additional potential between the band position and respective redox level referred to as overpotential (for both reduction and oxidation reactions), which is necessary to overcome kinetic constraints. The difference between the reduction and oxidation potentials governs the amount of stored energy during the photocatalytic reaction.

Losses

Not every electronic excitation leads to the desired photocatalytic reaction. A number of mechanisms are known which can lead to losses [18]:

1. Photon absorption. If the photon energy is below the semiconductor band gap, it can not be absorbed and its energy is lost. This is particularly pronounced for wide band gap semiconductors with an absorption onset in the blue or UV spectrum. If the photon energy is much larger than the band gap, the excess photon energy is quickly lost due to thermalisation.

2. Recombination. If the excited charges recombine rather than separate, this is referred to as charge recombination. The photon energy is fully lost if the charge recombines non-radiatively where the energy is dissipated as heat. When the charges recombine radiatively, it is a competitive pathway for the catalysis but the charge may be re-absorbed. A strong photoluminescence may indicate the absence of thermal recombination pathways promoted by trap states.

3. Kinetics. The necessity of an overpotential to increase the electron transfer rate represents another loss because it is utilised non-productively to drive the charge transfer. When sufficient amounts of products build-up, the back reactions become increasingly kinetically competitive and decrease the overall energy efficiency.

Sacrificial reagents

If the redox potential of the semiconductor lies above the one of water oxidation (typically observed with chalcogenides semiconductors), oxidation of lattice ions of the semiconductor itself (e.g. S^{2-}) can lead to dissolution of the particles. This process is referred to as *photo-oxidation*. Removing the holes rapidly is crucial to prevent photo-oxidation and can be achieved by addition of a sacrificial hole scavenger (or also referred to as sacrificial electron donor (SED)). These are typically reducing agents such as ascorbic acid or triethanolamine (TEOA). At the same time, they sacrifice the amount of stored energy by the difference between redox level of the SED and desired oxidation reaction. The electron donor is referred to as *sacrificial*, because it is consumed during the reaction. SEDs can also be used to balance the rates of the two half-reactions because they are often different and then the slower one becomes rate-limiting. This is the main reason why SEDs are commonly employed in photocatalysis to study and optimise half reactions and have been invaluable for this purpose [56]. Nevertheless, their replacement with a sustainable electron donor (or a useful oxidation reaction) remains as one of the ultimate goals in the field. In particular, the oxidation of water is desired to produce fuels at scale. Oxidation of freely available waste based on biomass [57] or polymers [58] might be another potential solution.

Electron transfer

One of the most widely used theories to describe electron transfer (ET) was developed by Marcus in the 1960s [59, 60] and can be applied to most QD–molecular acceptor systems [61].

The rate of ET is thereby governed by to two main contributions: ΔG, the change in free energy (*i. e.* the driving force) and λ, the reorganisation energy, which can be described as the work required to distort the reactant from its initial reaction equilibrium coordinate to the final equilibrium coordinate without any ET [61]. As the driving force increases, ET increases, which is referred to as the *normal* regime ($-\Delta G < \lambda$) until it reaches a maximum ($\Delta G = \lambda$), after which it decreases again (inverted regime, $-\Delta G > \lambda$) [62]. The prediction of an inverted regime has been experimentally confirmed for many molecular donor-acceptor systems [61, 63] but interestingly does not apply to QD-molecular donor-acceptor systems. A study on CdS, CdSe and CdTe of various sizes in combination with acceptor molecules found a monotonic increase in ET rate with increasing driving force, regardless of the acceptor, which implies the absence of an inverted regime for such QD-acceptor systems [62]. To rationalise this finding, the authors proposed an Auger-assisted model, in which excess energy is preserved by excitation of holes to a higher level enhancing the ET rate. This model was able to match the observed ET rates well. The model required that coupling of electrons and holes is

stronger than electrons with phonons with at large density of states, which is met for many excitonic nanomaterials.

Charge separation

The charge carriers need to transfer to the surface with a lifetime sufficiently long enough in order to participate in a chemical reaction. If the lifetime is too short, a large portion of the charges would recombine. The timescale of a chemical reaction is typically much longer (micro- to milliseconds) than that of excited charge carriers ($\sim$ nanoseconds) [18, 64, 65]. It is therefore a great challenge to increase the charge carrier lifetime. Some attempts include the formation of a semiconductor-metal junction, whereby the metal acts as an electron sink [66] or a semiconductor-semiconductor heterostructure [67].

As a result of the thermodynamic constraints for oxidation and reduction reaction and the interplay of light absorption, the choice of semiconductor becomes extremely difficult. A wide band gap semiconductor would provide higher driving force (*i.e.* faster charge transfer) for both oxidation and reduction, however, only absorbs high energy radiation and therefore a small fraction of the solar spectrum. A smaller bandgap would absorb more light but sacrifice oxidative and/or reductive power. Consequently, both factors, light absorption and thermodynamic energy potentials need to be well balanced. Upconversion of low energy photons [68], sensitisation with dyes [69] as well as z-scheme systems [70] have been suggested to overcome this intrinsic limitation.

1.2.3 Quantum Dots

Quantum Dots (QD) are defined as semiconductor crystals with a size of 2-20 nm which are synthesised in the colloidal state [71]. By lowering the particle diameter to a length below the Bohr radius of its exciton, electronic states become discrete [72]. As a consequence and in contrast to bulk material, the optoelectronic properties of Quantum Dots become a function of size (and shape) and this gives scientists the opportunity to alter such properties. This phenomenon has led to the naming of the particles as *quantum* by describing this principle as *quantum confinement*. An approximation by Brus allows to predict the energy terms of a particle [73, 74]: With decreasing particle size, the band gap increases and consequently the QD's absorption onset is shifted towards the blue part of the spectrum compared to the bulk.

Besides the tunability of optoelectronic properties (*e.g.* band gap), numerous other properties [55] make QDs particularly interesting for the use as light absorbers:

- QDs based on chalcogenides exhibit an extraordinarily strong light absorption with molar extinction coefficients of approximately 10^5-10^6 M^{-1} cm^{-1} [75, 76].

- Colloidal suspensions lead to a high degree of light scattering, which allows for the utilisation of reflected light that otherwise would be lost in case of a flat surface [77].
- The photogenerated charge carriers need to reach the material's interface for a subsequent chemical reaction. Due to the short carrier diffusion length in small particles, the extraction of photogenerated charges in QDs can be very fast. For example, ultrafast electron transfer within a QD/metal heterostructure from the QD to the metal nanoparticle was observed at the ps timescale, much faster than the electron-hole recombination pathway (1 - 100 ns timescale) [78].
- The extraordinarily large specific surface area (*i.e.* high surface-to-volume ratio) of colloidal QDs leads to a very large number of surface active sites (relative to mass/volume) for a catalytic reaction which is beneficial for the charge transfer kinetics. Additionally, the surface can be tailored through passivation with a plethora of capping ligands which allows tuning certain properties (surface charge, solubility, etc.) [79].

On the other hand, the large surface area can also lead to a fast rate of parasitic interfacial electron-hole recombination limiting the overall efficiency. Additionally, the small size of nanoparticles implies that the space charge layer is very small, this means that in the absence of a strong bias, the bands in nanoparticles are essentially flat [80] which can limit the charge-carrier separation efficiency [77].

Synthesis of colloidal QDs

In recent years, there has been an increasing interest in preparation of colloidal nanoparticles [81]. Here, the two most common synthetic strategies, *hot-injection* and *heat-up* methods are summarised in the following based on reference [82].

The formation of a nanoparticle can be divided into a nucleation and a growth period (Figure 1.6). The energy barrier for the nucleus formation is very high, hence a high supersaturation is required. The supersaturation thereby describes the fraction of the actual monomer concentrations divided by the equilibrium monomer concentration. Once particles have started to grow, the supersaturation is lowered promptly due to consumption of monomers - the nucleation is self-terminated (*burst nucleation*). It is thereby important to limit the nucleation period to a very short time to ensure all particles have a similar growth history which then leads to a monodisperse size distribution.

During the growth period, particles gain in size while the number of particles stays constant (Figure 1.6). When the monomer concentration is high (diffusion-controlled growth mode), larger particles grow slower than smaller particles which leads to a size-focusing

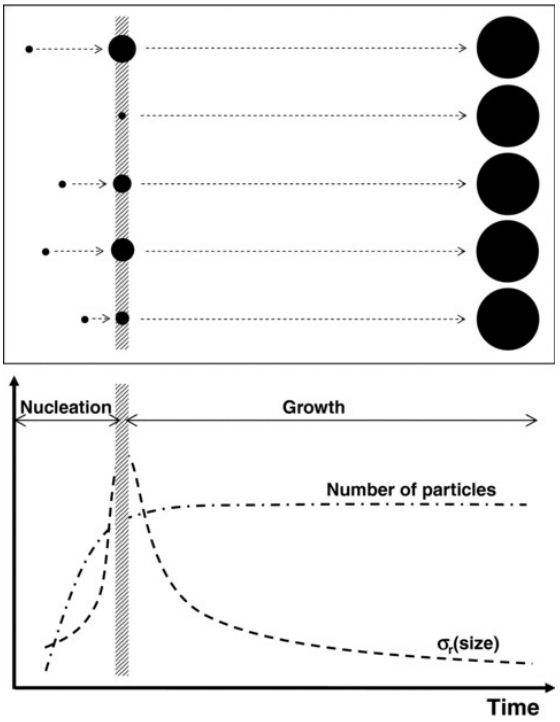

FIGURE 1.6: Schematic illustration of the size distribution control process. The vertical thick line (shaded) indicates the point in time at which the nucleation process is terminated, dividing the nucleation and growth periods. In the lower part of the figure, the time evolution of the number of particles and the relative standard deviation of the size distribution are shown. Figure reprinted from reference [83] with permission from *John Wiley and Sons*.

effect and aids a uniform size distribution. On the other hand, when the monomer concentration is low (reaction-controlled growth mode), one part of the particles continue growing while others dissolve in solution, also referred to as *Ostwald ripening*.

Both methods described herein, *hot injection* and *heat-up* require the presence of capping ligands during the formation process. Capping ligands are typically surfactant-like molecules with an alkylic chain to enable dispersability in organic solvents and a headgroup that anchors to the QD surface to passivate the surface and thereby provide colloidal stability in solution [84]. Crucial is thereby the binding energy at which the capping ligands binds to the particle surface. It needs to be weak enough so that the ligand can exchange on and off a forming nanoparticle so that the surface is accessible for further growth, but strong enough to prevent agglomeration [85].

Capping ligands also influence the nucleation and growth dynamics during the formation process which is very sensitive to the ligand concentration [86]. At high capping ligand concentration, the number of nuclei (during nucleation) is reduced due to complexation of monomers. At the same time the initial nuclei are smaller in the presence of high capping ligand concentration. Hence, the capping ligand reduces the rate of nucleation (due to the lower monomer concentration) and at the same time passivates nuclei as

they are formed. If the ligand concentration is too high, the nucleation is completely hindered but if it is too low, there is a lack of surface stabilisation. Consequently, the capping ligand concentration is a delicate balance and important parameter to achieve controlled nucleation and growth required to achieve a monodisperse size distribution. [86]. The choice as well as the concentration of capping ligand is thereby most often experimentally determined and makes defined nanoparticle synthesis rather challenging due to the large number of experimental conditions.

The *hot injection* method achieves the necessary level of monomer supersaturation through swift addition of a precursor solution to a solution containing capping agents at a high reaction temperature ($\sim 300°C$) [87]. To avoid Ostwald ripening, the reaction is stopped before the reaction becomes reaction-controlled. In contrast, the *heat-up* method builds up monomers gradually through heating of the precursor solution to the required temperature at which the nanocrystal start to form. Meanwhile, the nucleation is inhibited due to its high energy barrier. This eventually leads to a supersaturation high enough to trigger burst nucleation. In essence, both methods use the same principles but utilise a different way of achieving a high level of supersaturation.

1.2.4 The surface chemistry of Quantum Dots

With shrinking size, the surface of a particle becomes increasingly more important and can be the predominant factor for nanoparticle properties. It is therefore crucial to have precise control over the particle surface in order to control its properties and reactivity. Since the surface chemistry is highly tunable [88], it renders them particularly interesting for photocatalysis as outlined below.

Capping ligands saturate dangling bonds on the surface and passivate the exposed surface from its environment [79], essentially governing the particle's stability. The capping ligand protecting layer can be viewed as miniature self-assembled monolayer (SAM), which have been widely characterised on metal surfaces [89] (see below) and can act as a model for the capping ligand-nanoparticle interface. Capping ligands are employed already during the formation (nucleation and growth) of the particles because they control thermodynamic and kinetic aspects during synthesis [82]. For the synthesis, typically surfactant-like ligands with long lipophilic hydrocarbon tails (e.g. oleic acid, oleylamine) are employed and these "native ligands" passivate the particle surface in solution [90]. After particle formation, surface ligands can greatly influence the optoelectronic and surface properties of the particles as well as its solubility in various solvents. Since capping ligands can be exchanged readily [91], they open up a vast play-ground in order to tune properties towards a desired functionality.

The bonding of the ligand to the nanoparticle can be classified by the type of metal-ligand interaction (X-, L-, Z-type) [79, 92] and is particularly tailored towards II-VI semiconductors (Figure 1.7): L-type ligands coordinate datively to the metal surface atoms through a lone electron pair (e.g. amines, phosphines, phosphines oxides). X-type ligands can form a covalent two electron bond with a metal surface sites and thereby require one electron from the particle surface. Most often those bonds are described as ion pair (positively charged metal surface site, negatively charged ligand) which interact electrostatically (e.g. halides, thiolates, carboxylates, phosphonates). Z-type ligands interact by accepting electrons from electron-rich surface sites (e.g. $Pb(OOCR)_2$). Neutral L- and Z-type ligands tend to be more easily replaceable and interchange more commonly, whereas charged X-type ligands such as oleate are tightly bound [93]. However, also these tightly bound ligands can exchange with other X-type ligands in an associative pathway as shown for thiol-capped Au clusters whereby incoming and outgoing species exchange a proton [94]. The hard and soft (Lewis) acids and bases (HSAB) principle can be applied to predict the strength of the ligand-particle interaction [95]. For example, the robust Au-S bond is a good example of a 'soft' pair, whereas the 'hard' carboxylate binds poorly to Au particles.

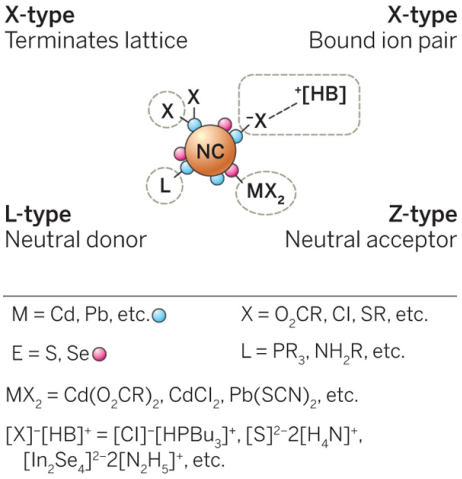

FIGURE 1.7: Illustration of the coordination of different types of ligands to metal-chalcogenide nanocrystals (NC). From [92], reprinted with permission from *AAAS*.

Capping ligands open up a plethora of opportunities to tailor QDs for various applications because they can, in principle, affect most properties. Most capping ligands affect solely the surface properties (charge density, ligand shell permeability, hydrophobicity) but some ligands extend their influence even into the electronic core. In the following, the "capping ligand toolbox" is briefly reviewed and exemplified starting with their influence on optoelectronic processes, followed by effects on surface properties. More comprehensive reviews are available [79, 96, 97]

Optoelectronic properties

Mid-gap states.
Electronic states between the valence and conduction band, so called trap-states, can act as recombination site and are therefore able to quench the photoluminescence (PL) of QDs. A capping ligand can form a bond with this mid-gap state, forming a new set of molecular orbitals which may be out of the band gap. Effectively, the band gap is thereby "cleaned-up" [98] and this can dramatically enhance PL of QDs. However, this behaviour is not universal and some ligands can introduce new mid-gap states and quench PL, as shown for thiol-ligands on CdSe-QDs [99]. The intermittence in emission of QDs was reduced in the presence of thiol capping ligands and this was explained with the electron donation from the thiol to the surface, effectively quenching the surface electron trap states [100]. Inspired by this initial finding, a follow-up study revealed that this effect is highly pH and concentration dependent: Time dependent PL experiments showed that thiolate, not the thiol, deactivates existing electron trap states at low concentrations which explains the enhanced PL, whereas at high concentrations, thiolates introduce new hole traps which decrease PL [101].

Absolute energy of electronic states.
Surface-bound ligands can generate an electric dipole and if it points towards the nanoparticle centre, its energy levels may shift up or down, depending on the ligand-induced interfacial and ligand-intrinsic dipole. Because valence and conduction bands are shifted in the same way, a change is not apparent in the UV-vis absorption onset or in PL spectroscopy, however, the absolute energy levels are critical for optoelectronic devices and catalysis and may be characterised for example with ultraviolet photoelectron spectroscopy. This effect has been exemplified for a variety of ligands on PbS-QDs [102].

Band gap.
Ligands that form strong metal-ligand bonds can create interfacial states with mixed QD-ligand character which can lead to a delocalisation of the photoexcited hole into the ligand shell, essentially relaxation of the quantum confinement. As a consequence, valence and conduction band may be shifted asymmetrically which implies a change in the band gap. This effect was reported for phenyldithiocarbamate (PTC) capping of CdSe quantum dots that reduced the optical band gap by 0.2 eV [103].

Charge transfer.
The nature of the capping ligand shell can affect the rate of photoinduced charge transfer to acceptor molecules in solution. For example, the length of HS-$(CH_2)_n$-COOH-capped CdSe QDs was correlated with ET rate to (poly)viologen acceptors. For shorter ligands ($n \leq 7$), a decrease in ET rate with n was observed, whereas for ($n \geq 10$) the ET

still decreased but much less than expected based on the trend for the shorter ligands. The observation was explained by the formation of ligand bundles on the QD surface which render the tunnelling process slow by denying viologen units access to the QD interface [104]. In a different example, the partial exchange of native oleate ligands with octylphosphine disordered the ligand shell in QD-catalysed C-C coupling, leading to an increase in the active surface area and ultimately accelerated hole transfer [105].

Surface properties

Solubility.
The composition of the particle ligand shell determines its solubility in various solvents. Most particles with their lipophilic native ligands are only soluble in organic solvents. The solubility in polar solvents can be enabled through the introduction of charged ligands with a carboxylate or ammonium group [106]. Alternatively, the native ligands may be removed in a process called "ligand stripping" and replaced with weakly coordinating anions [107] which renders the surface hydrophilic as well.

Surface charge.
The presence of charged functional groups in the capping ligand may not only enable the solubility in polar solvents but also facilitate electrostatic interactions with immobilised molecules. For example, modifying the surface charge enabled stronger interactions with electron acceptors such as a viologen cyclophane complex [108] or immobilisation of a molecular CO_2 reduction Fe-porphyrin electrocatalyst [109].

Surface proton concentration.
The local concentration of protons is a key determinant in QD-catalysed reaction because many reactions (*e.g.* CO_2 reduction) involve proton transfers. Capping ligands and its headgroups can thereby act as proton shuttles. This was exemplified with the reversible protonation of phosphonic acid headgroups by varying solution pH which was monitored by a slight red-shift (47-meV) of the band gap of CdS-QDs [110].

1.2.5 Thiol-QD interactions

Thiols are commonly used as capping ligand anchoring groups, particularly within this dissertation and will therefore be reviewed in the following.

Physical properties

The S-H bond dissociation energy (BDE) of alkanethiols is generally around 85-90 kcal mol^{-1} [111]. The BDE can be lowered through the presence of substituents that can stabilise the corresponding thiyl radical, for example aromatic residues. This effect can

be further promoted through electron-donating para-substituents on the aromatic ring, for example, an amino group, thus explaining the low S-H bond of 4-aminothiophenol of 70 kcal mol^{-1} [112]. The BDE is closely related to the pKa of thiols which similarly shows a strong dependence on the chemical structure of the organic residue neighbouring the thiol. Similar as before, the pKa is generally lower for residues that can stabilise the negative charge of the thiolate such as aromatic or electron withdrawing groups. For example, aromatic thiols exhibit a pKa of ca. 7, thioacetates of ca. 8 whereas aliphatic thiols have a significantly higher pKa of 10+ [113].

Reactivity

Radical formation.

A one electron oxidation leads to the formation of a thiyl radical:

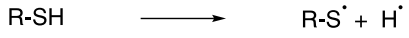

FIGURE 1.8: One electron oxidation of thiols leads to the formation of a thiyl radical.

For this reaction, relatively strong oxidation agents such as other radicals ($OH^{\bullet}$, $NO_2^{\bullet}$, O^{2-}) are needed. Alternatively, a photoinitiator may be used to generate a radical that abstracts a hydrogen from the thiol forming the thiyl radical [114]. The bond dissociation may be introduced via UV-light itself. The resulting thiyl radials are very reactive and commonly add to alkenes and alkynes which is known as the "thiol-michael-addition" [113].

Disulfide formation.

Thiols are commonly oxidised in a S-S coupling reaction forming a disulfide bridge (Figure 1.9) [115]:

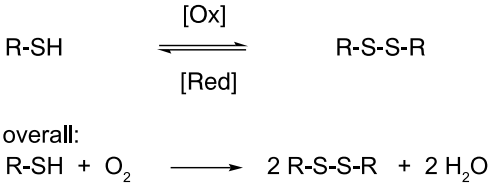

FIGURE 1.9: The oxidation of thiols can lead to the formation of disulfides.

Oxidation reagents include O_2, I_2, peroxides, etc. but the process is reversible with a reducing agent such tris(2-carboxyethyl)phosphine (TCEP) [116]. The oxidation with O_2 (under aerobic conditions), so-called "autoxidation" is typically facilitated by a metal catalyst and proceeds via a mechanism which involves the formation of a thiyl radical from a deprotonated thiolate [115]. Therefore, the lower the pKa of the thiol and easier

its deprotonation, the faster the oxidation proceeds. The disulfide formation may also be prevented at acidic conditions which ensure protonation of the thiol.

Because the thiol-QD interaction is reminiscent of the adsorbate-substrate interactions in SAMs [89], it is worthwhile to examine the known literature of thiol-substrate interactions on flat surfaces. Au is thereby the most widely characterised substrate amongst common SAMs due to its lack of an oxide layer and high chemical stability in water. In SAMs, the S-Au bond is considered a fairly strong bond with a strength of the homolytic Au-S bond of approx. -50 kcal/mol [89]. The interaction and the nature of the binding was examined on flat Au surfaces as well as Au nanoparticles. It was generally believed that the thiol-metal bond is well described as surface-bound thiolate with no hydrogen present in this bond [117]. Nevertheless, the fate of the hydrogen is ambiguous and the formation of H_2 was often proposed [118, 119]. By monitoring the open-circuit potential of a Au electrode, it was shown that the thiol adsorption proceeds via electron donation from the sulfur to Au while the S-H bond is weakened, which subsequently leads to dissociation and reduction of the proton to form H_2 [119]. In solution in the presence of oxygen, conversion to water was considered [89]. On the other hand, also the adsorption of 'intact' S-H has been predicted theoretically [118] and observed experimentally for methanethiol under vacuum on Au [120] and Ag [121]. This was confirmed in solution by a study of alkylthiols on Au-clusters which showed via NMR spectroscopy that under certain conditions (high ligand loading), thiols can bind to Au "intact" as a S-H thiol [122]. In conclusion, it is evident that sulfur forms a strong bond to many noble metal surfaces and therefore acts as an anchor, however, the exact nature of the adsorption/-chemisorption of the S-H group on metal surfaces is complicated and likely depends on pressure, solvent, and the nature of the ligand (*e.g.* chain length).

The dissociation of a hydrophilic thiol (mercaptopropanol) ligands on CdX (X = S, Se, Te) QDs was examined by quantifying the nanocrystal precipitation pH through titration [123]. Essentially, the ligands were believed to bind to the QD surface via thiolates. Through lowering the pH of the solution to a certain value (precipitation pH), the ligands will be protonated and detach from the nanoparticle surface and the latter precipitate out. Interestingly, the precipitation pH (ca. 5.8 for CdSe) was independent of the concentrations of both QDs and ligands and the nature of the acid counterions, but rather dependent on the size and bandgap of the particles.

A combined computational/experimental study of mercaptopropionic acid (MPA) on ZnS showed strong binding of the thiolate to Zn surface atoms accompanied by the removal of thiolic hydrogen [124]. Thiols were also reported to bind to ZnSe, the material of focus of this dissertation. Alkane- and hydroxyalkanethiols were shown to bind to the ZnSe surface from an ethanolic solution. FTIR showed that longer chain alkanethiols

form well-defined monolayers on ZnSe crystals whereas shorter alkanethiols exhibit less conformational order [125].

Photochemical oxidation of thiols

The oxidation of thiols is a common phenomenon (see above) and was also reported using photocatalysts instead of (sacrificial) oxidation agents.

An early report examined the photo-oxidation of thiols on CdSe nanocrystals for a range of thiols in the context of the nanocrystal's photostability [99]. It was shown that photogenerated holes in the nanocrystals were trapped onto the thiol ligands bound on the surface and subsequently oxidised to form disulfides, which dissolved in solution. If there were excess free thiols in solution, they could replace oxidised thiols on the surface and therefore further protect the nanocrystal from photo-oxidation. Once all thiols were depleted, the nanocrystal itself photo-oxidised.

Thiols may act as electron donors on Ni-decorated CdSe-QDs as photocatalysts and were oxidised to the corresponding disulfide and molecular hydrogen [126]. The mechanism was proposed to start with the initial deprotonation of the thiol, forming a thiolate, which reductively quenched photogenerated holes on the QD surface producing sulfur-centered radicals and subsequently coupled to form disulfides. In a follow-up study [127], the sulfur-centered radicals could be extracted in order to promote a different oxidation reaction, in this case the oxidation of alcohols to aldehydes and ketones. The employed thiol, mercaptopropionic acid (MPA) was considered a radical relay. The photo-oxidation of thiols to disulfides is not unique to QDs and has also been reported on perovskite nanocrystals [128] as well as iodide [129].

1.3 CO_2 Reduction

Within the scope of this dissertation, the emphasis of the photocatalytic reduction reaction (CO_2 vs. H^+) is towards CO_2 reduction, because the material investigated herein (ZnSe QDs) is active towards H^+ reduction without further modification (see outline in section 1.5). Therefore, CO_2 reduction is reviewed in this section in-depth and H^+ reduction is discussed alongside as a side-reaction. First, the fundamental principles of CO_2 reduction are reviewed on heterogeneous metal electrodes followed by molecular catalysts. An extract of the current literature of colloidal photocatalysts for CO_2 is presented thereafter. Finally, the combination of the latter materials forming so-called *hybrid* photosystems is summarised, consisting of colloidal light absorbers and molecular catalysts.

Generally, CO_2 reduction is challenging due to the stability of the CO_2 molecule [22]. CO_2 reduction may lead to a number of different products that are thermodynamically accessible and in addition, H^+ reduction which leads to the hydrogen evolution reaction is a competitive side-reaction with very similar half-cell potential. Some common reactions with corresponding half-cell potentials are depicted in the following [22]:

$$\begin{aligned}
CO_2 + 2H^+ + 2e^- &\rightarrow CO + H_2O & E^0 &= -0.53\ V \\
CO_2 + 2H^+ + 2e^- &\rightarrow HCOOH & E^0 &= -0.61\ V \\
CO_2 + 6H^+ + 6e^- &\rightarrow CH_3OH + H_2O & E^0 &= -0.38\ V \\
CO_2 + 8H^+ + 8e^- &\rightarrow CH_4 + 2\ H_2O & E^0 &= -0.24\ V \\
2H^+ + 2e^- &\rightarrow H_2 & E^0 &= -0.41\ V
\end{aligned}$$

(aqueous solution, pH 7, E^0 *vs.* normal hydrogen electrode (NHE), 25 °C, 1 atm, 1M)

Interestingly, the redox potentials for CO_2 reduction are near the potential for H^+ reduction which implies that in aqueous medium, there is always a competition with H_2 evolution. In addition, the CO_2 reduction reaction proceeds through several intermediates with often high kinetic barriers meaning that it proceeds at a lower rate than H^+ reduction. It is therefore a tremendous challenge in the field of CO_2 reduction to control and stir the reaction selectivity without excessive competition of H^+ reduction. In practice, a higher potential than the thermodynamic ideal (overpotential, as introduced above) is required to drive CO_2 reduction at a significant rate [29].

The two electron-products CO and formic acid (HCOOH) can be produced with relatively low overpotentials and high efficiencies on suitable catalysts, whereas multi-electron products tend to be kinetically challenging and require typically higher overpotentials and lower selectivities are observed [28]. C_{2+} products (ethylene, ethanol, propanol) can also be produced but few catalysts are capable of facilitating the challenging C-C coupling step efficiently. The question of the most desired reaction product is thereby controversially debated. Generally, multi-electron/multi-carbon products exhibit higher energy densities, however, the "normalised" energy density, *i.e.* the energy density per ET decreases, as for example shown for unbranched alcohols of various chain lengths with methanol offering a higher energy density than butanol [130]. At the current state of technology, short-chain simple building-block molecules are favourable and techno economic analyses have identified CO and formate as attractive targets, while also ethylene glycol and propanol show commercial potential [130, 131]. This PhD thesis was funded to a large degree by the *Christian Doppler Laboratory for Sustainable Syngas Chemistry*, which aims to develop materials to sustainably produce syngas. Aligned

with this goal, the focus within this dissertation is towards the generation CO from CO_2, which together with the by-product H_2 (syngas) renders a highly attractive and industrial relevant product. Syngas can be further converted to liquid fuels by established means of Fischer-Tropsch synthesis [31] and furthermore is a valuable substrate for the synthesis of building blocks for the chemical industry. The desired ratio for further use is thereby dependent on the use case. While a ratio of 1:1 (H_2 : CO) is required for the oxo-synthesis to aldehydes and oxo-alcoholes, a ratio in-between 1:1 and 2:1 is required for the Fischer-Tropsch process to liquid hydrocarbons, 2:1 is required for the synthesis of methanol and a ratio of 3:1 is used for methanation to produce methane [132].

1.3.1 CO_2 reduction mechanism

The fundamental mechanism of CO_2 reduction is better characterised on electrochemical surfaces rather than on photocatalysts so consequently the fundamentals of electrochemical CO_2 reduction are summarised in the following and many principles can be applied to photocatalysis as well [133].

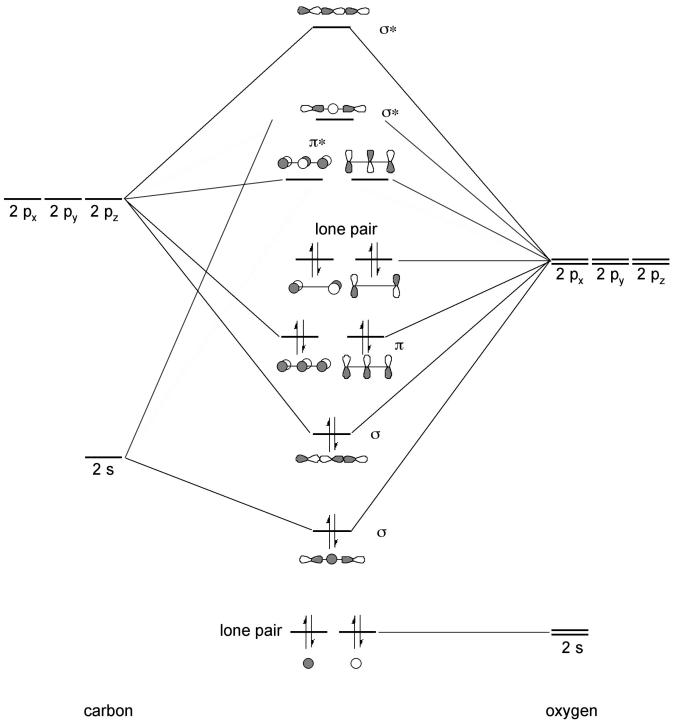

FIGURE 1.10: Molecular orbital (MO) diagram for a linear CO_2 molecule. Figure adapted from [134] under CC BY 3.0 licence.

The CO_2 molecule's high stability can be explained by the four occupied bonding molecular orbitals which are delocalised over the linear molecule, as depicted in Figure 1.10

[135]. Additionally, two non-bonding orbitals are occupied and localised at the two O-atoms. The lowest unoccupied molecular orbital (LUMO) is the anti-bonding $2\pi_u$ orbital with opposite signs of the central atom compared to the bonding $1\pi_u$. Occupying the LUMO through an electron transfer forms an anionic CO_2^- radical which is accompanied by bending of the molecule because this orbital can be stabilised in the bent form [136]. This reduction has a very negative redox potential of -1.9 V *vs.* NHE [137] but the anion has an appreciable average lifetime of ca. 60-90 μs [136] and thereby may be detected spectroscopically. However, this extremely negative redox potential does not take a stabilisation into account; an efficient catalyst can stabilise the radical by formation of a chemical bond which effectively lowers the required potential [28]. Indeed, nature has evolved extremely efficient catalysts such as carbon monoxide dehydrogenase (CODH) [138] and formate dehydrogenase (FDH) [139] which reversibly reduce CO_2 with minimal overpotential and almost unity selectivity. Besides the one-electron reduction of CO_2 to form CO_2^- (1), also a concerted proton-coupled electron transfers (PCET) have been proposed as first step in CO_2 reduction which lead to form either *COOH (2) or *OCHO (3) (Figure 1.11). In all cases, protons compete for surface sites to form adsorbed *H (4) which can lead to H_2 formation, a common by-product of CO_2 reduction in aqueous media, as described earlier.

$$CO_2 + e^- \rightarrow {}^*CO_2^- \quad (1)$$
$$CO_2 + H^+ + e^- \rightarrow {}^*COOH \quad (2)$$
$$CO_2 + H^+ + e^- \rightarrow {}^*OCHO \quad (3)$$
$$H^+ + e^- \rightarrow {}^*H \quad (4)$$

Surface bound intermediates are labelled with an asterisk in the following. The initial binding mode of the first intermediate was considered to determine the selectivity between CO and formate [140]. (1) and (2) bind to the surface via the C atom ("carboxyl intermediate") and lead to formation of CO, whereas *OCHO ("adsorbed formate intermediate") binds to the surface via the oxygen atoms (or one of them) leading to formate. The mechanism for CO is believed to further proceed via protonation of (1) to form (2) (as common intermediate) or direct to (2) followed by another PCET to form surface adsorbed *CO and subsequent desorption and release of CO (Figure 1.11). Experimental studies on metal electrodes found two major groups of metals which either prefer CO (Au, Ag, Zn, Pd) or formate (Pb, Hg, In, Sn), based on their binding energy for carbon-metal and oxygen-metal bonds [28, 141].

Cu is the only metal reported to produce other reaction products (besides CO and formate) including C_{2+} products (*e.g.* ethylene, ethanol, propanol, etc.) with high yields [28]. The multi-carbon products are believed to go through a common *CO intermediate and the unique feature of Cu was assigned to the "right" (*i.e.* intermediate) *CO adsorption energy relative to metals such as Au (low CO adsorption energy) where CO desorbs too fast and Pt/Ni, where CO adsorption is too strong to be further converted [142].

The $^*CO_2^-$ intermediate (1) is an often proposed intermediate for molecular electrocatalysts (transition metal complexes) where it is bound to a metal centre [143]. The metal centre is typically reduced before (for example from II to I) so electron density can then flow to CO_2 in order to form $^*CO_2^-$. Subsequent PCET or protonation leads to either *COOH or $^*COOH^-$intermediates (depending on pH) to finally release CO.

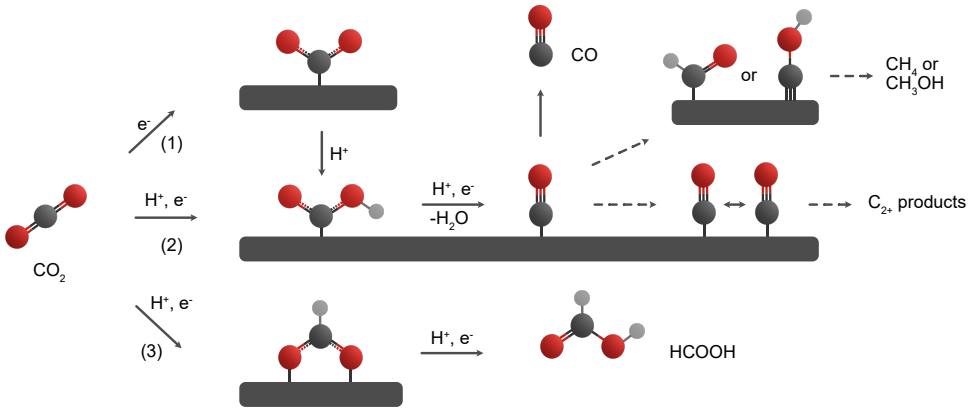

FIGURE 1.11: Overview of the most common electrochemical CO_2 reduction pathways on heterogeneous catalytic surfaces for selected reaction products.

In aqueous solution, CO_2 itself is being hydrated to form carbonic acid (H_2CO_3) which rapidly decomposes to H^+ and bicarbonate (HCO_3^-). The bicarbonate equilibria between $CO_2/HCO_3^-/CO_3^{2-}$ are pH dependent. Based on several reports that illustrate a linear reaction rate dependency to the CO_2 concentration, CO_2 is considered the main substrate in the reaction. Few reports suggest an active involvement of bicarbonate with formate as final product [28, 144, 145].

Computational investigations for CO_2 to CO reduction have found that the adsorption energies of reactive intermediates (here *COOH and *CO) are linearly correlated on most metals [146]. This explains why for example Au and Ag are good electrocatalysts for CO formation because they are limited by CO_2 activation and weakly bind *CO. In contrast, Pt, Pd or Ni are limited by the desorption of *CO, because the binding energy of the latter is too strong for efficient turnover. Based on this linear correlation, it is thereby impossible to increase the bonding strength of a single catalytic site for *COOH

without also affecting the adsorption energy of *CO. This phenomenon is referred to as *scaling relation*. The model also explains how enzymes catalyse CO_2 reduction reversible because the evolutionary optimised active site pocket allows to stabilise both intermediates differently, essentially deviating from the scaling relation. Braking scaling relations can be seen as one design principle for an efficient CO_2 reduction catalyst. It should be noted, that it is not the sole design principle and by itself does not guarantee a performant catalyst. It was suggested to aim to optimise a catalyst first by conventional means before attempting to break scaling relations (*e.g.* ligand stabilisation, nanoconfinement) [147].

1.3.2 Molecular CO_2 reduction catalysts

As briefly touched upon above (section 1.3.1), besides heterogeneous metal electrodes, CO_2 reduction can be facilitated by molecules based on transition metal complexes, so-called *molecular catalysts*. They can be employed in electrochemical processes by supplying electrons from an electrode surface but also by providing electrons from a photosensitiser/light absorber in a photo(electro)-chemical process. The literature on molecular CO_2 reduction catalysts is vast and has been reviewed in multiple exhaustive reports recently [13, 34, 148]. The following section aims to extract and present the most relevant catalysts, that either have been used in this work (based on earth-abundant metals such Fe, Co, Ni), have been employed in colloidal hybrid photocatalysts (see section 1.3.4) or can be considered as state-of-the-art.

It is noted that often the very best electrocatalysts were successfully employed in photocatalytic systems as well. There are several key measures to quantify a catalyst's performance:

1. The turnover numbers (TON) (with respect to the molecular catalyst) is a measure for the catalyst stability and defined as the number of product molecules divided by the number of catalyst molecules employed (TON = (n_{prod} / n_{cat}) [13]. The stated TONs cited in the following refer to the major carbonaceous reaction product (mostly CO).

2. The selectivity quantifies the catalyst's ability to produce one product preferably out of other products (selectivity = n_{prod} / n_{tot}) [13].

3. The onset potential E_{onset} indicates the minimum electrochemical potential necessary for a catalytic reaction to start for and can be determined by cyclic voltammetry [13].

4. The external quantum efficiency (EQE) indicates how efficiently absorbed photons are translated into reaction products and is defined as the number of product molecules formed divided by the number of incident photons used for irradiation ($EQE = z\ n_{prod} / n_{photon}$) where z equals the number of electrons (and consequently photons) necessary for the reaction [13].

One of the earliest examples of a CO_2 reduction molecular catalyst was reported by Hawecker, Lehn and Ziessel in the early 1980s with a Re(2,2'-bipyridine)$(CO)_3$X (X = Cl, Br, NCS) complex which has proven to be a selective catalyst for the electrochemical and photochemical evolution of CO [149–151]. Interestingly, the catalyst itself is photoactive and operates in the absence of an additional photosensitiser. This was studied in more detail and showed great dependence on the type of halogen ligand [152], however, light absorption was limited in the visible region. This limitation was overcome by attaching a Ru based photosensitiser with a strong visible light absorption forming a supramolecular dyad that served as catalytic motif [153, 154].

This early work inspired the discovery of many other metal complexes bearing polypyridyl ligands - for example based on Ru [155, 156]. The Ru bipyridine motif was successfully anchored to colloidal light absorbers (carbon nitride) by Ishitani and co-workers [157, 158] and also as part of the aforementioned dyad containing Ru photosensitiser and Ru catalytic units (RuRu') [159]. The latter system achieved remarkable activity for the production of formate ($TON_{Ru} = 33\ 000$) in organic solution and was also active in aqueous solution with reduced activity ($TON_{Ru} \sim 600$). The activity under aqueous conditions was further investigated and improved ($TON_{Ru} > 2000$) in a follow-up study [160]. This particular sensitiser-catalyst motif was subject to more studies, most recently on Al_2O_3 particles in which the adsorption density (surface coverage) of the supramolecular complex was related to the catalyst durability [161].

When the Re metal of the Re(2,2'-bipyridine)$(CO)_3$X was replaced with Mn, a new branch of molecular catalysts based on earth-abundant Mn was discovered [162]. These Mn complexes have also been used for photoreduction of CO_2. In combination with Ru photosensitisers, fac-Mn(bpy)$(CO)_3$Br was reported for CO_2 reduction to formate with a $TON_{Mn} = 149$ after 12 h irradiation in organic solution (DMF) [163]. An analogous fac-Mn(CN)(bpy)$(CO)_3$ catalyst evolved a mix of CO and formate under otherwise very similar conditions (Ru photosensitiser, TEOA-DMF solution) [164]. It should be noted that the Mn(bpy) motif is photolabile under irradiation of $\sim$ 410 nm light and releases CO upon excitation, which renders it unsuitable for certain photocatalytic applications [165].

A prominent class of molecular CO_2 reduction catalysts are metal tetraazamacrocycles (M(cyclam), M = Co, Ni). The ability of those complexes to reduce CO_2 electrochemically in a methanol-water mixture was reported by Eisenberg et al. [166]. Even in purely aqueous solution, the Ni-cyclam achieved a high activity for electrochemical CO_2 reduction (TON_{Ni} = 8000) on a mercury electrode with no H_2 detected [167]. Those promising results have sparked a large interest in cyclam-facilitated CO_2 electroreduction [168–170].

The encouraging electrochemical activity has led to the use of Ni(cyclam) based catalysts in purely photochemical systems as well [171–173]. The Ni(cyclam) was used in conjunction with a Ru bipyridine photosensitiser in aqueous ascorbate solution, however, the efficiency remained very low (TON < 5, EQE ∼ 0.06 %). Covalently connecting the Ru photosensitiser with the cyclam motif forming a supramolecular dyad did not improve the performance significantly [173].

The mechanism for the homogeneous CO_2 reduction by Ni(cyclam) was investigated computationally with a density functional theory study (Figure 1.12-A) [174]. In the first step, ET to the Ni centre reduces Ni^{II} to Ni^{I}, the "active" state, which forms a Ni-CO_2^- adduct. This binding only leads to a partial ET to CO_2 which is insufficient for its reduction. In the next step, the authors proposed a concerted proton-electron transfer which proceeds via an outer-sphere mechanism accompanied instantly by cleavage of the C-O bond via protonation from either H_3O^+or H_2CO_3, leading to a Ni-CO species. The final step involved desorption of CO. The reaction product CO was also predicted to inhibit catalysis by binding to Ni^+ which further prevents CO_2 binding and can ultimately lead to deactivation (poisoning) by reduction to Ni^0-CO.

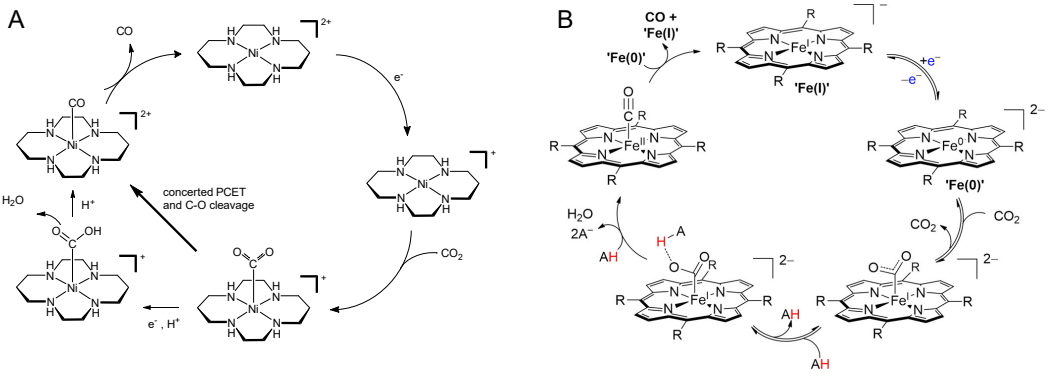

FIGURE 1.12: General mechanism for selected molecular co-catalysts for CO_2 to CO reduction. (A) Proposed mechanism for Ni cyclam promoted CO_2 reduction to CO, based on reference [174]. (B) General mechanism for Fe porphyrin catalysed CO_2 reduction, reprinted from [13].

Metal tetraphenyl porphyrins (M = Fe, Ni, Co) represent another widespread class of molecular CO_2 reduction catalysts. In particular, the adaptability of the molecule by functionalisation of the phenyl groups with various functional groups renders this family

of catalysts attractive and can impact the solubility, electronic properties, transition states amongst other properties [13]. Savéant and co-workers pioneered this catalyst and found Fe porphyrin as an efficient electrochemical CO_2 reduction catalyst in organic solution [175]. A general mechanism for Fe porphyrin catalysed CO_2 reduction is depicted in Figure 1.12-B. While the performance and stability of this early system was mediocre, a breakthrough in activity was achieved by introducing phenolic groups in all ortho positions which significantly accelerated electrocatalysis and was assigned to the local availability of protons associated with the phenolic -OH substituents [176]. Once again, in subsequent work, the performance of this catalytic motif was improved by introducing four charged trimethylanilinium groups which led to a record peak turnover frequency of 10^6 s^{-1} [177, 178]. The extraordinary activity was explained with coulombic stabilisation from the positive charges of the trimethylanilinium which may interact with the negative charge of the initial Fe^0-CO_2 adduct.

This prominent Fe porphyrin catalyst was subsequently employed in photocatalysis. By using an organic metal-free photosensitiser purpurin, it achieved a TON_{Fe} = 120 with almost unity selectivity in acetonitrile/water (1:9 v/v) solution [179]. The same catalyst was also shown to catalyse the 8-electron reduction of CO_2 to CH_4 when used with a highly reducing Ir photosensitiser in homogeneous acetonitrile solution [180]. Recently, the Sakai group demonstrated that a Co tetraphenylporphyrin with four negatively charged sulfonate groups, previously only associate with water oxidation [181], is active towards CO_2 to CO reduction with the aid of a $[Ru(bpy)_3]_2^+$ photosensitiser [182]. The homogeneous photosystem achieved a TON_{Co} of 926 with a high CO selectivity of 82% in fully aqueous solution.

Metal 2,2':6',2"-terpyridines (M = Fe, Co, Ni) were reported in the 1990's for CO_2 reduction [183] and more recently investigated electrochemically by Fontecave et al. It was found that the Ni terpyridines favour CO over H_2 selectively and that the Co-based complexes generate a mixture of CO and H_2, depending on the applied potential [184]. The competition between H_2 and CO for the Co-complex was further investigated by systematically changing substituents and it was found that the less active catalysts for H_2 evolution are the more selective CO_2 reduction catalysts [185]. In our research group, the Ni terpyridines were the first reported example of a hybrid heterogenised photosystem free of precious metals in which the molecular catalyst reduces CO_2 with electrons provided from the semiconductor quantum dot (more details see below) [186]. A Co terpyridine featuring a phosphonate group was used on a mesoporous TiO_2 scaffold with a light-harvesting silicon electrode, which represented the first example of a photocathode free of precious-metal components [187]. Under all tested conditions, the catalyst generated a mixture of H_2, CO and formate which was dependent on the composition of the solvent mixture (acetonitrile/water). The same catalyst showed a dependence

of the product selectivity on the applied potential on La- and Rh-doped $SrTiO_3$ and approached close to unity formate selectivity at 0.5 V *vs.* RHE [188]. This example illustrates how a catalyst's product selectivity can depend on many factors including the solvent, applied potential and chemical environment and will be discussed in more detail in section 1.4.

Co phthalocyanines have been known for CO_2 reduction since 1984 [189] and interest in this catalyst family sparked again recently. A perfluorinated cobalt analogue was reported to electrocatalytically reduce CO_2 in aqueous solution with high activity and selectivity and was successfully coupled to an anode for water oxidation [190]. The high activity was assigned to the inductive effect of fluorine substituents that make it less prone to product poisoning. Co phthalocyanines are particular suitable on carbon scaffolds; as demonstrated for immobilisation [191] or polymerisation [192] on a carbon nanotube electrode reaching high activities (FE $>$ 90%) and selectivities. In this research group, a Cobalt phthalocyanine was polymerised on mesoporous carbon nitride for efficient photocatalytic CO_2 to CO reduction in organic solvents [193].

First reported for CO_2 electroreduction in 1995 [194], metal quaterpyridine complexes based on Fe and Co were described in CO_2 photoreduction in 2016 [195]. In the presence of a $Ru(bpy)_3^{2+}$ photosensitiser, the Co complex achieved a remarkable TON_{Co} of 2660 for CO production with 98% selectivity in organic solution (acetonitrile) [195]. A number of follow-up studies have appeared since, in particular from Mark Robert and co-workers, reporting a Cu based analogue [196], mechanistic studies [197, 198] and interfacing it with carbon nanotubes [199]. The latter study showed efficient electrochemical CO_2 to CO reduction with near-unity selectivity in aqueous solution and demonstrated that this catalyst can perform on a nanoporous conductive carbon electrode approaching activities of noble metals electrocatalysts. Similarly, the Fe quarterpyridine analogue performed well in conjunction with mesoporous carbon nitride as light absorber (see below) [200]. Most recently, the Co quarterpyridine complex was covalently linked to mesoporous carbon nitride through an amide bond which led to selective CO production in acetonitrile while being remarkably robust ($\sim$ 4 days of irradiation) [201]. Synthetic modifications of this catalyst motif have led to a bimolecular analogue that selectively reduces CO_2 photochemically to formate or CO, which was adjustable depending on the conditions (basic vs. acidic) and assigned to the Co catalytic centres acting in synergy [202]. In a different synthetic approach, the quarterpyridine moiety was expanded by introducing phosphonate anchoring groups, which enabled it to perform on $Cu(In,Ga)Se_2$ (CIGS) semiconductor forming an earth-abundant photocathode operating in water [203].

Comparing the above-described range of molecular CO_2 reduction catalysts, a few universal themes become evident (here in the case of CO_2 to CO reduction). Generally,

the metal centre needs to be reduced as a first step. This enables in the second step for electron density to be transferred back towards the CO_2 molecule by binding the molecule in its bent CO_2^- form. Subsequent protonation or PCET lead to COOH or $COOH^-$, departure of H_2O, and ultimately to CO. This mechanistic pathway is thereby reminiscent of the one on heterogeneous metal electrodes with the difference of the catalytic site being a defined single-site metal centre. Molecular catalysts thereby offer the possibility to fine-tune, not only the intrinsic electronics but also to modify the immediate surroundings of the catalytic site. This approach can be used to introduce non-covalent interactions which may benefit catalysis or introduce anchoring groups to immobilise the catalyst on a certain template. This in parts explains why this molecular approach gained tremendous attention in laboratories around the world, even though their stability is often only on the order of hours/days and may impose limits on the practical applicability.

1.3.3 Colloidal photocatalysts

In addition to heterogeneous metal surfaces and defined molecular transition metal catalysts, CO_2 reduction can also be achieved on colloidal photocatalysts. The following section summarises the literature of colloidal photocatalysts in the absence of molecular catalyst, which is generally less systematic and lacks some of the mechanistic insights developed in heterogeneous electrocatalysis and molecular photocatalysis. The literature is vast [204, 205] and therefore a selection of examples is presented of systems that (1) operate in aqueous solution/suspension (in contrast to solid-state catalysts that operate in the presence of CO_2/water vapour) and (2) where evidence of the origin of CO_2 reduction was provided through isotopic labelling.

The mechanism of CO_2 reduction of the following reported literature excerpts is likely to depend on multiple factors such as the semiconductor type, specific surface facet, defects type and defect density [18].

Metal Oxides

TiO_2 is a common light absorber and widely studied photocatalyst. Sensitisation of TiO_2 particles (on a silica/Fe_3O_4 support) with dyes based on Ru(bpy) [206, 207] improved the light absorption of TiO_2 into the visible part of the solar spectrum and enabled methanol formation on the TiO_2 of up to 2.5 mmol g^{-1} after 2 days of irradiation. A different strategy to improve the TiO_2 photoactivity involves doping with heteroatoms, such as Cu. The latter was incorporated into the TiO_2 matrix and the resulting Cu-TiO_2 photoreduced CO_2 to formic acid and CO under UV-light in aqueous solution (2.5 and 26 μmol g^{-1} respectively) containing sulfide as electron donor [208].

Besides TiO_2, many other metal oxides were reported as photocatalysts in the context of CO_2 reduction. For example, Nb_3O_8 nanosheets [209], $La_2Ti_2O_7$ [210], $ZnGa_2O_4$ [211] and Zn-doped Ga_2O_3 [212] were shown to act as light absorbers and subsequently as photocatalyst for CO_2 to CO reduction when decorated (*i.e.* surface-modified) with common CO_2 reduction metals such as Ag or Cu (see section 1.3.1 above). However, the exact mechanistic pathway often remained unclear. In addition, various layered double hydroxides based on Ni and Al showed activity for CO and to a lesser extent for CH_4 from CO_2 reduction which depended on the Ni-Al ratio and the presence of counter ions, which showed peak performance for Cl^- attributed to quenching photogenerated holes [213].

Quantum Dots

The ability of bare QDs to catalyse CO_2 reduction is often very poor, so it is necessary to apply some surface modification strategy. Besides supplying molecular co-catalysts based on transition metal complexes (see section 1.3.4), doping with heteroatoms was reported as another method to enable light-driven CO_2 reduction. Doping Ni^{2+} into CdS-QDs significantly increased the activity towards CO_2 to CO reduction and the doping was shown to be essential rather than mixing Ni-salt with QDs or Ni-surface modification [214]. Interestingly, the Ni-doping only marginally changed the CdS band structure but rather acted as a catalytic site for CO_2 reduction. The Ni:CdS approached nearly unity selectivity towards CO with CH_4 as a marginal side product and effectively suppressing H_2 evolution, even though the reaction proceeded in aqueous medium.

CdSe QDs were also reported recently for CO_2 to methanol reduction and the tunable size was used in order to fine-tune the bandgap in a way to gain sufficient driving force for CO_2 reduction but insufficient for H_2 evolution thereby omitting the parasitic side reaction [215]. Separation of photogenerated charges and their diffusion length were further optimised by forming a composite with carbon nitride nanosheets which supplied a large area framework to immobilise the QDs.

Removal of MPA ligands and surface enrichment with Cd-sites improved the activity of CdSe-QDs for CO_2 to CO reduction reaching unprecedented 789 $mmol_{CO}$ g^{-1} h^{-1} in organic solvent (triethylamine/dimethylformamide) [216]. It was found that the Cd/Se ratio was key to achieve high activity and peaked for a 6.5 excess of Cd. Spectroscopic investigations led to the proposal of a mechanistic pathway that proceeds via a Cd-$C_2O_4^-$ intermediate, which was previously detected spectroscopically by Frei and co-workers [217].

Combining the two materials mentioned above based on CdX (X=S, Se) led to another improvement in activity. CdSe/CdS core/shell QDs photocatalytically convert CO_2 to

CO with high selectivity and an activity of up to 413 $mmol_{CO}$ g^{-1} h^{-1} in the presence of a sacrificial oxidation reagent in organic media [218]. The system also operated when coupled to a useful oxidation such as oxidation of 1-phenylethanol, however, with much lower activity. The mechanism was further investigated through DFT calculations. Interestingly, the CO_2 adsorbed on Se vacancies, not Cd, to form a surface adsorbed $^*CO_2$ which went via a PCET to $^*COOH$ and subsequently to H_2O and $^*CO$ which desorbed from the surface. This is similar to a common reported mechanism in metal-surface promoted electrocatalytic CO_2 reduction (section 1.3.1).

A new addition to the QD-photocatalyst library was recently introduced by $CuAlS_2$/ZnS core/shell QDs featuring a small bandgap of 1.5 eV [219]. The QDs were grown via asymmetric ZnS growth on $CuAlS_2$ through the epitaxy of two different crystal structures leading to an asymmetric morphology which aided its photophysics. The QDs were active for CO_2 to formate reduction without the need for an additional co-catalyst. The authors claimed that aqueous sodium bicarbonate, not CO_2 is the actual substrate without providing further mechanistic details.

PbS QDs were interfaced with TiO_2 particles to enable absorption (*sensitised*) of low frequency violet to orange-red light [220]. The PbS particles were able to inject electrons into the TiO_2 CB which was subsequently utilised for CO_2 to $CO/CH_4/C_2H_6$ reduction, however, the activity was very low (< 2 μmol product g^{-1} h^{-1}).

Material hybrids and others

CdS QD-deposits on a core of sodium trititanate nanotubes modified with elemental Cu deposits showed activity for CO_2 to multi-carbon products (C_{1-3}) under visible light irradiation. Photogenerated electrons were transferred from the CdS light absorbers via the nanotubes to the Cu catalytic sites which facilitated the multi-carbon product formation while photogenerated holes were quenched by water [221].

A Cu_2O/reduced graphene oxide composite achieved high activity for CO_2 to CO reduction [222]. The Cu_2O thereby acted as light absorber and reduced graphene oxide accelerated the transfer of photogenerated electrons by forming a heterojunction reaching a quantum efficiency of 0.34%.

CO_2 reduction was recently achieved on a three phase interface between Pt-decorated carbon nitride modified with a hydrophobic polymer. The surface was enriched with CO_2 in the hydrophobic pocket and enabled CO_2 reduction on the Pt sites while suppressing the competing H_2 evolution [223].

QDs based the emerging class of inorganic perovskites (*e.g.* $CsPbBr_3$) were also reported for photocatalytic CO_2 reduction, however, due to their limited stability in aqueous

solution only in organic solvents or in organic/water mixtures with a vast excess of organic solvent [224–226].

For completeness, it should be noted that also metal-organic frameworks (MOFs) were reported for photocatalytic CO_2 reduction, however, mainly in organic solvents [204, 227–229].

1.3.4 Colloidal hybrid photocatalysts

A hybrid photocatalytic system comprises a light harvester (photosensitiser/light absorber) and a molecular CO_2 reduction catalyst based on transition metal complexes. This strategy offers the advantage of combining the selectivity of molecular catalysts with a photosensitiser of choice, offering a range of options depending on the application. Because the molecular catalyst can also be used electrochemically, it is sometimes also called a molecular *electrocatalyst*. In this context of combining it with a solid-state light absorber or molecular photosensitiser, the molecular catalyst will be referred to as *co-catalyst*.

The following section summarises reports on colloidal hybrid photocatalysts with an emphasis on first row transition metal complexes (Fe, Co, Ni) and systems that operate in water. The section is grouped by the material class, starting with carbon-based light absorbers, followed by metal oxides and finally QDs. For completeness, it should be noted that systems based on precious metals and systems in an excess of organic solvent have been reported [42, 157, 159, 160, 230–234]. In particular, the formate-producing Ru-bipyridine motif, introduced in section 1.3.2, was subject of many reports, first on carbon nitride [157] and also as part of a molecular dyad with a Ru photosensitiser on Ag-decorated carbon nitride [159, 160] and on Ag-decorated TaON [230, 231]. The Ag thereby acts as "electron sink" to more efficiently extract photogenerated electrons and aids ET to the molecular unit.

Inspiration can be drawn from nature. Enzymes such as CODH or FDH, as introduced earlier (section 1.3.1), are able to reduce CO_2 with marginal overpotential. In recent years, these biocatalysts were successfully interfaced with artificial light absorbers and achieved remarkable activities. Especially TiO_2 was established as suitable catalytic scaffold (sensitised with molecular dyes to enhance its light absorption) and acted as excellent photocatalyst to drive CO_2 reduction with CODH and FDH [235, 236]. Interfacing enzymes with inorganic light absorbers is thereby not limited to TiO_2 or metal oxides and was also shown on CdS nanocrystals [237]. While this inspiring approach can teach scientists how to improve artificial catalysts and optimise electron transfer,

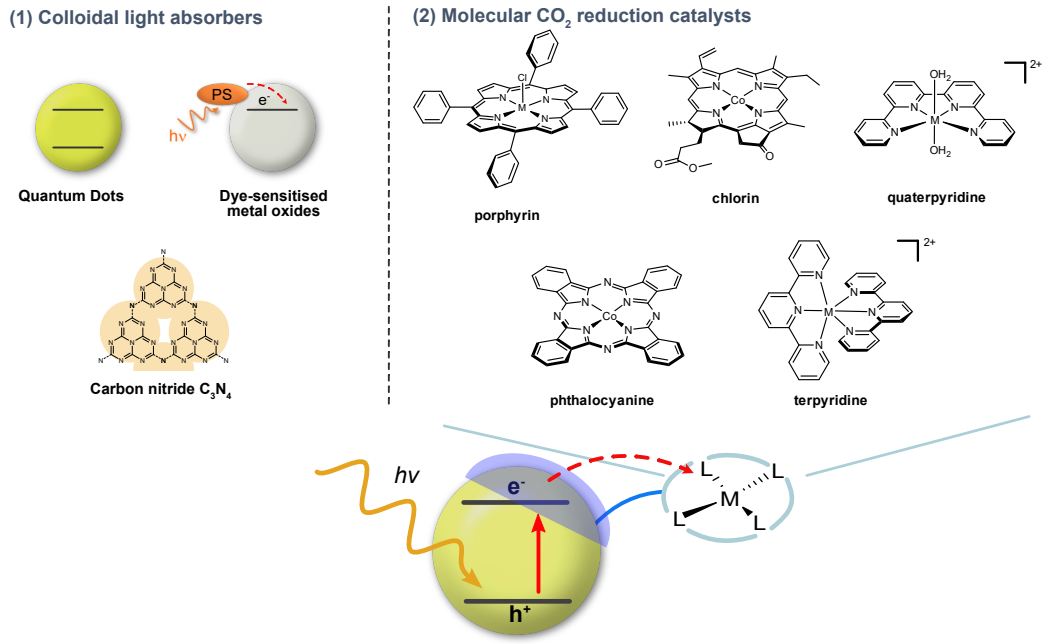

FIGURE 1.13: Overview of reported colloidal light absorbers and selected examples of molecular CO_2 reduction co-catalysts (based on first-row transition metals) which have been utilised in hybrid CO_2 reduction photocatalysts. Shown are the main catalytic motifs, anchoring groups have been removed for clarity.

the use of enzymes in practical applications is limited due to the lengthy purification, limited availability and low stability.

Carbon-based light absorbers

An Fe-porphyrin catalyst functionalised with four carboxyl groups was integrated with graphitic carbon nitride (C_3N_4) and showed CO_2 to CO reduction activity ($TON_{Fe} = 5.7$) with nearly unity selectivity under visible light irradiation in a methanol-water mixture [238]. The carboxyl groups were claimed to improve anchoring to C_3N_4 via H-bonding to the amino groups on C_3N_4 as well as lower the necessary reduction potential of the Fe catalytic centre due to their electron-withdrawing effect.

A Co-chlorin complex adsorbed on multi-walled carbon nanotubes was reported to reduce CO_2 to CO electrochemically [239] and in a follow-up study electrons could also be supplied photochemically with a Ru photosensitiser in the presence of TEA as electron donor [240]. The carbon nanotubes thereby acted as catalytic scaffold and may contribute to increase the local CO_2 concentration due to their hydrophobic nature (compare to section 1.4).

An Fe-quaterpyridine catalyst was combined with mesoporous graphitic carbon nitride (mpg-C_3N_4) and the hybrid photocatalyst exhibited high activity towards CO ($TON_{Fe} = 155$) with 97% selectivity in acetonitrile/TEOA solution [197]. The mesoporous nature of the employed C_3N_4 was shown to enhance catalysis by comparison to

graphitic (non-mesoporous) C_3N_4. The Co analogue of the quaterpyridine was recently covalently anchored on mesoporous carbon nitride through an amide linkage, which proved remarkably robust and helped to sustain activity in acetonitrile for several days (TON > 500, 98% CO selectivity) [201].

Mesoporous C_3N_4 was also utilised to in-situ polymerise a Co-phthalocyanine catalyst on the C_3N_4 surface [193]. This system achieved remarkably selective CO_2 to CO reduction under UV-visible light ($TON_{Co} = 90$) in acetonitrile and also showed some water tolerance. The drop in activity due to water was mainly attributed to phase separation of acetonitrile/TEOA/water and could be improved by employing dimethylacetamide as solvent which rendered the system to retain monophasic.

Dye-sensitised metal oxides

TiO_2 is the most common semiconductor within dye-sensitised metal oxides and its use traces back to the related field of dye-sensitised solar cells pioneered by Grätzel et al. [69]. However, the location of the TiO_2 conduction band provides too little driving force for most CO_2 reduction catalysts in purely aqueous solution [13]. Activity was only achieved in organic or organic/water mixtures in combination with a phosphonic-acid modified Re-(bipyridine)$(CO)_3$Cl catalyst [241]. In a similar study, the position of the TiO_2 flat-band potential was shown to shift positively with water addition explaining the low activity in purely aqueous solution [233]. A combination of Ru-dye-sensitised ZrO_2 and phosphonated Ni(cyclam) catalyst achieved CO_2 to CO reduction in water ($TON_{Ni} = 5$) [242]. Transient spectroscopy showed that the mechanism proceeds via an "on particle" pathway and direct electron transfer from the dye to the cyclam catalyst.

Quantum Dots

QDs have only recently been employed as light absorbers in hybrid CO_2 reduction catalysts [186]. One example utilised "ligand-free", BF_4^--capped CdS-QDs with a series of self-assembled Ni-terpyridine complexes as co-catalyst [186]. The CO selectivity was highly correlated to the co-catalyst loading and the highest selectivity (ca. 90%) was achieved with a thiol anchoring group on the terpyridine ligand, indicating the importance of a strong anchoring group in order to achieve efficient photocatalysis.

$CuInS_2$/ZnS core/shell QDs provided ample driving force for a positively charged Fe-porphyrin catalyst [109, 243] for CO_2 to CO reduction in water. The electron transfer from the light absorber to the catalyst was achieved by electrostatic association between the negatively charged capping ligand (mercaptopropionic acid, MPA) on the QDs and positively charged trimethylamino functional groups on the porphyrin catalyst. Additionally, the addition of various concentrations of K^+ allowed to fine-control

the agglomeration of the particles and their electrostatic interactions with the molecular catalyst.

A similar approach utilised the negative charge of MPA to electrostatically attract a dinuclear Co complex (Co_2L) bearing four positive charges [244]. The system achieved high activity for CO_2 to CO conversion in aqueous solution with 95% selectivity and a remarkable TON_{Co} of 1380.

An example for a covalent anchoring strategy was recently introduced by linking a Re bipyridine complex on $CuInS_2$-QDs via click chemistry [245]. The QDs were first capped with MPA to introduce a carboxyl group on the surface which was subsequently linked to dibenzocyclooctyne-amine by amidation followed by a Cu-free click reaction with azide-functionalised Re catalyst. Time-resolved infrared spectroscopy confirmed photoinduced electron transfer from the QDs to the attached Re catalyst which led to improved photoactivity compared to simply mixing the two compounds.

1.4 Local chemical environment effects in CO_2 reduction

Contents included in this section have been published as review article: A. Wagner, C. D. Sahm, E. Reisner, Towards Molecular Understanding of Local Chemical Environment Effects in Electro- and Photocatalytic CO_2 Reduction. Nat. Catal. ***2020****, 3, 775–786. Andreas Wagner contributed in researching/drafting the literature examples of this section and development of the classification scheme as well as the preparation of the figures in collaboration with the author.*

As touched upon in section 1.3.1, CO_2 reducing enzymes such as CODH and FDH are able to reduce CO_2 efficiently with marginal overpotential due to their evolutionary optimised active site pocket, even though their active centre metals are not considered amongst the most efficient metals (Mo, Fe, Ni) for CO_2 reduction. Furthermore, as discussed in 1.3.2, many molecular catalysts perform very differently depending on the support; for example a cobalt phthalocyanine is typically active towards CO_2 to CO reduction but also evolves significant amounts of methanol when immobilised on carbon nanotubes [246]. It becomes evident from the examples above that the local chemical environment is a key determinant in the design of efficient CO_2 reduction catalysts and can affect both activity and selectivity.

Therefore, this section summarises efforts that go beyond traditional single-site catalysis research and focuses on the modification of the local chemical environment of heterogeneous/heterogenised electro- and photocatalytic CO_2 reduction. Even though this thesis focuses purely on photo(electro)chemical CO_2 reduction, concepts and examples

from electrochemical CO_2 reduction are covered because many concepts are applicable to photochemistry as well.

1.4.1 Classification of local chemical environment effects

In this section, the term local chemical environment encompasses multiple physicochemical effects in close vicinity of the catalytic site that influence interfacial CO_2 reduction. The effects are classified in different sub-categories as illustrated in Figure 1.14. The examples are discussed in the following sections organised by the material-class such as surface, solution interactions and three-dimensional materials. A reference to the local chemical environment effect is given according to the classification introduced in Figure 1.14.

First, effects are distinguished that result in a modification of the intrinsic catalytic activity by changing the potential energy. This covers aspects that influence the energetics by changing the binding thermodynamics of the catalyst and thereby affect the reaction indirectly (*electronic modification, EM*). Spectator ligands can impact the activity of the catalytic centre to which they are bound to, but do not take part in the reaction mechanism (*EM-spec*). Catalysts are often deposited on a support material and may influence the catalytic centre through electronic interaction with the electrode surface (*EM-supp*). Anchoring groups are commonly used to attach (heterogenised) molecular catalysts to the electrode surface/support material and the nature of the anchoring group can in turn affect the reactivity of the catalytic centre (*EM-anch*). On the other hand, the intrinsic activity of a catalytic site can be affected directly by non-covalent interactions (*NCI*) on either substrate, product or reactive intermediates. This includes immobilised ligands (*NCI-im*), non-immobilised modulators and solvent-adsorbate effects (*NCI-sol*), confinement effects (*NCI-conf*) and adsorbate-adsorbate interactions (*NCI-ads*) in order to modify the reaction's chemical environment. Noteworthy, a stabilisation (or destabilisation) of a reactive intermediate bound to the surface can result in an accelerated (or decelerated) reaction, depending on the initial inherent material-adsorbate energy [247].

Second, there are many effects which influence the local concentration (*LC*) of components present in solution, for example CO_2, HCO_3^-, CO_3^{2-}, H_2CO_3, H^+/OH^-, water and counterions which influence CO_2 reduction as well as H_2 evolution. Diffusion gradients can develop due to the surface-mediated reaction (*LC-diff*) and differ from gradients that originate from differences in the local chemical environment (*LC-reg*). To illustrate this point further, it is useful to consider the local alkalinity which typically builds up in close proximity of the catalytic surface because both CO_2 reduction as well as proton

reduction consume protons during the reaction. This in turn affects the local CO_2 equilibrium and the concentration of all proton donors. This effect is more pronounced for morphologies which aid slow diffusion towards the catalytic centre such as nanostructured materials (*LC-diff*). In *LC-reg*, the local chemical environment directly affects the concentration profiles of components in solution without the reaction taking place (at equilibrium). For example, the introduction of a hydrophobic environment affects the solubility of CO_2 and the presence of water.

In the following sections, examples of local chemical environment effects are presented; electrocatalytic examples are followed by photocatalytic examples.

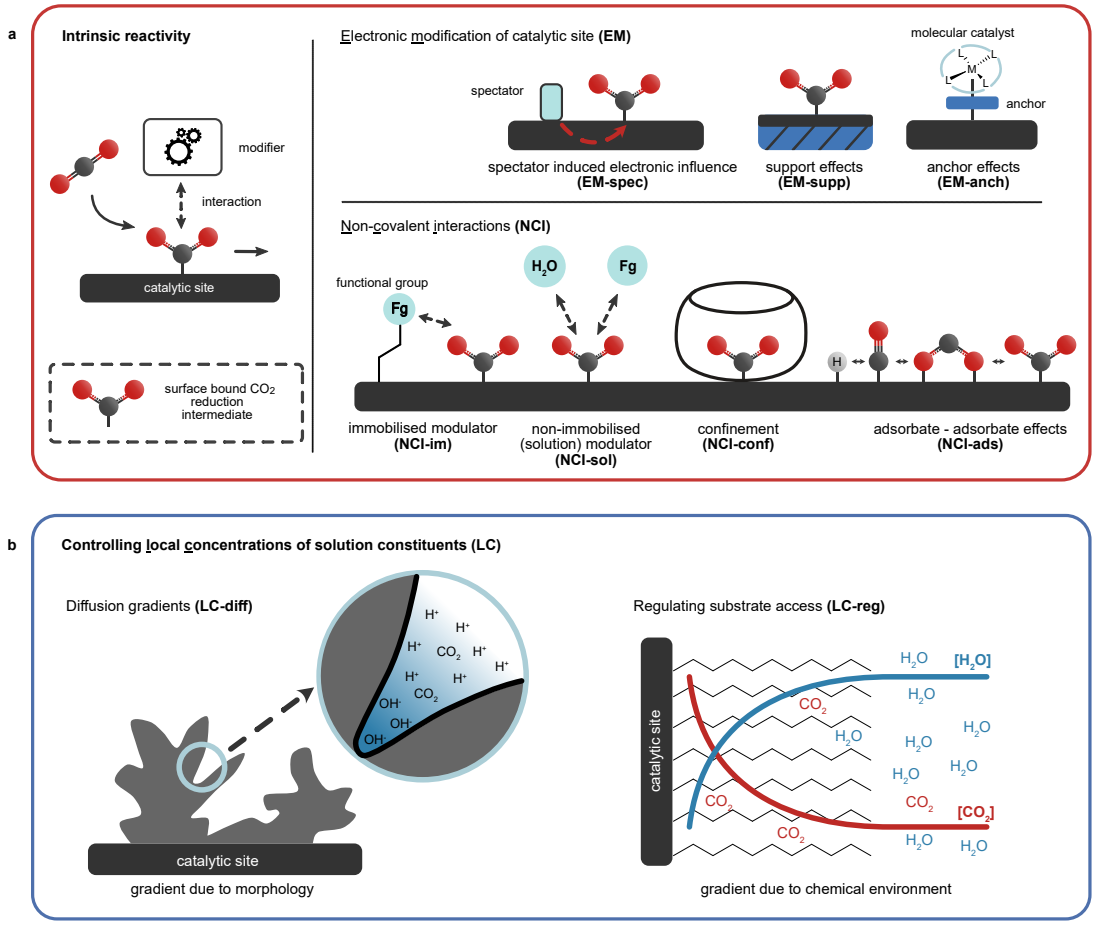

FIGURE 1.14: Classification of the local chemical environment effects in CO_2 reduction. Some categories can cover multiple effects (e.g. immobilised modulator can also behave as spectator inducing an electronic influence). The figure was adapted from reference [133] with permission from *Springer Nature*. *Andreas Wagner contributed in preparing this figure in collaboration with the author.*

1.4.2 Surface effects

Co-adsorbed species

Fundamentally, when a spectator molecule adsorbs on a catalytic interface, this reduces the number of sites available on this catalytic surface. Nevertheless, in CO_2 reduction, the activity of transition metal catalysts can be changed due to the formation of surface-adsorbed *CO during the reaction, because it weakens the binding energy of *H on the surface, which can lead to either inhibition or facilitation of H_2 evolution (depending on the type of the catalytic centre defining its inherent *H binding energy) [248]. This factor helps to explain noble metal electrocatalyst's high selectivity towards CO because of efficient suppression of H_2 evolution. Note, that the suppression of H_2 evolution does not automatically lead to better CO_2 reduction catalysts. This can be exemplified with an AuCd alloy where the incorporation of poor H_2 evolution catalyst Cd did not improve the performance of Au for CO_2 reduction [249].

Adsorbate-adsorbate interactions were found to play key roles in explaining activities of electrocatalysts. For example, the interplay between the adsorbed formate intermediate (*OCHO), adsorbed proton (*H) and adsorbed carboxyl intermediate (*COOH) was postulated as an explanation to rationalise the high CO-selectivity of Ag (*NCI-ads*) [250]. Specifically, *OCHO lowers the *H binding strength, which allows the reaction to proceed via the *COOH intermediate to yield CO.

Next to the effect of surface-adsorbed intermediates influencing each other, the competition of solvent and electrolyte components for binding sites influences the adsorption profiles of heterogeneous surfaces under catalytic conditions, which in turn can affect activity and selectivity [251]. Furthermore, inert *bridge*-bound *CO was spectroscopically detected on Au and Cu surfaces and has to be differentiated from *atop*-bound *CO which is catalytically active [252].

Molecular surface functionalisation

Functionalisation of catalytic surfaces with covalently bound molecules (which can feature specific functional groups) is essentially an extension of the concept of surface-bound spectator ligands. In the following, various functionalisation techniques are summarised and grouped according to their chemical nature.

Multiple ligands featuring a thiol group (**TH-4**, **TH-6**, **TH-9** (Figure 1.15)) were found to have a different reaction selectivity on Au and Ag [253–255]: Cysteamine (**TH-4**) was found to interact with *COOH leading to CO (*NCI-im*), while the carboxylate group of 2-mercaptopropionic acid (**TH-6**) was claimed to attract water near the catalytic site and thereby enhance H_2 evolution (*LC-reg*). An aminothiol with a longer hydrocarbon

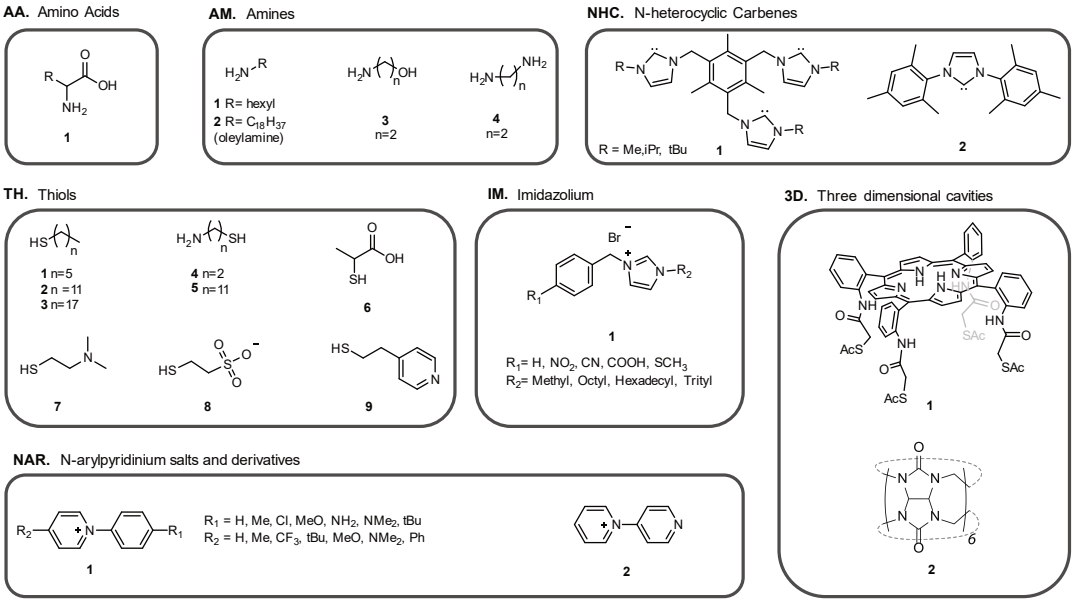

FIGURE 1.15: Surface-modifiers grouped into different classes used to modulate the local chemical environment around the catalytic site. AA: Amino acids, AM: Amines, NHC: N-heterocyclic carbenes, TH: Thiols, IM: Imidazolium, 3D: Three-dimensional cavities and NAR: N-Arylpyridinium salts and derivatives. The figure was adapted from reference [133] with permission from *Springer Nature*. *Andreas Wagner contributed in preparing this figure in collaboration with the author.*

spacer (**TH-5**) was found to be less effective. In addition, electron localisation based on the thiolate anchoring was proposed to support the stabilisation of intermediates [254]. Another study identified many surface modifiers, particularly amines (**AM-1, AM-2, AM-4**) and an alkylthiol (**TH-1**), which gave results that were comparable to cysteamine [256].

Modifying Cu electrodes with glycine (**AA-1**) was shown to increase the selectivity for hydrocarbons (methane and ethylene) [257]. The current density for hydrocarbon formation was enhanced (while the one for HER was reduced) although the total current density was reduced as well. This finding was rationalised by the stabilising interaction of NH_3^+ residues with *CHO (*NCI-im*) and blockage of the H_2 catalytic sites.

1-Octadecanethiol (**TH-3**) was used to alter a dendritic Cu electrode which resulted in enhanced faradaic efficiency (FE) for ethanol and ethylene generation which was associated with an increased hydrophobicity of the Cu electrode yielding to a higher local CO_2 concentration at the solution/electrode boundary (*LC-reg*) [258].

Cu was modified with a thin organic layer consisting of a set of dimerised N-substituted pyridinium additives (**NAR-1**) which led to inhibition of CH_4 and H_2 generation, while C_2 products were not affected. The authors proposed that the organic layer may suppress proton diffusion (*LC-reg*) or block catalytic sites for H_2 and CH_4 selectively [259].

Further spectroscopic investigations on **NAR-1** (R_1 = Me, R_2 = H) and **NAR-2** agree with a higher local pH for the organic layer obtained from **NAR-1**. It was found that N-heterocycles featuring free N-lone pairs (**NAR-2**) are in competition with CO for low-coordinated Cu sites and thus suppress the generation of more reduced intermediates and products [260]. More recently, the concept of N-arylpyridinium salts (**NAR-1**) was translated to a gas diffusion electrode (GDE) setup. The work discovered a stabilising influence of the N-centre with *CO that is *atop*-bound to the surface (*NCI-sol*) which was associated with the Bader charge of the N-centre [261].

A Pd electrode was modified with a tridentate N-heterocyclic carbene (NHC) ligand (**NHC-1**) which increased formate production [262] and was attributed to a higher electron density at the electrode due to the NHC modification. Further investigations based on DFT calculations showed a lowered energy barrier for both hydrogenations (direct *H transfer) of CO_2 to *COOH and *COOH to HCOOH. A different N-heterocyclic carbene (**NHC-2**) was employed to alter the surface of an Au electrode [263] and resulted in enhanced CO_2 to CO yield and selectivity. The effect was rationalised by σ-donation from the carbene in order to promote the first electron transfer to CO_2 (*EM-spec*). Furthermore, it was proposed that a geometric contribution from the NHC destabilises Au-Au bonds to create more defect sites which feature enhanced CO_2 reduction kinetics.

The surface of Au nanoparticles was functionalised with a tetradentate thioacetate porphyrin (**3D-1**) and resulted in improved electrochemical CO_2 reduction performance relative to ligand-free or oleylamine-capped (**AM-2**) particles. The effect was explained by improved adsorption of CO_2 on the Au surface that came with a lower energy barrier for the formation of a *COOH intermediate via a stabilisation effect (*NCI-im*). Electronic contributions (*EM-spec*) from the thiol were found to be insignificant [264].

A number of capping ligands based on imidazolium motifs were studied on Ag nanocrystals and multiple factors were found that are able to influence CO_2 reduction [265]. A nitro-group was identified as the best anchoring group which led to the highest FE for CO and was rationalised from electron donation to the Ag surface (*EM-spec*). The imidazolium group was the key determinant in interacting with CO_2 (see section 1.4.3) and an additional -octyl side chain aided catalysis through introducing a hydrophobic environment.

The concept of non-covalent interactions in order to tune the environment for CO_2 reduction initiated the use of host-cavity cucurbit[6]uril (**3D-2**) molecules on an Au electrode [266]. Spectroscopic work was able to confirm the reduction of CO_2 inside the cavity (*NCI-conf*) which represents the first step in building a 3D-controlled reaction environment around a heterogeneous catalytic site.

Capping ligands are a widespread tool to tune colloidal photocatalysts and have also been employed in the context of photochemical CO_2 reduction. An early example investigated capping ligands (**TH-2**, **TH-4**, **TH-8**) on CdS nanoparticles and their effect on the reactivity in organic solution. It was shown that the product selectivity of CdS was shifted from CO towards formate with increasing surface coverage of the hydrophobic alkylthiol ligand employed [267]. The authors proposed that CO was generated on Cd-sites, whereas formate on S-sites; the capping ligand would block Cd-sites selectively thereby leading to predominantly formate as the major reaction product (*LC-reg*). Amine-functionalisation of TiO_2 particles (**AM-3**) [268], carbon nitride (**AM-3**) [269] and reduced graphene oxide/CdS (**AM-4**) [270] was proposed to increase the affinity of the surface for CO_2 by chemisorption and subsequent conversion, even at low CO_2 concentrations (*LC-reg*). This observation is in contrast with the majority of electrochemical CO_2 catalysts, which typically are affected by a lower CO_2 concentration due to a first order rate dependence on the CO_2 concentration [252].

Support/Anchoring Effects

The fact that the selection of a carrier/support material can impact the catalytic activity is well established from thermal heterogeneous catalysis [271]. It is therefore unsurprising that there are multiple examples illustrating support effects within electro- and photocatalytic CO_2 reduction as well. A few highlights are presented in the following.

Molecular catalysts are commonly anchored ("heterogenised") on heterogeneous surfaces and the nature and process of the anchoring strategy can greatly affect the catalytic activity (*EM-anch*) [13, 272]. Co phthalocyanine, typically active towards CO_2 to CO reduction, was recently reported to also yield methanol with a FE of up to 40% when immobilised on carbon nanotubes [246]. The degree of coverage/loading of molecular catalyst [MnBr(2,2'-bipyridine)$(CO)_3$] was found to influence the CO_2 reduction activity of an assembly. It was shown that a high coverage results in an *in-situ* formed dimer which yields CO as the major product, whereas at low coverage, the mostly monomeric catalyst leads to formate [273]. Immobilisation of a Co bis(terpyridine) catalyst on a mesoporous TiO_2 electrode via a phosphonic acid anchor changed the reaction mechanism and reduced the overpotential compared to the freely diffusing analogue (*EM-anchor*). This finding was rationalised with the anchoring group which is non-innocent and can facilitate proton transfer to the catalytic centre [274].

In the field of photocatalysis, the concept of support effects can be translated to colloidal nanoparticles by means of core-shell structures. The addition of a basic metal oxide (*e.g.* MgO) shell around TiO_2 particles was proposed to increase the CO_2 chemisorption capacity and thus improved the photochemical CO_2 reduction [275]. A strong correlation was found between CO_2 chemisorption ability and the product formation rate, which

could be regulated by the basicity of the explored metal oxides. In a similar approach, layered double hydroxides based on Mg and Al were deposited on carbon nitride. The authors claimed to CO_2-enrich the surface in the form of interlayer CO_3^{2-} species and Mg was identified as the most suitable metal due to its highly basic cation [276]. Likewise, the introduction of a $Cr(OH)_x(CO_3)_y$ shell on Ag/Ga_2O_3 as light absorber was suggested to enhance the substrate concentration on the Ag surface which improved CO generation while suppressing competing H_2 evolution [277].

1.4.3 Solution interactions

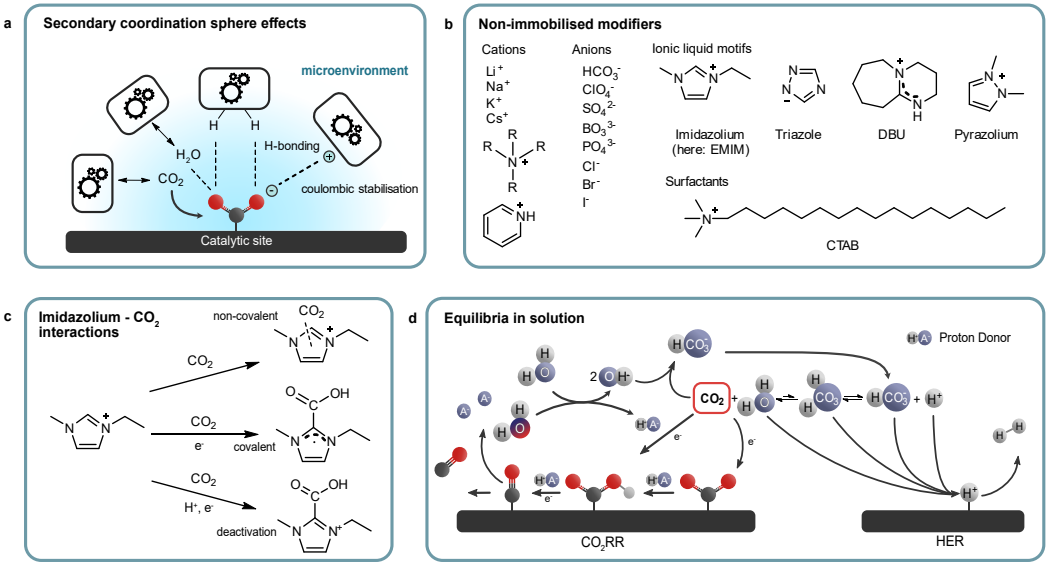

FIGURE 1.16: Local chemical environment effects in solution. (A) Different interactions with substrates such as CO_2 and H_2O and stabilising/destabilising second coordination sphere effects on surface bound intermediates. (B) Chemical structures of cation, anion, surfactant and ionic liquid modifiers. (C) Suggested reaction step of imidazolium-based IL mediating CO_2 reduction. (D) CO_2 is always in competition with H_2 evolution in aqueous solution and all solution constituents can affect each other. The figure was adapted from reference [133] with permission from *Springer Nature*. *Andreas Wagner contributed in preparing this figure in collaboration with the author.*

Besides species that are immobilised/adsorbed on the surface, the local chemical environment at the solid-liquid interface is also determined by interactions with species in solution. This includes cations, anions, additives such organic ionic liquids and surfactants, solvent molecules and CO_2 itself (Figure 1.16). Furthermore, the availability and concentration of proton donors is of high relevance for the competing H_2 evolution but also for CO_2 reduction. Many solution constituents qualify as proton donor (H_2O, H_2CO_3, HCO_3^- and H^+) and their relative presence is governed by the bicarbonate buffer equilibrium in aqueous media (Figure 1.16-d) which in turn is affected by CO_2 reduction: As described in section 1.3.1, in the first step, CO_2 reacts via electron transfer or via PCET to one of its various CO_2 reduction intermediates ($^*COO^-$, $^*COOH$,

*CO). Within the process of CO_2 conversion, two A^- and H_2O are by-products of the reaction and HA gets regenerated to form OH^-, enhancing the local alkalinity. OH^- can subsequently react chemically with CO_2 to form bicarbonate which reduces the local CO_2 concentration. At the same time, CO_2 and water quickly react to H_2CO_3 which decomposes rapidly to bicarbonate and H^+. Essentially, all reactions at the catalytic site (CO_2 reduction, H_2 evolution, CO_2/water/bicarbonate equilibrium, CO_2/OH^- equilibrium) are interconnected and affect each other, which renders selectively controlling the concentration of one species very challenging [278].

Cations

The presence and nature of alkali metal cations can, in principle, affect CO_2 reduction and was shown for various materials [279]. On the one hand, cations were shown to sustain a stable local pH and thereby stabilise the local CO_2 availability via buffering effects in the Helmholtz layer (*LC-diff*) [280]. On the other hand, the buffering capacity can not explain the influence of some cations on the activity for CO to C_2 products on Cu, because of the pH-independence of this rate-limiting step [281]. It was suggested that cations may also alter the reaction thermodynamics via non-covalent interactions with surface-bound intermediates (*NCI-sol*) [282].

The effect of cations can extend into the Helmholtz layer through electric fields and could be shown on many materials [283–285]. It was also shown that the different sizes of cations resulted in different surface charge densities affecting catalysis (*EM-spec*) [286]. Recently, computational investigations suggested that not only the electric field but also the interactions of cations with species in close proximity (water, CO_2, catalytic surface) affect CO_2 reduction [250]. The influence of cations in CO_2 reduction remains an active area of research [287].

Cu was subject to another study which assessed the interactions of alkyl ammonium cations featuring different chain lengths for CO conversion. It was found that the cations are not in competition for catalytic sites, but for longer chain lengths (>propyl) a replacement of water molecules close the electrode surface was suggested (*LC-reg*) [288].

Anions

The presence of various anions within the electrolyte during electrochemical CO_2 reduction can affect the product selectivity and is generally attributed to the anion's proton donor and buffering abilities [289]. Bicarbonate (HCO_3^-) is particular relevant for the many equilibria between CO_2 and other proton donors in solution (H_2O, H_3O^+, H_2CO_3) that influence pH-sensitive reaction on the interface [290, 291]. For H_2 evolution, HCO_3^- was found as a proficient proton donor on Au and the efficiency correlated strongly with

its concentration [252]. A CO_2 reduction intermediate transition state and its stabilisation was associated with a low concentration of hydronium (high OH^- concentration) under strongly alkaline conditions *(NCI-sol)* which rationalised a different product selectivity towards formate (rather than CO) [292].

The introduction of halides led to changes in the performance and selectivity of a Cu electrode. Besides a restructuring of the electrode surface, the influence on electrocatalysis was explained with charge donation of surface-adsorbed halides, which was most significant for iodide (*EM-spec*) [293]. The above selected examples illustrate that all solution constituents (cations, anions, solvent) require careful consideration and may act as competing reactants for surface sites to the substrates (CO_2, H^*) [251].

Ionic liquids

An early example of utilising ionic liquids (ILs) in electrochemical CO_2 reduction used 1-ethyl-3-methylimidazolium tetrafluoroborate (EMIM-BF_4) as additive in the electrolyte solution (18 mol%) with an Ag electrode. The authors suggested that the IL stabilises the CO_2 intermediate by forming a non-covalent adduct (Figure 1.16-c; *NCI-sol*) [294, 295]. Many reports of imidazolium-containing ILs have since appeared for CO_2 electroreduction, but the exact mechanistic influence remains controversial [296]. One proposal argued that catalysis proceeds via IL-CO_2 adducts formed by CO_2 binding to the Imidazolium-C_2 (Figure 1.16-c) [296, 297], but imidazolium cations with substituted C_2 centre showed similar reactivity, and the C_2-bound carboxylate was found as deactivation pathway due to its high stability [297, 298].

Second-coordination sphere stabilisation of $^*CO_2$ [298], H-bonding [299] and IL-mediated transport of CO_2 to the catalytic active site [300] have been reported with the IL being in close proximity to the active catalytic site (Figure 1.16-a, *NCI-sol* and *LC-reg*). The formation of a microenvironment was further supported by a study exploring the IL cation and anion as well as H_2O molecules effectively stabilising reactive intermediates on the surface of a Ag electrode [301]. Another study identified a potential-driven structural transition of the IL electrolyte in the double layer as a prerequisite for low-overpotential CO_2 reduction. In addition, a stabilisation of the high-energy $^*CO_2$ intermediate through non-covalent interactions of the imidazolium double layer film rather than an association with an individual imidazolium entity was proposed (*NCI-sol*) [302]. The structural transition induced a doubling of the electric field at the electrode surface and the concentration of water reduced the onset potential of this transition explaining the increased CO_2 reduction activity at higher water concentrations.

The promotional effect for CO_2 reduction is not unique for imidazolium-containing ILs (Figure 1.16-b) and other motifs include a superbasic IL with a tetraalkyl phosphonium

and a 1,2,4-triazole anion, which showed chemical binding to neutral CO_2 and thereby decreased the activation energy for formate production [303], a protic IL derived from 1,8-diazabicyclo[5.4.0]undec-7-ene that enhanced CO_2 reduction on Bi [304] and a pyrazolium IL with various organic substituents lowering the onset potential on Ag [305].

ILs have rarely been used in photocatalytic systems. A tetrabutylphosphonium pyridineoleate IL immobilised on a conjugated polymer as light absorber enabled direct capture of atmospheric CO_2 and H_2O and subsequent photocatalytic gas-phase conversion to CO [306]. The enhanced CO_2 reduction activity was attributed to favourable IL-CO_2 interactions. It is noted that some studies mentioned above were conducted in organic solution (acetonitrile) [297–299, 301, 303–305], and the concentration of IL and H_2O are varying significantly between different reports. Furthermore, the stability of imidazolium-based ILs during CO_2 reduction in water was found to be limited [307].

Organic surfactants

Organic surfactants are also known in the context of CO_2 reduction; for example cetyltrimethylammonium bromide (CTAB) which led to a reduction in H_2 evolution on several metal surfaces accompanied by an increase in CO/formate partial current densities [308]. The observation was rationalised with a rearrangement of H_3O^+ and Na^+ ions within the electrochemical double layer which led to reduction of concentration of competent proton donor for HER (*LC-reg*). Alkyltrimethylammonium surfactants with various lengths exhibited suppressed HER on Ag, which was most pronounced for dodecyltrimethylammonium bromide [309].

1.4.4 Three-dimensional materials

A third dimension at the electrode interface can add additional complexity but also open-up new routes of modifying the chemical environment by forming diffusion gradients (*LC-diff*) or changing the concentration of solution components close to the surface (*LC-reg*). In particular, the morphology can determine the buffer capacity within the diffusion layer due to slow diffusion within a 3D architecture, which is most pronounced in rough/porous structures (Figure 1.17-a) [310].

Metal-organic frameworks (MOFs) are a common group of materials which can modify the chemical environment for CO_2 electro- and photoreduction. For example, the earlier introduced molecular catalyst [MnBr(2,2'-bipyridine)$(CO)_3$] could be incorporated into MOF UiO-67 and exceeded its diffusional homogeneous equivalent for the production of formate (in DMF), which was ascribed to the robust nature of the MOF and inhibition of dimerisation of the Mn catalyst (Figure 1.17-b) [311].

Polymers can modify aspects of CO_2 reduction by both affecting heterogeneous catalysis as well as altering the local environment of molecular catalysts incorporated into polymeric scaffolds (Figure 1.17-c). They can not only provide a naturally (primarily hydrophobic) environment (*NCI-conf*) but also enable the inclusion of functional groups which can enhance CO_2 reduction (*EM* and *NCI*) directly and indirectly. Properties such as the porosity may influence access and release of molecular species and reduce blockage of heterogeneous catalytic sites. A number of polymer structures are depicted in Figure 1.17-c which were reported in the context of CO_2 reduction. A comprehensive survey is available elsewhere [133].

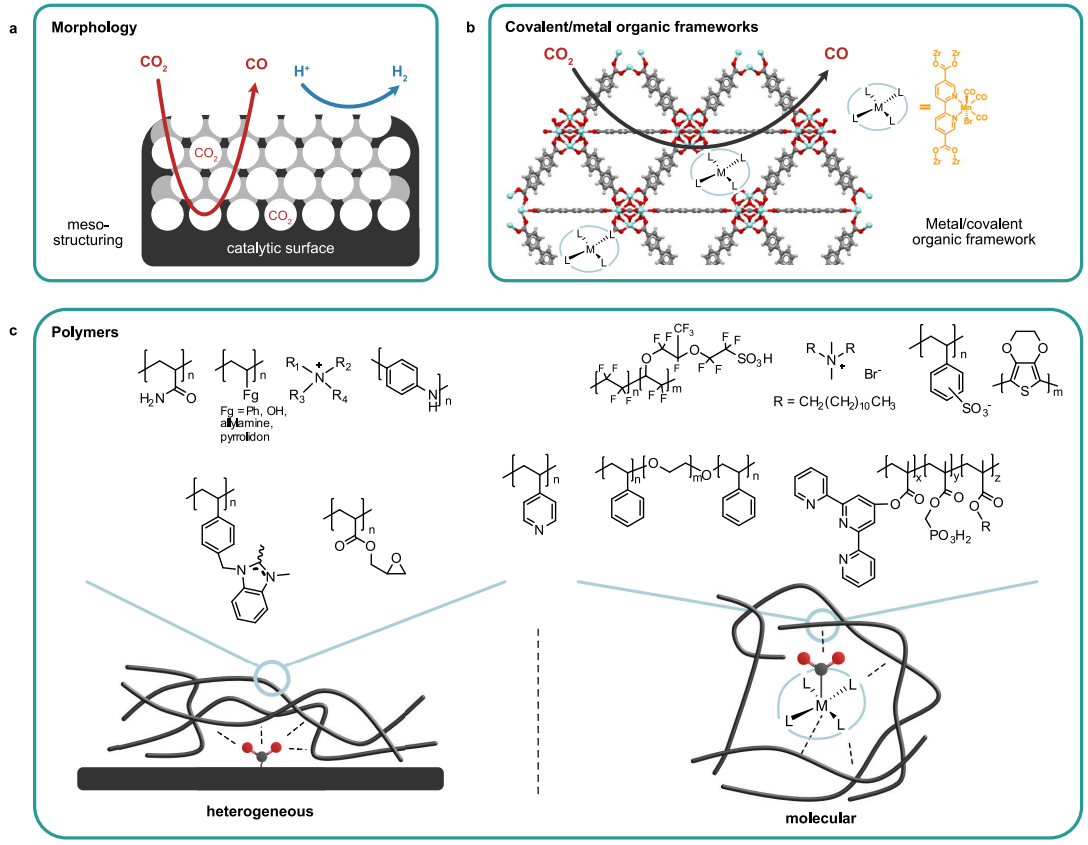

FIGURE 1.17: Local chemical environment effects in CO_2 reduction using 3D-catalyst architectures. a, Porous morphology suppressing H_2 evolution. b, Schematic illustration of UiO-67 MOF with an incorporated molecular catalyst. c, Polymeric structures used to modify heterogeneous electrocatalysts (left) and polymer-embedded molecular catalysts (right). The figure was adapted from reference [133] with permission from *Springer Nature*. *Andreas Wagner contributed in preparing this figure in collaboration with the author.*

1.5 Objective and Outline

Within the broader scheme of sustainable energy and solar fuels specifically, the objective of this dissertation is to generate synthetic syngas (a mixture of H_2 and CO) sustainably by reducing aqueous H^+ and CO_2, driven by visible light. This objective is aligned with the goals of the *Christian Doppler Laboratory for Sustainable Syngas Chemistry*, the initial funding body of this work. As mentioned in the introduction above (section 1.3), the desired ratio of H_2 and CO for the conversion of syngas to industrially relevant products varies in-between 1:1 and 3:1 (H_2 : CO). Within the overarching goal to produce syngas towards the generation of liquid hydrocarbon fuels, a ratio in-between 1:1 and 2:1 is required, hence the goal within this dissertation is to produce CO with a controllable CO-selectivity from 33% to 50%.

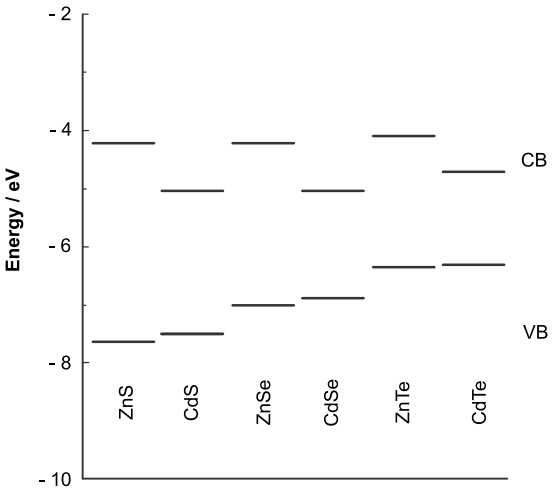

FIGURE 1.18: Band edge positions of selected semiconductors on an absolute scale. CB: conduction band. VB: valence band. Data obtained from reference [312].

This work explores approaches centred around ZnSe QDs as light absorber. The state-of-the-art photosystem for CO_2 reduction based on QDs as light absorber (at the beginning of this dissertation) was based on CdS QDs [186]. ZnSe in particular is selected due to the following reasons. First, ZnSe was recently introduced in the context of photocatalysis and showed very promising results in earlier work of the author of this dissertation (see below). Second, ZnSe thereby balances the general requirements for visible light-driven photocatalysis and provides ample driving force for the kinetically challenging CO_2 reduction. Its conduction band is negative enough (-1.4 V vs. NHE at pH 5.5 [313]) to provide sufficient bias for both H_2 evolution and CO_2 reduction while its (direct) bandgap (E_g = 2.7 eV, Figure 1.18) allows for utilisation of light in the visible part of the electromagnetic spectrum. In contrast to the previous state-of-the-art QD-based photosystem based on CdS [186], ZnSe provides significantly more reductive power which potentially enables to drive a wider variety of molecular catalysts more efficiently (Figure

1.18). Third, another added benefit of ZnSe is its lack of Cd, which is one of the more toxic elements and complements the scheme of developing sustainable solutions. Se is rather toxic as well, but in comparison to Cd, allows for significantly higher intake (one order of magnitude, per day and kilogram) [314, 315].

All photocatalytic processes are investigated in purely aqueous solution because of all solvents, water is by far the most sustainable and abundant. Besides, one of the long-term goals in photocatalytic CO_2 reduction is to couple it to water oxidation as the ultimate sustainable electron donor. Enabling photocatalysis in water is the first step towards this goal.

This work mainly focuses on the reduction reaction during photocatalysis. This is achieved by employing a sacrificial electron donor (see section 1.2.2) that quenches photogenerated holes rapidly so that the reduction side is limiting. This half-reaction can then be optimised and tuned individually. Arguably, this is not a long-term solution but rather a simplification to render the optimisation process more feasible. Replacement of the SED is one of the ultimate goals in the field, see section 1.2.2.

Note, the term *co-catalyst* during this dissertation refers to a distinct molecular unit based on a transition metal complex that itself is active towards CO_2 reduction when electrons are supplied from an external source.

State-of-the-art: ZnSe | Ni(cycP)

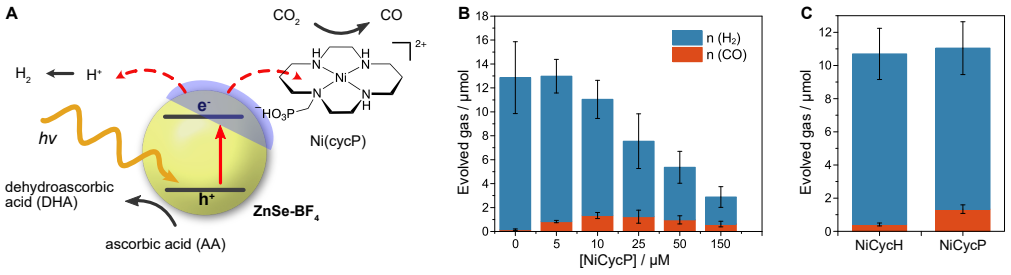

FIGURE 1.19: Overview of the state-of-the-art photocatalyst system developed previously [316, 317]: (A) Schematic representation of ligand-free ZnSe QDs (ZnSe-BF_4) combined with a molecular co-catalyst, Ni(cycP), for aqueous CO_2 reduction to CO. (B) Photocatalytic CO_2 reduction at varying co-catalyst loadings. (C) Photocatalyst performance depending on the employed co-catalyst. Conditions: 0.1M AA, 0.5 μM ZnSe-BF_4, 10 μM Ni(cycP); AM 1.5G, $\lambda > 400$ nm, 100 mW cm^{-2}, 4 h irradiation, pH 5.5, CO_2, 25 °C. Figure adapted from [317].

The initial work on ZnSe QDs as light absorbers in photocatalytic CO_2 reduction was conducted by the author of this dissertation during a *MSc* research project [316], which is briefly summarised in this paragraph (parts of this project were also published in [317]). Stearate-capped ZnSe QDs were synthesised followed by ligand exchange to yield BF_4^- stabilised ZnSe-BF_4 particles with an accessible surface for charge transfer processes. A hybrid photocatalyst was subsequently assembled by combining ZnSe-BF_4 QDs with

Ni(cycP), a phosphonic acid functionalised derivative of Ni(cyclam) (Figure 1.19-A). The phosphonic acid group thereby acts as an anchor to immobilise the co-catalyst on the QD surface (attachment of 7.8 % of the added co-catalyst to the particle surface, indicated by Ion-coupled plasma optical emission spectroscopy (ICP-OES)). A comprehensive screening for sacrificial electron donors found that only ascorbic acid (AA) yielded photocatalytic activity. During photocatalysis experiments (UV-filtered simulated solar light, aqueous AA solution) in the absence of a co-catalyst, only H_2 is evolved. In the presence of Ni(cycP), CO was produced at the expense of H_2 (Figure 1.19-B), indicating the competition between excited electrons being transferred to protons or the co-catalyst. In comparison, a freely-diffusing Ni(cyclam), Ni(cycH), showed three times lower CO_2 reduction activity (Figure 1.19-C). Under optimised conditions, the ZnSe | Ni(cycP) system reached a Ni(cycP)-based TON (CO) of up to 120 with a selectivity towards CO vs. H_2 of 8%. Varying the QD size showed that the largest QDs exhibited the highest photocatalytic activity which indicates that in the regime tested here (absorption onset 400 to 420 nm), light absorption in the visible spectrum out-competes a more reductive CB position. Transient absorption (TA) spectroscopy, carried out by A. Cowan and co-workers at the University of Liverpool, revealed a long-lived trap state just below the ZnSe CB which enables efficient charge transfer to immobilised Ni(cycP) on the ps timescale. This feature was considered a key factor to explain the high activity of the ZnSe | Ni(cycP) photocatalyst.

These encouraging results from the initial work represent the starting point for in-depth investigations during this doctoral dissertation. It should be noted that the ZnSe-BF_4 QDs are highly active towards H_2 evolution in the absence of a molecular co-catalyst and this was investigated in detail for analogues ZnSe nanorods [318]. Therefore, the objective herein is to enable ZnSe QDs to generate CO (from CO_2) in addition to H_2 and to control the product selectivity.

The first two parts of the dissertation are dedicated to the general methods and materials. Chapter 2 describes the synthesis and characterisation of the ZnSe QDs and its surface modification. Chapter 3 elucidates the method of conducting photocatalysis. Conventionally in this laboratory, photocatalysis is carried out in a (closed) batch reactor accompanied by the accumulation of products in the headspace followed by manual injection into a gas chromatograph. This setup is upgraded to a continuous-flow system with in-line gas chromatography. One of the key challenges for such a setup is to remain a high sensitivity, because of the constant removal of products from the reactor. The setup is custom-built and optimised towards photocatalysis in liquid solution and not only provides enhanced resolution but also operates in an essentially automated fashion. Besides the added convenience, this approach allows for higher throughput of photocatalysis experiments and provides high-quality time-resolved data.

Chapter 4 focuses on ZnSe QDs hybrid assemblies consisting of ZnSe QDs as light absorbers in combination with molecular catalysts (co-catalysts). In contrast to the previous work on ZnSe | Ni(cycP), the objective here is to study the ZnSe QDs more broadly as a versatile platform for a range of molecular catalysts based on earth-abundant metals. A comprehensive screening is conducted employing state-of-the-art molecular catalysts from several catalyst classes such as cyclams, porphyrins, terpyridines, phthalocyanines and quaterpyridines. The best performing systems are selected and studied in more depth while leveraging the new continuous-flow system. One emphasis of the study is on testing the hybrid photocatalysts under conditions such as low CO_2 concentration and aerobic conditions, which resemble more real-world scenarios. Those experiments are in parts enabled through the continuous-flow system.

Chapter 5 investigates the elimination of the above-mentioned co-catalyst. While some of the molecular catalysts feature extraordinary activities and tunability, many molecular catalysts are synthetically very demanding and can limit the long term stability of colloidal hybrid photosystems. In addition, it is an intriguing concept to activate QDs directly to reduce CO_2 without the aid of an additional catalyst from a purely scientific perspective. This section presents surface modification strategies for the photoreduction of CO_2 using the ZnSe QDs in the absence of an additional molecular catalyst and is inspired by developments in electrocatalysis focusing increasingly on the local chemical environment of the catalytic site.

Results described in the last experimental Chapter 6 aim to replace the sacrificial electron donor. While attempts to utilise other common electron donors or more useful oxidation reactions were unsuccessful, one alternative is to use the QDs in a photoelectrochemical setup. This arrangement allows to couple the reduction side reaction (H_2 evolution and CO_2 reduction) with a useful oxidation reaction. The ZnSe QDs are therefore used to construct a QD-sensitised photocathode based on $CuCrO_2$ as p-type electrode support in which the QDs act as light absorber and catalyst while photogenerated holes are quenched by $CuCrO_2$ under applied bias. $CuCrO_2$ is thereby a promising material because it was shown to exceed the conventional material for this purpose (NiO) when molecular catalysts are employed [319]. In the first step, various immobilisation techniques are screened followed by the aim to generate products with controlled potential photoelectrolysis, first targeting H_2 evolution and secondly the more challenging CO_2 reduction.

The outline of this dissertation is graphically summarised in Figure 1.20.

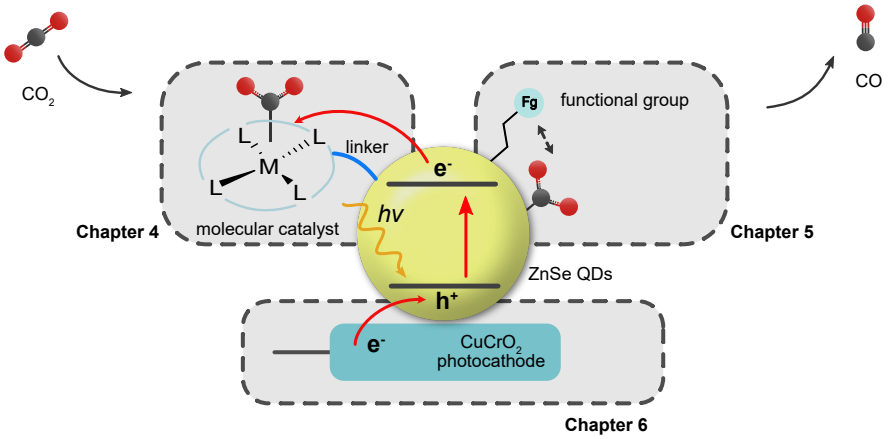

FIGURE 1.20: Graphical outline of this dissertation.

Chapter 2

General Methods and Materials

The Synthesis and Characterisation of ZnSe QDs as described herein is similar to the one reported by the author of this dissertation in [316] *and published in peer-reviewed article: M. F. Kuehnel, C. D. Sahm, G. Neri, J. R. Lee, K. L. Orchard, A. J. Cowan and E. Reisner, Chemical Science,* ***2018****, 9, 2501-2509 as well as subsequent publications by the author of this thesis that follow this dissertation.*

2.1 Synthesis and Characterisation of Quantum Dots

2.1.1 Preparation of ZnSe Quantum Dots

The preparation of ZnSe QDs is consistent throughout this dissertation and explained in the following. A range of various methodologies for the synthesis of the particles were reported in the literature [320] and a heat-up method was chosen mainly due to the ease of the experimental procedure as well as its relatively long reaction times, which renders monitoring of the growth process by UV-vis spectroscopy feasible [321].

The heat-up method involves heating Zinc stearate and selenium powder in a high boiling, coordinating solvent octadecene (ODE), to 300 °C for 90-130 minutes (Figure 2.1). The reaction time thereby depends on the exact heating rate and therefore requires monitoring by UV-vis spectroscopy. In practice, aliquots of the reaction solution were taken at regular time intervals (Figure 2.2). The particles grow consistently over the course of 2 h and the absorption onset plateaus at ca. 420 nm. Longer irradiation times lead to a flattening of the absorption curve. A growth period of 2 h was found to be a good compromise between shifting the absorption onset into the visible region of the electromagnetic spectrum without excessive broadening of the size distribution due to Ostwald ripening.

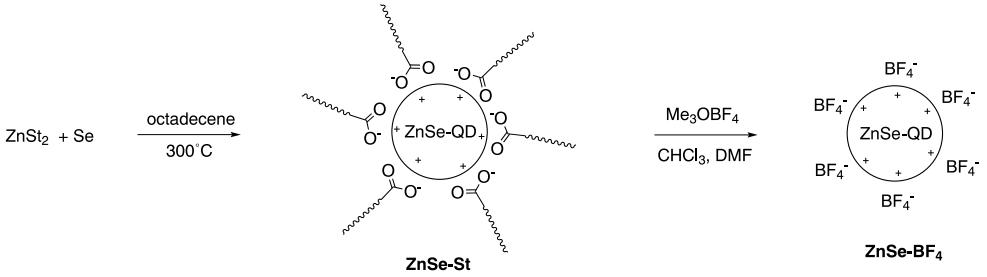

FIGURE 2.1: Preparation of ZnSe-QDs and subsequent surface modification of ZnSe QDs by reactive ligand removal using trimethyloxonium tetrafluoroborate.

Zinc stearate plays a double role; not only it acts as Zn precursor, it also provides stearate anions that function as organic capping ligands to stabilise the nanoparticle surface and prevent agglomeration. Selenium is activated by the solvent to form a Se-ODE complex which generates a tetrahydroselenophene derivative that works as precursor during ZnSe particle formation [321].

The as prepared particles are stabilised by stearate capping ligands (ZnSe-St). These capping ligands contain long alkylic organic chains which render the particles insoluble in aqueous solution, and additionally interfere with electron transfer processes on the QD surface [316, 322]. Consequently, the organic capping ligands were removed and replaced with weakly coordinating anions (Figure 2.1). This process is also referred to as *reactive ligand stripping* [107], a well established procedure in QD synthesis. It involves dropwise addition of a methylating agent, trimethyloxonium tetrafluoroborate (Me_3OBF_4) under an inert gas atmosphere until the particles precipitate. The carboxylate groups of stearate are methylated and thereby removed from the QD surface and replaced by weakly coordinating BF_4^-. The resulting particles are readily soluble in water and polar organic solvents such as DMF. The latter was found to be the best solvent in order to stabilise the particles in solution over long time periods for storage.

The ligand removal process was found to be extremely sensitive to the conditions employed during the ligand removal process (solvent volume, solvent composition, amount of Me_3OBF_4, etc.) which explains small batch-to-batch deviations during photocatalysis.

2.1.2 Characterisation of ZnSe QDs

First, the QDs were analysed by transmission electron microscopy (TEM). The micrographs of ZnSe-BF_4 show nearly spherical, individual particles with high crystallinity (Figure 2.3-A). The QD size distribution was assessed by measuring diameters of approx. 100 individual QDs (Figure 2.3-B). The average diameter of the particles was found to

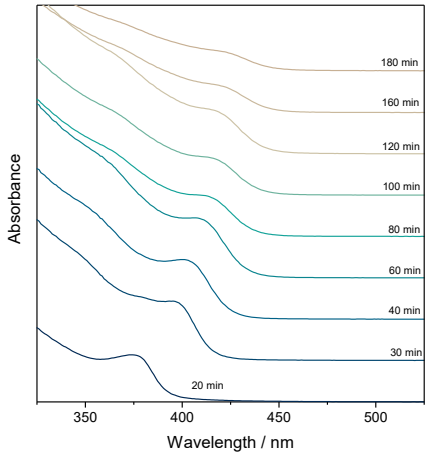

FIGURE 2.2: QD growth monitored via UV-vis spectroscopy. Aliquots taken at regular time intervals (stacked). Data obtained from [316]. Conditions: 300 °C, reaction solution diluted 1:10 with chloroform

be 4.66 ± 0.64 nm. The ligand removal process did not affect the shape and size of the particles significantly [317].

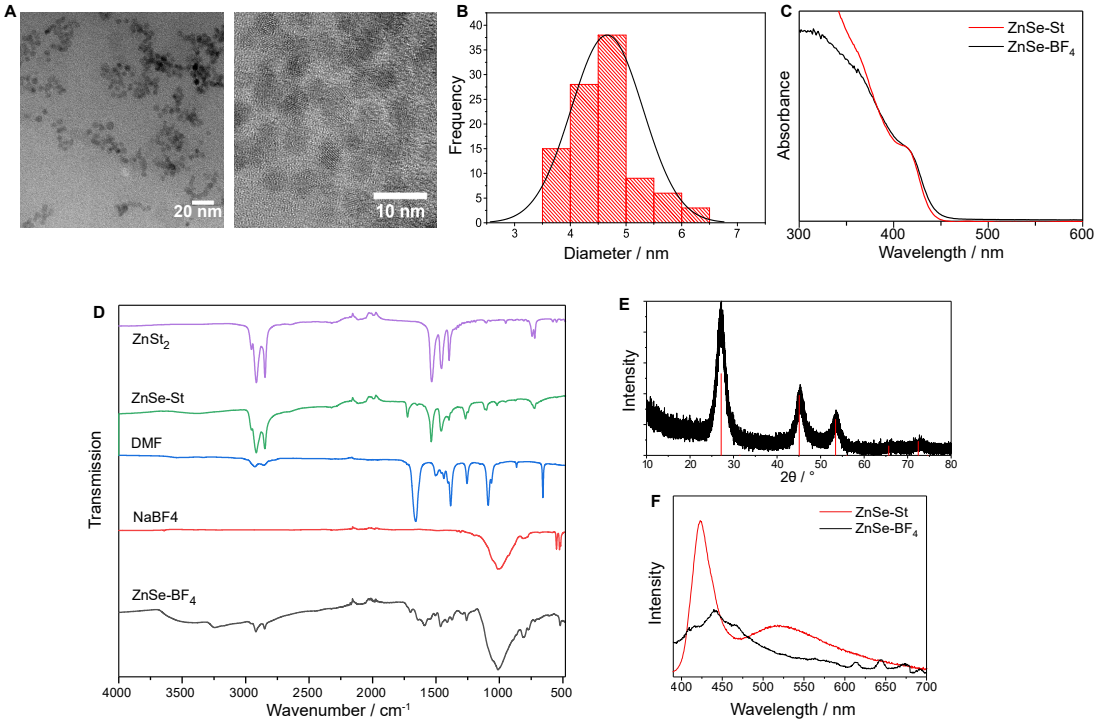

FIGURE 2.3: Characterisation of ZnSe QDs. (A) Transmission electron micrographs. (B) particle size distribution determined by TEM. (C) UV-vis absorption spectrum, 10μL QD stock solution in 1 mL DMF. (D) ATR-IR spectra of stearate capped QDs (ZnSe-St) and ligand free ZnSe-BF_4 in comparison to reference spectra. (E) Powder X-ray diffractogram. The overlay shows cubic zinc blende ZnSe reference (PDF 01-071-5978). (F) Photoluminescence (PL) emission spectra of ZnSe-St (in DMF) and ZnSe-BF_4 in H_2O (λ_{ex} = 360 nm).

The particles were further characterised by UV-vis absorption spectroscopy. Figure 2.3-C shows the absorption profile of ZnSe-BF_4 which feature a first excitonic absorption

maximum at 417 nm. The ligand removal did not affect the absorption onset.

Attenuated total reflection infrared (ATR-IR) spectroscopy allows to follow the ligand removal process (Figure 2.3-D). ZnSe-St exhibit strong signals from stearate, as confirmed by a reference spectrum of zinc stearate ($ZnSt_2$). After ligand removal, the stearate signals are reduced and a strong signal centred at 1000 cm^{-1} appears, assigned to the BF vibration. In addition, ZnSe-BF_4 exhibit signals from residual stearate as well as DMF as solvent.

Powder X-ray diffraction indicates a zinc blende crystal structure with broadening of the signals due to nanostructuring (Figure 2.3-E).

Photoluminescence (PL) spectroscopy of the particles before ligand stripping reveals a sharp emission maximum at 425 nm followed by a lower emissive tail towards longer wavelengths (λ_{ex} = 360 nm) (Figure 2.3-F). The ligand removal process changes the emission spectrum; the particles are less emissive and the spectra become more scattered, presumably due to some degree of agglomeration. The shape of the emission indicates the appearance of a range of mid-gap states below the conduction band, as the emission does not peak sharply but rather progressively tails over a range of 250 nm.

The particles were further analysed by electrokinetic zeta-potential measurements and dynamic light scattering (DLS), either in aqueous solution (pH adjusted to 5.5) as well as in the presence of ascorbic acid (AA, 0.1 M, pH 5.5). Ligand-free ZnSe-BF_4 QDs in aqueous solution exhibit a positive value of +20 mV which indicates a positive surface charge that is only partially balanced by BF_4^- (Figure 2.4). In the presence of AA, the zeta potential is lowered to -6 mV indicative of accumulation of negatively charged ascorbate on the QD surface. The influence of AA on the particles is also detected by quantifying the particle size in solution via DLS. ZnSe-BF_4 particles (aqueous solution) exhibit a particle size of 9.5 ± 2.1 nm, close to the diameter determined by TEM. It should be noted that DLS determines the hydrodynamic diameter of a solvated particle which includes the ligand/ion sphere and explains the larger value than the one obtained by TEM.

The QD concentration was calculated based on the average size of the particles (determined by TEM) the concentration of Zn and Se (determined by inductively-coupled plasma-optical emission spectroscopy (ICP-OES) analysis (appendix 2.2.2).

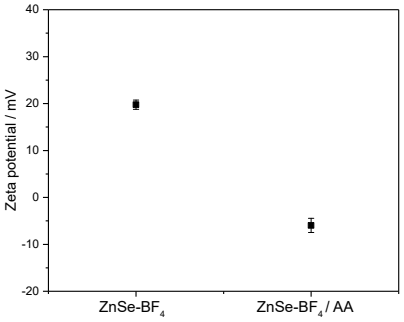

FIGURE 2.4: Electrokinetic zeta potential measurements of unfunctionalized ZnSe-BF_4 QDs in water or AA solution. Conditions: 0.5 μM ZnSe-BF_4, 0.1 M AA, pH 5.5

2.2 Experimental section

Parts of the experimental procedures to prepare and characterise ZnSe QDs (as described herein) are similar to the ones reported by the author of this dissertation in [316, 317].

All reagents were purchased from commercial suppliers and used without further purification unless otherwise stated: Zinc stearate (purum, Sigma-Aldrich), octadecene (90% techn., Sigma-Aldrich), selenium powder (99%, Sigma-Aldrich), methanol (99.8%, Fisher-scientific), acetone (laboratory reagent grade, Fisher-scientific), 1-butanol (99%, Alfa Aesar), trimethyloxonium tetrafluoroborate (96%, Sigma-Aldrich), L-ascorbic acid (99%, Sigma-Aldrich) were used as received. Anhydrous solvents were purchased from Acros Organics with the following purities: chloroform ($CHCl_3$, 99.9%), N,N-dimethylformamide (DMF, 99.8%). All aqueous experimental solutions were prepared with ultrapure water (DI water; Milli-Q, 18.2 MΩ cm).

The **pH** of aqueous solutions was measured using a Mettler Toledo S20 SevenEasy^{TM} pH meter that was daily calibrated with a 3 point calibration.

Inductively Coupled Plasma-Optical Emission Spectroscopy (ICP-OES) was carried-out by the Microanalysis Services (Dept. of Chemistry, Univ. of Cambridge) using a Thermo Scientific iCAP 7400. Samples were digested in nitric acid (1%) for analysis.

Ultraviolet-Visible (UV-Vis) spectra were recorded on an Agilent Cary 60 UV-Vis spectrophotometer using quartz glass cuvettes (1 cm path length).

Fourier-transform infrared (IR) spectra were recorded on a Thermo Scientific Nicolet iS50 FT-IR spectrometer in ATR mode. IR spectra of ZnSe-St and ZnSe-BF_4 were recorded by drying one drop of QD stock solution on an FTO-coated glass slide *in vacuo*.

Powder X-ray diffraction (XRD) was conducted using an X'Pert PRO by PANalytical BV instrument using CuK_α irradiation.

Transmission Electron Microscopy (TEM) images were collected using an FEI Phillips Technai F20 TEM, operating at an accelerating voltage of 200 kV, located at the Electron Microscopy Suite of the *Cavendish Laboratory*, Cambridge. Alternatively, TEM images were collected at the Dept. of Chemistry using a Thermo Scientific (FEI) Talos F200X G2 TEM, operating at an accelerating voltage of 200 kV. Samples were prepared by drop-casting a dilute QD-solution on holey-carbon coated Cu grids followed by evaporation of the solvent.

Zeta potential and dynamic light scattering (DLS) measurements of ZnSe-BF_4 (0.5 μM in water or AA, pH adjusted to 5.5 with NaOH/HBF_4) were conducted using a Malvern Zetasizer Nano ZS90 instrument at 25 °C.

Photoluminescence (PL) spectroscopy was recorded on an Edinburgh Instruments FS5 Spectrofluorometer using a Suprasil Quartz (QS) cuvette with 1 cm path length at room temperature.

2.2.1 Preparation of ZnSe-QDs

ZnSe-St

Stearate capped (ZnSe-St) QDs were prepared by using a modified literature procedure [321] as follows: A mixture of $ZnSt_2$ (758 mg) and Selenium powder (79 mg) in 65 mL octadecene (tech. grade) was degassed for 1.5 h at 50 °C in a 250 mL three-necked flask. The reaction was triggered by raising the temperature of the dark-brown-ish solution to 300 °C under inert gas atmosphere. The reaction was monitored using UV-VIS absorption spectroscopy by taking aliquots (100 μL) regularly. Aliquots were diluted with chloroform to a total volume of 1 mL and filtered with a syringe filter (Merck Millex-GN, 0.20 μm nylon membrane) before analysis. After reaching 300 °C, the reaction solution turned progressively yellow. The reaction was terminated when the desired particle size (determined by the UV-vis absorption onset) was reached (90-130 min) by removing the heating mantle and rapid cooling using an oil bath. The particles were precipitated using an acetone/methanol mixture (20:80), followed by centrifugation (7,000 rpm, 10 min). The residue was washed with methanol (twice) and butanol and re-dispersed in chloroform.

ZnSe-BF_4

Ligand-free ZnSe-BF_4 particles were prepared by reactive ligand removal using a modified literature procedure [322]. A ZnSe-St solution (3 mL, in chloroform) was dried *in vacuo*. Under a N_2 atmosphere, the residue was re-dispersed in a mixture of anhydrous $CHCl_3$ (3 mL) and anhydrous DMF (0.2 mL). Aliquots of stripping agent (Me_3OBF_4, 1.0 M in acetonitrile, typically 3-4 mL) were added slowly until the particles precipitated,

indicated by the solution turning cloudy. The resulting ligand-free particles were precipitated by centrifugation (7,000 rpm, 15 min), dried in air for 1 min, and re-dispersed in DMF (4-5 mL). The resulting slightly cloudy solution of ZnSe-BF_4 in DMF was further purified by centrifugation (7,000 rpm, 10 min) to give a black precipitate, a clear yellow solution and a cloudy white phase on top. The black precipitate and white phase were removed and the clear yellow solution was used for characterisation and photocatalytic experiments. The procedure can be repeated if the result was not satisfactory. Thus-prepared ZnSe-BF_4 can be handled in air for hours without decomposition but will gradually degrade over several days in air. To prevent degradation, the ZnSe-BF_4 solution was degassed by 4 freeze-pump-thaw cycles and stored under N_2 in the dark at 4 °C.

2.2.2 QD concentration determination

To calculate the QD concentration in the stock solution, the Zn^{2+} concentration in the ZnSe-BF_4 stock solution determined by inductively-coupled plasma-optical emission spectroscopy (ICP-OES), was divided by the number of Zn^{2+} ions per QD based on the mean volume of a QD (V_{QD}), the volume of a unit cell ($V_{Unit\ Cell}$) and the number of Zn^{2+} ions per unit cell ($N_{Zn,\ Unit\ Cell}$). The number of Zn ions per QD ($N_{Zn,\ QD}$) was calculated as follows: (Where d is the average diameter of a particle and a is the lattice length of a cubic unit cell:

$$N_{Zn,\ QD} = \frac{V_{QD}}{V_{Unit\ Cell}} \times N_{Zn,\ Unit\ Cell} = \frac{\frac{4}{3}\pi(\frac{d}{2})^3}{a^3} \times N_{Zn,\ Unit\ Cell}$$

Alternatively, the QD concentration can be calculated by dividing the Zn^{2+} or Se^{2-} concentration (determined by ICP-OES) by the number of Zn atoms per QD based on the mean particle diameter (TEM) and the bulk density of ZnSe (5.262 g cm^{-3}). Both methods yielded the same result.

Chapter 3

Development of a continuous-flow setup for photocatalysis

Parts of the contents of this section have been prepared/submitted for publication in peer-reviewed journals: C. D. Sahm, G. M. Ucoski, S. Roy and E. Reisner, Automated and continuous-flow platform to analyze photocatalytic semiconductor-metal complex hybrid systems for CO_2 reduction, ***2021*** *(submitted manuscript). The continous-flow methodology was also utilised in publications C. D. Sahm, E. Mates-Torres, N. Eliasson, K. Sokolowski, A. Wagner, K. E. Dalle, Z. Huang, O. A. Scherman, L. Hammarström, M. Garcia-Melchor, E. Reisner, Imidazolium-modification enhances photocatalytic CO_2 reduction on ZnSe quantum dots. Chemical Science,* ***2021****, Accepted Manuscript. DOI: 10.1039/D1SC01310F and C. D. Sahm, E. Mates-Torres, A. Ciotti, K. Sokołowski, G. Neri, A. J. Cowan, M. García-Melchor, E. Reisner, Tuning the local chemical environment of ZnSe QDs with dithiols towards photocatalytic CO_2 reduction.* ***2021****, in preparation and S. Roy, M. Miller, J. Warnan, J. J. Leung, C. D. Sahm, E. Reisner, Electrocatalytic and Solar-Driven Reduction of Aqueous CO_2 with Molecular Cobalt Phthalocyanine-Metal Oxide Hybrid Materials, ACS Catal.* ***2021****, 11, 3, 1868–1876. Results presented were obtained solely by the author of this thesis, with contributions from others as outlined here: Andreas Wagner contributed to the development of the continuous-flow methodology and mass-flow controller setup in collaboration with the author. The mechanical workshop of the Department of Chemistry aided in the physical assembly of the flow setup and parts of the tubing/connectors.*

3.1 Introduction & Motivation

Most experimental methodologies for gaseous product detection in photocatalysis are based on batch reactors in which reaction products accumulate in the headspace and are periodically, mostly manually, injected into a gas chromatograph (GC). The benefits of such a solution is that it is easy to implement and offers a high sensitivity because the products can accumulate before being detected. On the other hand, such systems are labour intense and the accumulation of products can lead to pressure build-up and catalyst poisoning [174].

The aim of this section is to develop a continuous-flow photocatalysis setup, in which photoreactors are constantly purged with a stream of CO_2 (or alternative gases) and directly connected to a GC in order to perform 'in-line' gas sampling. Compared to the conventional 'head-space accumulation' methodology, the continuous flow system offers a number of advantages:

- Since the photoreactor is directly connected to the GC, it does not require manual injections and the system can run in an automated fashion.
- The constant sampling leads to measurement frequency which is only limited by the run time of a GC analysis (ca. 4 min), typically higher than when samples are manually sampled.
- No product accumulation that can potentially poison a catalyst. For example, CO poisoning has been observed for Ni-catalysts [174]. Additionally, back reactions are reduced through the constant removal of reaction products.
- Ability to test different atmospheres by mixing CO_2, N_2 and air gas streams. (For example low CO_2 concentrations, aerobic conditions, etc.)

Because the product is constantly removed from the photoreactor, the continuous flow system sacrifices sensitivity. In contrast to the conventional method, one acquires a snapshot of product evolution rate (mol s^{-1}) rather than absolute number of product in mols.

This chapter describes the method development of the continuous flow-setup, its optimisation, calibration and exemplifies the data acquisition with the ZnSe | Ni(cycP) system which was introduced during the state-of-the-art part of the outline (section 1.5).

3.2 Method development

3.2.1 Setup

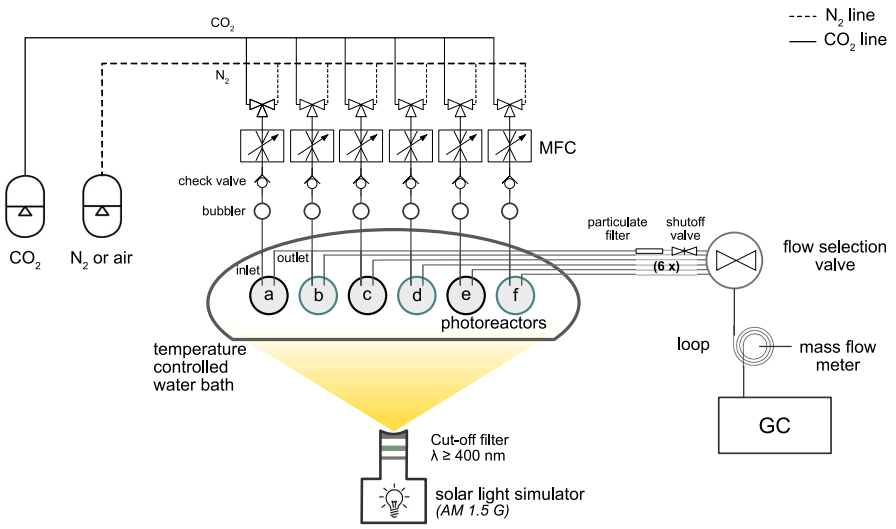

FIGURE 3.1: Schematic representation of the continuous-flow setup for photocatalytic CO_2 reduction with automated inline GC sampling.

The continuous-flow setup was assembled as illustrated in Figure 3.1 and Figure 3.2. For all technical details, please refer to section 3.4. Two gas cylinders containing either CO_2 or N_2 (or air) are connected to a set of three-way valves which attach to mass flow controllers (MFC) for each sample stream. The MFCs allow for precise control of the flow rates whereas the valve enables convenient switching between the desired balance gas. The outlet of each MFC is connected to a check valve in order to prevent build-up of underpressure which could potentially suck liquid in the reverse direction into the MFC. Each gas stream is further humidified with a simple gas bubbler filled with deionised water and then connected to the photoreactor with teflon tubing. The photoreactors are sealed with standard suba seal septa and conventional needles are used to provide both inlet and outlet by connecting the teflon tubing to the needle with a Luer lock fitting. The inlet needle (long) is immersed into the photoreactor solution whereas the outlet uses a short needle at the top of the headspace. Each sample outlet is connected with teflon tubing through a particulate filter and shut-off-valve to a flow-selection-valve controlled by the GC. The flow-selection-valve can be programmed to select one sample stream at a time and purge it through the sample loop and injected it into the GC, after which the next sample stream can be selected. Through the use of the flow-selection-valve one can measure multiple samples in parallel in one experiment by sampling through every sample one after the other. The frequency is thereby determined by the number of samples and the run time of a GC analysis, which is approximately 4.25 min. For example, one sample can be measured every 4.25 min; or two samples in parallel in

which each sample is injected every 8.5 min and so on. In a typical experiment, six samples (each sample injected every (25.5 min) were measured in parallel which was found to be a good balance between sample throughput and sufficient time resolution. This measurement frequency compares favourably to manual GC sampling where the measurement frequency can be often on the order of hours [193] and is mainly limited by human labour.

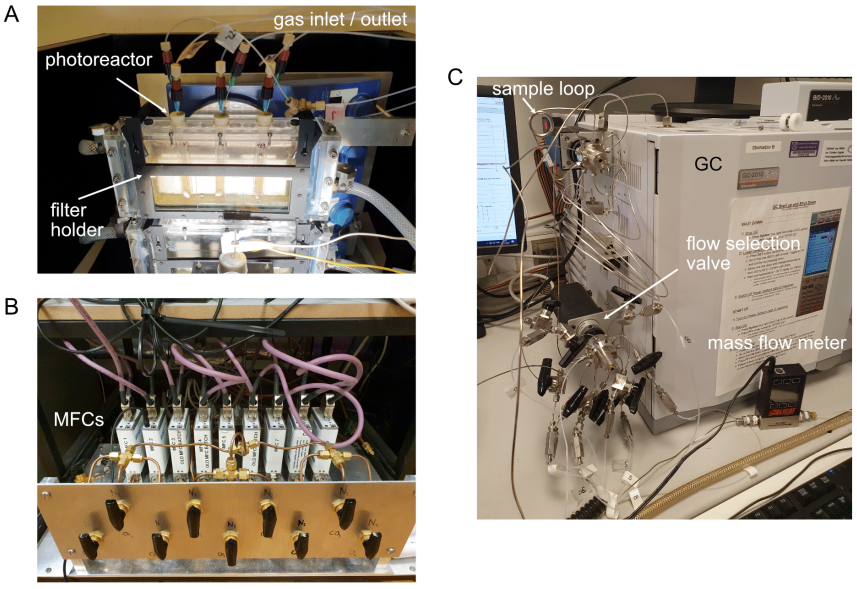

FIGURE 3.2: Photographs showing the continuous flow setup. (A) Photoreactors placed in the solar light simulator. (B) Mass flow controller (MFC) setup and gas selection valves. (C) Flow selection valve and inlets into the GC.

The outlet of the sample loop is connected to a mass flow meter to verify the set flow rate prior to an experiment and detect potential leaks. It should be noted that the system is very sensitive to leakage because of the absence of an internal standard. An internal standard would not provide an added benefit because its concentration in the sample loop is unchanged, independent of a fluctuating flow rate. Verifying the flow rate prior to starting an experiment is therefore a key objective to assure the setup was assembled correctly without leaks.

The GC consists of two separate columns, a pre- and a main-column connected to a high-sensitivity barrier discharge ionisation (BID) detector. The pre-column, made from a polymeric material, separates the (target) gases (H_2, CO, CH_4, N_2, O_2) from CO_2 and moisture and blocks the latter two gases from getting onto the main column, made from molsieve. This is achieved with the use of a backflush that reverses the flow direction on the pre-column after the target gases have passed and entered the main column. The backflush removes CO_2 and moisture out of the pre-column again and thereby protects the main column from damage.

Instead of the absolute amount of evolved product, the continuous flow setup outputs the momentary product evolution rate $\dot{n}_{gas}$ (in mol s^{-1}) corresponding to each injection, which is calculated using the following formula:

$$\dot{n}_{gas} = \frac{p * \dot{V} * \frac{Area\ GC}{f_i}}{R\ T} \tag{3.1}$$

where *Area GC* refers to the integrated peak area of a given gas, $\dot{V}$ to the set flow rate at the MFC (in sccm * (1/60) * (10^{-6})), p is the pressure in the photoreactor (ambient pressure, 101325 Pa), R is the universal gas constant, T is the temperature (298 K) and f_i is the response factor for each target gas determined by the calibration procedure (see section 3.2.3). Essentially, the peak area, as determined by the GC, is divided by the response factor to obtain the concentration of H_2 and CO (in ppm) in the sample loop. This value is further multiplied with the flow rate to yield $\dot{v}_{gas}$ which is then further converted to $\dot{n}_{gas}$ via the ideal gas low. The loop size (see below) is not part of this calculation because it is incorporated in the response factor during the calibration.

The continuous flow system offers the possibility to study photocatalysts under various atmospheres. By connecting two gas streams of different balance gases and varying the respective flow rates, it is feasible to vary the composition precisely as desired. For example, one could use a dilute stream of 50% CO_2 by mixing a pure CO_2 stream and a N_2 stream with the same flow rate.

3.2.2 Flow rate and sample loop size optimisation

The flow rate is a key variable which requires careful consideration because of its interplay with the sample loop size and the GC sensitivity. In principle, the higher the flow rate, the more product will be purged out of the photoreactor and sample loop and is not analysed. Therefore, a low flow rate is favourable in order to allow for some product accumulation within the sample loop and to remain a sufficient sensitivity. However, there are certain lower limits; at very low flow rates it is more prone to fluctuation and it gets increasingly difficult to avoid leakage and significant air peaks can be detected.

In order to increase the sensitivity, the sample loop size can be varied in-between 25 μL and 2 mL. The largest loop size should in principle lead to the highest sensitivity, however, it was found that the largest size the supplier Shimadzu recommends (2 mL) led to problems in separating CO_2 from the reaction products on the pre-column. This behaviour was assigned to overloading of the pre-column in which the backflush was not

able to remove all the CO_2 from the pre-column. A sample loop size of 1 mL was found to be more appropriate and gave consistent results.

A flow rate between 3.5 and 4.0 standard cubic centimetres per minute (sccm) (at a sample loop size of 1 mL) was found to be the optimum between high sensitivity and a stable, reproducible gas stream without significant leakage. For a set flow rate of 3.5 sccm, a CO peak large enough to be distinctively distinguished from background noise (ca. 2000 units) corresponds to a formation rate of $1.26 * 10^{-12}$ mol s^{-1} and represents the sensitivity limit. Most photocatalysts studied in this work well exceed this minimum rate.

3.2.3 Calibration

A standard gas mix for calibration was purchased containing each 2000 ppm H_2, CO and CH_4 in CO_2 as balance gas. The gas mixture was further diluted with CO_2 to reach concentration levels of 2000, 1600, 1200, 800, 400 and 200 ppm which were used to generate a calibration curve, as depicted in Figure 3.3. The slope of the linear fit of the curve gives the response factor, for a given sample loop size.

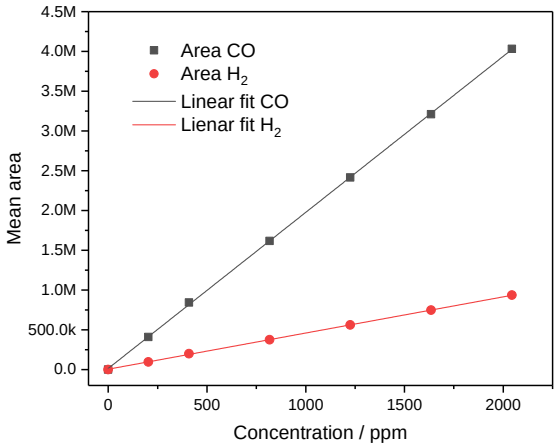

FIGURE 3.3: Calibration curve of the GC for H_2 and CO under continuous flow.

3.2.4 Qualitative assessment of the time between product generation and analysis

There is an inherent delay between product generation and quantification at the GC because the gaseous product needs to travel from the photoreactor vial (7.91 mL volume) through a set of tubing, filters, shut-off valves and loop in order to reach the GC injector

for the measurement. In order to qualitatively determine this period and find out if this can potentially lead to a delay of the time-dependent product evolution curves, an experiment was performed: At a given time, a known quantity of H_2 was manually injected into the photoreactor with a syringe and the amount of H_2 was monitored via GC (Figure 3.4). If the interval between injection and measurement is chosen to be 4 min (approximately the run time of one GC measurement), only small quantities of H_2 (< 0.2 nmol s^{-1}) are detected. When the interval is only 2 min, much larger quantities (> 1 nmol s^{-1}) are measured and decay to close to 0 in subsequent injections. This observation indicates that at the chosen flow rate (4.0 sccm), the majority of H_2 is being purged out of the system in less than 4 min. In consequence, the time between product generation and analysis is significantly less than 4 min and beyond the resolution of the flow system and unlikely to cause misinterpretation of the flow data. It should be noted that this is a simple qualitative assessment to avoid misinterpretation of product evolution rates in subsequent parts of this dissertation. (Note that the continuous-flow system is not useful to accurately quantify a sudden addition of gaseous product due to its momentary nature and the dependence on the exact time when the measurement was commenced. It is much rather suited to quantify continuous generation of products.)

Furthermore, a test was performed to determine if there are differences if the injection is done into the headspace of an empty photoreactor or directly into the solution of a common sacrificial electron donor (0.1 M ascorbic acid (AA) solution, pH 5.5). If the interval is 4 min, the amounts of H_2 quantified when injected into solution are slightly lower compared to an injection into the headspace, but this trend is reversed when the interval is only 2 min (Figure 3.4). This observation suggests that H_2 reached the GC even faster when it is injected into AA solution, presumably due to the stirring that was employed when a solution was present and/or the reduced headspace volume in this case.

In conclusion, the experimental data suggests that the time between H_2 product generation (in the photoreactor) and detection (at the GC) is qualitatively below ~ 4 min and no product loss due to dissolution in electron donor solution occurs. It was assumed that the same applies to CO.

3.2.5 Example: ZnSe | Ni(cycP)

A first test of the newly developed continuous flow setup was performed with a well-known hybrid photocatalyst system consisting of ZnSe-BF_4 QDs in combination with molecular co-catalyst Ni(cycP). (For a structure of Ni(cycP), please refer to Figure 1.19.) The raw data is shown in Figure 3.5. Depicted is one experimental condition in three

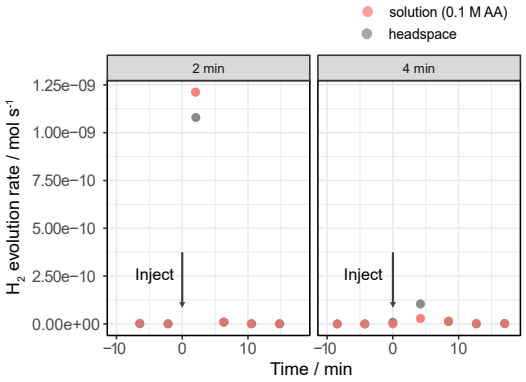

FIGURE 3.4: Continuous-flow photocatalysis method development. Quantification of manually injected H_2 into the photoreactor and monitored via GC depending on the interval between injection and measurement (left: 2 min; right: 4 min). Conditions: injection volume 50 μL product at a CO_2 constant flow of 4 sccm.

identical replicates. The different samples (*i.e.* light vials) are distinguishable by the plot shape. The formation rate is not constant but varies greatly over time. There is a lag phase (induction time) until the system performs at peak turnover (H_2 after ca. 180 min, CO after 50 min) after which the formation rates decline over time, CO faster than H_2. The reason for the strong decline in CO formation rate is presumably the stability of the molecular catalyst which may be poisoned, decomposed or detaches from the QD surface, which was shown to be the limiting factor before [317]. The evolution of H_2 due to proton reduction proceeds on the QD surface and is therefore much more stable over time and slowly decays due to agglomeration of the QDs as well as accumulation of ascorbic acid's oxidation product dehydroascorbic acid on the QD surface [318] or disintegration of the QDs. The product formation rates exhibit a sufficiently low deviation in-between replicates of identical conditions and the standard deviation was found to be around 10% to 15%.

Data processing & visualisation

The data processing and visualisation for the continuous flow photocatalysis is consistent throughout this dissertation and will be exemplified for CO in more detail in the following. The methodology is similar for H_2.

The raw data acquired from the GC quantification, $\dot{n}_{CO}$, is depicted in Figure 3.6-A and represents a snapshot of a product evolution rate. Integration of the formation rate over irradiation time leads to the total amount of evolved product, a unit commonly reported in the literature. This was achieved by numerical integration of the formation rate using the trapezoidal method for each sample individually (Figure 3.6-B). The three independent replicates of identical conditions were averaged by calculating the mean and standard deviation over irradiation time. For the mathematical details, please refer to the experimental section 3.4. For visual display, the values of each individual

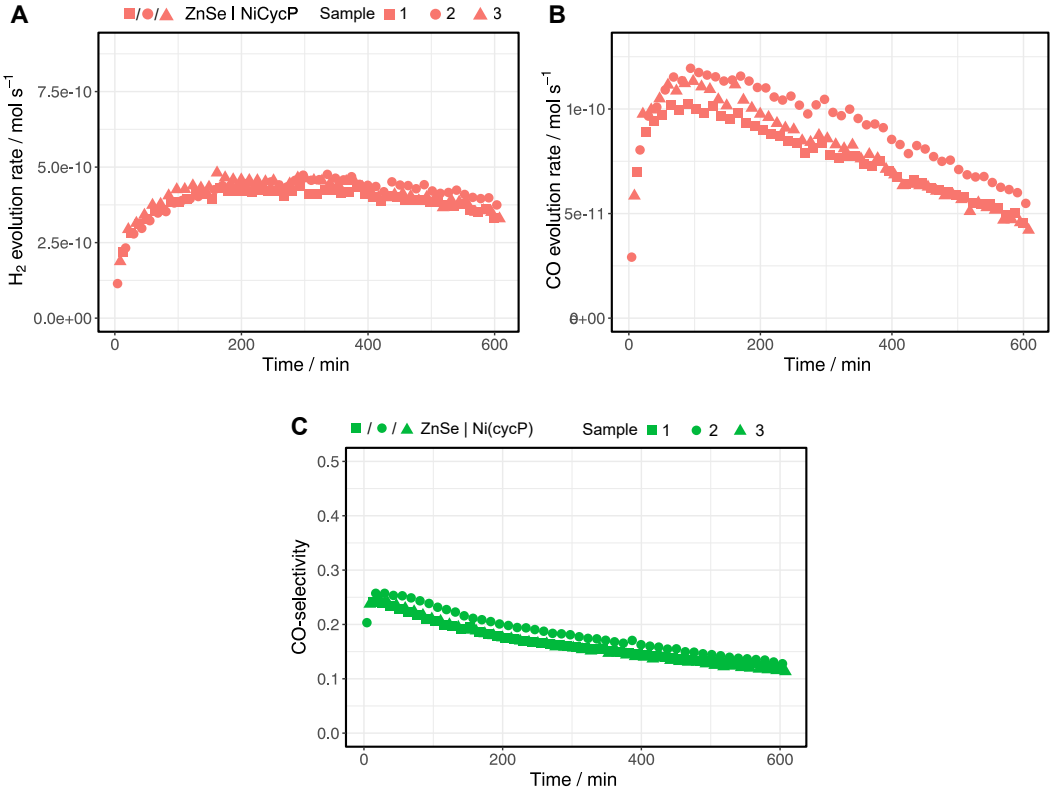

FIGURE 3.5: Photocatalytic CO_2 reduction and H_2 evolution using ZnSe | NiCycP - raw data. (A) H_2 evolution rate. (B) CO evolution rate. (C) CO-selectivity calculated as the ratio of CO divided by the sum of H_2 and CO. Conditions: 0.1M AA, 0.5 μM ZnSe-BF_4, 10 μM NiCycP; AM 1.5G, $\lambda > 400$ nm, 100 mW cm^{-2}, pH 5.5, 4.0 sccm CO_2 flow, 25 °C.

sample are plotted as transparent scatter (in the same shape, with 50% transparency), whereas the mean is represented as a smoothened continuous line. In order to display the uncertainty of each experimental condition - *i.e.* the standard error - the standard deviation is visualised as shaded area surrounding the mean (mean ± standard deviation) where the transparency is proportional to the standard deviation. The result appears as a vertical 'cloud' of uncertainty and is similar to plotting the standard deviation as an error bar/ribbon around the mean, but is aesthetically more pleasing [323]. This visualisation is performed for both, product formation rate as well as total amount of product (Figure 3.6-C,D).

3.2.6 Concentration dependence

The influence of varying the overall photocatalyst concentration was examined in Appendix A.1. In short, more photocatalyst leads to higher product evolution rates (*i.e.* the intensities of the rate curves are enhanced), however, there is no major influence on the overall curve shape such as the induction period.

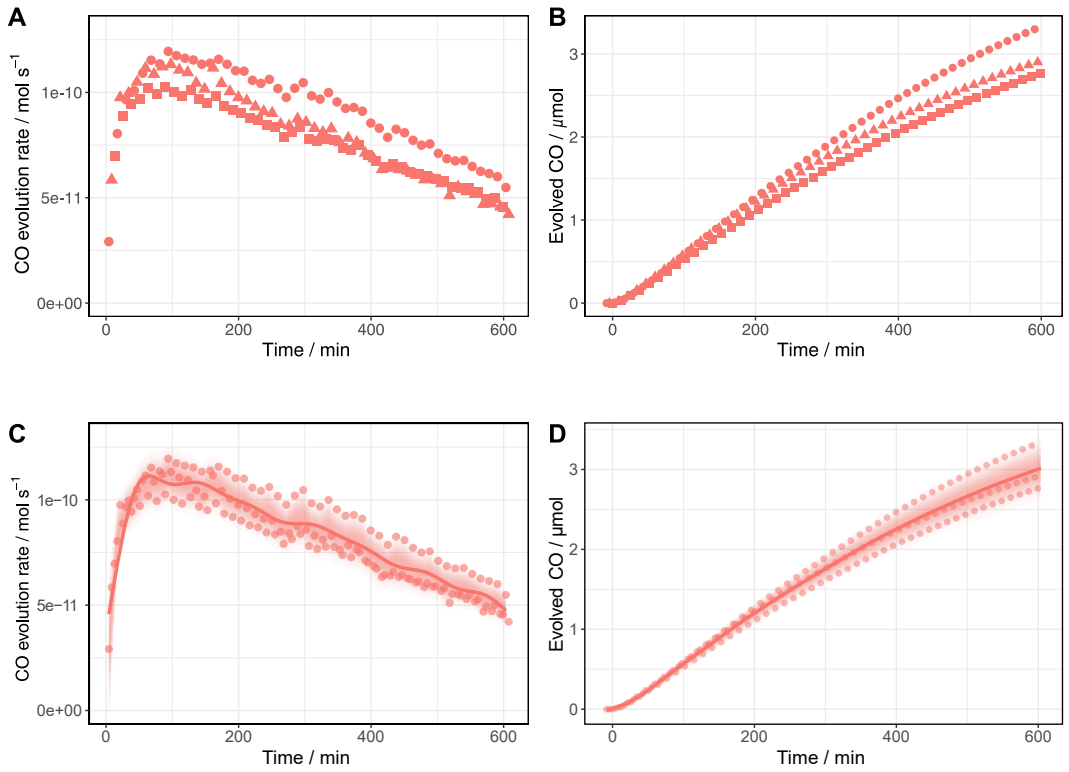

FIGURE 3.6: Data processing and visualisation for CO of continuous-flow photocatalysis using ZnSe | NiCycP. (A) Raw data: CO evolution rate. (B) Integrated CO evolution rate, i.e. total amount of product. (C) Averaging and error visualisation of CO evolution rate. (D) Averaging and error visualisation of evolved CO.

3.3 Conclusions

In conclusion, a continuous-flow setup for photocatalysis was successfully developed and tested with a well-known state-of-the-art photocatalyst ZnSe | Ni(cycP). The data analysis, visualisation and error reporting were described. The setup offers not only an increased measurement frequency (compared to manual sampling) and added flexibility in terms of reaction atmospheres, but also adds convenience because once the tubing is assembled, it can be operated without further human interaction for elongated irradiation times (*e.g.* overnight). This setup is the foundation for further high-quality analysis of photocatalytic systems throughout this dissertation.

3.4 Experimental section

Constant flow-setup with automated product quantification.
The inlet of the photoreactor was connected to a Mass Flow Controller (Brooks GF040) supplying a stream of CO_2 (CP Grade, BOC, humidified with a water bubbler) with a

flow rate of 4.0 sccm. The flow rate at the GC outlet was verified prior to the experiment with an Alicat gas flow meter to avoid gas leakage. The outlet of the photoreactor was connected to a flow selection valve controlled by a Shimadzu Tracera GC-2010 Plus gas chromatograph for product quantification of the gaseous reaction products (see below). Six samples (two triplicates of identical conditions) were typically analysed in parallel. The photoreactor was purged for a further 45 min in the dark and sampled via online GC quantification. The first two injections of each sample were used to determine a "background" peak which was subtracted from further injections. The photoreactor was then irradiated by a solar light simulator (Newport Oriel, AM 1.5G, 100 mW cm^{-2}). The temperature was maintained constant with a water bath at 25 °C. The six samples were evenly distributed within the light simulator to account for possible variations of the light intensity depending on the position in the simulator. UV irradiation was filtered with a 400 nm cut-off filter (UQG).

The Shimadzu Tracera GC-2010 Plus gas chromatograph (GC) used a barrier discharge ionization detector, kept at 300°C, and was equipped with a Hayesep D (2 m * 1/8" OD, 2 mm ID, 80/100 mesh, Analytical Columns) pre-column and a RT-Molsieve 5A (30 m * 0.53 mm ID, Restek) main column in order to separate H_2, O_2, N_2, CH_4 and CO while hindering CO_2 and H_2O to reach the Molsieve column. He carrier gas (Grade 5.0, BOC) was purified (HP2-220, VICI) before entering the GC. The temperature of the column was kept constant at 85°C. The gaseous flow from the flow selection valve was passed through a loop (volume 1.0 mL) and injected approximately every 4.25 min into the GC. The GC calibration was performed with a known standard for H_2, CO and CH_4 (2040 ppm H_2/2050 ppm CO/2050 ppm CH_4 in balance gas CO_2, BOC) by diluting the mixture with pure CO_2.

Data analytics.

The data was processed and visualised using the statistical programming language *R* with the *tidyverse* library [324, 325]. First, the flow rates were corrected by subtracting a "background" peak obtained in the dark prior to irradiation (a marginal CO background peak was noticed depending on the residual amount of oxygen present in the sample stream - a feature of the gas chromatograph and not the sample). Second, the momentary product evolution rate corresponding to each injection was calculated using the following formula:

$$product\ evolution\ rate = \frac{p * \dot{V} * \frac{Area\ GC}{f_i}}{R\,T}$$

where p is the pressure in the photoreactor (ambient pressure, 101325 Pa), $\dot{V}$ is the flow rate (4.0 sccm), R is the universal gas constant, T is the temperature (298 K) and f_i is the response factor for each gas determined by the calibration procedure. Third,

the total amount of evolved product was calculated using trapezoidal integration of the product evolution rates. The three independent replicates of identical conditions were averaged by calculating the mean and standard deviation over irradiation time and sample. For visual display, the actual values for each sample are plotted as transparent scatter, whereas the mean is represented as a smoothened continuous line. In addition, the standard deviation is visualised by the shaded area surrounding the mean where the transparency is proportional to the standard deviation. Specifically, the calculated standard deviation is used to compute a Gaussian density for that standard deviation, plotting a cloud with the opacity proportional to the density. This appears as a vertical "cloud" of uncertainty [323].

Chapter 4

QD-molecular catalyst hybrids

Parts of the contents of this section have been prepared for publication in a peer-reviewed journal: C. D. Sahm, G. M. Ucoski, S. Roy and Erwin Reisner, Automated and continuous-flow platform to analyze photocatalytic semiconductor-metal complex hybrid systems for CO_2 reduction, ***2021*** *(submitted manuscript). Results presented were obtained solely by the author of this thesis, with contributions from others as outlined here: Alex Cowan and co-workers (University of Liverpool) provided Ni(cycP) and Ni(cycH). Kristian E. Dalle provided the trimethyl-functionalised Fe tetraphenly porphyrin Fe(tpp-TMA4) and screened its activity. Geani M. Ucoski provided Co(tppsS3N1) and screened its activity. Souvik Roy provided Co(qpy) and the phthalocyanines and screened their activity.*

4.1 Introduction & Motivation

As outlined in section 1.5, a promising molecular co-catalyst based on a phosphonated Ni-cyclam was successfully combined with ZnSe quantum dots previously [317]. This study, however, was limited to macro-cycles based on various Ni-cyclams only. In this section, the objective is to explore if the ability of ZnSe QDs to drive an efficient molecular catalyst is unique to Cyclam structures and if it can be expanded to different classes of molecular catalysts. Additionally, the newly developed continuous-flow system offers more possibilities how to perform light experiments with a much-improved time resolution and higher throughput and has rarely been used in the context of photocatalytic CO_2 reduction in the literature. Particularly, one aim is to study the QD-molecular co-catalyst hybrids more broadly under various atmospheres, such as low CO_2 concentration, aerobic conditions and various light intensities which all resemble more real-world scenarios. For example, the supply of CO_2 for the generation of solar fuels is an

obstacle because the concentration of atmospheric levels of CO_2 (ca. 400 ppm) to 100% represents a huge energy penalty compared to others energy carriers such as H_2, which originate from freely available water [326]. The same argument applies to cost: even the most optimistic scenarios predict a price between 94 and 232 USD/t-CO_2 [327] in order to capture CO_2 from the atmosphere. Therefore, it is highly desirable to develop catalysts that can operate under lower CO_2 concentration such as readily available flue gas (CO_2 concentration 10-25 %). Similarly, the presence of O_2 can often be detrimental for the activity of common CO_2 reduction catalysts, however, may be present in more real-world scenarios, especially, when CO_2 reduction would be coupled to water oxidation. Lastly, if the sun is utilised as primary energy source for photocatalysis, it is intriguing to study the effect of a varying light intensities (e.g. morning/afternoon) and how they affect catalysis.

Furthermore, one particular objective is to study the competition of CO_2 reduction with proton reduction which leads to the H_2 evolution reaction (HER). The large concentration of protons in aqueous media renders this side-reaction inevitable, especially since the bare ZnSe-BF_4 QDs are highly active towards HER [318]. A successful hybrid photocatalyst can efficiently transfer photogenerated electrons to the co-catalyst for CO_2 conversion and limit the HER side reaction. Different anchoring strategies will be explored and how they affect electronic communication and the product selectivity. A H_2:CO ratio between 1:1 and 3:1 is desirable because of the overarching goal to generate syngas within this dissertation.

This chapter commences with a comprehensive molecular catalyst screening in combination with the ZnSe QDs. The best performing catalysts are selected and investigated in further detail. In subsequent experiments, the influence of low light intensity, low CO_2 concentration and aerobic conditions are tested and complemented by post-catalysis characterisation, performance evaluation and long-term experiments. The proposed hybrid photocatalyst system is illustrated in Figure 4.1.

Please note that the term "ZnSe QDs" always refers to the unfunctionalised ZnSe-BF_4 QDs (see Chapter 2) and a different surface modification is always specified.

4.2 Results & Discussion

4.2.1 Screening

Selection of catalysts

In the first step, a range of common molecular CO_2 reduction co-catalysts were screened

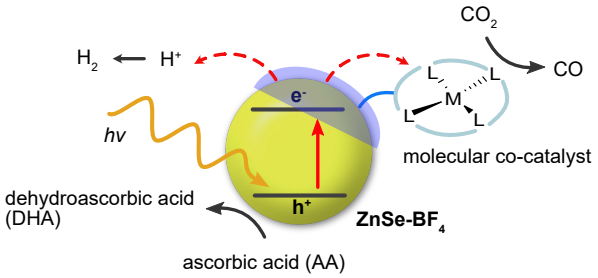

FIGURE 4.1: Schematic representation of the developed hybrid photocatalysts in this section: ligand-free ZnSe QDs (ZnSe–BF_4) combined with molecular co-catalysts for CO_2 to CO reduction in water under continuous-flow. Aqueous protons compete for CB electrons which leads to H_2 evolution, an inevitable side-reaction for this photocatalyst in aqueous media.

in combination with ZnSe-BF_4 QDs. Co-catalysts were selected with two main objectives in mind: First, the major reaction product amongst carbonaceous products should be (exclusively) CO because of the overall goal to produce syngas as well as the ease of quantification via the newly developed in-line gas chromatography setup. Second, only catalysts that employ earth-abundant metals such as Fe, Co and Ni were selected in order to avoid precious metals which can potentially impose limits on the scalability of such a photosystem. An overview of the selected catalysts is given in Figure 4.2 and Table 4.1.

The phosphonic acid-functionalised Ni(cycP) was included as well-known co-catalyst for comparison and benchmarking together with its non-modified analogue Ni(cyclam) [317].

Two representative catalysts out of the Ni(bis(terpyridine)) family were selected because they showed activity and a high selectivity for CO when anchored on CdS-QDs in purely aqueous solution - one of the first examples of a molecular catalyst-QD hybrid phototcatalyst [186]. Co equivalents of the same catalyst group were not included in this screening because they were reported to evolve formate in addition to CO, depending on the solvent mixture and applied potential [188, 274].

A Co(quarterpyridine) was chosen due to its exceptionally high activity (TON = 2660 with 98% selectivity towards CO) which was reported first combination with organic or Ru-based organic photosensitisers in homogeneous (organic) solution [195] and subsequently also in aqueous solution when immobilised on carbon nanotube electrode [199].

A trimethylamine functionalised Fe(tetraphenyl-porphyrin) was selected as a prominent example of the porphyrin catalyst family due to the many reports of this catalyst, for example when sensitised by an organic dye [179] and much enhanced performance when combined with a highly reducing Ir-photosensitiser, that led to the production of CH_4 in addition to CO [180].

The recently introduced Co(porphyrin) catalyst, bearing four negatively charged sulfonate groups Co(tppS4) [182] was included in this screening. The charged sulfonate

groups generally aid water solubility. Within this research group, synthetic modifications of a Co(porphyrin) with sulfonate groups has led to a Co(porphyrin), modified with three negatively charged sulfonate groups and one amine group and was included as well.

Lastly, two examples of the phthalocyanine catalyst class [328] were tested featuring either negatively charged sulfonate groups or positively charged trimethylammonium groups. The charged functional groups not only enable water solubility but are expected to increase interactions with the QD surface. Uncharged phthalocyanines (as well as tetraphenylporphyrins) were excluded in this study due to their lack of water solubility.

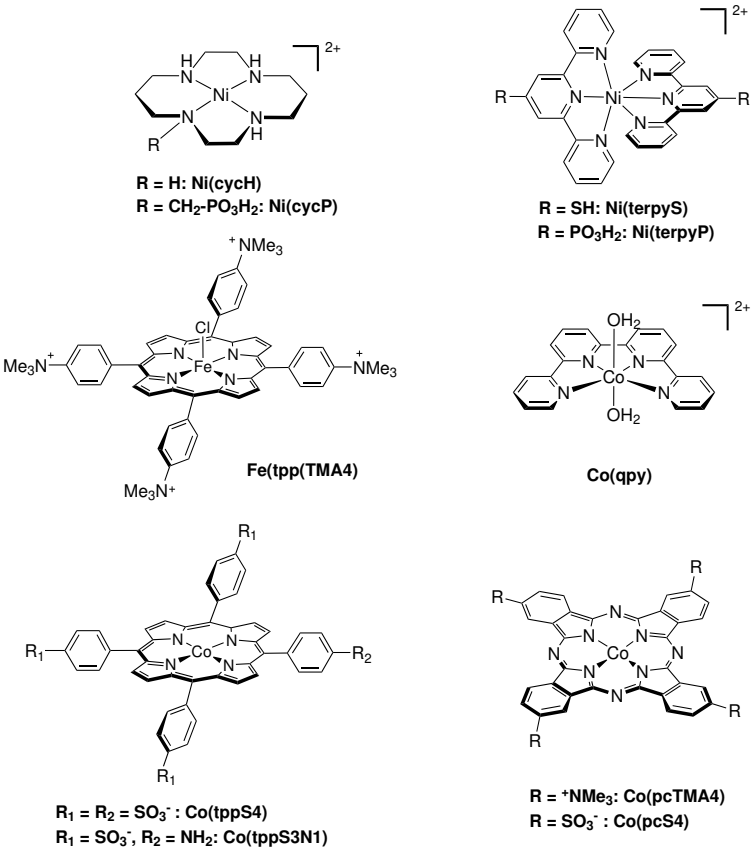

FIGURE 4.2: Overview of employed molecular co-catalysts in this study.

Screening results

The hybrid photocatalyst systems were assembled by adding a co-catalyst solution (20 to 50 $mol_{co\text{-}cat}$ $mol_{QD}{}^{-1}$, typically in water, or a 1:1 mixture of water/acetonitrile for the terpyridine-based catalysts) to a solution of ZnSe-BF_4 QDs (in DMF) followed by dilution in aqueous AA solution (pH 5.5). The photocatalytic activity was then screened by irradiating the CO_2-saturated samples under UV-filtered simulated solar light irradiation (AM 1.5G, $\lambda > 400$ nm, 100 mW cm^{-2}) accompanied by accumulation of gaseous reaction products in the headspace and subsequent quantification via GC. Table 4.1 depicts the results of the co-catalyst screening. During the initial screening, high activity was detected for Ni(cycP), Co(qpy) and both sulfonate-modified porphyrins (Co(tppS4) and Co(tppS3N1)). The results are surprising, because the often-employed Ni(terpyridines), successfully combined with CdS previously [186], showed no or negligible activity, even though they feature amongst the lowest onset potential when heterogenised on an electrode (Table 4.1). A similar observation applies to the phthalocyanines, also low onset-potential catalysts, which show little (Co(pcS4)) or no activity (Co(pcTMA4)). To account for the possibility of some catalysts to generate formate ($HCOO^-$) besides CO, the liquid phase was examined using ^{1}H-NMR spectroscopy but no significant amounts of formate were detected. This is in particular relevant for the terpyridines which have been shown to display potential-dependant product selectivity (H_2 vs. CO vs. formate) [188].

Even though the conduction band of the ZnSe QDs is sufficiently negative (-1.4 V *vs.* NHE at pH 5.5 [313]) and capable of driving all the herein tested molecular catalysts, the screening results highlight that it is not trivial to successfully couple a molecular co-catalyst with QDs purely based on thermodynamic considerations (*i.e.* E_{onset}). The photocatalytic activity of such a hybrid photosystem is a function of numerous variables including thermodynamic and kinetic constraints: In addition to the thermodynamic requirement (QD CB more negative than co-catalyst onset potential), the electron transfer (ET) from the QD must be faster than charge recombination which requires good electronic communication between co-catalyst and light absorber with limited back electron transfer (see section 1.2.2). Most QD-molecular acceptor charge transfer (CT) processes can be described via Marcus theory [61]. In contrast to molecular donor-acceptor systems, for QD-molecular acceptor system, the rate of ET thereby increases exponentially/monotonically with the difference in free energy $-\Delta G_0$, *i.e.* the driving force, and does not show an inverted regime in which the ET rate decline, due to Auger-assisted processes (please refer to the introduction section 1.2.2 for a detailed explanation) [62]. Consequently, ET from ZnSe QDs should be faster towards the low-onset potential co-catalysts (terpyridines/phthalocyanines) from a purely thermodynamic point of view. Nevertheless, other factors such as the chemical nature and geometrical factors may

Catalyst	**Abbreviation**	**Catalyst class**	**Photocatalytic activity**	E_{onset} / V *vs.* NHE
$[Ni(cyclam)]^{2+}$	Ni(cycH)	Cyclam	low	-1.05 (pH 4.0)
$[Ni(cyclamPO_3H_2)]^{2+}$	Ni(cycP)	Cyclam	high	-1.13 (pH 4.0)
$[Ni(terpyridineSH)_2]^{2+}$	Ni(terpyS)	Bis(terpyridine)	not detected	-0.75 (pH 6.7) [186]
$[Ni(terpyridinePO_3H_2)_2]^{2+}$	Ni(terpyP)	Bis(terpyridine)	low	-0.85 (pH 6.7)[186]
$[Co(quarterpyridine)(OH_2)_2]^{2+}$	Co(qpy)	Quarterpyridine	high	-0.90 (pH 4.0)
$[Fe(tetraphenylporphyrin(NMe_3)_4Cl)]^{4+}$	Fe(tppTMA4)	Porphyrin	low	-1.26* (DMF) [180]
$[Co(tetraphenylporphyrin(SO_3)_4)]^{4-}$	Co(tppS4)	Porphyrin	high	-0.8 (pH 4.0)
$[Co(tetraphenylporphyrin(SO_3)_3(NH_2))]^{3-}$	Co(tppS3N1)	Porphyrin	high	-0.85 (pH 4.0)
$[Co(phthalocyanine(NMe_3)_4)]^{4+}$	Co(pcTMA4)	Phthalocyanine	not detected	-0.7 to -0.9 (pH∼7)**
$[Co(phthalocyanine(SO_3)_4)]^{4-}$	Co(pcS4)	Phthalocyanine	low	-0.7 to -0.9 (pH∼7)**

TABLE 4.1: Results of the screening of molecular co-catalysts in the presence of ZnSe-BF_4 QDs for photocatalytic CO_2 reduction. Photocatalytic activity classification: high: CO evolution > 0.5 μmol; low: CO evolution < 0.5 μmol. Not detected if n (CO) $<$ CO background from QDs. Please refer to B.1 for all details. E_{onset} determined via cyclic voltammetry (Figure B.2) if literature value not available. *estimate, converted from DMF, reported value: -1.50 V vs. SCE (DMF) **estimated from similar Co phthalocyanines analogues found in the literature [191, 192, 328]). General conditions: product accumulation in the headspace, 0.1 M AA, 0.5 μM ZnSe-BF_4, 10 to 25 μM co-catalyst AM 1.5G, $\lambda > 400$ nm, 100 mW cm^{-2}, CO_2, 25 °C.

circumvent efficient ET. For example, both terpyridines and phthalocyanines feature a large degree of conjugation between the anchor/charged functional group and the core with restricted torsion, in contrast to the porphyrins, which are conjugated but with unrestricted torsion. Such a configuration can favour fast ET to the co-catalyst but potentially also induce fast recombination by back ET to ZnSe, as shown for a Co(terpyP) and TiO_2 [329]. In addition, if the ET is much faster than the uptake of electrons by the catalyst, excess electrons may potentially aid the degradation of the co-catalyst. Thus, the observation that some molecular catalyst do not exhibit activity in conjunction with the ZnSe QDs is likely due to kinetic constraints. In summary, ZnSe QDs demonstrate that unlike the Cd-counterparts (specifically CdS) [186] are able to drive a range of molecular catalysts previously inaccessible.

As a result of the initial screening, Ni(cycP), Co(qpy), Co(tppS3N1) and Co(tppS4) were selected as co-catalysts for further in-depth analysis (below). The selection not only represents a range of various macrocycles, but also different anchoring strategies: Co(qpy) interacts with ZnSe-QDs purely diffusional while Ni(cycP) features a phosphonate anchoring group. Co(tppS3N1) and Co(tppS4), however, exhibit charged functional groups that may facilitate electrostatic interactions with the highly charged QD surface.

4.2.2 Co-catalyst survey

The photocatalytic performance of ZnSe-BF_4 QDs was systematically studied under continuous flow (as described in Chapter 3) with the above selected co-catalysts Ni(cycP), Co(qpy) and Co(tppS3N1). The two similar porphyrins Co(tppS3N1) and Co(tppS4) will be compared further below.

The QD concentration was kept constant at 0.5 μM and the co-catalyst concentration at 10 μM, which represents a loading of 20 catalyst molecules per QD. This loading is typically a good compromise between the specific activity of the co-catalyst (turnover numbers) and high overall product generation (Figure B.1).

All hybrid catalysts exhibit high activity at this co-catalyst loading (Appendix B.1). Additionally, all catalysts were briefly optimised towards their ideal pH in-between 4.5 and 6.5. Co(qpy) and Ni(cycP) showed the highest activity at pH 5.5 whereas Co(tppS3N1) showed peak performance at pH 4.5 (appendix B.1).

Most experiments throughout this section were conducted at very similar conditions and will be referred to as ***standard flow conditions*** and only deviations from those will be mentioned specifically:

- 0.1 M AA, 3 mL total volume, pH 4.5 (Co(tppS3N1)), pH 5.5 (Ni(cycP)), pH 5.5 (Co(qpy)) after saturating with CO_2
- 0.5 μM ZnSe-BF_4
- 10 μM co-catalyst
- AM 1.5G, 100 mW cm^{-2}, $\lambda > 400$ nm
- Constant flow of CO_2 (4.0 sccm)
- 25 °C

The results of the photocatalytic survey are depicted in Figure 4.3 and Table B.2. ZnSe-BF_4 QDs in the absence of co-catalyst evolve H_2 by reducing aqueous protons (Figure B.4) as reported previously [318]. CO production is enabled in the presence of the co-catalysts: ZnSe | Co(qpy) reaches peak turnover for CO after ca. 100 min after which the CO evolution rate declines rapidly and mostly H_2 is generated. This observation may be explained with the diffusional nature of Co(qpy). The co-catalyst interacts with the QD-surface (as seen by the high initial activity within the first 100 min) and is able to utilise photogenerated electrons for CO_2 reduction. The rapid loss of CO activity may be due to decomposition of the co-catalyst or weak anchoring (majority of

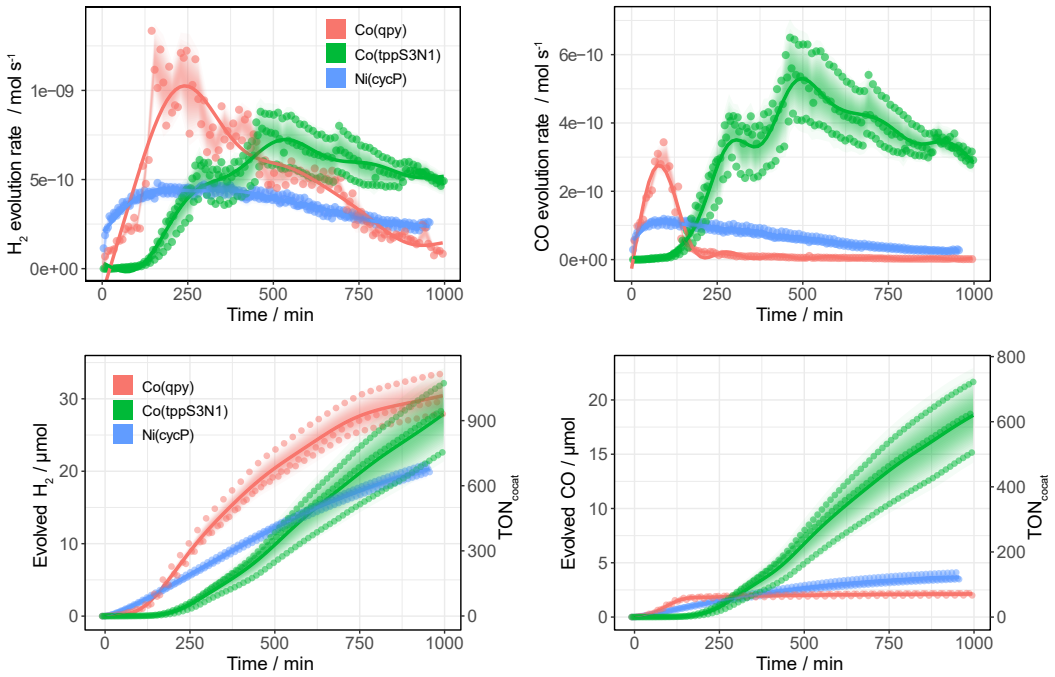

FIGURE 4.3: Survey of photocatalytic CO_2 reduction in the presence of ZnSe-BF_4 and various co-catalysts Co(qpy), Ni(cycP) and Co(tppS3N1). Note, the fluctuating trend in both HER and CO evolution rates of Co(tppS3N1) after 300 min may be due by experimental error caused by the MFCs. Standard flow conditions.

co-catalyst in solution) and will be investigated further below. ZnSe | Ni(cycP) shows a lot higher stability which can be rationalised with its phosphonate anchoring group. There is a small induction period for both HER and CO evolution, however, the generation of CO remains relatively steady over the course of hours and only declines slowly, presumably due to a higher quantity of attached/undamaged Ni(cycP) on the surface. ZnSe | Co(tppS3N1) exhibits a different behaviour: There is a significant induction period for both HER and CO_2 reduction. This is a surprising finding and suggests a strong anchoring of the catalyst to the QD surface, otherwise more HER would be visible in the first 200 min of the experiment, because the bare QDs are highly active towards the HER. After ca. 200 min, the hybrid catalyst starts to evolve both H_2 and CO. Clearly, the active co-catalyst species needs to be generated *in-situ*. (This induction period will be investigated further below.) The evolved H_2 may well originate from the porphyrin co-catalyst itself, as reported in the literature for Co(tppS4) [182]. The CO evolution rate peaks only after 500 min at significantly higher rates compared to the two other catalyst assemblies, reaching an unprecedented $TON_{Co(tppS3N1)}$ (CO) of 619 after 1000 min of irradiation. In comparison, ZnSe | Co(qpy) and ZnSe | Ni(cycP) reach a $TON_{co\text{-}cat}$ (CO) of 71 and 116, respectively after the same irradiation time.

Controls & isotopic labelling

One of the most important controls in CO_2 reduction is ^{13}C-isotopic labelling. Particularly for photocatalysts in the presence of organic electron donors and solvent residues, it is of vital importance to prove the origin of evolved CO from CO_2 in order to exclude any other carbon source that may contribute through decomposition reactions. All best performing co-catalyst-QD hybrids were therefore tested under an atmosphere of $^{13}CO_2$ under optimised conditions and the headspace was analysed via gas phase transmission Fourier-transform infrared (FTIR) spectroscopy after irradiation. For ZnSe | Co(qpy), ZnSe | Ni(cycP) and ZnSe | Co(tppS3N1) the vibration associated with CO is shifted from 2142 cm^{-1} to 2095 cm^{-1} compared to a reference spectrum of ^{12}CO (Figure 4.4) which confirms its assignment as ^{13}CO [330]. This observation clearly proves that all the evolved CO originates from CO_2 and no other carbon sources contribute towards the detected reaction product.

No other reaction products (*e.g.* methane, methanol) were detected. Only traces of CO and mostly H_2 were produced in the absence of a co-catalyst and no gaseous products were detected in a series of deletional control experiments in the dark or absence of QDs or AA, demonstrating that all components of the photocatalytic system are required (Table B.3).

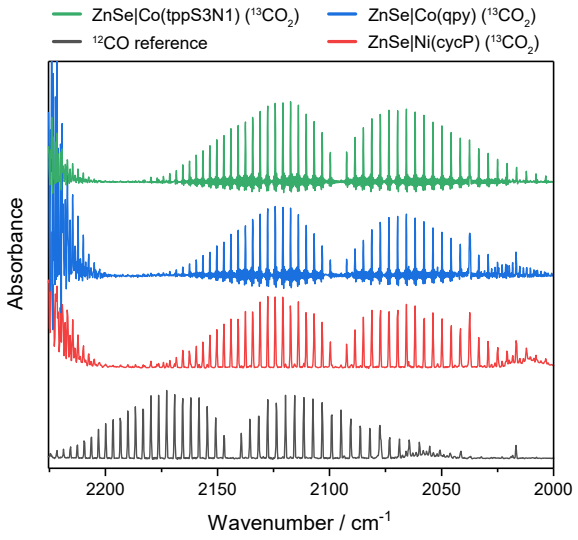

FIGURE 4.4: ^{13}C-Isotopic labelling: Gas-phase transmission FTIR spectra of the CO vibration depending on the employed CO_2 isotopologue. Samples ZnSe | Co(qpy), ZnSe | Ni(cycP) and ZnSe | Co(tppS3N1) under an atmosphere of $^{13}CO_2$ compared to a reference spectrum of ^{12}CO. Conditions: AM 1.5G, $\lambda > 400$ nm, 100 mW cm^{-2}, 0.5 μM ZnSe-BF_4, 10 μM co-catalyst, 0.1 M AA, pH 4.5 (Co(tppS3N1), pH 5.5 (Ni(cycP) and Co(qpy)), CO_2, 25°C, 1000 min irradiation with product accumulation in the headspace.

Co-catalyst attachment

The attachment of the co-catalysts to the QD-surface was quantified via the following protocol: First, the UV-vis absorption spectrum of the co-catalyst was recorded.

Second, QDs were added (ratio 20 mol_{cocat} mol_{QD}^{-1}) and precipitated via centrifugation. Next, the UV-vis spectrum of the supernatant was re-recorded and the amount of co-catalyst immobilised on the QD surface was calculated from the change in absorbance intensity. As depicted in Figure 4.5-A and Table B.4, the absorption spectrum of Co(qpy) is nearly unchanged, confirming its diffusional nature and lack of immobilisation. Co(tppS3N1), however, exhibits a drastically lowered absorption intensity (based on the signal at 420 nm) which was translated to an attachment of 84% of the amount of employed co-catalyst (Figure 4.5-B). The zwitterionic species with three negatively charged sulfonate groups and one (presumably) positively charged amine group is clearly a proficient anchoring strategy with the highly charged QD surface. Electrokinetic zeta potential measurements (conducted in Chapter 2) confirm that the ZnSe-BF_4 exhibits a positive potential (+20 mV) which rationalises the attachment of oppositely charged Co(tppS3N1) (Figure 2.4). This electrostatic assembly also shows a higher attachment than Ni(cycP) with its dedicated, "traditional" phosphonate surface-bound anchoring group. The attachment of Ni(cycP) to ZnSe QDs was previously quantified via ion-coupled plasma optical emission spectroscopy (ICP-OES) of 7.8% [317]. Ni(cycP) does not feature a distinct UV-vis absorption profile.

Figure 4.5-C depicts the QD-co-catalyst hybrid's activity and selectivity towards CO depending on the co-catalyst attachment. While all co-catalyst feature different intrinsic activities, which renders a "fair" comparison impossible, it can be deducted that the activity, and in particular the selectivity towards CO, correlate strongly with the co-catalyst attachment. This observation can be rationalised with the QDs ability to generate H_2 in the absence of a co-catalyst. The more co-catalyst is immobilised on the QD surface, the more photogenerated charges can be extracted and transferred to the co-catalyst and utilised for further CO_2 conversion. This finding is also in line with a range of Ni(terpyridine) co-catalysts which were systematically compared on CdS-QDs. The photocatalytic activity correlated strongly with the co-catalyst anchoring and peaked for a Ni(terpyridine) with a thiol-anchoring group [186].

4.2.3 Comparison of Co(tppS3N1) with Co(tppS4)

In order to further understand the high activity of Co(tppS3N1), the two sulfonate-modified porphyrins were further tested and benchmarked against each other (Figure 4.6). While Co(tppS3N1) exhibits a significantly longer induction period compared to Co(tppS4) for both H_2 and CO, Co(tppS3N1) eventually evolves CO at higher rates and overtakes Co(tppS4). After 1000 min of continuous irradiation, ZnSe | Co(tppS3N1) produces 18.6 ± 3.3 μmol CO (TON_{Co} = 619) whereas ZnSe | Co(tppS4) generated

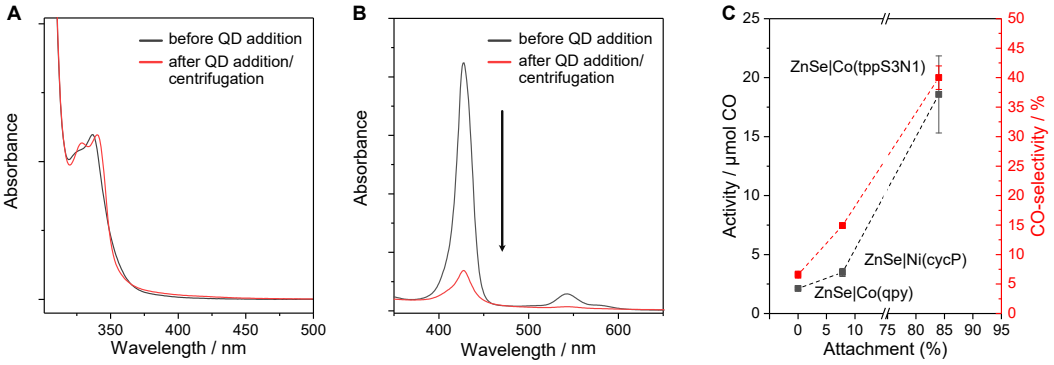

FIGURE 4.5: Co-catalyst attachment quantification. UV-vis absorption spectrum of (A) Co(qpy) (50 μM in H_2O containing 10 mM AA)) and (B) Co(tppS3N1) (10 μM in H_2O) before addition of QDs followed by centrifugation. (C) Plot of attachment of co-catalyst (in % immobilised per employed ligands) vs. photocatalytic activity and CO-selectivity.

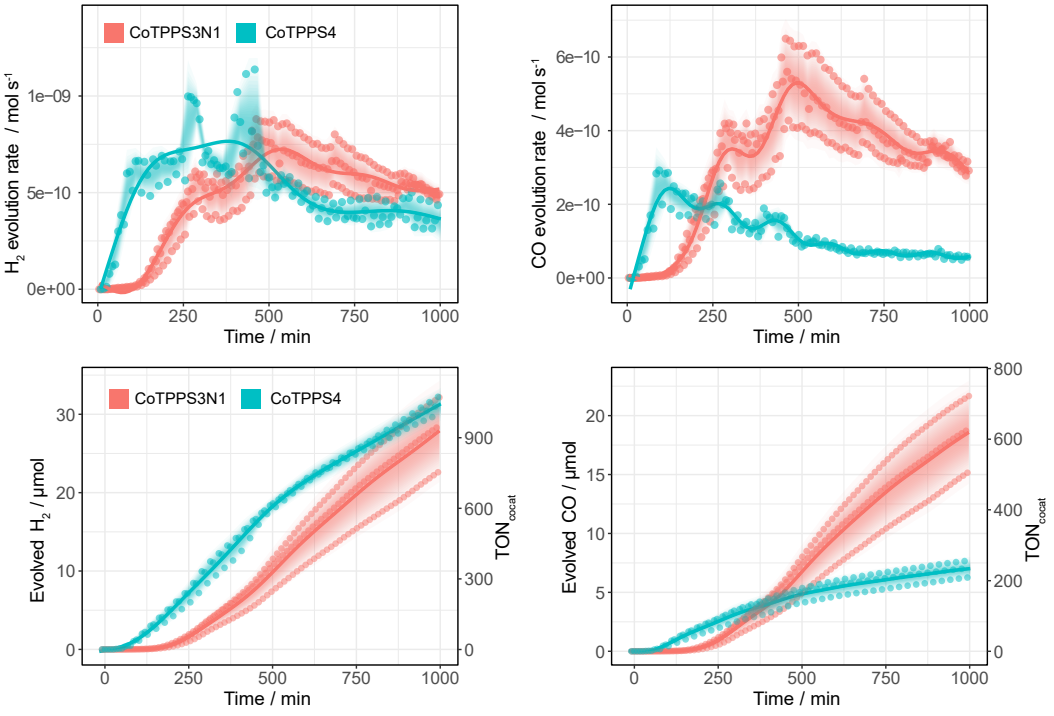

FIGURE 4.6: Comparison of the photocatalytic CO_2 reduction activity of Co(tppS3N1) *vs.* Co(tppS4) in the presence of ZnSe-BF_4. Note, the fluctuating trend in both HER and CO evolution rates of Co(tppS3N1) after 300 min may be due by experimental error caused by the MFCs. Standard flow conditions.

7.0 ± 0.7 μmol CO (TON_{Co} = 233). In the following the origin of this distinct induction period is investigated.

Both molecular catalysts attach equally well to the QDs with approximately 86% (Co(tppS4)) and 84% (Co(tppS3N1)), respectively, of the amount of employed catalyst (Table B.4). This finding indicates that the affinity of the co-catalyst to the QD surface is not the cause of the different performance. Co(tppS4) was previously shown to exist initially as Co^{III} in aqueous solution and requires reduction to Co^{II}, facilitated by AA (independent of light), in order to enter the catalytic cycle (Figure 4.7-A, the full mechanism is depicted in Figure B.5). This initial reduction was accompanied by a slight blue-shift of the absorption spectrum. In the following, this initial Co^{III} to Co^{II} was monitored via UV-vis spectroscopy by recording a spectrum of the catalyst in AA solution at regular time intervals (Figure 4.7-B). The spectrum of Co(tppS4) indeed exhibits the blue shift of the main absorption feature from 425 nm to 412 nm within 1 min of addition of AA. The shift is followed by a reduction in intensity of the 412 nm signal accompanied by a broad feature growing at 585 nm. In comparison, Co(tppS3N1) exhibits only a marginal shift of the main absorption feature at 427 nm upon addition of AA, which is gradually lowered in intensity in subsequent time intervals. A broad growing feature at ∼ 580 nm is visible as well, likewise to Co(tppS4). Notable is the time scale of both reactions: While Co(tppS4) requires approx. 25 min to reach a steady-state signal, Co(tppS3N1) takes significantly longer (120 min) to reach the final steady absorption profile. This period (120 min) matches precisely with the induction period of Co(tppS3N1) under photocatalytic conditions in which no activity is observed (Figure 4.6).

Besides the Co^{II}/Co^{I} couple and catalytic onset, a cyclic voltammogram of Co(tppS3N1) also showed a redox couple at + 1.1 V vs. NHE, which was assigned to Co^{III}/Co^{II} (Figure B.3). This renders the reduction of Co^{III} by AA feasible (E_{ox} (AA^{-}) = + 0.78 V vs. NHE (pH 6.7) [182]).

Next, it was explored if the induction period seen in photocatalysis can be accelerated/eliminated by priming the co-catalyst in the presence of AA. Therefore, an experiment was conducted in which the photocatalyst system was assembled and stirred in the dark in the presence of all components (ZnSe | Co(tppS3N1 | AA, Figure 4.8, green trace) for 2 h before irradiation. A different sample consisted of only co-catalyst dissolved in AA solution (Co(tppS3N1 | AA, red trace) which was left for 2 h prior to addition of ZnSe and irradiation. In comparison to the standard experiment (blue trace), stirring the fully assembled catalyst system did not affect the induction period (Figure 4.8). However, when Co(tppS3N1) was pre-reduced in the presence of AA (and absence of ZnSe), the induction period vanished and the hybrid catalyst showed an almost instant onset

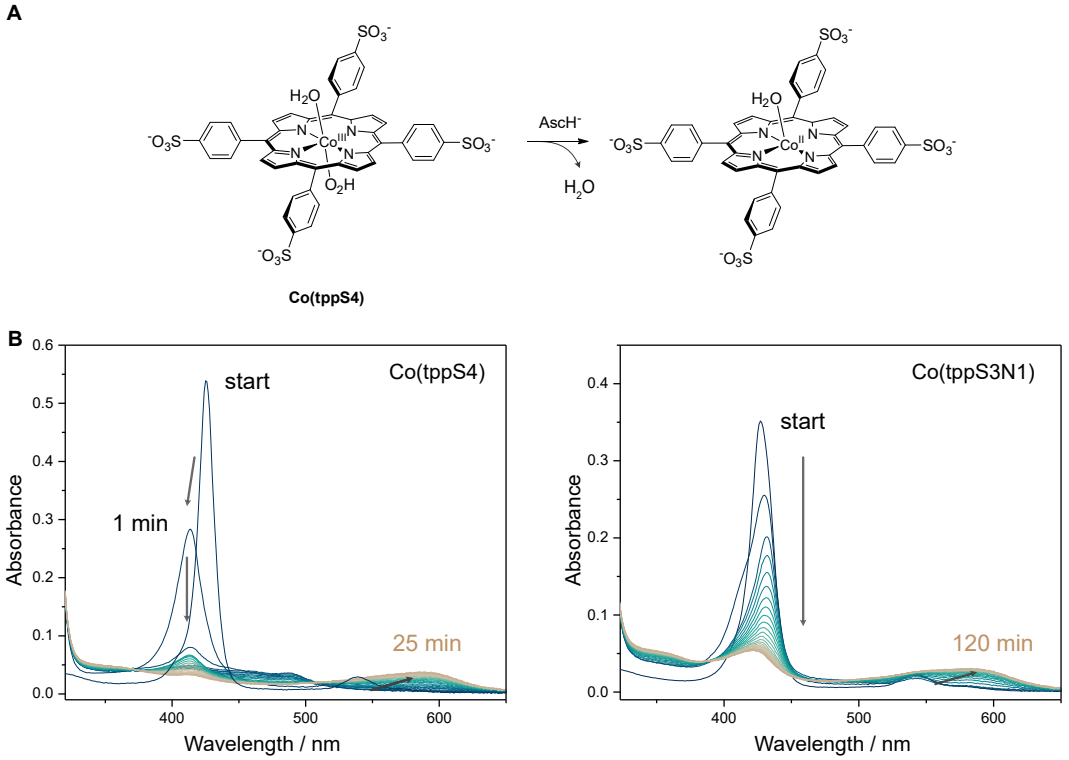

FIGURE 4.7: (A) Reduction of Co(tppS4) in the presence of AA [182]. (B) UV-vis absorption spectra of Co(tppS4) and Co(tppS3N1) (1.7 μM in water) in the presence of 0.1 M AA (pH 4.5) recorded every 1 min and 5 min, respectively. "Start" refers to the spectrum in purely aqueous solution in the absence of AA.

after addition of ZnSe followed by irradiation. This observation strongly supports the hypothesis that the origin of the induction period is the slow initial reduction of Co^{III} to Co^{II}. The reason why the QDs are particularly inefficient at reducing the catalyst is questionable and is further complicated by the observation that the QDs seem to "shield" the co-catalyst when it is immobilised on the QD surface from the initial reduction. The co-catalyst clearly shows a different redox behaviour when it is in a different environment (immobilised on the QD surface) compared to when it freely diffuses in the bulk solution.

Due to its superior photocatalytic performance after overcoming the induction period, Co(tppS3N1) was consequently selected over Co(tppS4) as the porphyrin for the following investigations and experiments.

4.2.4 Induction period investigations

Having assigned the distinct induction period of ZnSe | Co(tppS3N1 to an initial Co^{III} to Co^{II} reduction, the other hybrid photosystems (ZnSe | Ni(cycP), ZnSe | Co(qpy)) feature a notable period in which the product evolution rate increases until it reaches its

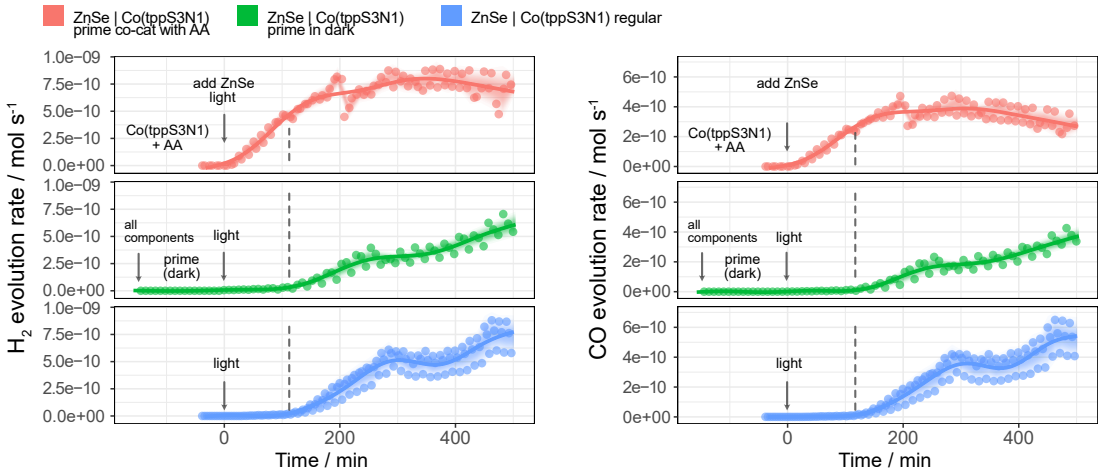

FIGURE 4.8: Priming Co(tppS3N1) in the presence of AA and its influence on photocatalytic activity using ZnSe-BF_4. Standard flow conditions.

peak performance: ZnSe | Ni(cycP) requires ∼ 60 min in order to reach peak turnover whereas the CO evolution rate of ZnSe | Co(qpy) peaks after ∼ 70 min. This initial lag phase could be caused by either the QDs or the co-catalyst. In a further experiment, the influence of the two compounds was decoupled by irradiating the QDs in the absence of a co-catalyst for 2 h (priming) after which the co-catalyst was added while the photocatalysis experiment was running. Co(qpy) did not exhibit a significant accelerated CO evolution rate and showed a slight broadening of the time dependent CO evolution trace (Figure 4.9). Ni(cycP), however, is active towards CO from the first injection onwards followed by a decaying activity curve. The overall lower activity when Ni(cycP) is added to the QD solution under irradiation conditions is presumably due to insufficient co-catalyst attachment: The co-catalyst attachment is assumed to be lower when the co-catalyst is added to the dilute QD solution, whereas during the normal assembly procedure, the co-catalyst is added directly to a highly concentrated QD stock solution. It is concluded that Ni(cycP) does not possess an "intrinsic" activation period whereas Co(qpy) is possibly limited by slow diffusion. (Priming the QDs in the case of ZnSe | Co(tppS3N1) did not lead to a change in activity since the limiting factor is the initial reduction of the co-catalyst, as shown above.)

The photocatalytic results point towards the QDs as the intrinsic origin of the initial lag phase. This is in accordance with the profile of the HER of ZnSe QDs in the absence of a co-catalyst, which exhibit the lag phase as well (Figure B.4). The exact origin of the lag phase can not be answered conclusively within the scope of this chapter but is presumably related to accumulating photogenerated electrons at or close to the ZnSe CB (and trap states). Initial time delays are not unique for colloidal photosystems, as shown for an assembly consisting of carbon nanodots as light absorber and methylviologen as

electron acceptor. The UV-active reduced methylviologen species was monitored *in-situ* and the results fitted with a kinetic model. The initial time delay was hypothesised to be influenced two-fold from 1) an activation barrier which requires surpassing before ET can proceed (due to internal rearrangement within the light absorbers that alters orbital energies) and 2) filling of trap states with excited electrons via collisions [331]. Morphological changes/surface restructuring as contribution to the lag phase can not be excluded at this point as well.

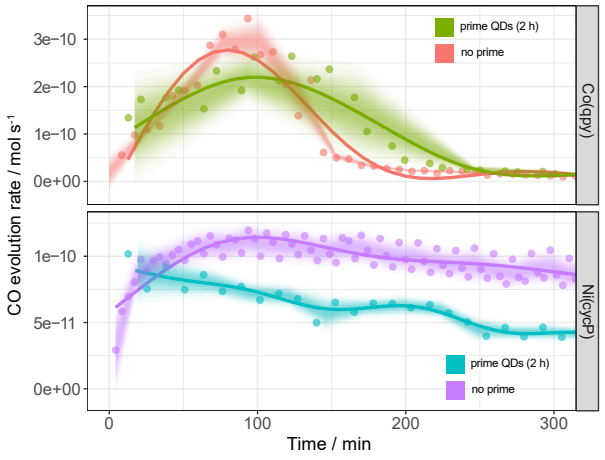

FIGURE 4.9: Priming ZnSe QDs during irradiation before addition of molecular co-catalysts; t = 0 refers to the time the experiment was started (no prime) and the time the co-catalyst was added to a solution of the QDs which have been irradiate for 2 h (prime QDs). Otherwise standard flow conditions.

4.2.5 Long-term photocatalysis

Long-term photocatalytic experiments were conducted in order to better understand the limiting factors for the different QD hybrid photocatalysts. After a given irradiation time when the CO evolution rate had dropped significantly, a similar amount (20 mol_{cocat} $mol_{QD}{}^{-1}$) of fresh co-catalyst was added to the photosystem and the production of H_2 and CO monitored (Figure 4.10).

Addition of fresh Co(qpy) after 500 min leads to a rapid recovery of the activity towards CO approaching its initial activity. Surprisingly, the addition of fresh co-catalyst suppressed H_2 indicating that Co(qpy) besides its lack of anchoring group interacts with the QDs strongly and is able to utilise most photogenerated electron towards CO evolution. Decomposition of AA and/or Co(qpy) followed by accumulation on the QD surface may contribute to suppressing competing HER.

For the electrostatic assembly of ZnSe | Co(tppS3N1), addition of fresh Co(tppS3N1) after 1300 min suppresses both H_2 and CO production in-line with its strong attachment to the QD surface. With continuous irradiation time, both reaction products start to

onset product evolution again, however, at lower rates compared to the fresh assembly. The significant induction period matches with the observation from section 4.2.3 with the slow initial Co^{III} to Co^{II} reduction as origin of the long induction period.

Addition of fresh Ni(cycP) after 1300 min yields a measurable increase in activity towards CO, however, the activity remains significantly lower than its initial CO evolution rate and fluctuates to a certain extent. The HER is not substantially affected by the addition of fresh co-catalyst. The reason for the lower recovery of activity for ZnSe | Co(tppS3N1) and ZnSe | Ni(cycP) (in comparison to Co(qpy)) could be related to the molecular catalyst's stronger binding affinity for the QD surface which leads to accumulation of poisoned/degraded catalyst on the surface in addition to oxidation products from AA. In addition, the irradiation time after which fresh Co(qpy) was added to the system was shorter in the case of ZnSe | Co(qpy) which might contribute to the activity recovery. For all three QD-molecular catalyst assemblies, the addition of fresh co-catalyst leads to an at least partial recovery of the CO activity. This finding illustrates that the co-catalyst stability is likely a substantial part of the limiting factors towards long-term activity.

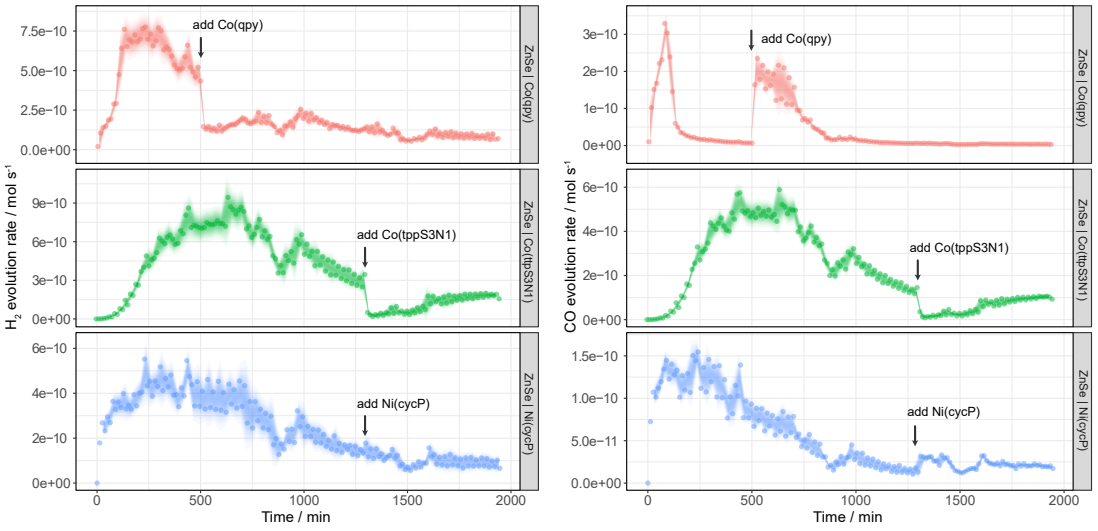

FIGURE 4.10: Long-term photocatalysis with addition of 20 equiv. of additional molecular co-catalyst after 500 min (Co(qpy)) and 1300 min Ni(cycP), Co(tppS3N1). Otherwise standard flow conditions.

4.2.6 Performance evaluation

The external quantum efficiency (EQE) is an important performance measure in photocatalysis because it indicates how efficiently absorbed photons are translated into reaction products [13]. It is defined as the number of product molecules formed divided by the number of incident photons used for irradiation:

$$EQE\ (\%) = \frac{z\ N_{product}}{N_{photon}}\ \cdot\ 100$$

With
$N_{product} = n(CO)\ N_A$,
$N_{photon} = E_{tot}/E_{photon}$,
$E_{photon} = h\nu = hc/\lambda$,
$E_{tot} = I\ A\ t_{irr}$
z refers to the number of transferred electrons which are utilised for the reaction. For the two electron reaction CO_2 to CO, it follows z = 2, which is often used in the literature for the calculation of the EQE. Nevertheless, it should be noted that for the current system, there is no proof that after the first electron transfer, the second electron originates from light-induced processes too and may be facilitated by ascorbate radicals, hence z = 1 was assumed - a more conservative approach to calculate the EQE.
it follows:

$$EQE\ (\%) = \frac{nCO\ N_A\ h\ c}{t_{irr}\ \lambda\ I\ A}\ \cdot\ 100$$

where $N_{product}$ is the number of CO molecules, *n(CO)* is the amount of moles of CO, N_A is the Avogadro constant, N_{photon} is the number of photons, E_{tot} is the total energy used for irradiation, E_{photon} is the energy of a photon, h is the Planck constant, c is the speed of light, λ is the irradiation wavelength, t_{irr} is the irradiation time, I is the light intensity and A is the irradiated area

The EQE was exemplary determined for ZnSe | Co(tppS3N1), which exhibits the highest photocatalytic activity tested within this work. At 1.5 mW cm^{-2} and 400 nm monochromatic illumination, ZnSe | Co(tppS3N1) achieved an EQE_{CO} = 1.52 ± 0.28 % (Table B.5, average over 3 h) which is on the same order of magnitude as ZnSe | Ni(cycP) (EQE_{CO} = 1.7 ± 0.15 %, EQE adjusted for z = 1 for comparability) [317]. (To avoid excessively long induction periods, the photocatalyst system was primed using high intensity AM 1.5G irradiation until peak performance was reached before the EQE was determined, see experimental section for details).

The performance reported herein ($TON_{co\text{-}cat} \sim 600$, $EQE_{CO} > 1.5\%$) obtained by hybrid ZnSe | Co(tppS3N1) is amongst the highest within reported colloidal photocatalyst systems that operate free of precious metals in aqueous solution. Additionally, the activity translates to a TON per QD (*i.e.* sensitiser) above 12 380, which underscores the QDs as platform for CO_2 reduction and is in contrast to many homogeneous systems

which often employ an excess of photosensitiser molecules. A higher activity was reported for a mercaptopropionic acid modified CdS nanocrystals in combination with a dinuclear cobalt catalyst which reached a TON_{cocat} = 1380 (22 h) with an impressive CO selectivity of 95% in fully aqueous solution [244]. However, the study did not report the light intensity used during photocatalysis which makes a comparison cumbersome. The Co(tppS4) analogue reached a TON_{cocat} = 926 (EQE = 0.81 %) in homogeneous aqueous solution although only in the presence of excess of precious metal [$Ru(bpy)_3^{2+}$] photosensitiser. Photosystems consisting of earth-abundant materials have reached high activities (TON_{cocat} = 155, EQE > 4%) in organic solution, in particular the Co quarterpyridine (and its Fe analogue) when linked to mesoporous carbon nitride (TON_{cocat} ~ 500, EQE ~ 4%) [200, 201]. Higher activities have been accomplished with catalysts based on precious metals for CO_2 reduction to formate: Anchoring dinuclear Ru complexes on Ag-loaded graphitic carbon nitride exhibited activity (TON > 2000, up to 98% selectivity, EQE = 0.2%) in aqueous solution and an exceptional TON > 33 000 when organic solvents were used instead of water [159, 160].

4.2.7 Post-catalysis characterisation

TEM micrographs of the QDs after irradiation show the formation of some larger aggregates but nevertheless retain a nanocrystalline morphology/structure (Figure 4.11-A). The stability of the QDs was further affirmed by UV-vis spectra collected after photocatalysis. The increased scattering of the absorption profile suggests particle agglomeration, however, the absorption onset of the QDs retains similar compared to the stock solution and a sample stirred in the dark (Figure 4.11-B). X-ray photoelectron spectroscopy (XPS) was unable to detect signals from the co-catalyst metal and its oxidation state because the concentration of Ni/Co was below the detection limit of XPS. While those analyses do not contain information about the molecular catalyst, it demonstrates that the ZnSe particles are stable (within the timescale of photocatalysis) and retain their key morphological and photophysical properties.

4.2.8 Influence of light intensity

The light intensity used for irradiating the photocatalyst is essentially a measure of the number of photons that reach the photocatalyst and governs the number of photogenerated electrons available for catalysis. In semiconductor facilitated photocatalysis, the influence of the light intensity can be simplified for two extreme cases of light intensity [332]. At high light intensities, charge recombination predominates over the chemical reaction and as a result a dependence of the reaction rate on the square root of light

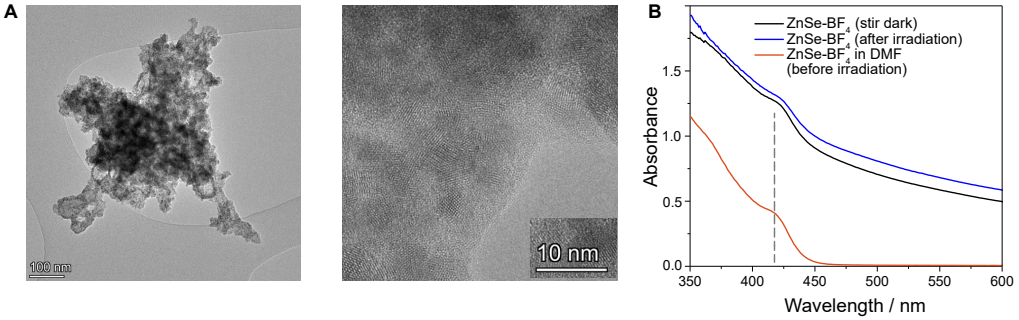

FIGURE 4.11: Post catalysis characterisation. (A) Transmission electron micrographs of ZnSe-BF_4 after irradiation (16 h) showing aggregated structures and well-dispersed particles. The particles were precipitated after photocatalysis via centrifugation. (B) UV-vis characterisation of the photocatalyst after irradiation in comparison a sample that was stirred in the dark and before irradiation.

intensity is found [333]. At low light intensities, the rate increases linearly with the light intensity. Nevertheless, the lower light intensity, i.e. changing the flux of available electrons can impact the ratio of evolved H_2 vs. CO, typically because a given molecular catalyst can only take up a limited number of electrons per time unit (ET transfer rates from QDs are on the order of 10^9 - 10^{10} s^{-1} [96, 317] whereas the timescale for chemical transformations are on the order μs to s [18].

In this section, the light intensity was systematically lowered from 100% (which represents 100 mW cm^{-2} of the AM 1.5G spectrum) to 50% and 20% of this intensity in order to study the relative activities of the generated reaction products, at a given time point (1000 min) (Figure 4.12). The full data-set can be found in appendix B.6.

For both ZnSe | Co(qpy) and ZnSe | Ni(cycP), the total amount of evolved products follows a near linear dependence on the light intensity (I $\leq$ 50%, Figure 4.12-A) showing that the photosystem operates in the linear regime.

Lowering the light intensity of the diffusional assembly ZnSe | Co(qpy) affects the activity of both HER and CO_2 reduction, however, CO is less affected than H_2. At a given time point (1000 min), while HER is marginally below a near linear trend (reduction) in activity, whereas CO deviates from this relation significantly enhancing the overall CO selectivity from 6.5% ($I = 100\%$) four-fold to 24.4% ($I = 25\%$). The ratio of evolved H_2 and CO is not steady but changes with irradiation time (Figure 4.13). Co(qpy) remains a higher CO selectivity for longer irradiation times at lower light intensities which is an indication that the co-catalyst disintegrates slower with a lower number of available electrons. Nevertheless, the $TON_{Co(qpy)}$ is not improved and saturates in-between < 70 ($I = 100\%$) and < 40 ($I = 20\%$) (Figure B.6-B).

The anchored co-catalyst hybrid ZnSe | Ni(cycP) exhibits enhanced CO selectivity as well, however, less pronounced than Co(qpy) (Figure 4.12). Interestingly, in the beginning of the experiment (ca. 25 min), the lowest light intensity sample (25%) exhibits the lowest CO selectivity. This trend is reversed over the course of the experiment, CO selectivity slightly increases and is the highest after 100 min (Figure 4.13).

The activity at lower light intensities for both H_2 and CO is greatly diminished in the case of the electrostatic assembly ZnSe | Co(tppS3N1, non-primed). This is presumably related to its long induction period. The number of available electrons may not be sufficient to generate the active species within the time frame of this experiment. This finding confirms that the induction period (Co^{III} to Co^{II}) is facilitated by light and proceeds from photogenerated QDs and not from AA, when the co-catalyst is immobilised on the QD surface. This is in-line with the experiments from priming the photocatalyst in the dark or in the presence of AA (and absence of QDs).

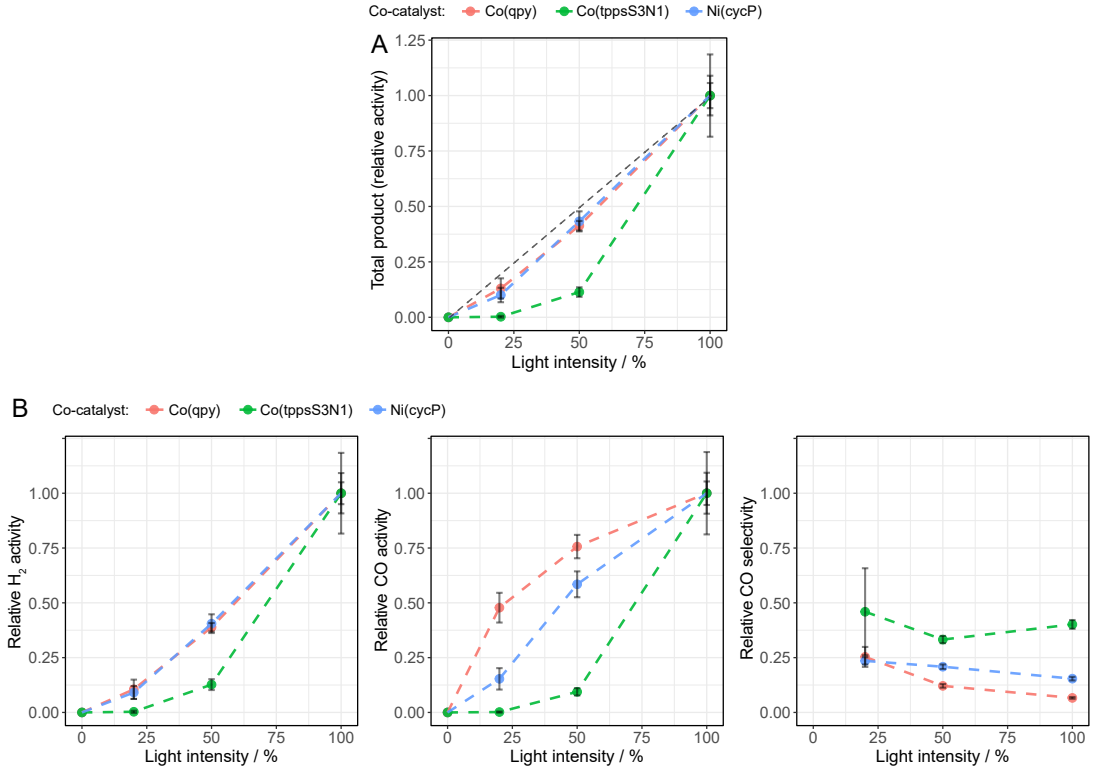

FIGURE 4.12: Relative activity of photocatalytic CO_2 reduction depending on the light intensity in the presence of ZnSe-BF_4 QDs and various co-catalysts after 1000 min irradiation. CO selectivity defined as n (CO) / (n (CO) + n (H_2)). (A) Total products formed (relative activity). (B) Relative H_2, CO and CO-selectivity. 100% light intensity refers to 100 mW cm^{-2} of the AM 1.5G spectrum. Otherwise Standard flow conditions.

The experiments above demonstrate that excess photogenerated electrons on ZnSe QDs are utilised towards the HER. Lowering the light intensity in the case of the weekly anchoring Ni(cycP) and diffusional Co(qpy), allows for higher proportion of electrons to be

transferred to the co-catalyst for CO_2 reduction rather than for competing HER. However, the changes in CO selectivity are limited and remain $< 50\%$ in any case. This effect is not visible for the strongly anchoring electrostatic assembly (ZnSe | Co(tppS3N1)) because it is already much more selective initially and essentially performs worse overall.

Influence of the light intensity on the induction period

Evaluating the product evolution curves of the two weakly anchoring co-catalysts Co(qpy) and Ni(cycP) reveals a more pronounced induction period (Figure B.6). The increasing delay until the photocatalyst reaches its maximum turnover with lower light intensities is especially visible for ZnSe | Co(qpy), for both H_2 and CO. CO_2 reduction reaches peak activity after 40 min ($I = 100\%$) compared to 275 min at $I = 20\%$ intensity. For ZnSe | Ni(cycP), this effect is less pronounced and expressed in a flattening of the rate curves towards longer irradiation times at lower light intensities. These observations show that the induction period is partly governed by the availability of photons, in line with the priming experiments of the QDs under irradiation (see above).

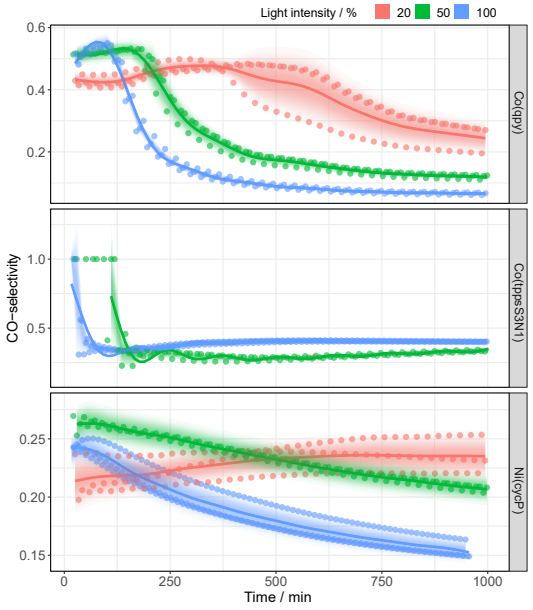

FIGURE 4.13: CO selectivity over time of photocatalytic CO_2 reduction depending on the light intensity in the presence of ZnSe-BF_4 QDs and various co-catalysts. 100% light intensity refers to 100 mW cm^{-2} of the AM 1.5G spectrum. 20% trace from Co(tppS3N1) was removed because the CO selectivity could not be accurately determined due to the overall low quantities of products evolved. CO selectivity defined as n (CO) / (n (CO) + n (H_2)). Otherwise standard flow conditions.

4.2.9 Low CO_2 concentration

In the following, the influence of lowering the CO_2 concentration of the continuous-flow stream from 100% to 20% is investigated. The latter concentration was chosen because it is a realistic concentration level that is found in flue gas (refer to section 4.1) and

secondly represents the lowest level one can accurately obtain using the continuous-flow setup by diluting a CO_2 stream 1:4 with N_2 (0.8 sccm is the lower boundary for the MFC). At 20% CO_2, all three QD-co-catalyst hybrids evolve marginally less H_2 than at 100% CO_2, whereas the relative CO activity is drastically lowered to 26% - 38% (Figure 4.14 and Appendix B.7). The pH was kept constant during the experiments for each respective photosystem. The drop in HER at lower CO_2 concentration is surprising and presumably associated with minor inconsistencies between the desired and actual pH during the reaction and close to experimental error of identical replicates. The loss in CO activity (20% CO_2) represents a significant reduction in activity and demonstrates that the availability of CO_2 is limiting at this concentration. In the literature, photocatalysts were presented, which are able to reduce CO_2 with almost no loss in activity down to 10% [334]. The latter photocatalyst system achieved this exceptional activity via insertion of CO_2 ("capture") into the Re-O bond of triethanolamine coordinated to the CO_2-reducing Re metal centre.

The reduced activity at lower CO_2 concentration observed for all hybrid photocatalysts herein agrees with results obtained from CO_2 electroreduction on heterogeneous electrodes (e.g. Au) which have found a first-order rate dependence on the partial pressure of CO_2, i.e. the concentration of CO_2 [252]. The authors suggested that catalysis is limited by the electron transfer to CO_2 to form the CO_2^- intermediate. The exact reaction order for the herein tested photosystems remains to be determined (more data points would be required). If a first-order rate dependence is assumed, this explains the lower activity and why all hybrid photocatalysts exhibit different activities even though the supply of CO_2 is limiting, because the molecular catalysts have different rate constants to form the metal-CO_2^- intermediate. More complex kinetics such as those observed during enzyme catalysis (e.g. Michaelis-Menten) show a non-linear dependence of the reaction rate to the substrate concentration and may also be appropriate to describe the CO_2-limited activity.

It would be intriguing to select more concentration levels (e.g. 50% and 75%), however, was not chosen to continue due to the low activity at 20% CO_2 concentration.

4.2.10 Aerobic conditions

The tolerance towards O_2 is another interesting aspect in colloidal CO_2 photoreduction. One of the long-term goals in photocatalytic CO_2 reduction is to couple the reduction reaction with water oxidation (instead of using a sacrificial electron donor) which would produce O_2 as a side-product. Therefore, the CO_2 reduction reaction needs to tolerate low levels of O_2. This tolerance towards O_2 is particularly challenging because O_2 can

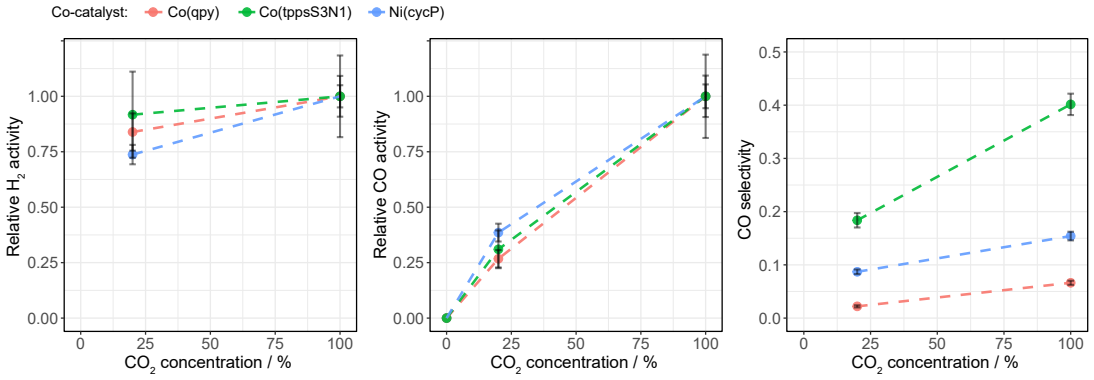

FIGURE 4.14: Relative activity of photocatalytic CO_2 reduction depending on the CO_2 concentration in the presence of ZnSe-BF_4 QDs and various co-catalysts after 1000 min irradiation. 20% CO_2 was achieved by diluting a CO_2 stream with N_2 1:4. CO selectivity defined as n (CO) / (n (CO) + n (H_2)). Otherwise Standard flow conditions.

quench photogenerated electrons and is therefore considered parasitic in most cases as it competes with CO_2 reduction. In addition, reactive oxygen species can decompose the molecular catalytic unit. However, it was shown that in certain cases the presence of O_2 can enhance the overall performance. For example, CdS-QDs operated favourably under aerobic conditions which was assigned to regulating electron uptake by O_2 and thereby preventing degradation through an excess of photogenerated electrons [335]. Even though this self-induced photo degradation is not a major concern with ZnSe, all three hybrid photocatalysts were tested under a stream of 5% O_2 in CO_2 balance gas to evaluate the impact on the HER *vs.* CO_2 reduction.

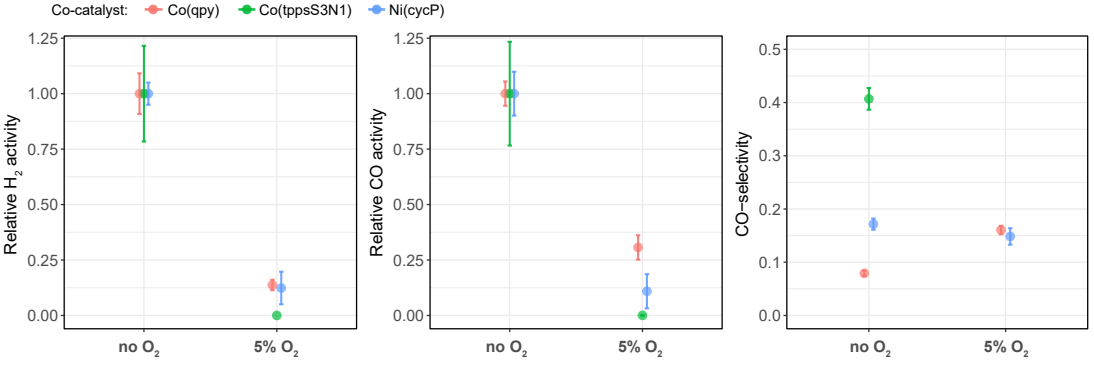

FIGURE 4.15: Relative activity of photocatalytic CO_2 reduction depending on the the presence of 5% O_2 using ZnSe-BF_4 QDs and various co-catalysts (600 min irradiation). The gas mixture was prepared by mixing a stream of CO_2 with a stream of air (4.21 : 1). CO selectivity defined as n (CO) / (n (CO) + n (H_2)). Otherwise standard flow conditions.

The presence of O_2 leads to diminished photocatalytic activity (Figure 4.15, the full data set can be found in appendix B.8): While ZnSe | Co(tppS3N1) does not exhibit any activity for both H_2 and CO, ZnSe | Ni(cycP) shows a reduction to approx. 12%, whereas ZnSe | Co(qpy) shows 27% relative activity in the presence of O_2. For Co(qpy), HER is suppressed more than CO_2 reduction thereby enhancing the CO-selectivity from

8% (anaerobic) to 16% in the presence of O_2. For Ni(cycP), the CO-selectivity remains unaffected with or without O_2. This observation may be (again) explained with the diffusional nature of Co(qpy), that leaves the QD surface accessible to O_2 to take up electrons from the ZnSe conduction band. Nevertheless, O_2 is detrimental to all photocatalyst systems tested here. In particular, the presence of O_2 seems to decompose the Co(tppS3N1) catalyst because it does not exhibit any activity at all. In contrast to the stability enhancement for CdS-QDs, no stability improvements for neither H_2 nor CO were observed in the presence of O_2 (Appendix B.8).

4.2.11 AA oxidation kinetics

Monitoring the oxidation reaction when employing a sacrificial electron donor is rarely conducted in photocatalytic experiments. It is commonly assumed that AA is oxidised to dehydroascorbic acid (DHA) while supplying electrons to quench photogenerated holes at the ZnSe VB. However, DHA can be further decomposed while providing electrons for the photocatalytic reaction and this pathway is generally complicated and may lead to a range of oxidation products that may impact the overall reaction and efficiency [336, 337].

In order to find out if this is the case for the photocatalyst presented during in this work, the AA oxidation was monitored for one (arbitrary selected) example (ZnSe | Ni(cycP)). The experiment was conducted similarly as previously under standard flow conditions. In addition, D_2O (instead of H_2O) was used as solvent to allow for quantification of liquid products via ^{1}H-NMR spectroscopy by taking aliquots at regular intervals (see experimental section 4.4 for more details). With continuous irradiation, signals assigned to the AA's oxidation product DHA (4.18, 4.29 and 4.60 ppm)) start to appear. The total amount of gaseous reaction products (H_2 + CO) matches the amount of generated DHA well within the first 240 min of the experiment (Figure 4.16). No other liquid reaction products could be detected. This observation demonstrates the clean oxidation of AA to DHA accompanied by the reduction of protons and CO_2 to H_2 and CO, within the first 240 min. A stoichiometric ratio is expected since all reactions (oxidation of AA, reduction of protons and CO) involve two electrons. The fact that both curves match well is a sign that all electrons provided by AA indeed lead to the formation of the two expected/desired products (H_2 + CO) and precludes the formation of other species and side reactions.

At longer irradiation times (360 min) the DHA generation outpaces the sum of gaseous products, which could be due to O_2 leakage (after several uses of the septum) and

consuming electrons, a common side reaction in photocatalysis (see section 4.2.10). Interestingly, at even longer irradiation times (480 min), the amount of DHA decreases, even though no other oxidation products could be detected at significant levels. Besides the possibility of this being an experimental outlier, one possible explanation could be decarboxylation of DHA, which would lead to release of CO_2 and subsequent removal of DHA out of solution. The possibility of DHA decarboxylation was described in the literature [338] but due to the complicated nature of the AA/DHA decomposition pathway [336, 337] it would be expected to detect intermediate products before full conversion of DHA to CO_2.

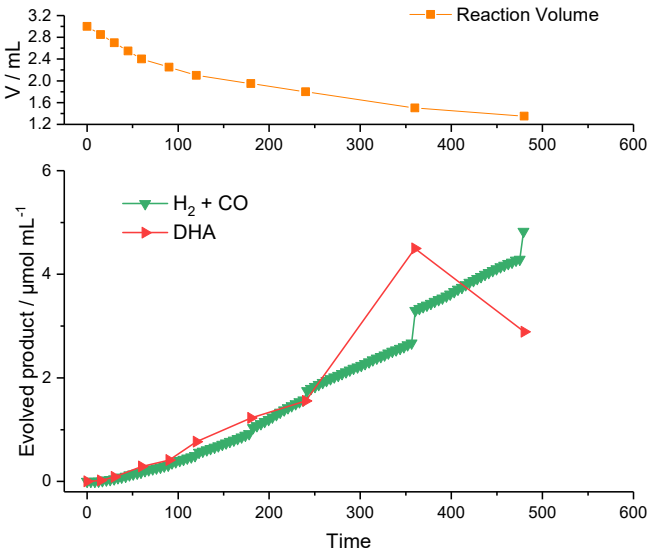

FIGURE 4.16: Comparison of liquid AA oxidation products with evolved gaseous products. Photocatalytic CO_2 reduction in the presence of ZnSe | Ni(cycP). Gaseous reaction products analysed by in-line GC chromatography. Liquid products quantified via ^{1}H-NMR spectroscopy. The declining total reaction volume is due to the liquid aliquots and accounted for by normalising for 1 mL reaction volume. Conditions: 0.1 M AA in D_2O, otherwise standard flow conditions.

4.3 Conclusions

In summary, it was shown that ZnSe-BF_4 QDs can drive a range of molecular co-catalysts based on Ni or Co for visible light-driven CO_2 reduction. The QDs were thereby able to supply photogenerated electrons to molecular co-catalysts that are of diffusional nature, possess a phosphonate anchoring group or assemble on the surface due to electrostatic interactions (by introducing negatively charged functional groups). The different anchoring strategies were compared and quantified with the electrostatic assembly leading to near quantitative immobilisation of the co-catalyst, whereas traditional anchoring groups (phosphonate) or diffusional co-catalysts attached to much lesser extents. A

Co-tetraphenylporphyrin featuring three sulfonate and one amine group thereby exhibited the benchmark photocatalytic activity in combination with ZnSe-BF_4, evolving 18.6 μmol of CO and reaching an unprecedented TON_{Co} (CO) of 619 after 1000 min of irradiation with a CO-selectivity of $> 40\%$. This photocatalytic activity is the highest obtained on ZnSe QDs and amongst the highest in colloidal photocatalytic CO_2 reduction using earth-abundant materials in aqueous solution. The distinct induction period of this benchmark photocatalyst was assigned to slow Co^{III} to Co^{II} reduction as prerequisite to enter the catalytic cycle and could be accelerated by priming (pre-reducing the co-catalyst in AA solution). The photocatalytic activity of the hybrid photosystems could be partially recovered through the addition of fresh co-catalyst solution, in particular for the diffusional catalyst assembly. Lowering the light intensity for Co(qpy) and Ni(cycP) was able to enhance the selectivity towards CO by regulating the supply of photogenerated electrons. Lowering the CO_2 concentration led to diminished activity towards CO while not affecting HER significantly, demonstrating that the reaction is limited by the supply of CO_2. The hybrid photocatalysts showed a very limited tolerance towards the presence of O_2 - only Co(qpy) exhibited an enhanced CO selectivity under aerobic conditions. Overall, this work advances the understanding of QD-molecular catalyst hybrids and presents a versatile nanoparticulate semiconductor platform to achieve CO_2 reduction using benign, earth-abundant components that operate in fully aqueous conditions. Further investigations may reveal why the Co(tppS3N1) is a superior catalyst compared Co(tppS4) and characterise the influence of the amine (vs. one sulfonate) group during catalysis.

4.4 Experimental section

ZnSe-BF_4 QDs were prepared as described in Chapter 2. The physical characterisation techniques are described in Chapter 2 as well. The experimental procedure of the photocatalyst assembly, batch photocatalysis, isotopic labelling and EQE is similar to the ones reported by the author of this dissertation in [316, 317].

4.4.1 Preparation of molecular catalysts

Ni(cycH) and Ni(cycP) were prepared as reported previously [170] by Alex Cowan and co-workers (University of Liverpool). Fe(tpp$(TMA)_4$) was prepared according to literature procedure [177] and kindly provided by Kristian Dalle in collaboration with Marc Robert and co-workers. Co(pcS4) was prepared according to literature procedure [339] and kindly provided by Souvik Roy. Co(pcN4) was synthesised by Souvik Roy and the procedure is described in appendix B.3.

Ni(terpyS)

Ni(terpyS) was prepared as reported previously [186]. $Ni(BF_4)_2{\cdot}6\ H_2O$ was dissolved in acetonitrile (500 μM, 20 mM) and added to a vial containing 2,2':6',2"-terpyridine-4'-thiol (terpyS, 20 μmol, 98%, HetCat, Switzerland). Acetonitrile (1 mL) was added and the resulting mixture sonicated for 10 min to give a clear orange stock solution.

Ni(terpyP)

Ni(terpyS) was prepared as reported previously [186]. $Ni(BF_4)_2{\cdot}6\ H_2O$ was dissolved in acetonitrile (500 μM, 20 mM) and added to a vial containing 2,2':6',2"-terpyridine-4'-phosphonic acid (terpyP, 20 μmol, 98%, HetCat, Switzerland). Acetonitrile (1 mL) was added and the resulting mixture sonicated for 10 min to give a clear orange stock solution.

Co(qpy)

The ligand 2,2':6',2":6",2'-quaterpyridine, (qpy) was synthesised by Souvik Roy, see appendix B.3 for the full synthetic details. The ligand qpy (60 mg) was dissolved in N_2-purged chloroform ($CHCl_3$) and $CoCl_2 \cdot 6\ H_2O$ (46 mg in 4 mL MeOH) was added dropwise. The resulting solution turned gradually red and a brown solid started to form. The mixture was stirred for a further 2 h and the brown precipitate was collected by filtration, washed with $CHCl_3$ and methanol (MeOH) to remove unreacted starting materials. Elemental analysis for $C_{20}H_{18}Cl_2CoN_4O_2$: C, 50.44; H, 3.81; N, 11.76; found: C, 50.02; H, 4.15; N, 11.26.

Co(tppS3N1)

Co(tppS3N1) was kindly provided by Geani Ucoski, see appendix B.3 for the full synthetic details. The compound was further purified by filtration over celite using MeOH as solvent and precipitated with an excess of acetonitrile (10:1). The final compound was collected as a dark purple solid and dried *in vacuo*. ^{1}H-NMR (D_2O, 500 MHz): $\delta =$ 9.30 (s, 8H), 8.50 - 8.35 (m, 8H), 8.31 - 8.25 (m, 8H). MS (ESI, negative mode) (m/z) calcd (100%) for $[C_{44}H_{27}N_5O_9S_3Co]^{2-}$: 462.0157; found 462.0174. Elemental analysis for $C_{44}H_{26}CoN_5Na_3O_9S_3 \cdot 9\ H_2O$: C, 45.76; H, 3.84; N, 6.06; found: C, 45.67; H, 3.51; N, 5.81.

Co(tppS4)

The ligand, 5,10,15,20-tetrakis(4-sulfophenyl)-porphyrin (50.87 mg, >85%, TCI Chemicals) and $Co(BF_4)_2 \cdot 6\ H_2O$ were dissolved in 20 mL water. The pH was adjusted to 7.5 with NaOH (1 M) which resulted in a colour change from dark green to dark red. The solution was degassed and refluxed for 24 h under N_2. An aliquot of the reaction mixture analysed by UV-vis spectroscopy indicated completion of the metallation. The reaction mixture was filtered to remove insoluble materials and dried *in vacuo*. The compound was further purified by filtration over a celite column in MeOH (three times)

in order to remove excess $Co(BF_4)_2$ salt. The product was precipitated with a ten-fold excess of acetonitrile and collected as a dark-purple solid and dried in vacuo. ^{1}H-NMR (D_2O, 500 MHz): δ = 9.42 (s, 8H), 8.48 (d, J=7.7 Hz, 8H), 8.30 (d, J=7.7 Hz, 8H). Elemental analysis for $C_{44}H_{24}CoN_4Na_4O_{12}S_4 \cdot 5\ H_2O \cdot 4\,CH_3OH$: C, 44.41; H, 3.88; N, 4.32; found: C, 44.40, H, 3.94; N, 4.29.

4.4.2 Photocatalytic CO_2 reduction

Photocatalyst assembly

A ZnSe-BF_4 stock solution (54.91 μM in DMF, 27.3 μL) and a co-catalyst solution (2.0 to 5.0 mM in water (1:1 water/acetonitrile mixture for the terpyridine catalysts) were added to a Pyrex glass photoreactor (Chromacol 10-SV, Fisher Scientific) containing a magnetic stirrer bar. The mixture was diluted with ascorbic acid (0.1 M in water, pH adjusted to 4.5 or 6.5 with NaOH, depending on the sample) to a total solution volume of 3 mL. The photoreactor was then sealed with a rubber septum.

Photocatalysis

The co-catalyst screening, ^{13}C-isotopic labelling and EQE determination experiments were conducted by accumulating gaseous products in the headspace under steady-state conditions. Hence, the samples were purged with CO_2 (containing 2 % CH_4 as internal standard) for 10 min in the dark; the solution pH decreased from 6.5 to 5.5 after purging due to saturation with CO_2 ((or remained constant at 4.5 if this was the pH prior to purging). The photoreactor was then placed in a water bath maintained at 25 °C, stirred and irradiated by a solar light simulator (Newport Oriel, AM 1.5G, 100 mW cm^{-2}). UV-light was filtered using a 400 nm cut-off filter. After a desired time interval, the product distribution was quantified through manual headspace gas analysis (50 μL, using a Hamilton gas-tight syringe) by gas chromatography using a Shimadzu Tracera GC-2010 Plus gas chromatograph kept at 130 °C using a barrier ionisation discharge (BID) detector and a molsieve column with He as the carrier gas.

For **^{13}C-isotopic labelling**, photocatalysis experiments were performed as described above but using $^{13}CO_2$ (>99 atom% ^{13}C, Sigma-Aldrich) as the headspace gas. After 1000 min (16.7 h), the photoreactor headspace was transferred to an evacuated gas IR cell (SpecAc, 10 cm path length, KBr windows) and a high-resolution gas-phase transmission spectrum was recorded.

Photocatalysis under continuous-flow was conducted as described in section 3.4.

External quantum efficiency

Photocatalysis samples were prepared with a modified procedure using a flat-sided quartz

cuvette (1 cm path length, airtight) as the photoreactor. Co(tppS3N1) was first dissolved in AA solution (1.2 mL, 0.1 M, pH adjusted to 4.5). After 2 h, ZnSe-BF_4 QD stock solution was added to give a 1 μM concentration and the sample was purged with CO_2 (containing 2% CH_4 as internal standard). The sample was primed by irradiation for 200 min with a solar light simulator as stated above. The cuvette was then purged again with CO_2/CH_4 (2 %) and irradiated with monochromatic light ($\lambda = 400 \pm 5$ nm, A = 0.80 cm^2) using an LOT Quantum Design MSH-300 monochromator. Aliquots of headspace gas were taken periodically and analysed by gas chromatography (as described above). The EQE was calculated according to the formula given in section 4.2.6.

^{1}H-NMR spectroscopy, monitoring AA

Aliquots (150 μL) were taken at regular intervals while the sample was continuously purged and irradiated with simulated solar light, diluted to a total volume of 500 μL with D_2O and the aliquot directly analysed via ^{1}H-NMR spectroscopy. ^{1}H-NMR spectra were recorded on a Bruker AVANCE 500 with a TCI Cryoprobe system (500 MHz) at 256 scans. Deuterated (3-(trimethylsilyl)-2,2,3,3-tetradeuteropropionic acid (TMSP-d4, 50μL of 5 mM stock solution, in D_2O) was used as internal standard to allow for the exact concentration determination. Residual DMF present in the solution was used as additional reference in order to account for deviations in manually taking samples with a syringe.

4.4.3 Electrochemical characterisation

Cyclic voltammetry (CV) was performed in a one-chamber-flask. For Ni(cycP) a Hg/Au amalgam working electrode was freshly prepared by dipping a gold wire (1.0 mm diameter, 99.999%) into liquid mercury for exactly 2 min. For Co(qpy) and Co(tppS4) and Co(tppS3N1) a glassy carbon working electrode was used. The cell was assembled by placing the working electrode together with an Ag/AgCl reference and a Pt mesh counter electrode into co-catalyst (1.0 mM) dissolved in 0.1 M aqueous $NaClO_4$ (1 mL). The cell was sealed and purged with either N_2 or CO_2 for 15 min. CVs were recorded using an Ivium CompactStat or BioLogic VSP potentiostat with a scan rate of 100 mVs^{-1}. The potentials were converted from Ag/AgCl/KCl(sat'd) to normal hydrogen electrode (NHE) by adding +0.2 V.

Chapter 5

The influence of capping ligands in QD-promoted CO_2 reduction

Parts of the contents of this section have been submitted for publication in peer-reviewed journals: C. D. Sahm, E. Mates-Torres, N. Eliasson, K. Sokołowski, A. Wagner, K. E. Dalle, Z. Huang, O. A. Scherman, L. Hammarström, M. García-Melchor, E. Reisner, Imidazolium-modification enhances photocatalytic CO_2 reduction on ZnSe quantum dots. Chemical Science, ***2021****, accepted manuscript, DOI: 10.1039/D1SC01310F and C. D. Sahm, E. Mates-Torres, A. Ciotti, K. Sokołowski, G. Neri, A. J. Cowan, M. García-Melchor, E. Reisner, Tuning the local chemical environment of ZnSe QDs with dithiols towards photocatalytic CO_2 reduction,* ***2021****, in preparation. Results presented were obtained solely by the author of this thesis, with contributions from others as outlined here: Eric Mates-Torres, Anna Ciotti and Max García-Melchor (Trinity College Dublin) conducted DFT simulations. Nora Eliasson and Leif Hammarström (Uppsala University) performed transient absorption (TA) spectroscopy studies. Kamil Sokołowski and Zehuan Huang (University of Cambridge) conducted ITC and NMR titrations in collaboration with the author. Kristian E. Dalle (University of Cambridge) synthesised the first two intermediates during the synthesis of MEMI.*

5.1 Imidazolium modification

5.1.1 Introduction & Motivation

In section 4, it was shown that ZnSe QDs are an efficient platform in order to drive molecular catalysts based on transition metal complexes by providing photogenerated electrons. While those hybrid photosystem can achieve very high activities (with even

higher activities reported in the literature [244]), they nevertheless require two distinct functional materials (light absorber + molecular catalyst). In particular, the synthesis of some molecular catalyst can be highly challenging and their stability under photocatalytic conditions can often be the limiting factor for the overall performance. It is therefore intriguing to enable CO_2 reduction on the light absorber itself, essentially eliminating the need for an additional molecular co-catalyst based on transition metal complexes. In the literature, only a few examples of QD-based photocatalytic systems that operate in the absence of an additional co-catalyst have recently emerged in order to render QDs active for CO_2 reduction through doping [214] or surface enrichment with Cd-containing catalytic sites [340]. Recently, it was shown that CdSe/CdS QDs reduce CO_2 without a sophisticated surface modification strategy, however, the approach was limited to organic solvents [218].

In section 1.4 it was shown that the local chemical environment of CO_2 reduction catalytic sites is considered a key determinant in the design of efficient catalysts. A range of functional groups were reported for surface functionalisation approaches stretching from amino acids to N-arlypyridinium compounds. In particular, imidazolium based ionic liquids (ILs) stand out as a chemical motif due to their influence on CO_2 electroreduction (see introduction, Figure 1.16) although the mechanistic details still remain controversial [296, 341, 342]. In electrochemical CO_2 reduction, early studies reported that the additive 1-ethyl-3-methylimidazolium tetrafluoroborate (EMIM-BF_4) in the electrolyte solution (18 mol%) with a Ag electrode stabilises the $^*CO_2^-$ intermediate through complexation to effectively lower the initial activation barrier [294]. Follow-up studies have proposed the participation of the IL-imidazolium motif in CO_2 reduction by forming IL-CO_2 adducts [343, 344], whereas others showed secondary coordination sphere effects through (coulombic) stabilisation [298] electric fields [302], H-bonding [299], attraction of CO_2 to the catalytic active site [300, 345] or formation of a favourable microenvironment [301] in close proximity to the active centre. The use of imidazolium-ILs in photochemical CO_2 reduction is far less explored. A tetrabutylphosphonium pyridine-oleate IL was used as a medium for direct air capture of atmospheric CO_2 and subsequent photocatalytic conversion on a conjugated polymer [306]. EMIM-BF_4 was used in a homogeneous photochemical system containing a Ru dye and Co^{II} salt, but the exact role of the IL remained unclear [346].

In this section, surface modification strategies are explored in order to promote photocatalytic CO_2 reduction on ZnSe QDs in the absence of an additional molecular co-catalyst based on transition metal complexes. Capping ligands thereby represent a versatile toolbox in order to introduce functional groups to the QD surface and can attach to the surface through a thiol group. ZnSe QDs are particularly encouraging towards this goal because besides HER activity, control experiments in the absence of molecular catalysts

revealed trace amounts of CO (Table B.3). It is envisioned that this activity may be improved with the right surface modification and this approach is investigated in this section. After an initial screening of various capping ligands, an imidazolium-containing thiol ligand is selected and its interactions with the QD surface elucidated via NMR spectroscopy and isothermal titration calorimetry. Subsequently, transient absorption spectroscopy and DFT simulations are employed for mechanistic investigations.

5.1.2 Catalyst preparation and screening

"Ligand-free" ZnSe-BF_4 QDs were prepared as described in section 2.1. The ZnSe-BF_4 QDs, free of native or organic capping ligands, were used as starting point for further surface modification because it enables precise control over the ligand capping and loading (in contrast to a full ligand exchange).

The capping ligands employed are dual functional: First, they feature a thiol group which strongly binds to the QD surface [186] and secondly possess an additional chemical functional group (amine, carboxylic acid, pyridine, imdidazolium). N-(2-mercaptoethyl)-dimethylamine (MEDA), mercaptopropionic acid (MPA) and 4-mercaptopyridine are commercially available. A capping ligand featuring an imidazolium group, 3-(2-mercaptoethyl)-1-methyl-imidazolium (MEMI) was synthesised by reacting 1-methyl-imidazole with 1,2-dibromoethane, followed by substitution of bromide with thioacetate and subsequent hydrolysis in dilute HCl to yield the thiol-modified imidazolium compound MEMI (Figure 5.1, see experimental section 5.1.8 for synthetic details and full characterisation).

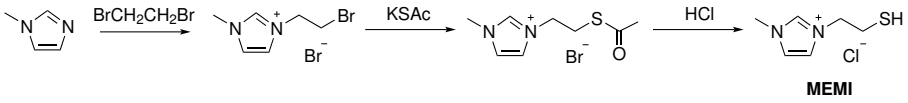

FIGURE 5.1: Synthetic scheme towards 3-(2-mercaptoethyl)-1-methyl-imidazolium (MEMI).

An initial screening of the capping ligands was conducted because all the selected functional groups (amine, carboxylic acid, pyridine, imidazolium) were reported in the context of surface modification of catalytic surfaces in CO_2 reduction (see section 1.4.2). Introduction of an amine group (MEDA) as well as a pyridine group (4-mercaptopyridine) through ligand capping on the ZnSe surface enhances CO generation by a significant margin compared to non-functionalised ZnSe-BF_4 (Figure 5.2). A carboxylic acid group (MPA) does not enhance CO generation. The highest activity was found for the imidazolium capping ligand MEMI. Consequently, MEMI was selected and studied in more detail in the following, not only because it features the highest activity amongst the ligands tested here but also due to the wealth of reports on imidazolium containing ILs

in heterogeneous electrocatalytic CO_2 reduction (section 1.4.3) which render this ligand of particular interest to the broader CO_2 reduction community.

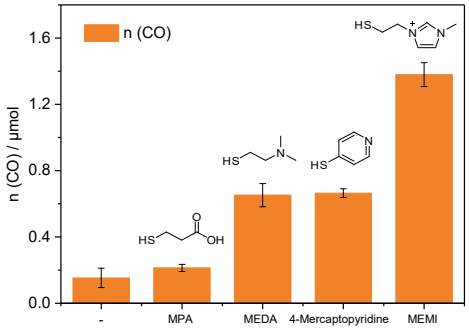

FIGURE 5.2: Capping ligand screening: Influence of capping ligands on the CO_2 photoreduction in the presence ZnSe-BF_4; Competing H_2 evolution not shown. Conditions: product accumulation in the headspace. 0.1 M AA, 0.5 μM ZnSe-BF_4, 50 μM capping ligand; AM 1.5G, $\lambda > 400$ nm, 100 mW cm^{-2}, pH 5.5, 20 h irradiation, CO_2, 25 °C, two independent replicates.

5.1.3 Ligand-QD interactions

Interactions of the capping ligand MEMI with ligand-free ZnSe-BF_4 QDs in aqueous solution were first studied by liquid-phase ^{1}H-NMR spectroscopy and isothermal titration calorimetry (ITC).

NMR spectroscopy has recently shown to be a useful method to probe interactions of small molecules with the surface of colloidal nanocrystals, providing insights into binding equilibria and allowing distinction between bound and free ligands [306, 347, 348]. Binding is typically indicated by disappearance or significant broadening of the signals stemming from protons localised in close proximity to nanocrystal interfaces, arising from their slow and non-uniform tumbling [349, 350]. The affinity of MEMI to the ZnSe-BF_4 QDs was studied by ^{1}H NMR spectroscopy (D_2O, 25°C, Figures 5.3-A,B, and Figure C.1). In a standard titration experiment, small quantities of MEMI (*i.e.,* 2 equiv. (mol MEMI per mol QD) per injection) were added stepwise to a suspension of ZnSe-BF_4 QDs. For quantities of MEMI $<$ 12 equiv. per ZnSe-BF_4 QD, the signals of the ligand essentially vanish, which suggests a strong binding affinity of MEMI to the QD interfaces (Figures 5.3-A, B). However, when the amount of MEMI is $>$ 12 equiv., a linear increase in signal intensity of sharp peaks assigned to MEMI is observed, indicative of accumulation of MEMI in the bulk solution. These ^{1}H NMR spectra suggest that single ZnSe-BF_4 QDs are able to accommodate up to 12 MEMI molecules (surface coverage ca. 20%, see experimental section for details) tightly bound to the QD interfaces, leaving accessible surface area for other species (including solvated MEMI), which interact in a weaker/dynamic manner.

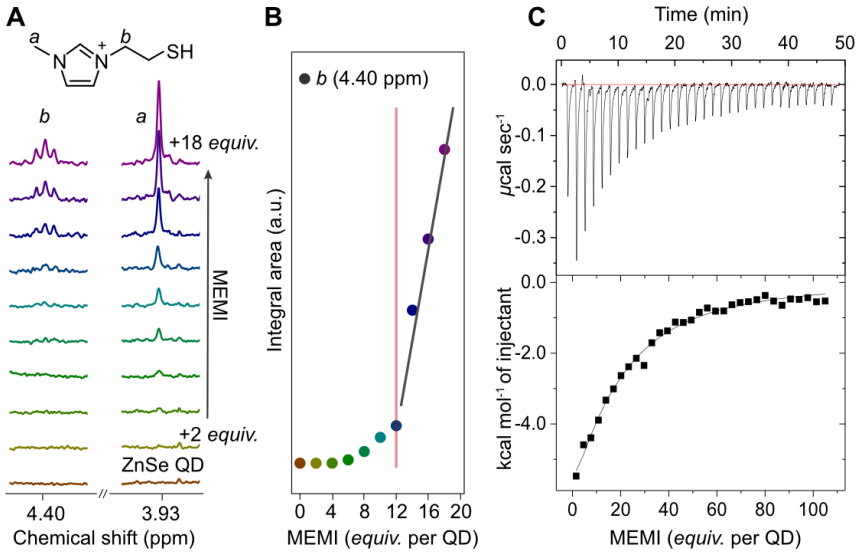

FIGURE 5.3: Ligand-QD interactions investigated by ^{1}H-NMR and ITC titration experiments. (**A**) ^{1}H-NMR spectroscopy titration experiment with aliquots of MEMI being added to a D_2O suspension of 5 μM ZnSe-BF_4 QDs (2 equiv. (mol MEMI per mol QD) per step). Selected signals (3.9 and 4.4 ppm) are shown for clarity. (**B**) The signals characteristic for MEMI (*i.e.*, 4.4 ppm) start to disappear at < 12 equiv. per ZnSe-BF_4 QD, suggesting that a ZnSe-BF_4 QD is able to accommodate approximately 12 MEMI molecules. Additional data and the full spectrum are shown in the appendix (Figure C.1). The fitted lines guide the eye. (**C**) ITC curve and plot obtained by titration of MEMI into an aqueous ZnSe-BF_4 QD solution (1 μM). Kamil Sokolowski contributed to preparing this Figure.

The strong interaction between MEMI and the QDs was further corroborated by ITC, a quantitative technique for determining thermodynamic binding parameters of interactions in solution. Widely used in bio- and supramolecular chemistry [351, 352], ITC is increasingly being used to study interactions of ligands with colloidal nanoparticles [353–355]. The technique measures the energetics, *i.e.* the heat released/absorbed associated with an interaction in solution at a constant temperature. The experiment is performed by titrating one reactant (*e.g.* a ligand) to a solution of the second reactant (*e.g.* a particle) and monitoring the heat release after each addition. Experimentally, the applied thermal power is measured as a function of time which is required to keep the temperature in the titration cell constant following an injection and is directly proportional to the reaction's heat release [356].

Titration of MEMI into ZnSe-BF_4 QDs shows a significant exothermic response (-6 kcal mol^{-1}) at low ligand concentration that rapidly saturates (Figure 5.3-C, Figure C.2), indicating a strong affinity of MEMI for the QD surface.

Further data analysis and fitting of the ITC data allows for the determination of thermodynamic properties. A widely used framework is the *multiple sets of independent binding sites* or also referred to as *independent binding site* model [356, 357]. The model comes with the following assumptions:

Parameter	**Fit** $\pm \sigma$
N	17 ± 5
K	2.5 x 10^4 ± 1.5 x 10^4 M^{-1}
ΔH	-2.1 x 10^4 ± 3.3 x 10^3 cal mol^{-1}
ΔS	-51 ± 11 cal mol^{-1} deg^{-1}

TABLE 5.1: Thermodynamic fitting parameters for the interaction of MEMI with ZnSe QDs based on four independent replicates. N: Number of binding sites. K: binding constant, ΔH: binding enthalpy, ΔS: entropy.

- A macromolecule/particle possesses an (arbitrary) number of sets of binding sites
- The binding sites are non-interacting
- All sites in the same set possess a similar intrinsic affinity for the ligand molecule

Fitting of the ITC data with the *one set of independent binding sites* binding model (see Figure C.2 for details) estimated the binding affinity, here given as the binding constant (K) of the reaction to be 2.5 x 10^4 M^{-1}. (The binding constant is a special case of the general equilibrium constant associated with the reaction between a particle (P) and a ligand (L) (P + L -> P-L) and its unit is therefore M^{-1}.) The number of binding sites (N) was approximated to be N = 17 ± 5, which is in good agreement with the NMR data. The thermodynamic fitting parameters are summarised in Table 5.1.

Electrokinetic zeta-potential measurements further corroborate the attachment of MEMI to the QD surface. Addition of positively-charged MEMI to a suspension of ZnSe-BF_4 QDs changed the electrokinetic zeta potential of the QDs (+20 mV) to even more positive values (+30 mV), indicative of the decoration of ZnSe-BF_4 QD interfaces with the ligand.

5.1.4 Photocatalytic CO_2 reduction

The photocatalytic activity of the ZnSe-BF_4 QDs was studied under a constant flow of CO_2 and automated in-line gas chromatography (aqueous AA solution, pH 6.5) as described in section 3. Besides previously reported HER [318], non-functionalised ZnSe-BF_4 display a marginal activity towards CO evolution (Figure 5.5, Table C.1), as also shown during the initial screening. After 10 h of continuous irradiation, a total of 0.64 ± 0.11 mmol CO $g_{ZnSe}{}^{-1}$ is produced with a modest CO-selectivity of < 3%. Note, the unit to report CO evolution is given in mol per gram of ZnSe, because this the most common unit in the literature for colloidal photocatalysts in the absence of molecular catalysts. The origin of generated CO was confirmed from reduced CO_2 by ^{13}C-isotopic labelling experiments (Figure C.3) to exclude any contribution from decomposition of residual organic impurities or solvents.

The addition of 100 equiv. per QD of the freely diffusing IL EMIM-BF_4 (Figure 5.4) to the solution reduces HER activity to about half (Figure 5.5-A) and enhances CO formation (1.06 ± 0.06 mmol CO $g_{ZnSe}{}^{-1}$ after 10 h irradiation, CO-selectivity $< 5\%$) (Figure 5.5-B). This observation agrees with the activity-enhancing effect of EMIM-BF_4 in previously reported electrochemical systems [294].

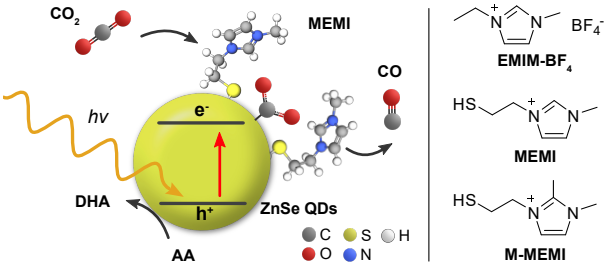

FIGURE 5.4: Schematic representation of the photocatalyst system consisting of ligand-free ZnSe-BF_4 QDs (yellow sphere) modified with the capping ligand MEMI or M-MEMI for visible light-driven CO_2 to CO reduction in water using ascorbic acid (AA) as the sacrificial electron donor. DHA: dehydroascorbic acid.

Direct immobilisation of the imidazolium moiety on the QD surface via a thiol anchoring group gives ZnSe | MEMI (100 mol MEMI per mol QD, Figure 5.4). This ligand-QD assembly significantly further enhances the production of CO (1.78 ± 0.23 mmol CO $g_{ZnSe}{}^{-1}$ after 10 h irradiation, $TON_{QD} = 277$) at the expense of HER, leading to a CO-selectivity of up to 18% (Figure 5.5). After 10 h irradiation, this represents a 6.4-fold increase in CO selectivity over the non-functionalised ZnSe-BF_4 (Table C.1). Both product evolution rates (H_2 and CO) decay over longer irradiation times (Figure 5.6), which is presumably mainly governed by accumulation of oxidation products (DHA) on the QD surface (as investigated previously [358, 359]), aggregation processes and the resultant reduction of the overall surface area, slow degradation of the QDs and/or loss/decomposition of the capping ligand MEMI. Considering the TEM and UV-vis analysis of QDs after photocatalysis (Figure 4.11), the chemical stability of the particles is likely not the limiting factor and suggest that the photocatalytic activity is mainly limited by QD surface changes due to their aggregation processes, accumulation of DHA and/or loss of ligand as the main contributions.

Next, it was explored if the amounts of evolved H_2 and CO could be modulated with the loading of MEMI on the QD surface (Figure C.4). A molar ratio of 25 significantly enhances the initial CO formation rate over non-functionalised QDs by a factor of two. Higher loadings do not accelerate the CO production rate further, which saturates within the first 100 min of the experiment, regardless of the ligand loading (Figure C.4-B, Figure 5.6). This observation agrees with ^{1}H-NMR spectroscopy titration experiments and ITC measurements, where only a small number of ligands (*ca.* 10-20) strongly interact. Nevertheless, higher loadings (molar ratio $50 - 100$) further suppress HER (Figure C.4-A)

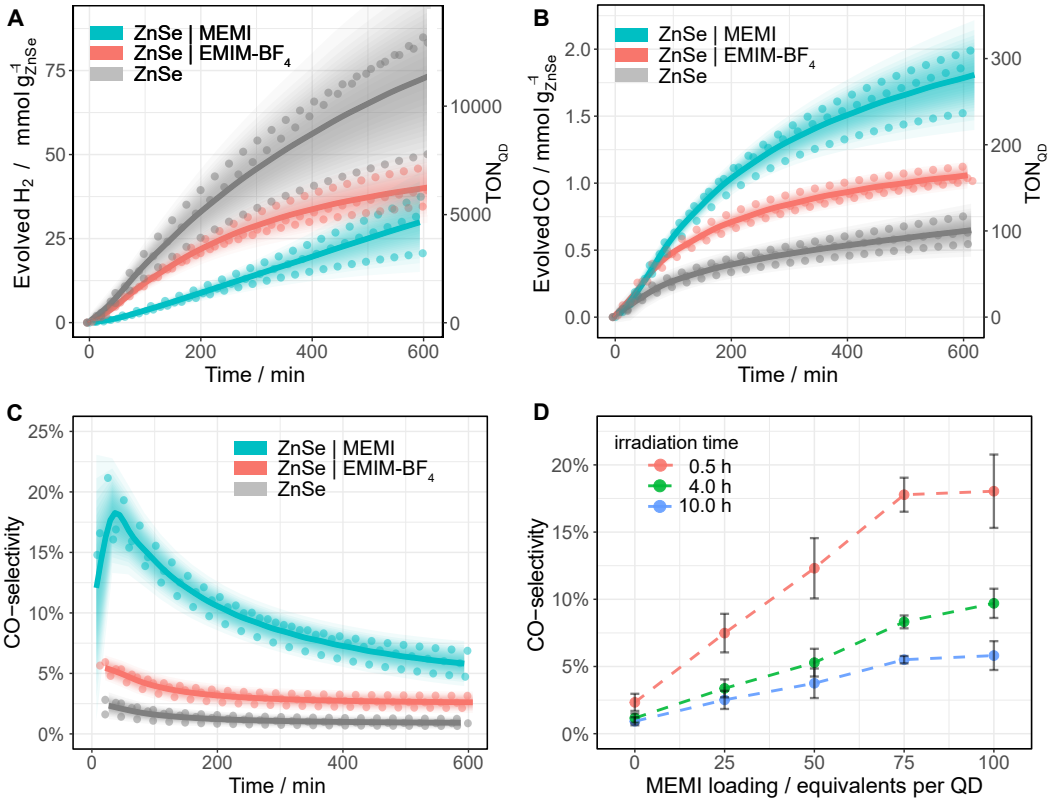

FIGURE 5.5: Photocatalytic reduction of aqueous CO_2 in the presence of ligand-free ZnSe-BF_4 QDs and modified QDs ZnSe | EMIM-BF_4 or ZnSe | MEMI: (A) H_2 and (B) CO evolution and (C) CO selectivity as a function of irradiation time; 0.5 μM ZnSe-BF_4, 50 μM EMIM-BF_4 or MEMI, molar ratio 100 (ligand to QD). (D) CO-selectivity as a function of the MEMI loading for ZnSe | MEMI. Conditions: AM 1.5G, $\lambda > 400$ nm, 100 mW cm^{-2}, 0.5 μM ZnSe-BF_4, 0.1 M AA, pH 6.5, CO_2 constant flow (4 sccm), 25°C.

and maintain enhanced CO formation at longer irradiation times (t > 200 min) (Figure C.4-D, Figure 5.6). Notably, at a given irradiation time, a near-linear correlation between the MEMI loading (between 0 and 75 equiv. per QD) and CO-selectivity is observed, which levels off at a high molar ratio of 100 (Figure 5.5-D). These observations suggest that the strongly interacting MEMI ligands promote CO_2 reduction while higher loadings further block HER through the weak/dynamic interaction of the MEMI ligands with the QDs. The excess ligands may also allow to replenish decomposed/desorbed ligands after longer irradiation times.

Only traces of formate (< 3% of carbonaceous products, Table C.3) are formed and no other CO_2-reduction products (*e.g.* methane, methanol) are detected. Only negligible amounts of CO are produced under N_2 flow (Figure C.5) and no gaseous products are detected in the dark or in the absence of QDs or AA, demonstrating that all components of the photocatalytic system are required (Table C.2). ^{13}C-labelling also confirmed CO_2 as the sole origin of CO in the presence of MEMI (Figure C.3). In order to rule out the possibility that the influence originates purely from the presence of a thiol group, a

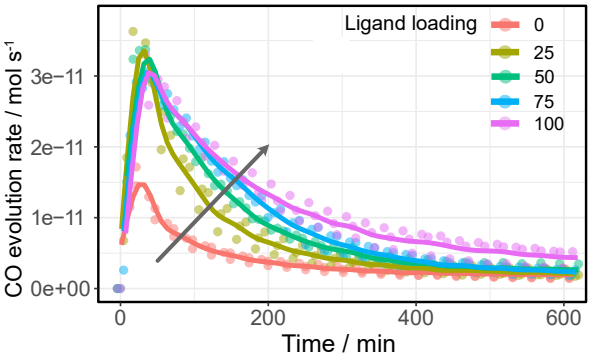

FIGURE 5.6: CO-formation rate of ZnSe-QDs in the presence of varying amounts of MEMI (overlay of Figure C.4-B).

control experiment was conducted with a ligand consisting of a thiol with no additional functionality, 1-butanethiol (BuSH), which resulted in a similar product distribution compared to non-functionalised ZnSe QDs (Figure C.6). This result indicates that the imidazolium functional group on the ligand is essential for the suppressed HER and enhanced CO production relative to bare ZnSe. Next, the possibility was considered if the thiol group could be oxidised under photocatalytic conditions, which would effectively render it an electron donor, as previously reported [126, 360]. However, ^{1}H-NMR spectroscopy of a ZnSe | MEMI solution after 1 h of solar irradiation did not show any signals from a potential disulfide product (Figure C.7).

It was previously reported that the imidazolium motif in ILs can participate in electrochemical CO_2 reduction either by *in-situ* formation of a carbene [343] and subsequent attack of CO_2, or by directly forming a CO_2-IL adduct after $1e^-$ reduction of the imidazolium ligand (see section 1.4.3) [296]. Both mechanistic pathways involve a carbene intermediate and the imidazolium could essentially be considered a co-catalyst. In order to probe the feasibility of such a pathway for the ZnSe | MEMI system, an analogue of MEMI was prepared which is methyl-protected at the imidazolium C_2 position (M-MEMI) to effectively inhibit the formation of a carbene (see experimental section 5.1.8 for synthetic details). In a photocatalytic benchmark experiment, ZnSe | M-MEMI exceeds ZnSe | MEMI in both CO formation and CO-selectivity reaching an unprecedented 2.38 ± 0.19 mmol CO $g_{ZnSe}{}^{-1}$ after 10 h irradiation (TON_{QD} (CO) = 370) with an improved selectivity towards CO of 12.0% (Figure 5.7, Table C.1). This observation precludes an imidazolium-mediated CO_2 reduction mechanism. In contrast, a CO_2 reduction pathway that proceeds via the ZnSe surface is proposed, which is supported by the ability of QDs to reduce CO_2 even in the absence of MEMI.

While the CO selectivity remains < 20% in any case, the changes in product selectivity are notable as the CO-selectivity of ZnSe | M-MEMI is enhanced 13-fold compared

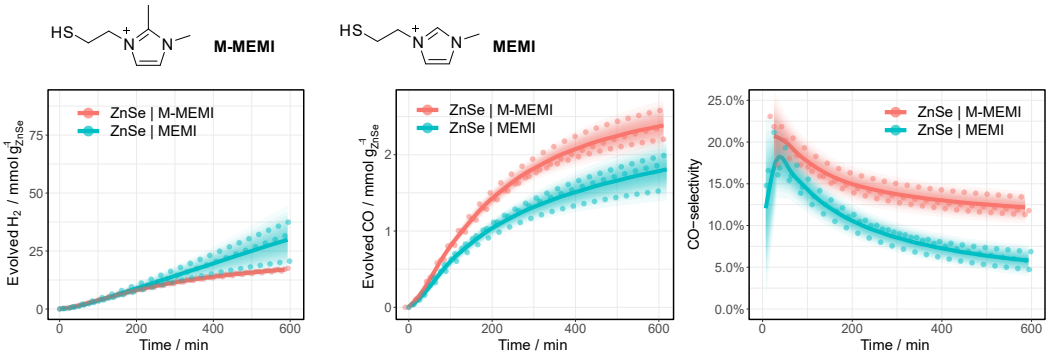

FIGURE 5.7: Benchmarking photocatalytic CO_2 reduction of ZnSe | M-MEMI vs. ZnSe | MEMI. Conditions: AM 1.5G, $\lambda > 400$ nm, 100 mW cm^{-2}, 0.5 μM ZnSe-BF_4, 50 μM capping ligand, 0.1 M AA/$NaHCO_3$, pH 6.5, CO_2 constant flow (4 sccm).

to non-functionalised ZnSe-BF_4 under optimised conditions, which underscores the potentially wide-ranging impact of this conceptionally novel ligand modification strategy. The average external quantum efficiency (EQE_{CO}) for the best performing system (ZnSe | MEMI) was 0.14 ± 0.06 % (400 nm monochromatic light, 1.0 - 1.5 mW cm^{-2}, 2 h, Table C.4). Additionally, the rate of CO evolution (238 μmol g_{QD}^{-1} h^{-1}) is amongst the highest for QD-photocatalysed CO_2 to CO reduction in aqueous solution [205], with higher activities only being reported in organic solvents using monochromatic blue LEDs as the light source [218, 340], or in the presence of a transition metal-based molecular co-catalyst (Chapter 4). In comparison to the QD molecular catalyst hybrids (Chapter 4), the activity is approximately one order of magnitude lower (TON_{QD} = 370 for ZnSe | M-MEMI vs. TON_{QD} = 6500 for ZnSe | Co(tppS3N1), 10 h irradiation).

5.1.5 Charge Carrier Dynamics

The excited state dynamics of aqueous ZnSe and ZnSe | MEMI (1:100) were monitored by transient absorption (TA) spectroscopy experiments. The samples were pumped with 400 nm pulses and probed in the UV-Vis/NIR region at varying pump-probe delays ($\Delta t_{p\text{-}p} \leq 8$ ns), see the experimental section 5.1.8 and Figure C.9 for further details. The transient spectra of the QDs (Figure 5.8-A) show long-lived (> 8 ns) negative bands at 410-450 nm and 365-405 nm, as well as a positive signal(> 525 nm) extending into the NIR (Figure C.10-A). Similar features were observed in a previous TA study on these QDs [317], apart from the higher energy negative band (denoted XB2) owing to the previous lack of probe coverage in the UV. Herein, derivative-like features are observed in the early-time TA spectra (inset of Figure 5.8-A), attributed to Coulomb induced biexciton shifts [361, 362], resulting in photo-induced absorption (PIA) signals at the lower energy sides of the negative signals. The PIA signals decay within a few hundred femtoseconds, indicating carrier relaxation to the band edge states, leaving the optical

response to be dominated by state filling effects [362]. The negative bands after carrier relaxation ($\Delta t_{p\text{-}p} \approx 350$ fs) are assigned to the bleaching of valence band-conduction band (VB-CB) excitonic transitions (denoted XB1 and XB2), with dynamics that reflect a single band edge population. Specifically, XB1 and XB2 are associated with two distinct transitions (Figure 5.8-B, II) that involve the VB edge ($VB_{h,L}$) and a deeper hole state ($VB_{h,U}$) that share a common CB electron state, in accordance with TA studies on the II-VI analogues of ZnSe [362–364]. At probe delays $\Delta t_{p\text{-}p} >$ 350 fs the maxima of XB1 and XB2 experience a redshift with a concomitant band broadening (brown → yellow → red spectra in Figure 5.8-A). This alludes to the presence of optically active sub-band trap states, in line with previous studies on similar ZnSe materials [364–367].

The trapped carrier nature was revealed by introducing AA (10 mM, pH ~6.7) as a hole scavenger, allowing the decoupling of electron and hole dynamics. A hole-contribution to the positive transient was evidenced by the ultrafast removal of A1 (> 525 nm) in the presence of AA (Figure 5.8-D: ZnSe | MEMI | AA, note that the influence of MEMI is discussed further below). A1 is assigned specifically to trapped holes, as reported previously [317]. The dynamic redshifts of XB1 and XB2, however, are preserved in the presence of AA. Previously, the presence of optically allowed band-to-trap transitions was evidenced by the faster recovery of a distinct sub-band bleach (λ_{bleach}: 550 nm) upon electron transfer events from the QDs to a co-catalyst. Herein, the energetically distinct hole states (Figure 5.8-B) share a common electron trap state ($S_{T,CB}$), seemingly in much closer proximity to the CB edge, which upon CB-to-$S_{T,CB}$ trapping events result in the bleaching of sub-band transitions ($XB1_T$ and $XB2_T$: III) superimposed on the low-energy side of the VB-CB excitonic resonance (XB1 and XB2: II). The average of electron trapping rates is reflected in the redshift dynamics (Figure 5.8-C), following the CB-edge state filling sensitive recovery of XB1/XB2 (red trace) and correlated growth of $XB1_T$/$XB2_T$ (grey-green-violet trace) as population transfer proceeds.

The passivation of uncoordinated bonds on the QD surface is expected to lower the density of trap states related to surface defects which, in the present system, could manifest as attenuated VB-to-$S_{T,CB}$ transition probability. This is reflected in the TA dynamics as a smaller wavelength shift with time of the bleach maximum ($\Delta\lambda_{bleach}$ inset Figure 5.8-D: ZnSe | MEMI | AA, Figure C.10-B,D: ZnSe | MEMI) from initial to final times ($\Delta t_{p\text{-}p}$: ~ 150 fs to 8 ns, horizontal bars) upon the addition of 100 equiv. per QD of the thiol functionalized MEMI ligand compared to the neat QDs (orange/violet vs green spectra) – consistent with fewer CB-to-$S_{T,CB}$ trapping events. The dynamics of the A1 band remains unperturbed upon MEMI binding (see Figure C.10-C), which implies that the ligand does not influence hole-trap states. These observations support a high ZnSe-MEMI binding affinity, and indicate that at least a subset of the ZnSe trap states ($S_{T,CB}$) can be associated with unpassivated surface sites. The CB-related

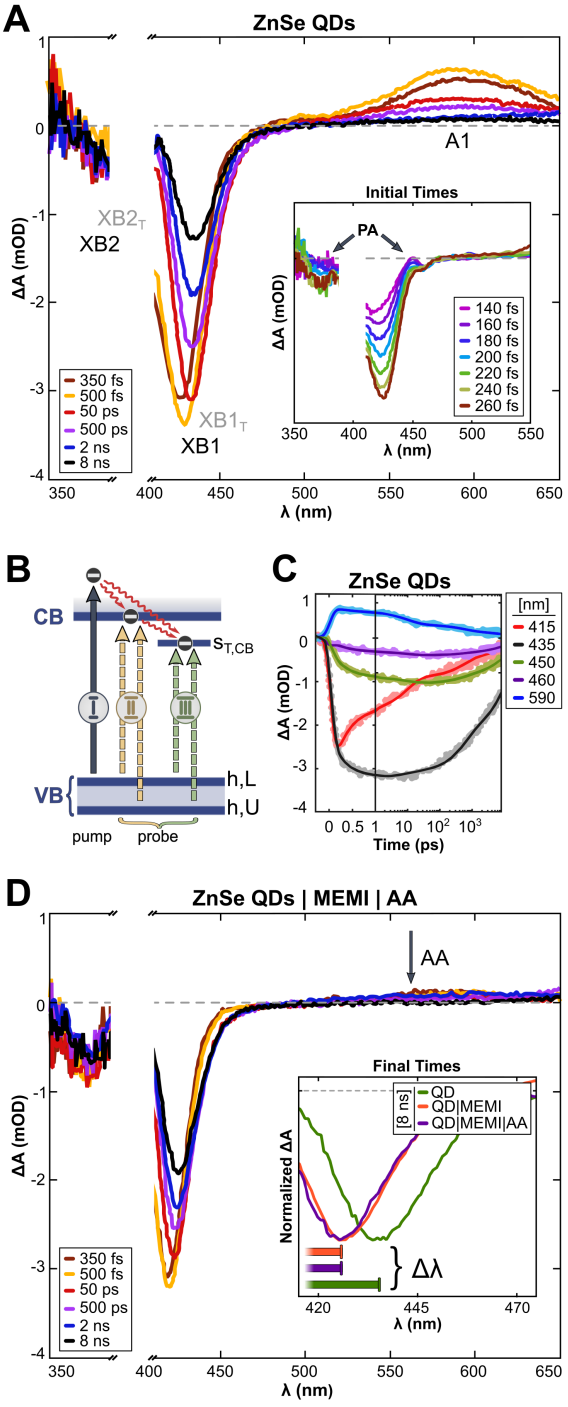

FIGURE 5.8: **(A)** Differential absorbance (Δ-A) spectra recorded by transient absorption (TA) experiments of aqueous ZnSe-QDs. Pump: 400 nm. Inset: early-time TA spectra. **(B)** Schematic diagram of optical transitions related to the I) pump, II) probe: VB-to-CB excitonic transitions (XB1 and XB2), and III) probe: VB-to-CB trap transitions ($XB1_T$ and $XB2_T$). **(C)** Kinetics of ZnSe QDs extracted from the transient spectra presented in (A). **(D)** Δ-A spectra of ZnSe QDs in an aqueous ascorbate (AA, 10 mM, pH: 6.7) solution with 100 equiv. per QD of thiol functionalized MEMI ligand. Inset: 8 ns TA spectra of ZnSe, ZnSe | MEMI and ZnSe | MEMI | AA. The horizontal bars illustrate the magnitude of the dynamic redshift experienced by the bleach bands, ranging from 150 fs (left) to 8 ns (right). The Figure was created by Nora Eliasson.

trap states are likely metal cation based [362, 368], indicating a ZnSe(Zn)-MEMI(thiol) binding site.

Overall, the TA experiments reveal that the MEMI ligand influences the charge carrier dynamics of the QDs, and that this effect most likely is surface-defect related with a ligand binding site corresponding to unpassivated Zn. The high surface-to-volume ratio, resulting from the abrupt terminations of the crystal lattice, leaves ligand-free QDs with a large portion of electronic trap states that can have a detrimental effect on the charge separation ability. Control experiments with BuSH, however, clearly indicate that surface passivation alone is not sufficient to explain the enhanced CO_2 reduction activity and selectivity in ZnSe | MEMI compared to the unpassivated QDs. Furthermore, the lack of an observable change in the trapped-hole dynamics in the presence of MEMI, monitored through TA experiments, rules out the possibility that the observed changes in photocatalytic activity from addition of MEMI are due to MEMI affecting the hole dynamics; this is in line with the photocatalytic control experiments above in which MEMI did not act as electron donor. Whether the ability of the unpassivated QDs to reduce CO_2 results from charge transfer involving the remaining CB population, or whether trapped electrons are accessible to CO_2 in the present system, remains to be explored, but can be key information in the design of ligands in similar systems where trap states may have an adverse effect on, or promote, charge separation. These experiments point unequivocally towards a more unique role for the imidazole-based ligands, which extends beyond the intrinsic QD charge carrier dynamics into the second-coordination sphere. This assumption is corroborated by the observation that MEMI affects both reaction products differently (suppresses HER, enhances CO), which further affirms an influence beyond the intrinsic photophysics in the second-coordination sphere.

5.1.6 DFT calculations

Having excluded a ligand promoted mechanism as well as the influence of MEMI on the intrinsic charge carrier dynamics to explain the enhanced CO formation activity promoted by MEMI, secondary-coordination sphere effects of MEMI on QD-surface promoted CO_2 reduction were explored next: The mechanism of CO_2 reduction has been widely investigated on numerous electrocatalytic materials (see introduction, section 1.3.1), but the exact nature of the pathway and intermediates is under debate and depends on the nature of the catalytic site [28, 369]. For CO_2 to CO reduction, the pathway is believed to proceed either via an electron transfer (ET) to form a surface stabilised $^*CO_2^-$ radical (where * denotes a surface active site) or via a concerted proton-coupled electron transfer (PCET) to yield *COOH. This first step is typically the most energy demanding, hence unravelling the nature of the first intermediate is essential for

the elucidation of the reaction mechanism and rationalisation of the catalytic activity. To assess the catalytic competence of the ZnSe-QDs toward CO_2 to CO reduction and shed light on the overall mechanism, a comprehensive computational investigation was conducted by means of periodic DFT calculations using the Perdew-Burke-Ernzerhof (PBE) functional with Grimme's D3 dispersion corrections (see experimental section 5.1.8 for details). Firstly, the predominant morphology of the ZnSe-QDs was investigated by modelling their equilibrium shape via the Wulff construction method. The resulting equilibrium crystal shape consisted of a rhombic dodecahedron exposing exclusively the (220) lattice plane (Figure C.11), in agreement with previous theoretical works [370]. The coverage of MEMI ligands on the ZnSe(220) surface was subsequently investigated, ultimately leading to a 50% coverage (relative to the available Zn surface sites) as the most energetically favourable (Figure C.12). Once the resting state of the ZnSe | MEMI system was assessed, the HER activity was assessed on both the bare and MEMI-terminated ZnSe(220) surfaces, with and without the presence of a photogenerated electron. After assessing the *H coverage on all possible active sites of both systems (Figure C.13), calculations revealed that both the bare ZnSe and ZnSe | MEMI systems can only promote HER atop the Zn surface atoms and in the presence of a photogenerated electron. Hence, it is concluded that the enhanced catalytic performance of ZnSe | MEMI QDs in these experiments is due to the stronger binding of the MEMI ligands through the thiol group compared to that of H atoms, which block the HER-active Zn surface sites hindering this competing reaction. This finding is in line with the observation from TA spectroscopy that MEMI passivates Zn sites, which simulations pinpoint as the main responsible for the HER.

Next, the CO_2 activation was assessed on the bare and MEMI-functionalised surfaces, with and without the presence of a photogenerated electron. Importantly, all the attempts to adsorb CO_2 on the bare ZnSe(220) surface were unsuccessful, resulting in the dissociation of CO_2 from the surface into the gas phase. A similar result was obtained on the neutral ZnSe | MEMI system, and only when a photogenerated electron was introduced in the simulation, CO_2 could be stabilised on the Zn surface sites. The resulting structure, depicted in the two panels of Figure 5.9-A, displays a Zn-C distance of 2.280 Å and an O–C–O angle of 137.7^o, while the C–O bond lengths are increased compared to the gas phase CO_2 from 1.176 Å to *ca.* 1.236 Å. Further insight was obtained from the calculated magnetic moments and Bader charge analysis on the C and O atoms closest (O_A) and farthest (O_B) from the surface, which indicated that the photogenerated electron is delocalised between the adsorbed CO_2 and the QD surface. Hence, it was concluded that CO_2 is activated upon interacting with the photogenerated electron on the QD surface, leading to a negative charge density and radical behaviour build up,

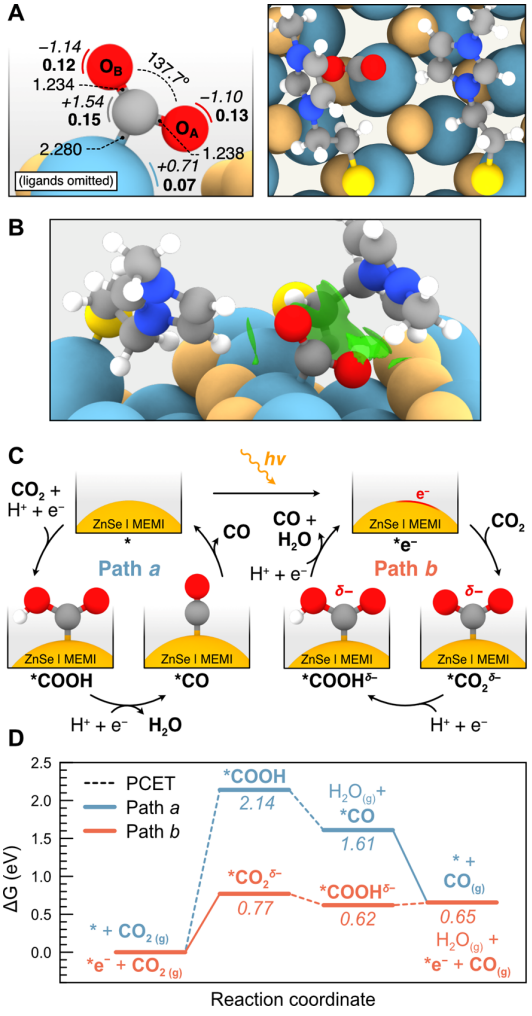

FIGURE 5.9: (A) Side (left) and top (right) views of the $^*CO_2^{\delta-}$ intermediate with the relevant bond distances (in Å) and angles. Calculated atomic Bader charges (in e) are displayed in italics beside each atom, while magnetizations (in B) are shown in bold. Note that neighboring MEMI ligands have been omitted in the side view for clarity. Color code: C (grey), O (red), H (white), S (yellow), Zn (teal), Se (orange). (B) Side view representation of the NCI isosurfaces (with an isovalue of 0.35 e-/a.u.3) responsible for the stabilisation of the $^*CO_2^{\delta-}$ intermediate. (C) Scheme illustrating the two proposed pathways for the CO_2 to CO reduction on the ZnSe | MEMI system in the absence (Path a, in which the reaction begins with a PCET) and presence (Path b, starting with an ET) of a photogenerated electron. (D) Calculated Gibbs energy diagrams for the CO_2 to CO reduction via Path a (in blue) and Path b (in orange) at the experimental conditions (see experimental section for details). Steps involving a PCET are denoted as a dotted line. The structures of all the reaction intermediates are shown in Figure C.14. *The Figure was created by Eric Mates-Torres.*

which is denoted as $^*CO_2^{\delta-}$. It is also noted that, although $^*H$ and $^*CO_2^{\delta-}$ bind preferentially on the same surface Zn sites, the functionalisation of the QD surface with MEMI ligands has an opposite effect on the HER and CO_2 reduction activity. In particular, the partial coverage of MEMI ligands hinders the HER by decreasing the amount of accessible Zn active sites for this reaction, while also enabling the stabilisation of the $^*CO_2^{\delta-}$ intermediate on the surface and consequently promoting CO_2 reduction over HER on the remaining sites, in agreement with experiments from photocatalysis and charge carrier dynamics.

In the following, the influence of the MEMI ligands on the stabilisation of the adsorbed $^*CO_2^{\delta-}$ is investigated by analysing the non-covalent interactions (NCIs) using the Critic2 software [371, 372]. This approach allows for the pseudo-quantitative measurement of intermolecular interactions including electrostatic interactions, H-bonding, van der Waals interactions and steric effects, and has been successfully applied to the coverage analysis of other functionalised QDs [373]. The NCI isosurfaces responsible for the stabilisation of the $^*CO_2^{\delta-}$ on the ZnSe | MEMI system are shown in 5.9-B, while the breakdown of these interactions is presented in Figure 5.10. Notably, two distinct interactions stand out as the most attractive ones, corresponding to a π-p interaction between the aromatic imidazole ring and the O_A 2p orbital, and a H-bonding interaction between the imidazole ring of a neighbouring MEMI and O_B. These strong attractive interactions are followed by three relatively weaker attractive interactions, associated to longer H-bonding and van der Waals interactions, and three weak repulsive interactions, mainly due to steric effects. Electrostatic interactions induced by the positive charge of the imidazolium moiety were found to be of lower influence. Importantly, the combination of these attractive and repulsive NCIs, which have not been computationally quantified to date, are essential for the stabilisation of the $^*CO_2^{\delta-}$ intermediate, as confirmed by the observed desorption of CO_2 upon removal of either the surface ligands or the photogenerated electron. Hence, it is concluded that both the MEMI ligands and the photogenerated electron work cooperatively to activate and stabilise CO_2 on the ZnSe-QD surface.

An alternative way to activate CO_2, commonly proposed in the literature, is via a PCET to form $^*COOH$ [369]. A schematic representation of this process and the subsequent reduction to $^*CO$ from both $^*COOH$ and $^*CO_2^{\delta-}$ is presented in Figure 5.9-C (Paths *a* and *b*, respectively). The likelihood of these reaction pathways on the ZnSe | MEMI system was assessed leading to the Gibbs energy profiles shown in Figure 5.9-D. According to these calculations, the CO_2 to CO reduction through the two consecutive PCETs (Path *a*) is rendered unlikely based on the high energy required for the initial CO_2 activation, *i.e.* 2.14 eV. In contrast, the activation of CO_2 via the photogenerated

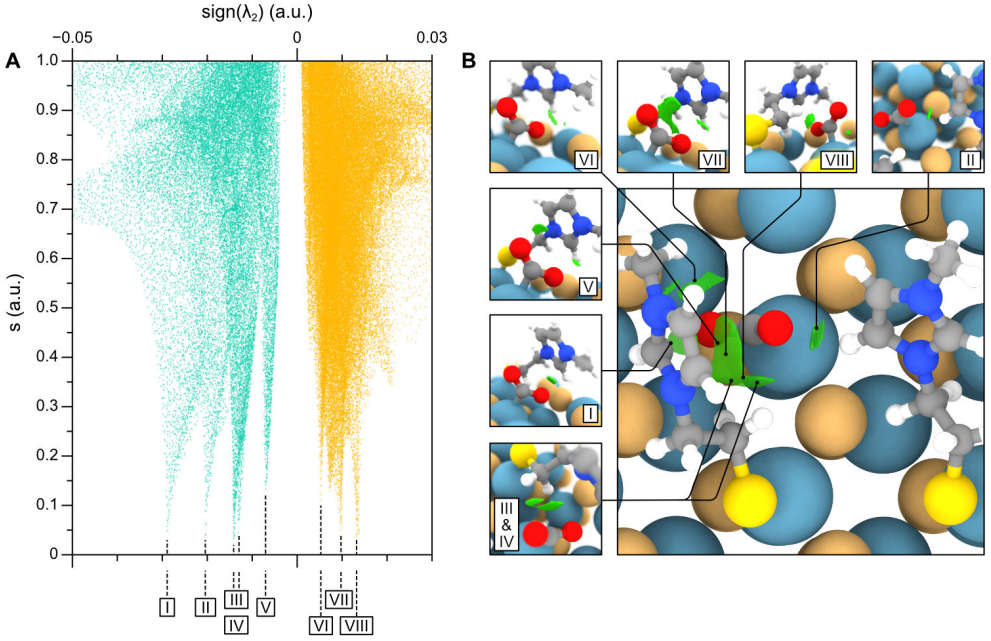

FIGURE 5.10: Assignment of non-covalent interactions. (**A**) Plot of the reduced density gradient (s) as a function of the electron density multiplied by the sign of the second eigenvalue of the Hessian matrix ($\text{sign}(\lambda_2)\rho$) for the ZnSe | MEMI system with the adsorbed $^*CO_2^{\delta-}$ intermediate. Peaks correspond to attractive and repulsive interactions, assigned based on the value of $\text{sign}(\lambda_2)\rho$ below and above 0 a.u., respectively. Thus, the further the peak is from the origin, the stronger the attractive or repulsive interaction. (**B**) Representation of the non-covalent interactions between the MEMI ligands and $^*CO_2^{\delta-}$. Isosurfaces are plotted with an isovalue of 0.35 $e^-/(\text{a.u.})^3$. The separate interactions are also shown and assigned to their corresponding peaks in (A). *The Figure was created by Eric Mates-Torres.*

electron-mediated mechanism (Path b) was found to require a considerably lower energy, *i.e.* 0.77 eV, making this pathway feasible at the experimental conditions. The feasibility of Path b proceeding via a rate-limiting ET step to form $^*CO_2^{\delta-}$ is further supported by experiments conducted at a lower pH, which only accelerated HER and not CO formation (Figure C.8).

Once $^*CO_2^{\delta-}$ is formed via Path b, the reaction may proceed through an exergonic PCET which yields a *COOH intermediate with a negative charge density ($^*COOH^{\delta-}$) as revealed by the Bader charge analysis (Figure C.14). This species, which lies 0.62 eV above the separate reactants, has also been predicted to be a key intermediate in the CO_2 reduction catalysed by cobalt complexes [374]. The generated $^*COOH^{\delta-}$ intermediate subsequently undergoes a second PCET step which requires only 0.03 eV resulting in the desorption of both CO and H_2O and leading to the regeneration of the ZnSe | MEMI with the photogenerated electron. Overall, the highest energy point in this Path b corresponds to the initial activation of CO_2 to form $^*CO_2^{\delta-}$, highlighting the importance of the cooperative effect between the MEMI ligands and the photogenerated electron in the stabilisation of this intermediate. While predicting a mechanistic pathway solely via

computational simulations is not complete proof yet, it shows that a pathway is feasible under experimental conditions. Further spectroscopic investigations (i.e. time resolved *in-situ* IR spectroscopy) may further elucidate the reaction mechanism.

5.1.7 Conclusions

A straightforward surface modification strategy with organic molecular species was reported to enhance the photocatalytic CO_2 to CO reduction activity of ZnSe QDs. Immobilisation of an imidazolium moiety promotes CO formation while suppressing the competing HER on the QD surface. To the best of the author's knowledge, this is the first time that colloidal QDs have been activated for CO_2 reduction by modifying the chemical secondary environment through design of a capping ligand without the requirement of an additional molecular co-catalyst based on transition metal complexes. It should be noted that because MEMI reduces the activation energy during the conversion of CO_2, it may also be considered a *catalyst*. The CO selectivity can be modulated with the imidazolium loading, yielding up to a 13-fold increase compared to the non-functionalised ZnSe-BF_4. Finally, mechanistic insights are provided through TA spectroscopy and periodic DFT calculations, which pinpoints (unpassivated) Zn atoms of the QD surface as the active sites for CO_2 to CO reduction. This process is shown to involve a photo-reduced QD which renders a $^*{CO_2}^{\delta-}$ species stabilised by the surrounding imidazolium group on the QD surface as the key reaction intermediate. Simulations also reveal that imidazolium ligands hinder the competing HER by blocking the surface Zn active sites. The results not only advance the understanding of interactions of imidazolium groups with CO_2 reduction intermediates but can also open new routes in the surface design of photocatalysts without the use of precious metals or synthetically demanding molecular co-catalysts based on transition metal complexes.

5.1.8 Experimental section

ZnSe-BF_4 QDs were prepared as described in Chapter 2. The physical characterisation techniques are described in Chapter 2 as well.

^{1}H Nuclear magnetic resonance (NMR) titration experiments. ^{1}H-NMR spectra were recorded on a Bruker AVANCE 500 with a TCI Cryoprobe system (500 MHz). Chemical shifts are recorded in D_2O in ppm with the internal reference set to the solvent peak at $\delta = 4.80$ ppm. In a typical NMR titration experiment, 1 mL of a 5 μM ZnSe-QD solution in D_2O is mixed with specific amounts of capping ligand stock solution (typically 10 μL of a 0.5 mM in D_2O) inside an NMR tube under an atmosphere of N_2. All NMR titration spectra were measured with 256 scans.

Calculation of the surface coverage. The surface coverage was calculated according to the following formula:

$$Surface\,coverage = \frac{N_{MEMI} \cdot SA_{MEMI}}{SA_{QD}} = \frac{N_{MEMI} \cdot SA_{MEMI}}{4\pi r^2}$$

The surface area of a QD (SA_{QD}) was approximated using the equation for the surface area of a sphere taking into account the average QD diameter of ~4.5 nm. For a MEMI ligand, a surface occupation area (SA_{MEMI}) of ~1 nm was assumed and then the number of MEMI ligands (N_{MEMI}) and their surface occupation was divided by the surface area of a QD.

Isothermal titration calorimetry (ITC). ITC experiments were carried out using a Malvern Microcal Auto-ITC200. During a typical ITC titration, ZnSe-BF_4 QD (1 or 2 μM, 200 μL) solution was placed inside the sample cell and the capping ligand solution (0.5 or 1 mM) in the syringe is stepwise titrated to the QD solution. In order to avoid background signals from DMF (as native solvent of the QDs), the concentration of DMF was kept constant (3.12 %, v/v) in the solutions within the cell and the syringe. Each experiment was conducted at 298.15 K and allowed to equilibrate prior to an initial 60 s delay. One titration experiment consisted of 1 injection of 0.6 μL and 32 consecutive injections of 1.2 μL with 90 s intervals between injections. Control titrations were carried-out to quantify any background heat caused by dilution between the solvent mixtures and ligand solution. The MEMI-solvent control titrations were subtracted from the MEMI-QD titrations. The obtained ITC curves were fitted by MicroCal Analysis Centre software using one set of independent sites binding model [355].

Zeta potential. Zeta potential measurements of ZnSe-BF_4 (0.5 μM) and in the presence of MEMI (100 equiv. per QD) were conducted in aqueous solution (neutral pH) using a Malvern Zetasizer Nano ZS90 instrument at 25°C.

External quantum efficiency (EQE). The EQE was measured as described in 4.4. The samples were "primed" for 25 min under full AM 1.5G irradiation conditions to reach peak turnover before the EQE determination was started.

Preparation of 3-(2-mercaptoethyl)-1-methyl-imidazolium bromide (MEMI). 3-(2-Bromoethyl)-1-methylimidazolium bromide was synthesised according to an adapted literature procedure [375]. 1-Methylimidazole (4.0 mL, 50 mmol) was dissolved in a solution of anhydrous diethyl ether (25 mL) and 1,2-dibromoethane (20 mL, 230 mmol) slowly added. The resulting solution was stirred slowly at room temperature (RT) under an inert atmosphere and a colourless crystalline product deposited over several

days. The solution was removed using a canula filter, and the solid 3-(2-bromoethyl)-1-methylimidazolium bromide washed with dry diethyl ether. Yield: 8.65 g, 64%. ^{1}H-NMR (400 MHz, DMSO-d^{6}) δ (ppm) = 9.29 (s, 1H), 7.87 (m, 1H), 7.78 (m, 1H), 4.64 (t, J = 5.9 Hz, 2H), 3.96 (t, J = 5.9 Hz, 2H), 3.90 (s, 3H). ^{13}C-NMR (101 MHz, DMSO-d^{6}) δ (ppm) = 136.99, 123.71, 122.34, 50.04, 35.89, 31.56.

3-(2-(Acetylthio)ethyl)-1-methyl-imidazolium bromide was prepared using a modified literature procedure [343]. Solid potassium thioacetate (846 mg, 8.6 mmol) was added to 3-(2-bromoethyl)-1-methyl-imidazolium bromide (2.0 g, 7.4 mmol) in anhydrous acetonitrile (20 mL) and the resulting mixture stirred overnight under reflux. After cooling to RT the solution was removed from precipitated KBr by canula filtration, the solvent removed in vacuo, and the residue thoroughly dried to afford pale-yellow-white 3-(2-(acetylthio)ethyl)-1-methyl-imidazolium bromide. Yield: 1.89 g, 96%. ^{1}H-NMR (400 MHz, DMSO-d^{6}) δ (ppm) = 9.19 (s, 1H), 7.79 (m, 1H), 7.71 (m, 1H), 4.36 (t, J = 6.4 Hz, 2H), 3.86 (s, 3H), 3.32 (t, J = 6.4 Hz, 2H), 2.35 (s, 3H). ^{13}C-NMR (101 MHz, DMSO-d^{6}) δ (ppm) = 194.51, 136.93, 123.55, 122.56, 48.06, 35.80, 30.55, 28.59. ATR-IR (neat): 3403br, 3140m, 3060s (C-H), 2981s, 2854w (CH_2), 1687s (C=O), 1577s (Im^+), 1560s (Im^+), 1454m, 1426m, 1356m, 1337w, 1300m, 1277w, 1220w, 1166s, 1130m, 1107m, 1044w, 1021w, 1008w, 952br, 757br, 719w, 700w, 680w, 646m, 620m.

3-(2-(Acetylthio)ethyl)-1-methyl-imidazolium bromide was added into a 50 mL Schlenk flask and dried in vacuo. Hydrochloric acid (HCl, 1M, 17.3 mL) was degassed by purging with nitrogen for 1 h and added to the flask. The resulting mixture was stirred for 63 h under inert gas atmosphere at 40 °C. The reaction product was isolated by evaporating the by-products and solvents. The 3-(2-Mercaptoethyl)-1-methyl-imidazolium bromide produced was kept under inert conditions before use in order to prevent aerobic disulfide formation. Yield was not obtained accurately due to the viscous, hygroscopic nature of the compound. ^{1}H-NMR (400 MHz, DMSO-d^{6}) δ(ppm) = 9.16 (s, 1H), 7.78 (m, 1H), 7.73 (m, 1H), 4.33 (t, J = 6.5 Hz, 2H), 3.87 (s, 3H), 2.95 (dt, J = 8.4 Hz, 6.5 Hz, 2H), 2.68 (t, J = 8.4 Hz, 1H). ^{13}C-NMR (100 MHz, DMSO-d^{6}) δ (ppm) = 136.79, 123.57, 122.34, 51.25, 35.78, 23.91. ATR-IR (neat): 3403br, 3138m, 3072s (C-H), 2851w (CH_2), 2425br, 1975w, 1630m (C=C), 1577s (Im^+), 1560s (Im^+), 1451m, 1425m, 1384w, 1359w, 1336m, 1300m, 1281w, 1251w, 1164s, 1089w, 1021w, 960br, 827br, 751br, 711w, 666w, 643m, 620m. Elemental analysis calcd. (%) for $C_6H_{11}N_2S_1Cl_{0.5}Br_{0.5}$ x $(H_2O)_{1.25}$: C 32.26, H 6.09, N 12.54, found C 32.15, H 6.17, N 12.33. HRMS: (m/z) calcd. for $C_6H_{11}N_2S^+$: 143.0637 $[M]^+$; found 143.0627.

Preparation of 3-(2-mercaptoethyl)-1,2-dimethyl-imidazolium bromide (M-MEMI).

3-(2-Bromoethyl)-1,2-dimethyl-imidazolium bromide was synthesised according to literature procedure [376] and re-crystallized in a methanol/ethyl acetate mixture (50:50). Yield (after recrystallisation): 2.77 g (65%). ^{1}H NMR (400 MHz, DMSO-d^{6}) δ (ppm) = 7.72 (d, J = 2.1 Hz, 1H), 7.68 (d, J = 2.1 Hz, 1H), 4.60 (t, J = 6.0 Hz, 2H), 3.90 (t, J = 6.0 Hz, 2H), 3.79 (s, 3H), 2.63 (s, 3H). ^{13}C NMR (101 MHz, DMSO-d^{6}) δ (ppm) = 144.97, 122.44, 121.14, 48.54, 34.91, 31.29, 9.53.

3-(2-(Acetylthio)ethyl)-1,2-dimethyl-imidazolium bromide was synthesised according to modified literature procedure [377]. 3-(2-bromoethyl)-1,2-dimethyl-imidazolium bromide (0.5 g) was combined with potassium thioacetate (201.1 mg) in anhydrous acetonitrile (10 mL) and the resulting mixture was stirred overnight under reflux. KBr was removed by filtration and the off-white precipitate was collected by drying in vacuo. Yield: 330 mg (94%). ^{1}H NMR (400 MHz, DMSO-d^{6}) δ (ppm) = 7.63 (d, J = 2.0 Hz, 1H), 7.61 (d, J = 2.0 Hz, 1H), 4.30 (t, J = 6.7 Hz, 1H), 3.75 (s, 3H), 3.24 (t, J = 6.7 Hz, 1H), 2.62 (s, 3H), 2.34 (s, 3H). ^{13}C NMR (100 MHz, DMSO-d^{6}) δ (ppm) = 194.81, 144.83, 122.16, 121.32, 46.71, 34.74, 30.48, 27.96, 9.35. ATR-IR (neat): 3414*br*, 3400*w*, 3174*w*, 3111*m*, 3073*s* (C-H), 3042*m*, 2987*w*, 2966*s*, 2954*m*, 2917*w*, 2906*w*, 2891*m*, 2760*w*, 2430*w*, 1740*w*, 1705*s* (C=O), 1670*w*, 1587*m*, 1533*s*, 1514*m*, 1470*m*, 1458*w*, 1432*m*, 1415*s*, 1393*w*, 1372*w*, 1360*m*, 1349*s*, 1340*m*, 1310*w*, 1268*s*, 1245*w*, 1167*m*, 1119*s*, 1094*s*, 1062*w*, 1045*w*, 1028*m*. 999*w*, 979*w*, 967*s*, 954*m*, 876*w*, 779*s*, 732*m*, 706*w*, 680*m*, 667*s*, 614*s*, 585*w*, 529*w*, 495*w*, 480*w*, 445*w*.

3-(2-mercaptoethyl)-1,2-dimethyl-imidazolium bromide (M-MEMI) was synthesised by loading 3-(2-(acetylthio)ethyl)-1,2-dimethyl-imidazolium bromide (120 mg) into a Schlenk flask and drying in vacuo. Hydrochloric acid (HCl, 1 M, 10 mL) was degassed by purging with nitrogen for 1 h and added to the flask. The resulting mixture was stirred for 98 h under inert gas atmosphere at 45 °C. The reaction product was isolated by evaporating the by-products and solvents and was kept under strict inert conditions before use in order to prevent aerobic disulfide formation. ^{1}H NMR (400 MHz, DMSO-d^{6}) δ (ppm) = 7.65 (d, J = 2.1 Hz, 1H), 7.63 (d, J = 2.1 Hz, 1H), 4.28 (t, J = 6.7 Hz, 2H), 3.76 (s, 3H), 2.89 (m, 2H), 2.69 (m, 1H), 2.61 (s, 3H). ^{13}C NMR (100 MHz, DMSO-d^{6}) δ (ppm) = 144.72, 122.29, 121.06, 49.83, 34.71, 23.65, 9.44. ATR-IR (neat): 3414*br*, 3174*w*, 3109*m*, 3058*s* (C-H), 3020*m*, 2987*w*, 2957*s*, 2945*w*, 2922*m*, 2441*m*, 1773*w*, 1670*w*, 1588*m*, 1537*s*, 1514*m*, 1456*s*, 1432*w*, 1413*s*, 1373*m*, 1362*m*, 1344*m*, 1305*w*, 1266*m*, 1241*m*, 1222*w*, 1165*m*, 1119*m*, 1094*w*, 1058*w*, 1034*m*, 951*w*, 889*w*, 814*m*, 789*s*, 731*m*, 703*w*, 672*w*, 658*m*, 626*w*, 579*w*, 478*w*, 444*w*. Elemental analysis calcd. (%) for $C_7H_{13}N_2S_1Br$ x $(H_2O)_{0.06}$:

C 35.29, H 5.55, N 11.76, found C 35.57, H 5.57, N 11.49. HRMS: (m/z) calcd. for $C_7H_{13}N_2S^+$: 157.0794 $[M]^+$; found 157.0788.

Photocatalytic CO_2 reduction

Sample preparation. A ZnSe-BF_4 stock solution (64.1 μM in DMF, 23.40 μL) and a capping ligand solution (5.0 mM in water, typically 30 μL) were added to a Pyrex glass photoreactor (Chromacol 10-SV, Fisher Scientific) containing a magnetic stirrer bar. The mixture was diluted with ascorbic acid (AA, 0.1 M in water, pH adjusted to 7 with NaOH) to a total solution volume of 3 mL. $NaHCO_3$ powder (25 mg) was further added to increase the pH to 8.3. The photoreactor was then sealed with a rubber septum and pierced with two needles (inlet and outlet).

Constant flow-setup with automated product quantification. The photocatalytic CO_2 reduction experiments were conducted as described in section 3.4.

Femtosecond Transient absorption (TA) spectroscopy

Femtosecond transient absorption (fs-TA) experiments were performed using a Ti:sapphire (Ti:Sa) based amplifier (Libra, Coherent Inc.) with an integrated Ti:Sa Kerr-lens mode-locked fs-seed laser and Q-switched Nd:YLF optical pump. The system operates at 800 nm (1.5 mJ, FWHM: 45 fs) with a 3 kHz repetition rate. The laser fundamental was split into a high-intensity pump and probe by a beam splitter. The probe was directed towards the UV-Vis-NIR sample chamber (TAS, Newport Corp./Helios IR, Ultrafast Systems) where the super-continuum (UV-Vis/NIR) was generated from a calcium fluoride/sapphire (CaF_2/Al_2O_3) crystal. The pump was frequency-doubled (∼400 nm) using a birefringent barium borate (BBO) crystal and attenuated (25-400 μW, 20-300 nJ/pulse) in the sample chamber using a neutral density filter. Prior to the sample cell, the pump was interrupted periodically by a chopper so that every second pulse were allowed to generate an excited population. The pump-probe delay time ($\Delta_{\text{p-p}}t \leq 8$ ns) was controlled by a mechanical optical delay line in the probe beam path, allowing the time-evolution of the differential absorbance between the pump induced excited state spectrum and the unpumped ground state spectrum to be recorded (silicon diode array: home built, Newport custom made). The instrument response function (IRF) was typically 140-160 fs and the number of scans for each measurement was limited to <7 scans (1500 integration) to avoid photodamage.

Sample preparation and Measurements

The ZnSe-BF_4 (754 μM in DMF) quantum dots (QDs) and MEMI capping ligand (50 mM/100 mM in water) stock solutions were stored in Schlenk flasks under an inert atmosphere (∼4℃). The samples (ZnSe; ZnSe | MEMI, 1:100; ZnSe | AA, 1:1000; ZnSe | MEMI | AA, 1:100:1000) were prepared with a final ZnSe concentration of 5-10 μM ($\geq$ 87 % H_2O vs DMF) and put in quartz cuvettes (1 mm pathlength) sealed with teflon caps and parafilm. All samples were prepared fresh on the day of measurements, including the AA stock solution (AA/NaOH, 50 mM, pH: ∼6.7, purged with inert gas). It should be noted that the QDs are easily prone to agglomeration, but all measurements were repeated on multiple occasions using on both of the individually prepared QDs. All features and dynamics reported in the main article (pump energy: 70 nJ: linear regime) were consistent across all measured samples of the same type, apart from in the neat ZnSe QD, where slight deviations were observed in the wavelength shift magnitude of the bleach maximum (Figure 5.8-D vs. Figure C.10-D). With MEMI present, the $\Delta\lambda_{\text{bleach}}$ was consistent across all measurements. Slight sample-to-sample variations are not surprising considering the differences between the spectral response reported for these QDs in Reisner (2018) and the present study (see main section), likely owing to the TA signals' sensitivity to the surface conditions (see main section) of the ligand

stripped QDs. The shape of the superimposed transients can therefore be expected to vary, reflecting differences in the relative weights of the signal amplitudes.

Data Analysis

All data treatment was performed in SurfaceXplorer Data Analysis Software (Ultrafast systems). Initially, the individual scans were analysed carefully to check for inconsistencies and the build up of photoproducts. For all TA reported spectra, the background and scattered pump light was extracted from the compiled datasets (scan average). The spectra were subsequently fitted with a polynomial function for chirp-correction, which ensures that time-zero is set equal at all probe wavelengths.

Computational methods

DFT calculations reported in this study were performed using the Perdew-Burke-Ernzerhof (PBE) functional [378] as implemented in the Vienna *Ab Initio* Simulation Package (VASP) software, version 5.4.4. The core electrons of Zn, Se, S, O, N, C and H atoms were replaced by projector-augmented wave (PAW) pseudopotentials [379], while their valence electrons were expanded in plane waves with a kinetic energy cut-off of 500 eV, using a scaling constant of 0.05 Å and a force-based convergence criteria of 0.015 eV $Å^{-1}$. Dispersion corrections were added using the zero-damping DFT-D3 method by Grimme [380] to account for non-covalent interactions (NCIs). The bulk structure of ZnSe was retrieved from the Materials Project database [381] and the equilibrium lattice constant was optimised by fitting the energy of a number of bulk ZnSe structures with lattice parameters ranging between ±5% of its initial value to the Birch-Murnaghan equation of state, sampling the reciprocal space using Γ-centred k-point grids of 3×3×3, 5×5×5, 7×7×7 and 9×9×9. Ultimately, a Γ-centred k-point grid of 5×5×5 was selected with a k-point density of 0.87 Å for surface calculations following a convergence criterion of 1 meV $atom^{-1}$. Molecules were calculated at Γ-point with at least 15 Å of vacuum along the three axes.

The energies of the 4-layered slabs of the (111), (200), (220) and (311) facets were calculated with a vacuum of at least 15 Å perpendicular to the surface. The bottom two layers were fixed to their bulk positions, whereas the two topmost layers were allowed to relax. This configuration was chosen based on walltime and energy convergence criteria. Surface energies were calculated with the following formula:

$$\gamma_i = \frac{E_{slab} - nE_{bulk}}{2A}$$

Where E_{slab} corresponds to the calculated energy of the optimised 4-layer slab, nE_{bulk} is the energy of the optimised bulk multiplied by the number of bulk units in the slab,

and A is the sectional surface area. The calculated surface energy values for the different facets are presented in Table C.6. The Wulff construction method was applied to determine the ZnSe QD morphology in equilibrium conditions, using the Wulff module implemented in the Pymatgen library [382]. After confirming that MEMI binds only on the coordinatively unsaturated Zn surface atoms of ZnSe through the thiol group, we proceeded to assess the relative stability of different ligand concentrations by adsorbing 1 or 2 MEMI ligands on the surface Zn atoms of ZnSe(220) surfaces with the following multiplicities: $p(1\times1)$, $p(2\times1)$ and $p(2\times2)$, effectively achieving coverages of 12.5 %, 25 %, 50 % and 100 %, respectively (representing the percentage of surface Zn sites saturated with MEMI ligands). The adsorption energy of the MEMI ligands on these surfaces was calculated as follows:

$$\Delta E = E_{ZnSe\cdot nMEMI} - E_{ZnSe} - n \cdot E_{MEMI}$$

Where $E_{ZnSe\cdot nMEMI}$ corresponds to the energy of the MEMI-covered ZnSe(220) slab, E_{ZnSe} is the energy of the bare ZnSe slab and nE_{MEMI} is the energy of the isolated MEMI ligand multiplied by the number of ligands in the unit cell. The normalised energies of adsorption of each coverage are depicted in Figure C.12. The most stable coverage of 50 % (ZnSe | MEMI) was used for mechanistic studies, represented by two MEMI ligands, each adsorbed on one of the four Zn surface sites in a $p(2\times1)$ ZnSe(220) surface; further adsorption of MEMI on either of the two additional sites was found to be endergonic due to the steric hindrance imposed by the imidazolium rings of the adsorbed ligands. A similar method was employed to calculate the adsorption of H atoms on the surface, wherein the energy of the hydrogen was replaced by one-half of the energy of molecular hydrogen following the computational hydrogen electrode model [383]. Similarly to the MEMI ligands, our simulations indicate that H atoms adsorb predominantly atop the surface Zn atoms. Furthermore, calculations show that the presence of a photogenerated electron is essential to lower the H adsorption energy with respect to the neutral system, from 2.15 eV to 0.36 eV on the bare surface and from 1.87 eV to 0.15 eV on the ZnSe | MEMI system, which is theorised to favour HER [384]. Hence, the presence of a photogenerated electron is required to promote HER on the bare and ZnSe | MEMI systems, in agreement with experiments, and hindering of HER on the ZnSe | MEMI system stems from the blockage of Zn active sites due to the stronger adsorption energy of MEMI compared to H.

Gibbs corrections to the energy were computed including the zero-point energy (ZPE), vibrational enthalpy and entropy terms obtained by means of the Thermochemistry module implemented in the Atomic Simulation Environment (ASE) package, at the experimental temperature of 298 K. In the calculation of the Gibbs energy corrections

for the different molecules, a pH of 6.5 was considered, partial pressures of CO_2 of 1 atm and H_2O of 0.035 bar (which is the pressure at which the gas and liquid phases of H_2O are in equilibrium at 300 K), and the experimentally detected concentration of CO of 3 μM.

Adsorption Gibbs energies of the different reaction intermediates on the ZnSe | MEMI system were calculated as follows:

$$\Delta G_{*CO_2^{\delta-}} = G_{*CO_2^{\delta-}} - G_{*e^-} - G_{CO_2}$$

$$\Delta G_{*COOH^{\delta-}} = G_{*COOH^{\delta-}} - G_{*e^-} - \left(G_{CO_2} + \tfrac{1}{2}G_{H_2}\right)$$

$$\Delta G_{*COOH} = G_{*COOH} - G_{*} - \left(G_{CO_2} + \tfrac{1}{2}G_{H_2}\right)$$

$$\Delta G_{*CO} = G_{*CO} - G_{*} - (G_{CO_2} + G_{H_2} - G_{H_2O})$$

Where Gibbs energies of the $^*CO_2{}^{\delta-}$, $^*COOH^{\delta-}$, $^*COOH$ and $^*CO$ intermediates in the ZnSe | MEMI system, respectively. The $^*COOH$ and $^*CO$ intermediates take part in the pathway in which CO_2 is adsorbed following a PCET step (Figure 5.9, Path *a* in the main section), while the $^*CO_2{}^{\delta-}$ and $^*COOH^{\delta-}$ intermediates belong to the mechanism where the first step involves an electron transfer to activate CO_2 (Path *b* in the main text). G_{*e^-} and G_* are the Gibbs energies of the ZnSe | MEMI including or omitting an additional electron for the aforementioned first and second mechanisms, respectively; and G_{CO_2}, G_{H_2} and G_{H_2O} are the Gibbs energies of the CO_2, H_2 and H_2O molecules in the gas phase. Note that a * denotes an adsorbed species. The Gibbs energy of the overall reaction was calculated as follows:

$$\Delta G_R = G_{CO} + G_{H_2O} - (G_{CO_2} + G_{H_2})$$

The analysis of the NCIs stabilising the $CO_2{}^{\delta-}$ intermediate and facilitating CO_2 activation in the first mechanism were assessed by computing the reduced density gradient, $s(r)$, as a function of the electron density, $\rho(r)$, by means of the Critic2 software [372], as described elsewhere [373].

All the computational data reported in this work, including the cartesian coordinates and energies of all the modelled structures, is accessible via the following ioChem-BD online dataset, DOI: *10.19061/iochem-bd-6-36*

5.2 Surface modification with dithiols

5.2.1 Introduction & Motivation

Dithiols are a class of organic compounds with two thiol (R-SH) functional groups - not to be confused with disulfides, molecules that feature a disulfide bridge (R-S-S-R). Dithiols are unexplored in the field of photocatalytic CO_2 reduction and were discovered in this context by the author of this dissertation while interfacing redox enzymes with QDs (data not included) which require activation using dithiothreitol (DTT) as reducing agent. It was quickly discovered that the influence of DTT stems from its dithiolic nature and its interactions with the QD surface.

Within the literature of nanocrystals, dithiols have been reported in various contexts such as multidentate anchors, cross-linkers and as hole quenchers. A report on dithiols examined the ligands with bidentate binding/anchoring groups and showed an enhanced affinity for QDs in comparison to monodentate ligands [385, 386]. A range of rigid and flexible dithiols with different lengths was investigated as a method to cross-link CdTe QDs and the formation of aggregates was followed using TEM and PL spectroscopy [387]. Another study investigated the PL emission quenching of dithiols on CdSe and CdTe QDs and assigned it to hole quenching [388]. Monolayers of dithiol (1,6-hexanedithiol or 1,10-decanedithiol) were grown on CdS nanoparticles without mutual aggregation of particles and the particles retained their semiconducting properties [389]. The functionalisation of CdS nanoclusters was investigated with electrospray mass spectrometry and found that 1,4-benzenedimethanethiol binds to the surface and that the second thiol group does not readily lose its proton can not bind to the Cd surface due to the rigidity of the benzene ring [390].

In this section, the influence of linear dithiols (2 - 8 carbon centres) including 1,2-ethaneditihol, 1,4-butanedthiol, 1,6-hexanedithiol and 1,8-octanedithiol on photocatalytic CO_2 reduction on ZnSe QDs is investigated. This study is motivated by preliminary experiments which suggested that shorter dithiols enhance CO_2 reduction on the bare ZnSe surface and that longer dithiols (such as DTT in the initial experiment) if an additional molecular co-catalyst based on a Ni-cyclam is employed as the main catalytic site. Therefore, in the first step, the dithiol-QD interactions are examined systematically with mainly NMR spectroscopy and the agglomeration behaviour with dynamic light scattering. In the next step, the influence on CO_2 photoreduction is investigated and benchmarked to a set of controls of monothiols and mercaptoalcohols. Finally, a set of DFT calculations elucidates the possibility of the non-innocence of the second thiol group. The section concludes with a discussion highlighting the proposed interactions.

5.2.2 Dithiol-QD interactions

Interactions of dithiols with ligand-free ZnSe-BF_4 QDs in aqueous solution were studied by liquid-phase ^{1}H-NMR spectroscopy. A range of dithiols with increasing length (2 - 8 carbons) in-between the two thiol groups (1,2-ethanedithiol (EDT), 1,4-butanedithiol (BuDT), 1,6-hexanedithiol (HexDT) and 1,8-octanedithiol (OctDT)) were chosen as targets to study the dithiol-QD interactions in-depth. All ligands show significant but different effects in CO_2 photoreduction depending on if a molecular co-catalyst Ni(cycP) is present (see photocatalysis section below).

The choice of solvent for the titration is a key variable to consider but can add additional complexity: Ideally, the titration is performed under fully aqueous conditions for both titrant and QD solution (*i.e.* in D_2O), however, the solubility of the dithiols in purely aqueous solution is not sufficient. While all dithiols dissolve initially in D_2O (as determined by ^{1}H-NMR spectroscopy with a reference compound), phase segregation occurs over time and the dithiols separate out of aqueous solution. Therefore, alternative solvents were explored. DMF-d7 would be a natural choice because it is used as solvent for the QDs and therefore already present in the system, but nevertheless exhibited a large broad background signal at approximately 0.8 to 1.3 ppm when added to a QD solution as a control experiment, presumably due to its strong coordinative nature which renders it an excellent solvent for the QDs. Acetonitrile-d3 (ACN-d3) was therefore chosen because it gave a much smaller background signal at around 0.76 ppm (Figure C.15). It dissolves all dithiols well and can also be used to dissolve the QDs, hence avoid solvent induced precipitation. Nevertheless, having different solvents for titrant and QD solution during the titration is not ideal because the solvent mixture is continuously changing over the course of the titration causing some signals to continuously move in their chemical shift. (It was not considered useful to deviate from D_2O as solvent for the QDs because this would render the experiments not comparable to the light experiments.) In order to ensure that excessive ligand during the NMR titration would be visible in (mostly aqueous) solution, a control experiment was conducted in which a defined amount of the ligand stock solution was added to D_2O to give 100 μM (equivalent to 50 ligands per QD, in ACN-d3) and used as reference to assign signals.

Titration of dithiols

Defined quantities of EDT (*i.e.*, 25/50/75/100/200 equiv. (mol_{EDT} per mol_{QD}) per injection) were added stepwise to a suspension of ZnSe-BF_4 QDs in D_2O (Figure 5.11). For quantities of EDT $\leq$ 100 equiv. per ZnSe-BF_4 QD, the signals of this ligand essentially vanish, which suggests a strong binding affinity of EDT to the QD interface. Only after the addition of 200 equiv. of ligand, the proton signal assigned to EDT appeared

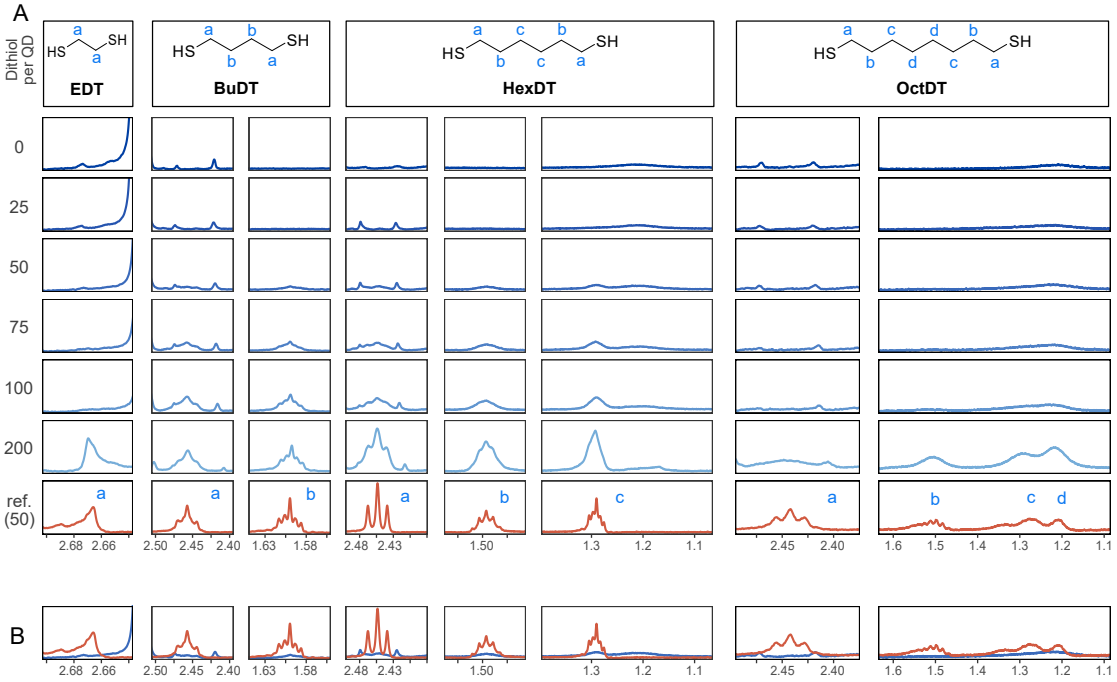

FIGURE 5.11: Interactions of dithiols with ZnSe-QDs. (A) ^{1}H-NMR spectroscopy titration experiment with aliquots of dithiol (in ACN-d3) being added to a suspension of 2 μM ZnSe-BF_4 QDs. Intensities are not to scale (in-between ligands) and were adjusted for optimal visibility. The spectra were referenced to the residual acetonitrile signal at 1.94 ppm. (B) Overlay of the reference ligand spectrum (100 μM) in the absence (orange) and presence of ZnSe (2 μM, blue) indicating of significant suppression and bradening of the signals from ligands in the presence of the QD surfaces.

in solution. This observation suggests that the QD surface can accommodate at least 100 EDT ligands.

In contrast, signals assigned to BuDT arise in solution from $\geq$ 50 equiv. per QD, suggesting a weaker affinity for the QD surface, compared to EDT (Figure 5.11). A similar observation is found for HexDT and may be rationalised with the larger size of these two ligands which occupy more space compared to the shorter EDT. It is notable that the ligand signals are significantly broadened in the presence of QDs compared to a reference spectrum in D_2O (interpretation see below).

The degree of broadening increases from BuDT to HexDT indicated by the lack of fine structure of the NMR signals, which is most notable for HexDT protons from (c) methylene groups located in the central part of the molecule. An overlay of the ligand signal at 100 μM (equivalent to 50 ligands per QD) in the absence of QDs with the same sample concentration in the presence of QDs clearly shows the reduced signal intensity due to interactions of the ligands with the QDs (Figure 5.11-B).

Proton signals assigned to an OctDT reference spectrum (in D_2O) appear at $\sim$ 100 to 200 equiv. per QD. However, the signals assigned to the central protons (c, d) at 1.2 to

1.3 ppm, appear slightly earlier, but overlap with residual solvent signal already present in the QD solution and additionally exhibit strong broadening. The cause of the overall lower intensities may be related due to the signal broadening which reduces the peak intensity and stretches out over a larger range of chemical shift. In addition, the lack of ligand signals in solution at lower loadings ($<$ 200 equiv. per QD) may be promoted by the (low) solubility of the dithiols in aqueous solution which decreases with longer dithiols.

Further in-depth analysis of the ^{1}H-NMR spectroscopy titration experiments was performed by examining the integrals of the ligand signals throughout the titration (Figure 5.12-A). EDT is only visible at 200 equiv. per QD. BuDT and HexDT vanish for $<$ 25 equiv. and follow a near linear increase from 25 to 200 equiv. per QD. OctDT exhibits generally lower signal intensities which vary depending on the proton signal. A very strong increase in intensity is notable from 100 to 200 equiv. per QD for the protons (d) at the centre of the molecule which coincides with intense broadening of the signals.

Interpretation

The results from NMR titration experiments suggest the existence of three QD-ligand interaction regimes. In the first regime, the ligands interact very strongly with the QD surface presumably due to covalent binding to the QD surface. Within this regime, the influence of the QD surface on the tumbling of the protons is so strong that the NMR signals essentially vanish, as seen for MEMI (section 5.1). All dithiols tested here showed this interaction for $\leq$ 25 equiv. per QD. In the second regime, the signals associated with the ligands are detectable by NMR but exhibit broadening. This broadening indicates that the ligands are in close vicinity of the QD surface which leads to an anisotropic chemical environment for the protons that causes the peaks to broaden - essentially caused by a superposition of many slightly shifted peaks. Because this broadening increases in the order BuDT, HexDT, OctDT with increasing dithiol hydrophobicity, the peak broadening is assigned to hydrophobic interactions. This regime may be described as a solvation sphere in which (weakly) interacting ligands accumulate due to hydrophobic interactions with each other and is detectable for BuDT/HexDT/OctDT from $>$ 25 equiv. per QD. The strong broadening in the case of OctDT likely causes the overall lower signal intensities because it prevents the correct signal integration. In addition, the intensities of different protons signals of BuDT and HexDT from $\geq$ 50 equiv. per QD are nearly identical which is an indication that all protons interact within the solvation sphere equally and no orientation is preferred. The third regime is the accumulation of ligands in the bulk solution, indicated by sharp signals similar to a reference in the absence of QDs. This regime was not detected for all dithiols within the herein tested conditions.

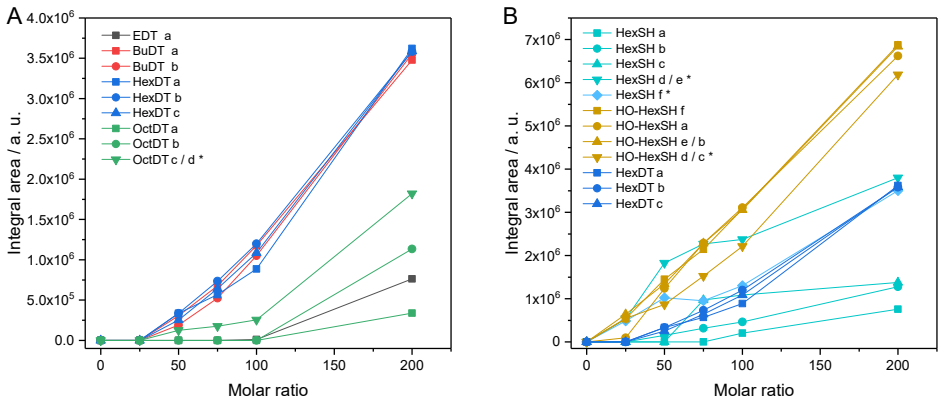

FIGURE 5.12: Interactions of dithiols with ZnSe-QDs. Integrated areas of ^{1}H signals from NMR titrations of (A) various dithiols and (B) HexDT vs. HexSH vs. HO-HexSH. The integrals are normalised for one proton in order to account for varying number of protons per signal.

Titration of dithiol analogues

In order to further elucidate the interactions of dithiols with ZnSe QDs, the titration experiments were extended to analogues comprised of only one thiol (monothiol) as well as mercaptoalcohols, which possess a hydroxy group instead of a second thiol functionality (Figure 5.13). 1-Hexanethiol (HexSH) and 1,6-mercaptohexanol (HO-HexSH) were chosen as representatives with six carbon centres and with a comparable length to HexDT. Protons assigned to HO-HexSH are detectable already from $\geq$ 25 equiv. per QD (Figure 5.13) and increase linearly until 200 equiv. per QD (Figure 5.12-B). This finding suggests a weaker affinity for the QD surface compared to HexDT which is presumably further aided by the increased hydrophilicity introduced through the hydroxy group. The lack of hydrophobic interactions is indicated by the peak shape which remains as defined/sharp and suggests accumulation of ligands in the bulk solution. In contrast, the monothiol equivalent, HexSH, features five distinct signals which appear to various degrees from $\geq$ 25 equiv. per QD (Figure 5.13 and Figure 5.12-B). Interestingly, terminal protons (a, b, c) in closer vicinity to the thiol group appear later at lower intensities compared to the protons towards the other end of the molecule (d, e, f) (signals d/e overlap with a residual solvent signal (DMF) which was subtracted, signal f overlaps with surface-coordinated ACN and therefore can not simply be subtracted (light blue)). This observation confirms that the thiol indeed prefers a conformation with the thiol pointing towards the QD surface. In addition, all signals show distinct broadening in accordance with hydrophobic interactions as seen with HexDT.

Types of interactions

Composing the data from all ^{1}H-NMR titration experiments yields to the following proposed types of interactions (Figure 5.14 and Table 5.2): Monothiol HexSH binds to the

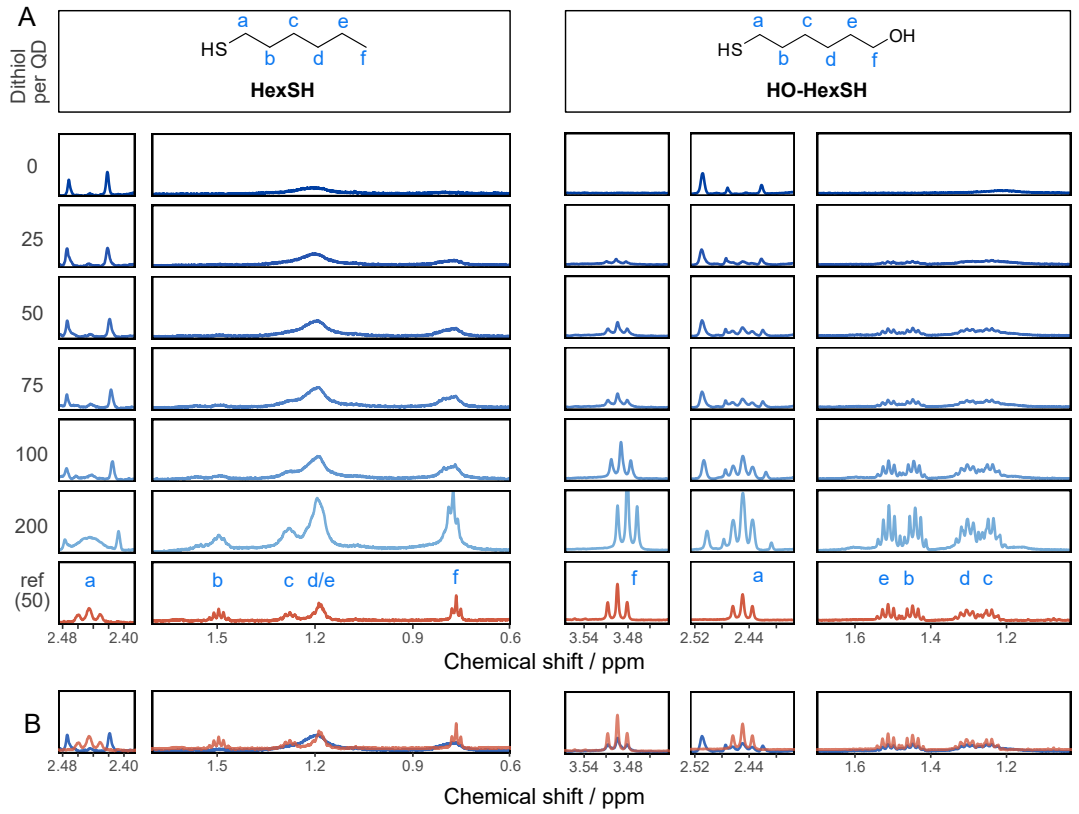

FIGURE 5.13: Interactions of dithiol-analogues (1,6-mercaptohexanol (HO-HexSH) and 1-hexanethiol (HexSH)) with ZnSe-QDs. (A) ^{1}H-NMR spectroscopy titration experiment with aliquots of ligand (in ACN-d3) being added to a D_2O suspension of 2 μM ZnSe-BF_4 QDs. Intensities are not to scale (in-between ligands) and were adjusted for optimal visibility. (B) Overlay of the reference ligand spectrum (100 μM) in the absence (orange) and presence of ZnSe (2 μM, blue).

QD surface through the thiol group whereas dithiols interact with the surface stronger which pinpoints towards interactions of both thiols with the QD surface. Dithiols (C_{4+}) and monothiol HexSH introduce a significant degree of hydrophobicity on the QD surface and exchange (slowly) with free ligands in solution. HO-HexSH interacts with the QD surface weaker compared to dithiols and the terminal hydroxy group is likely to stretch into solution and interact with surrounding water molecules thereby removing any hydrophobic effects. Any exchange with ligands in the bulk is very fast due to the sharp nature of the signals. Note, the dataset does not contain information on the binding modes of the strongly-bound ligands on the surface.

The study of dithiol-QD interactions via ITC is (unfortunately) not feasible due to the extremely large heat generated from mixing different solvents (background signal).

Experiments to study the influence of the presence of dithiols on the binding affinity of molecular co-catalyst Ni(cycP) were unsuccessful because the transition metal complex exhibited very weak NMR signals compared to the ligands which renders it impossible to resolve effects within the sensitivity limits of the NMR spectrometer.

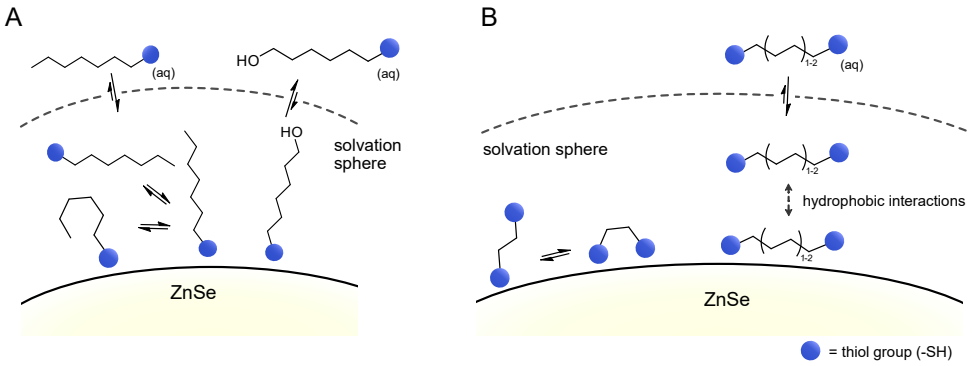

FIGURE 5.14: Proposed binding modes of dithiols with ZnSe QDs in comparison to monothiols and mercaptoalcohols

Ligand	**Class**	**No. ligands (strongly interacting)**	**Type of interactions**
EDT	Dithiol	100	covalent
BuDT	Dithiol	25-50	covalent, hydrophobic interactions
HexDT	Dithiol	25-50	covalent, hydrophobic interactions
OctDT	Dithiol	50-100	covalent, hydrophobic interactions
HexSH	Monothiol	25-50	covalent, hydrophobic interactions
HO-HexSH	Mercaptoalcohol	< 25	covalent

TABLE 5.2: Summary of interactions of various dithiols with ZnSe QDs in comparison to HexSH and mercaptohexanol.

Cross-linking

Dithiols and in particular EDT are commonly employed as crosslinking agents in colloidal chemistry because both thiols can bind to different QDs [391]. Dynamic light scattering (DLS) was employed to systematically analyse the particle size of the QDs in solution and to elucidate the influence of the dithiols. Stepwise addition of EDT to ZnSe-BF_4 indeed increases the particle size from $\sim$ 10 nm (no ligand) to 250 nm (200 equiv. per QD), whereas HexDT increases the particle size as well but levels of at 67 nm (100 equiv. per QD) (Figure 5.15-A). This observation underscores the ability of EDT to cross-link particles which seems to be more feasible for EDT than HexDT. However, the agglomeration is not unique to dithiols: HexSH increases the particle size linearly with increasing loading suggesting a build-up of a ligand layer that causes some degree of cross-linking as well (Figure 5.15-B). HO-HexSH shows this influence already at a molar ratio of 50 equiv. per QD and plateaus thereafter. In-between 0 and 25 equiv. per QD, essentially all ligands tested (except for EDT) do not cause aggregation, which is in-line with the strong-interaction regime detected during NMR experiments. This suggests that agglomeration only occurs after saturation of the ligands on the surface. It can be concluded, that all ligands promote some degree of QD agglomeration

in aqueous solution presumably due to thiol-thiol cross-linking (EDT) or interparticle ligand facilitated interactions (hydrophobic, H-bonding, etc.) with each other (HexDT, HexSH, HO-HexSH). (BuDT and OctDT have not been tested.)

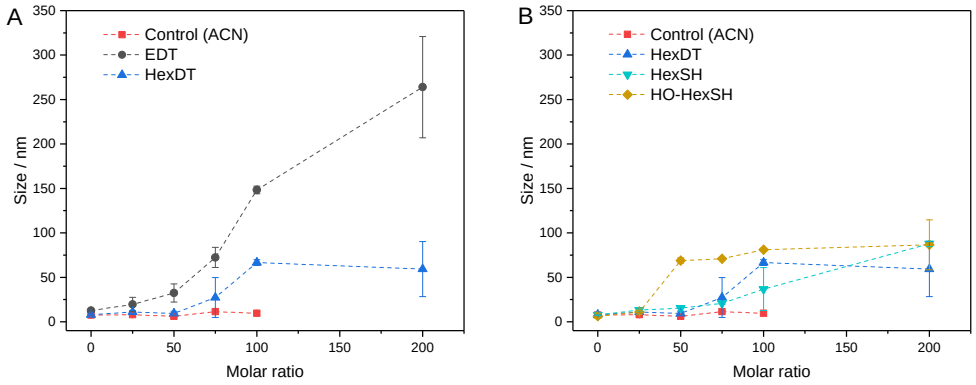

FIGURE 5.15: Dynamic light scattering (DLS) data of ZnSe-BF_4 QDs (0.5 μM) and in the presence of dithiol ligands (and analogues) in aqueous solution (neutral pH). Dithiol ligands were added stepwise from a stock solution (0.5 mM in acetonitrile). The control titration consists of only solvent (acetonitrile) added to a suspension of QDs to rule-out solvent and time effects. Shown is the number mean. The lines were added to guide the eye.

Photophysical characterisation

While the UV-vis absorbance spectra indicate that dithiols do not exhibit a strong influence on the absorption onset (Figure 5.16-A), reports in the literature have demonstrated the agglomeration of QDs in solution by photoluminescence (PL) spectroscopy. Agglomeration was indicated by a strong decrease in emission intensity due to energy transfer between neighbouring QDs [387]. PL spectroscopy (λ_{ex} = 360 nm) of ZnSe |dithiol did not show a significant reduction of the emission intensity upon addition of dithiol to an aqueous suspension of ZnSe-BF_4 QDs (Figure 5.16-B). This result implies that while the particles form larger clusters in the presence of certain ligands (as confirmed by DLS), the ligand shell does not allow for inter-particle electron transfer which would be expressed in PL emission quenching.

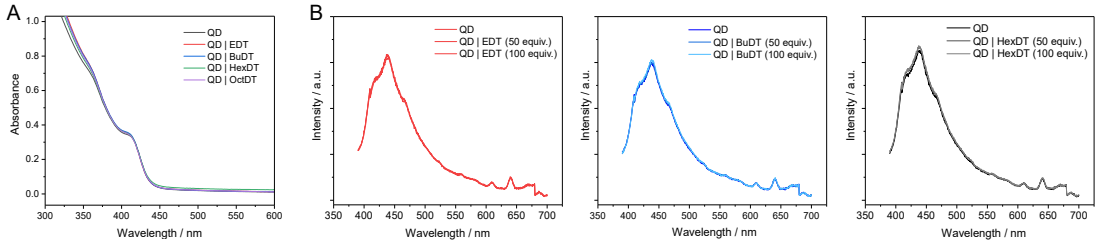

FIGURE 5.16: Photophysical characterisation of the influence of dithiols on ZnSe QDs. (A) UV-vis absorption spectroscopy. (B) Photoluminesence spectroscopy (emission intensitiy) of various ZnSe QDs in the presence and absence of various dithiols (λ_{ex} = 360 nm).

5.2.3 Influence on photocatalytic CO_2 reduction

The influence of dithiols on photocatalytic CO_2 reduction was systematically studied with two established and previously reported model systems based on ZnSe-BF_4 QDs (Section 5.1 and section 4 and reference [317]). In the first case, the bare ZnSe surface is utilised for CO_2 reduction whereas in the second case, an additional molecular co-catalyst, phosphonic-acid functionalised Ni-cyclam (Ni(cycP)) is used as the main site for CO_2 reduction in conjunction with the QDs. Ni(cycP) was chosen because it was the state-of-the-art co-catalyst (on ZnSe QDs) when this project was started and did not exhibit the long induction period associated with (the more performant) Co(tppS3N1). The photocatalytic performance was investigated under continuous flow with similar conditions as described in the previous section 5.1 (pH 6.5 in aqueous AA solution). The dithiols are unexpectedly able to activate the bare ZnSe-BF_4 for enhanced CO_2 reduction and a strong dependence on the dithiol length was found (Figure 5.17, C.16, Table C.7). After 10 h irradiation, the short dithiol (EDT, length ca. 4.3 Å, molar ratio 100 $mol_{dithiol}$ mol_{QD}) enhances CO_2 reduction from 0.15 ± 0.03 μmol CO (unfunctionalised) to 0.94 ± 0.19 μmol, whereas longer dithiols (BuDT, HexDT, OctDT, length > 6.8 Å) exhibit a much less distinct effect (CO activity in-between 0.46 to 0.14 μmol) at a similar loading. In addition, essentially all dithiols tested in this study are able to inhibit HER significantly without a strong dependence on the dithiol length leading to enhanced CO-selectivities (Figure 5.17-A).

Next, the influence of the same set of dithiols was tested in the presence of a molecular co-catalyst Ni(cycP). The dithiol loading was lowered from 100 to 50 equiv. ($mol_{dithiol}$ mol_{QD}) to allow for space for the molecular catalyst (20 equiv. $mol_{Ni(cycP)}$ mol_{QD}). The QD-co-catalyst hybrid (ZnSe | Ni(cycP)) exhibits a dependence on the employed dithiol as well (Figure 5.17, Table C.7). In contrast to the first case (absence of Ni(cycP)), the optimum dithiol length is in-between four and six carbon centres (length 6.8 Å to 9.3 Å) and a short dithiol such as EDT does not show improved CO activity (Figure 5.17-B). Under optimised conditions, ZnSe | Ni(cycP) | HexDT yields 4.05 ± 0.25 μmol CO, a four-fold enhancement from ZnSe | Ni(cycP) which produces 1.09 ± 0.18 μmol CO. Increasing the dithiol length has a near-linear effect in suppressing HER for ZnSe | Ni(cycP) (Figure 5.17).

The employed dithiols are linear, aliphatic with terminal thiol groups which renders the dithiol molecule highly flexible. In order to find out if this flexibility is a prerequisite for the enhanced CO activity found above, the flexible dithiols were benchmarked to a "rigid" analogue, benzene-1,4-dithiol (BenzDT), featuring an aromatic moiety in-between terminal thiol groups at a similar thiol-thiol length (6.4 Å) compared to BuDT (6.8 Å). While BuDT exhibits a significant impact on CO formation

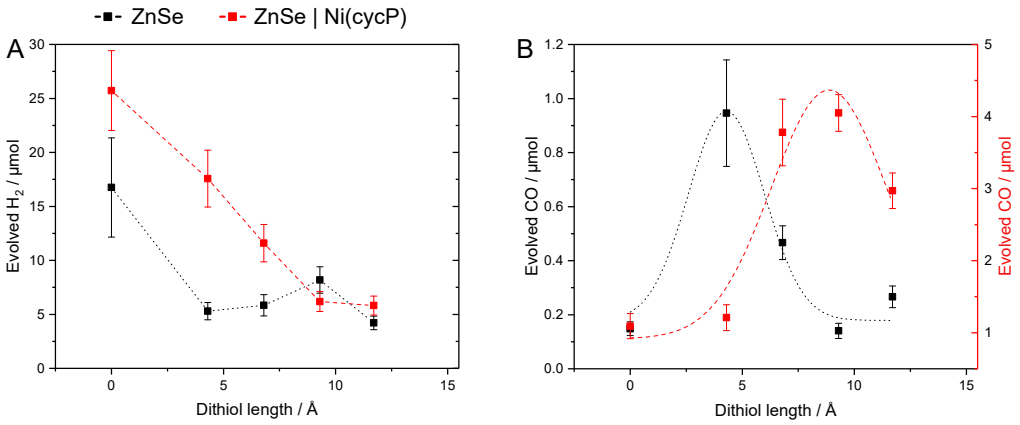

FIGURE 5.17: The influence of dithiols in photocatalytic CO_2 reduction in the presence of ZnSe-BF_4 QDs. (A) Evolved H_2 and (B) evolved CO. Conditions: ZnSe | dithiol: 50 μM dithiol, pH 6.5; ZnSe | Ni(cycP) | dithiol: 25 μM dithiol, 10 μM Ni(cycP), pH 5.5; 10 h irradiation. Conditions: AM 1.5G, $\lambda > 400$ nm, 100 mW cm^{-2}, 0.5 μ ZnSe-BF_4, 0.1 M AA/$NaHCO_3$, CO_2 constant flow (4 sccm), 25°C. Dashed lines added to guide the eye.

in both cases (presence and absence of Ni(cycP)), BenzDT suppresses HER but only marginally increases CO production proving that the flexibility of the dithiol is indeed necessary for the observed enhancement effect (Figure 5.18). Next, two benchmark cases (ZnSe | EDT and ZnSe | Ni(cycP) | HexDT) were compared to their mercaptoalcohol analogues at a comparable molecule length in order to elucidate if the terminal hydroxy group can cause an effect. ZnSe | mercaptoethanol (HO-EtSH) indeed enhances CO formation (0.56 ± 0.06 μmol) compared to unfunctionalised ZnSe-BF_4, approx. 50% compared to ZnSe | EDT (Figure 5.18-A, B). Surprisingly, HER is only marginally affected and comparable to unfunctionalised ZnSe-BF_4. A similar observation was found for ZnSe | Ni(cycP) | mercaptohexanol (HO-HexSH), which enhances CO evolution notably but does not suppress HER (Figure 5.18-C, D). Monothiols (BuSH, HexSH) were found to not affect the product selectivity at all compared to unfunctionalised ZnSe-BF_4 (Figure 5.18): Both HER and CO remained unaffected.

The influence of the marginally different pH employed for both cases (pH 6.5 for ZnSe | dithiol and pH 5.5 for ZnSe | Ni(cycP) | dithiol) was excluded as the origin of the observed changes in product selectivity. If the pH is reversed, CO production is significantly lower than at their optimised pH conditions and the trend that EDT exhibits higher activity in the absence of Ni(cycP) and HexDT in the presence of Ni(cycP) is retained (Figure C.18, Table C.9). ZnSe | dithiol at 50 equivalents ($mol_{dithiol}$ mol_{QD}^{-1}) showed increased HER and CO formation which still peaks with EDT demonstrating that the changes in product selectivity are not caused by the dithiol loading (Figure C.19). It was refrained from performing the reverse control (100 $mol_{dithiol}$ mol_{QD}^{-1} in the presence of Ni(cycP) because it was previously shown that increasing the ligand loading

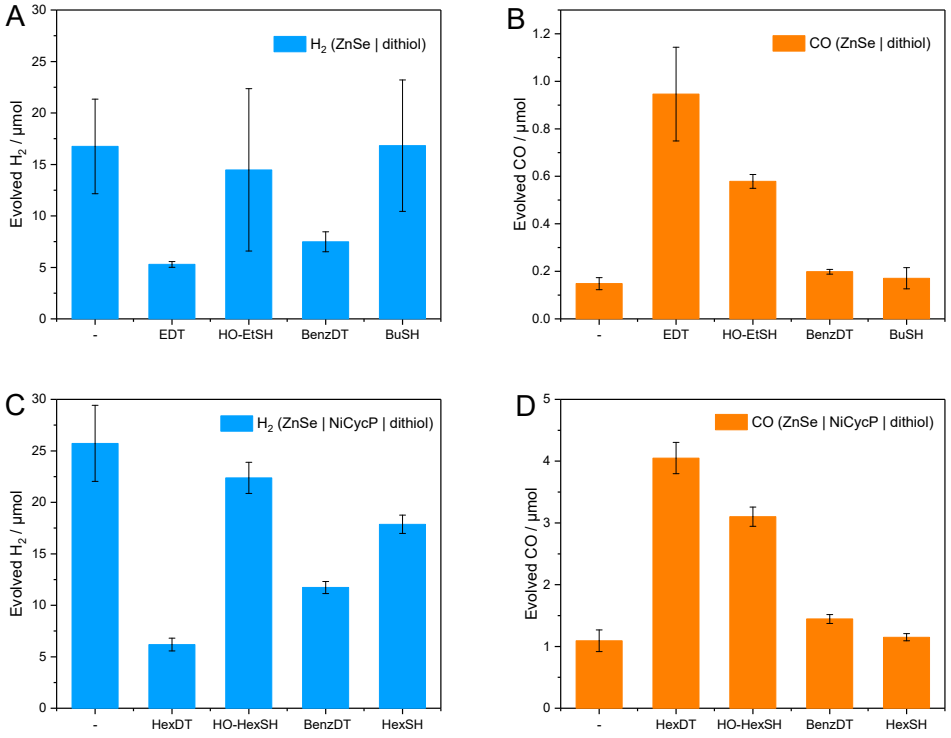

FIGURE 5.18: Benchmarking control ligands in photocatalytic CO_2 reduction. (A, B) Evolved H_2 and CO in the absence of transition-metal complex co-catalyst, ZnSe | ligand (benchmark EDT) 50 μM ligand, pH 6.5. (C, D) Evolved H_2 and CO in the presence of a co-catalyst: ZnSe | Ni(cycP) | ligand: (benchmark HexDT) 25 μM dithiol, 10 μM Ni(cycP), pH 5.5. Conditions: AM 1.5G, $\lambda > 400$ nm, 100 mW cm^{-2}, 10 h irradiation, 0.5 μM ZnSe-BF_4, 0.1 M AA/$NaHCO_3$, CO_2 constant flow (4 sccm), 25°C.

to 100 equivalents diminishes CO formation presumably due to competition for surface sites between the ligand and the transition-metal complex co-catalyst [317].

The origin of evolved CO was confirmed from CO_2 via ^{13}C-isotopic labelling for the best-performing cases (ZnSe | EDT and ZnSe | Ni(cycP) | HexDT) in order to exclude contributions from other carbon sources (Figure C.21). No products were evolved in the absence of electron donor, QDs or light indicating that all components of the photocatalyst system are required for photocatalytic activity (Table C.8). In addition, this finding highlights the observation that dithiols do not act as sacrificial electron donors for this particular photocatalyst system.

5.2.4 DFT calculations

To assess the possibility of the dithiols to promote CO_2 reduction through a set of non-covalent interactions in the secondary coordination sphere, a computational investigation based on periodic density functional theory (DFT) was conducted, similar to ZnSe | MEMI. Therefore, the ZnSe surface and equilibrium crystal shape were modelled

as described in section (5.1.6). Two cases were considered which represent the benchmark activity for the bare QD surface (ZnSe | EDT) and in the presence of co-catalyst Ni(cycP) (ZnSe | HexDT | Ni(cycP). The results presented below are preliminary and do not allow for quantitative energy profiles (ΔG) yet, but provide a qualitative assessment of the interactions.

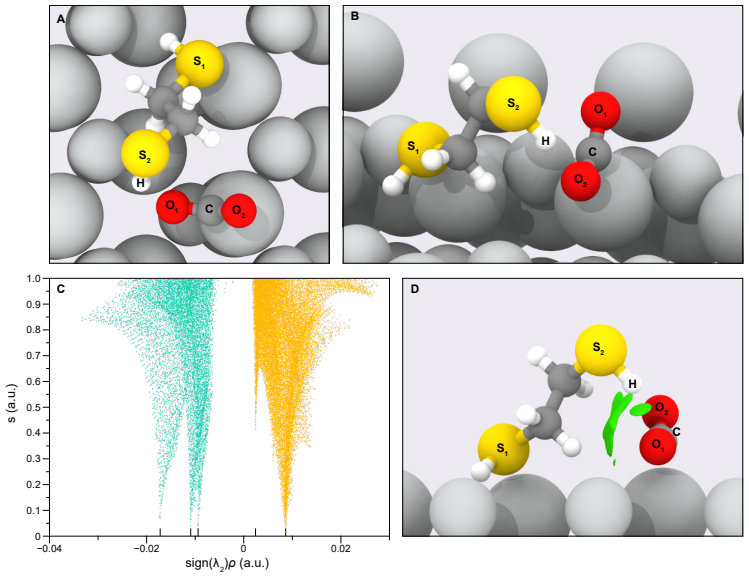

FIGURE 5.19: Interactions of EDT with a $^*CO_2^{\delta-}$ intermediate. (A) Top-down view and (B) side view. (C) Assignment of non-covalent interactions. (D) Side view representation of the NCI isosurfaces (green) responsible for the stabilisation of the $^*CO_2^{\delta-}$ intermediate. Colour code: C (dark grey), O (red), H (white), S (yellow), Zn/Se (light grey).

For ZnSe | EDT, the EDT adsorption was assessed on the bare QD surface assuming 100 strongly interacting equiv. of EDT per QD, as determined by NMR experiments. In this high-coverage regime, EDT was found to bind to Zn surface sites through one thiol (monodentate) or both thiols (bidentate) which exhibit relatively similar adsorption energies implying that they are in fast equilibrium. After assessing the possibility that the hydrogen atoms from the adsorbed thiol groups could dissociate homolytically and remain adsorbed on the surface, it was found that thiol moieties preferentially bind to the Zn sites in their protonated state (-SH). When CO_2 and a photogenerated electron were added to the simulation, CO_2 relaxed into the previously predicted surface-bound $^*CO_2^{\delta-}$ intermediate, which could be effectively stabilised by EDT in close proximity through a set of NCIs. The NCIs consists of attractive and repulsive interactions dominated by strong (attractive) H-bonding between the S-H and the oxygen of $^*CO_2^{\delta-}$ as the main contribution, explaining the net stabilisation effect, accompanied by a series of long-distance van der Waals interactions and steric effects that correspond to weak attractive and repulsive interactions, respectively. EDT has thereby the ideal length to find a conformation of one thiol binding to Zn surface while the other one can stabilise $^*CO_2^{\delta-}$ (Figure 5.19).

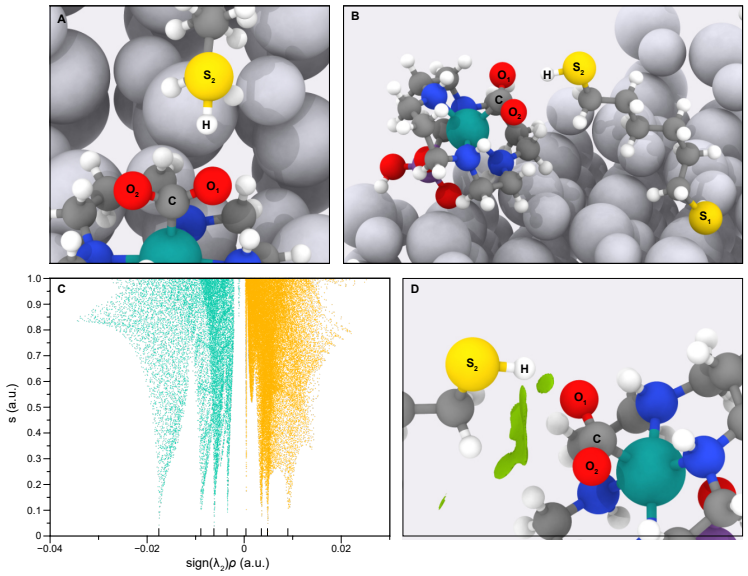

FIGURE 5.20: Interactions of HexDT with a $^{*}CO_2^{\delta-}$ intermediate in the presence of Ni(cycP). (A) Top-down view and (B) side view. (C) Assignment of non-covalent interactions. (D) Side view representation of the NCI isosurfaces (green) responsible for the stabilisation of the $^{*}CO_2^{\delta-}$ intermediate. Colour code: C (dark grey), O (red), H (white), S (yellow), Ni (teal), Zn/Se (light grey).

For ZnSe | HexDT, the co-catalyst Ni(cycP) was first adsorbed on the ZnSe surface through the singly deprotonated phosphonate (PO_3H^-), accounting for the state of the moiety in the experimental pH) on all possible adsorption sites on the ZnSe surface, resulting in Ni(cycP) being preferentially bound to a Zn site, similarly to CO_2 and EDT. HexDT was subsequently added, also being preferentially bound to the Zn sites, assuming 25 strongly interacting ligands as determined by NMR. In the presence of CO_2 and a photogenerated electron, $^{*}CO_2^{\delta-}$ bound to the Ni centre (as confirmed by [174] as the first intermediate in Ni(cyc)-promoted CO_2 reduction) could be again stabilised by means of a similar set of NCIs governed by H-bonding from the thiol group of HexDT (Figure 5.20). In the case of the co-catalyst, the longer length of the dithiol (six carbon centres) helps to find the ideal conformation for an efficient H-bonding to occur, in contrast to shorter dithiols. A longer dithiol (e.g. OctDT) is expected to have a lower likelihood to find this ideal conformation.

In summary, the results from DFT calculations pseudoquantitatively indicate that the second thiol group introduced through dithiols can help to stabilise reactive intermediates during CO_2 reduction. The short dithiol (EDT) is thereby suited to stabilise the intermediate on the bare surface, whereas the longer ones (e.g. HexDT) in the presence of molecular co-catalyst Ni(cycP). HER is believed to be affected similarly as described for MEMI (see above), in which the ligands occupy surface sites previously accessible to HER and render the remaining sites more active towards CO_2 reduction.

5.2.5 Discussion

It becomes evident from results from NMR titration experiments, DLS and DFT calculations that the effects seen during photocatalysis could stem from multiple effects as summarised during the classification of local chemical environment effects in Figure 1.14. While spectator induced electronic effects (*EM-spec*) are unlikely and the UV-vis/PL profiles remain unchanged in the presence of dithiols, effects on the QD steady-state photophysics are discarded. This leaves two conceivable effects promoted by dithiols: First, dithiols can introduce a hydrophobic environment (increasing with the dithiol length) which was demonstrated during NMR experiments and could regulate substrate access and may provide a favourable environment for the co-catalyst (Ni(cycP)) to operate (*LC-reg*). Second, the (secondary) thiol moiety can impact surface adsorbed intermediates, specifically the surface-bound $^{*}CO_2^{\delta-}$ intermediate through a set of NCIs (*NCI-im*), as demonstrated during DFT simulations. Lastly, implications on the charge transfer dynamics can not be excluded at this point and were observed for similar particle-ligand systems [104] but should generally lead to lower ET transfer rates to acceptor molecules with longer ligands, which contrasts photocatalytic experiments conducted herein.

The hydrophobic environment can explain a suppression of HER and enhanced CO_2 reduction due to a lower local water concentration and increased CO_2 concentration. However, this theory fails to explain why no enhancement effect is observed for BuDT/HexDT on the bare ZnSe surface, unless the effect is related to the lower capacity for the QDs for BuDT/HexDT. The local hydrophobic environment also falls short of rationalising why monothiols (BuSH/HexSH) can not enhance CO_2 reduction even though they provide a hydrophobic environment. The fact that they also do not suppress HER is surprising and could be related to a lower stability that hides the effect during photocatalysis after short irradiation times. On the other hand, mercaptoalcohols enhance CO_2 reduction to a lesser extent than dithiols, but still significant compared to non-functionalised QDs. The fact that they lack HER suppression as well is a further argument against hydrophobic effects as the only cause because the hydroxy group essentially suppresses hydrophobic interactions.

The particle agglomeration (DLS) is considered an unlikely contribution for the observed effects because even though all ligands tested caused some formation of aggregates (< 250 nm) (in particular EDT), this is small in comparison to the effect of AA which leads to aggregates of ~ 1600 nm. The addition of EDT to those AA-aggregates did not further enhance the agglomeration but rather led to a reduction in agglomerate size (Figure C.22).

The argumentation above pinpoints to effects beyond the hydrophobic solvation sphere to explain the observed results during photocatalysis. The DFT simulations provide a framework which can rationalise the length dependent promotion of CO_2 in the absence of a transition-metal complex co-catalyst for a short dithiol (EDT) and a longer, flexible dithiol (HexDT) in the presence of a co-catalyst (Ni(cycP)). The DFT simulations currently neglect the solvation sphere (due to computational constraints) and thereby do not account for hydrophobic and solvent effects. Therefore, it can not be precluded that the hydrophobic environment in the case of BuDT/HexDT additionally contributes to enhanced CO_2 reduction. Mercaptoalcohols are expected to be able to improve CO_2 reduction similarly as dithiols through H-bonding with the $^*CO_2^{\delta-}$ intermediate. The reason why both monothiols and mercaptoalcohols fail to suppress HER in contrast to MEMI and dithiols is questionable at this point, but could be related to the absence of a positive charge which repels protons accessing the surface (in the case of MEMI) and/or the less demanding sterics as well as a lower anchoring stability during photocatalysis to the QD surface. One prerequisite for the NCI stabilisation is that the thiol needs to bind in a (partially) monodentate way (or in fast equilibrium) with the other thiol being protonated. Attempts to detect such "free" thiols on the QD surface through commercial thiol detection kits based on fluorometric or colorimetric probes failed due to side reactions/interference with the QDs. Further spectroscopic investigations might elucidate the observed effects and may be able to confirm free thiol groups on the QD surface.

5.2.6 Conclusions

In summary, a surface modification strategy based on dithiols was presented that promotes photocatalytic CO_2 reduction in the absence and presence of an additional molecular co-catalyst (Ni(cycP)), depending on the dithiol length. The dithiol-QD interactions were studied quantitatively using ^{1}H-NMR spectroscopy which allows to determine the number of strongly interacting ligands and revealed a solvation sphere dominated by hydrophobic interactions for the longer dithiols (C_{4+}). Photocatalytic CO_2 reduction using ZnSe-BF_4 QDs in aqueous ascorbate solution showed that EDT activates the QDs for CO_2 reduction (similar to MEMI) accompanied by a reduction of HER activity on the bare QD surface. In the presence of co-catalyst Ni(cycP) as main catalytic site, a longer dithiol such as HexDT further accelerated CO_2 reduction while suppressing HER. A series of control experiments of employing monothiols and mercaptoalcohols render the hydrophobic effects unlikely as sole explanation of the observed changes during photocatalysis. DFT calculations provide a framework to rationalise the length dependent influence during photocatalysis. EDT was thereby found to have the suitable length

to stabilise a $^{*}CO_2^{\delta-}$ intermediate on the QD surface through H-bonding, whereas the length and flexibility of HexDT allows to stabilise a similar $^{*}CO_2^{\delta-}$ intermediate on the Ni(cycP) co-catalyst. The DFT calculations are preliminary and the hypothesis above needs further confirmation of a complementary technique. For example, further IR spectroscopic investigations or alternatively detection kits that are specific to thiol groups may be able to confirm the presence of free thiol groups on the QD surface.

5.2.7 Experimental section

ZnSe-BF_4 QDs were prepared as described in section 2.2. The physical characterisation techniques are described in section 2.2 as well. ^{1}H-NMR spectroscopy titration experiments and DFT calculations were performed similar to described in section 5.1.8. Photocatalytic experiments were conducted as described in section 3.4.

Chapter 6

QD-sensitised photocathodes

Parts of the contents of this section, ZnSe particles with a different morphology (nanorods), have been published in a peer-reviewed journal: M. F. Kuehnel, C. E. Creissen, C. D. Sahm, D. Wielend, A. Schlosser, K. L. Orchard and E. Reisner, Angewandte Chemie International Edition ***2019****, 58, 5059–5063. The ZnSe nanorods were optimised for* H_2 *evolution but otherwise share a lot of similarities with ZnSe QDs, as used in this section. Results presented were obtained solely by the author of this thesis, with contributions from others as outlined here: Charles E. Creissen prepared and provided* $CuCrO_2$ *electrodes and contributed to quantifying the activity of* $CuCrO_2$ *| ZnSe photoelectrodes in collaboration with the author. Sam Cobb operated the SEM when acquiring scanning electron micrographs and EDX spectra.*

6.1 Introduction & Motivation

Throughout this dissertation, ZnSe QDs exhibited photocatalytic activity in solution only in the presence of a sacrificial electron donor (SED), specifically ascorbic acid (AA). Other common electron donors failed to effectively quench photogenerated holes at the ZnSe valence band. The necessity for an SED is a major obstacle for this photocatalyst because consumption of a SED renders the whole system non-sustainable. The objective of this section is therefore to replace the SED and quench photogenerated holes on an electrode forming a *photocathode*. This approach would enable utilisation of the highly active ZnSe QDs in a photoelectrochemical (PEC) setup and facilitate coupling of the reduction half reaction at the photocathode with a photoanode with a more useful oxidation reaction (e.g. as water oxidation or waste conversion).

Electrode materials require a semiconductor of p-type nature in order to accept and transport photogenerated holes from the light absorber. In order to form an efficient photocathode, a number of key requirements need to be considered:

- Large bandgap to avoid visible light absorption which would compete with light absorption of the light absorber
- High conductivity, particularly high hole mobility to allow for fast charge transport
- Anodic VB position as it determines the photocurrent onset potential but negative enough to allow for hole quenching of the light absorber
- Optical transparency to allow light transmission

NiO has emerged as the most prominent example of a p-type semiconductor for PEC approaches [392]. It was originally used in dye-sensitised solar cells [393] and subsequently utilised in dye-sensitised photocathodes as well [394]. However, NiO photocathodes suffered from a number of drawbacks including fast charge recombination, hole traps on the surface and low hole mobility which limited the efficiency of such systems [395–397]. Recent work has shown that a $CuCrO_2$ structure surpasses the activity of NiO for H_2 evolution upon co-immobilisation of an organic dye with a Ni-bis(diphosphine) catalyst [319]. $CuCrO_2$ is a semiconductor with a wide-bandgap (E_g = 3.1 eV), that crystallises in a Delafossite-type crystal structure and shows great promise due to its high hole mobility, p-type conductivity, and facile synthesis [319].

Instead of using molecular dyes as light absorbers, QDs have also been employed in photoelectrochemical approaches and several QD-sensitised photocathodes have been developed for photoelectrochemical H_2 production [54]. The vast majority of those systems were based on NiO as electrode material. The use of QDs in photoelectrochemical CO_2 reduction is more rare but a few systems have been reported recently (see below).

The few reported systems include the decoration of NiO photocathodes with CdSe-QDs which operated in aqueous solution of $KHCO_3$ [398]. The photocathode produced H_2, CO and CH_4 and interestingly the product selectivity was dependent on the QD size because the latter varied the driving force for CO_2 reduction due to the location of the CB. Smaller QDs (diameter ca. 2.4 nm) gave the highest photocurrents with up to 100 μA cm^{-2}.

Electrostatic assemblies of polycationic polymers and CdTe quantum dots were used to modify ITO electrodes and the resulting photocathodes were active towards CO_2 reduction and produced H_2, CO, CH_3OH, and HCOOH [399, 400]. There was no isotopic labelling provided even though the presence of large amounts of polymer on the electrode

could potentially be a source of carbonaceous reaction products due to decomposition at the applied potential of -450 mV *vs.* Ag/AgCl.

Co-sensitisation of Mn-doped CdS and CdSeTe quantum dots on TiO_2/FTO support enabled CO_2 to methanol reduction in an ionic liquid electrolyte with H_2 as a by-product [401]. The ability to produce methanol was highly dependent on the presence of the IL because aqueous $KHCO_3$ electrolyte was much less active. The mechanism was proposed to proceed first via light absorption of the QDs and subsequent electron transfer into the TiO_2 CB on which CO_2 reduction proceeded with the imidazolium IL stabilising a CO_2 reduction intermediate. Under visible-light irradiation the photocathode produced methanol with a rate of 54.6 μM cm^{-2} h^{-1} and isotopic labelling confirmed CO_2 as the origin of the reaction products.

In organic media, graphene oxide encapsulated perovskite QDs on ITO support were reported for CO_2 to CO reduction with a yield up to 1.05 μM cm^{-2} h^{-1}, however, no isotopic labelling was provided [402].

$CuInS_2$ QDs were used as light absorbers and immobilised on NiO in order to drive a molecular Re catalyst for CO_2 reduction [403]. The hybrid systems achieved photocurrents up to 25 μA cm^{-2} at 0.87 V *vs.* NHE with a faradaic efficiency for CO of 32%. Photogenerated holes were efficiently transferred to the NiO VB whereas the excited electrons could be passed on to the molecular catalyst for CO_2 reduction.

Inspired by the successful combination of $CuInS_2$-QDs and NiO, the aim of this section is to expand the scope of ZnSe QDs in a stationary setup and utilise its high photocatalytic activity with the state-of-the art $CuCrO_2$ electrode material to form a QD-sensitised $CuCrO_2$ photocathode for the production of solar H_2 and CO. The proposed photocathode is illustrated in Figure 6.1.

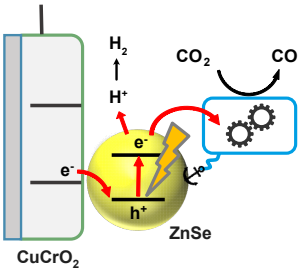

FIGURE 6.1: Illustration of the proposed outline for a $CuCrO_2$ | ZnSe-QD photocathode. QDs are used as light absorbers while photogenerated electrons are quenched from a $CuCrO_2$ electrode. The blue square represents a surface modification to promote CO_2 reduction on ZnSe QDs (e.g. molecular catalyst, capping ligands).

Performance evaluation

In order to quantify the performance of photoelectrochemical cells, several measures are of high importance.

- Linear sweep voltammetry (LSV). The applied potential between working and reference electrode is varied (typically anodic to cathodic) while the current response is measured. This voltammetric method can be coupled to light irradiation and then exhibits the photocurrent, which is the additional current between dark and light conditions at a given potential. Such a LSV under (chopped) light irradiation contains a high amount of information such as photocurrent onset, photocurrent, dark current, nature of the electrode and degradation/side reactions. Nevertheless, the current response does not necessarily originate from the (desired) catalytic reaction exclusively and therefore it is important to conduct photoelectrolysis.

- Controlled potential photoelectrolysis (CPPE). The applied potential is kept at a constant potential while (chopped) light irradiation is used to determine the steady-state photocurrent. The photoelectrolysis under constant irradiation can be extended over several hours and coupled to product detection, typically via GC for the gaseous reaction products in order to test the ability of the photoelectrode to generate actual products.

- Faradaic efficiency (FE). The faradaic efficiency (or faradaic yield) describes the efficiency in which charge transferred during catalysis to generate products. It is defined as

$$FE\,(\%) = z * F * \frac{n_{product}}{Q} * 100 \tag{6.1}$$

  where z is the number of electrons transferred in the faradaic process, F the Faraday constant (96,485 C mol^{-1}), $n_{product}$ the amount of generated products in mol, Q the total charge passed during the reaction as determined by integrating the current over time. The FE indicates how much of the transferred charges actually contribute towards the desired reaction and helps identify contributions from (parasitic) side reactions.

Note, that in the following the RHE (reversible hydrogen electrode) scale is used (for convention). It is the pH independent analogue of the NHE scale (as used in chapter 3) and takes the pH into account (for details please refer to the experimental section 6.5).

6.2 QD deposition & photocurrent optimisation

As a first step of the design of the photocathode, various deposition techniques were explored with the aim to optimise photocurrents. A photocurrent is the first sign that the photogenerated holes can be quenched by the electrode.

One objective was to leverage the potential and versatility of capping ligands as a tool to enhance the interaction of the QD films with the $CuCrO_2$ surface. Thiols are known to bind well to the QD surface and certain functional groups (carboxyl, phosphonic acid) have a high affinity for metal oxides such as $CuCrO_2$ [13]. The ideas for immobilising QD films on $CuCrO_2$ are outlined in Figure 6.2A. Mercaptoethylphosphonic acid (MEPA) and mercaptopropionic acid (MPA) were chosen due to their phosphonic acid and carboxylic acid anchoring group, respectively, which are known to have a high affinity for the electrode surface. Mercapto-ethyl-trimethylammonium (META) was chosen due to its positive charge which might enable electrostatic interactions with the partially negatively charged $CuCrO_2$ surface. The QD-films were assembled using either drop-casting or spincoating techniques with slightly varying procedures as summarised in Table 6.1.

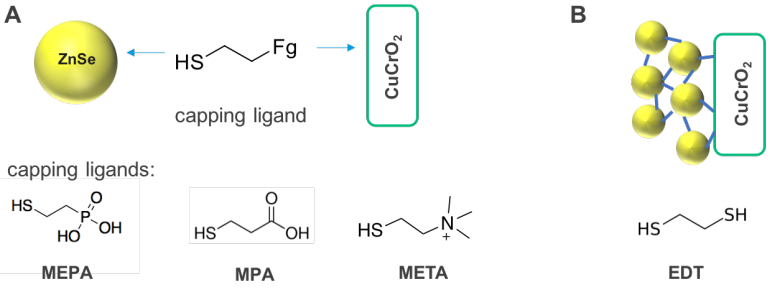

FIGURE 6.2: QD immobilisation strategies using capping ligands. (A) Use of capping ligands to link QDs to the $CuCrO_2$ surface. (B) Use of ethane dithiol (EDT) as a cross-linker.

Unfortunately, none of these immobilisation strategies based on capping ligands led to improved photocurrents compared to simply dropcasting ligand-free ZnSe-BF_4 QDs, determined by linear sweep voltammetry (LSV) under chopped light illumination (Table 6.1).

Simply dropcasting small amounts of ZnSe-BF_4 in a volatile solvent (acetonitrile) followed by evaporation yielded photocurrents of ca. 14 μA cm^{-2} at 0 V *vs.* RHE. This photocurrent is on the same magnitude as the dye/catalyst co-sensitised $CuCrO_2$ system [319]. A typical LSV under chopped light illumination for the dropcasting method compared to a blank $CuCrO_2$ is shown in Figure 6.3. The enhanced photocurrents compared to the bare $CuCrO_2$ electrode with an onset potential of approximately +0.6 V *vs.* RHE indicate the capability of photoexited ZnSe QDs ($E_{VB,\ ZnSe}$=+1.6 V *vs.* RHE) to inject holes into the valence band of $CuCrO_2$ ($E_{VB,\ CuCrO_2}$ = +1.0 V *vs.* RHE) [319].

The photocathode was further analysed via scanning electron microscopy (SEM) and energy-dispersive X-ray spectroscopy (EDX). A cross-sectional micrograph of the electrode reveals a $CuCrO_2$ thickness of approximately 400 nm with a thin coating of ZnSe particles (Figure 6.4). EDX spectra confirmed an even distribution of the ZnSe particles over the entire electrode surface from a top-down view and a cross-sectional mapping

Linker/Capping	**Deposition method**	**j @ 0 V vs RHE / μA cm^{-2}**
ZnSe-BF_4 (no capping ligand)	Dropcast 4 μL	10.2
	Dropcast 8 μL	13.5
	Dropcast 12 μL	2.56
	Spin Coating (3 μL, x3)	7.92
ZnSe-BF_4 | MEPA	Dropcast (8 μL) pre-capped QDs*	4.76
	Capping on Electrode**	4.04
	Capping then heated under Ar	3.20
ZnSe-BF_4 | MPA	Soaking in pre-capped QD solution***	1.61
	Capping on Electrode	5.60
ZnSe-BF_4 | EDT (Cross Link)	Soak (pre-treat in EDT) and dropcast ZnSe-BF_4	3.57
	Soak (pre-treat in EDT) and dropcast ZnSe-St	0.80
	Pre-treat and spin coat ZnSe-BF_4 (5 μL, x3)	6.18
ZnSe-BF_4 | META	Spin Coating pre-capped QDs (5 μL, x3)	4.94
	Soaking 4 h of pre-capped QDs	8.84
	Soaking overnight pre-capped QDs	8.22

TABLE 6.1: Overview of photocurrents of a $CuCrO_2$ | ZnSe photocathode using different immobilisation strategies. *'pre-capped' refers to incubating QDs with capping ligand solution before deposition on the electrode; **'Capping on electrode' refers to depositing the QD film on the electrode first after which capping ligand solution is added; ***'Soaking' refers to soaking the electrode in a dilute solution of QDs and/or capping ligand.

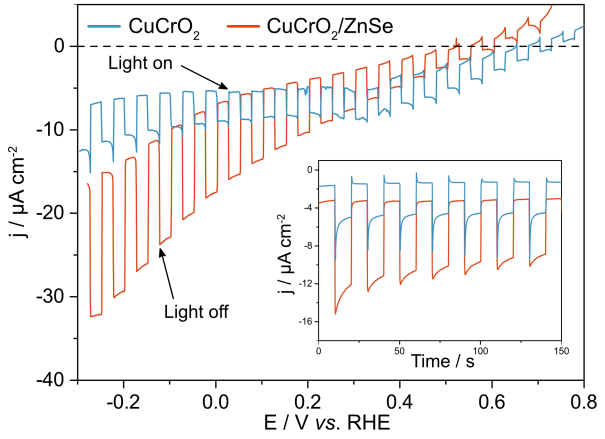

FIGURE 6.3: Linear sweep voltammetry (LSV) and chronoamperometry (inset) at E_{app} = 0 V *vs.* RHE) of the (flat) $CuCrO_2$ | ZnSe photocathode under chopped light illumination. Conditions: Aq. 0.1 M Na_2SO_4, pH 5.5, 100 mW cm^{-2}, AM 1.5G, $\lambda > 400$ nm, scan rate 5 mVs^{-1}, active area 1.0 cm^2.

confirmed the $CuCrO_2$ layer on top of ITO glass with a dispersed coating of ZnSe (Figure D.2).

Inspired by reference [391], where the authors used ethane dithiol (EDT) as a cross-linking agent in order to create better conducting QD films on ITO electrodes, QD films were treated with EDT, but no improved photocurrents were detected (Figure 6.2B and Table 6.1).

Encouraged by a study from Eisenberg *et al.* [404], a layer-by-layer approach was tested, in which smaller QDs (larger E_g) are immobilised first followed by larger QDs (smaller E_g) thus creating a gradient for photogenerated electrons to be extracted from the conduction band - a so called 'rainbow' photocathode. A batch of QDs was freshly synthesised in four different sizes ranging from 400 to 420 nm in their first excitonic absorption onset. Compared to a similar amount of a single-sized dropcasted QDs, the layer-by-layer approach did not yield improved photocurrents (Appendix D.1).

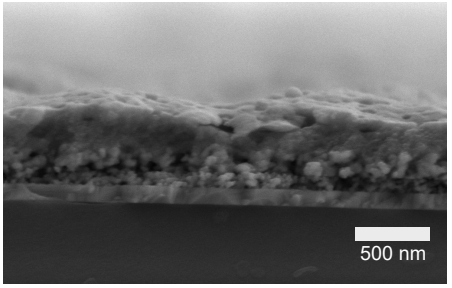

FIGURE 6.4: SEM image (cross-sectional) of the as-assembled $CuCrO_2$ | ZnSe-BF_4 photocathode.

In conclusion, for the following experiments, the simple but most effective deposition technique, dropcasting ZnSe-BF_4 QDs on the electrode was used to prepare QD films on the $CuCrO_2$ electrode. More sophisticated deposition and anchoring strategies utilising the capping ligand toolbox were unsuccessful - presumably because the capping ligands interfere with charge transfer processes. While enhanced photocurrents are no guarantee for high photoelectrochemical activity, this result confirms the ability of $CuCrO_2$ to act as a hole quencher and renders further experiments for product generation promising.

6.3 Controlled potential photoelectrolysis

Having optimised the photocurrents and the QD deposition technique, the next step consists of quantifying reaction products via controlled potential photoelectrolysis (CPPE) with the modified $CuCrO_2$ | ZnSe electrodes which was conducted under illumination (front side at 100 mW cm^{-2}, AM 1.5G, $\lambda > 400$ nm) at an applied potential of $E_{app} = 0$

V *vs.* RHE. In any case, QDs were immobilised on the $CuCrO_2$ electrode by dropcasting as described in the previous section.

6.3.1 H_2 evolution

The first attempts were targeted towards HER under an atmosphere of N_2 with the goal to utilise the exceptional high activity of the QDs for proton reduction before the more challenging CO_2 reduction is attempted.

CPPE with $CuCrO_2$ | ZnSe electrodes maintained at E_{app}= 0 V vs. RHE produced 38 ± 9 nmol H_2 with a FE of 4.3 ± 1.3 % after 4 h of irradiation (Table D.1). Illumination was started 100 s after the electrolysis was commenced and led to a steady photocurrent over the course of 4 h (Figure 6.5). A control sample of bare $CuCrO_2$ evolved significantly less H_2 (5 ± 2 nmol) (appendix D.1). Overall, the results confirmed that the highly reducing ZnSe CB-electrons are extracted to reduce aqueous protons and subsequently evolve H_2. Although the performance is modest at best, it demonstrates that the ZnSe QDs photocatalyst can operate in a photoelectrochemical cell in the absence of a sacrificial electron donor. The low efficiency is likely due to a non-ideal interface of the QD-electrode assembly which is significantly impacted by charge-recombination that ultimately limits the number of photogenerated electrons available for catalysis. Additionally, the position of the $CuCrO_2$ valence band might not be suitable (i.e. not reductive) enough to enable efficient hole quenching. Furthermore, several other factors may contribute to the overall low faradaic efficiency: First, it was previously reported that $CuCrO_2$ electrodes exhibit a small cathodic dark current which was ascribed to Cu^{2+} to Cu^{+} reduction with concomitant O_2 deintercalation [319, 405]. Second, detection of gaseous reaction products at the quantities herein described imposes a significant challenge for accurate quantification due to the solubility of the gases in the electrolyte solution. This was examined for H_2-evolving PEC cells in which ca. 60% of the H_2 remained in solution after 3 h of CPPE which leads to an underestimation of the total yield/efficiency [406]. This problem was partially addressed through rapid stirring followed by an equilibrium period to let the gases diffuse into the headspace, before the GC quantification was commenced, but nevertheless will contribute to an underestimation of the total FE.

6.3.2 CO_2 reduction

In order to extend the scope of the $CuCrO_2$ | ZnSe electrode towards CO_2 reduction, molecular CO_2 reduction co-catalysts were employed. The co-catalysts were typically introduced by adding dilute catalyst solution on top of the $CuCrO_2$ | ZnSe electrode and

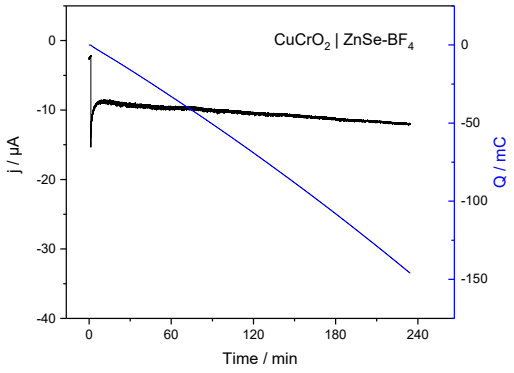

FIGURE 6.5: CPPE of a $CuCrO_2$ | $ZnSe\text{-}BF_4$ photocathode. Conditions: 0.1 M Na_2SO_4, pH 5.5, $E_{app} = 0$ V *vs.* RHE, illumination of 100 mW cm^{-2}, AM 1.5G, $\lambda > 400$ nm, 1 cm^2 active area.

letting the system assemble for 3 h (referred to as 'soak'). Alternatively, the co-catalyst was introduced by pre-loading the co-catalyst on the QDs, before dropcasting of the latter (referred to as 'pre-assemble'). First, the phosphonated Ni-cyclam co-catalyst was used (entry 1-2), followed by the newly developed $ZnSe\text{-}BF_4$|MEMI that was introduced in the previous chapter (entry 3). All the systems produced none (or negligible amounts) of CO over the course of 1-4 h but significantly more if the photoelectrolysis was extended overnight. However, control experiments under N_2 atmosphere (entry 4) and bare $CuCrO_2$ under CO_2 (entry 5) revealed CO production as well, suggesting that some of the measured CO (entries 1-3) did not necessarily originate from reduced CO_2 and/or that bare $CuCrO_2$ may reduce traces of CO_2. These attempts were declared unsuccessful and future experiments were only considered promising if the product generation significantly exceeds the one of the control experiments. The inability of the $CuCrO_2$ | ZnSe | co-catalyst assemblies to reduce CO_2 is presumably a combination of a low CO selectivity due to the medium anchoring of the co-catalysts tested herein to the QDs. This is particularly troublesome in a PEC configuration because after the electrode assembly, no co-catalyst remains in solution that can potentially replenish desorbed/decomposed co-catalyst on the surface. Stronger anchoring co-catalyst such as the sulfonated Co porphyrins (Chapter 4 might overcome this limitation in future experiments.

Inverse-Opal $CuCrO_2$ electrodes

A recent study developed in this laboratory improved on the novel $CuCrO_2$ electrode material by forming an *inverse-opal (IO)* structure that features an ultra-high surface area (Figure D.3) [407]. The nanostructured electrode should - theoretically - enable immobilisation of a much larger number of QDs due to the large pore size and specific surface area and therefore lead to higher photocurrents and improved charge transfer.

Entry	Photocathode	Cat-deposition	Conditions	n (H_2) [nmol]			n (CO) [nmol]		
				1-2 h	3-4 h	o/n	1-2 h	3-4 h	o/n
1	$CuCrO_2$|ZnSe-BF_4|Ni(cycP)	Soak	CO_2	5	n/a	50	-	n/a	6
2	$CuCrO_2$|ZnSe-BF_4|Ni(cycP)	Pre-assemble	CO_2	11	16	37	-	-	9
3	$CuCrO_2$|ZnSe-BF_4|MEMI	Pre-assemble	CO_2	-	5	25	-	-	3
4	$CuCrO_2$|ZnSe-BF_4|Ni(cycP)	Pre-assemble	N_2	-	n/a	20	-	n/a	2
5	$CuCrO_2$	-	CO_2	-	-	11	-	-	9

TABLE 6.2: CPPE results of (flat) $CuCrO_2$ | ZnSe photocathodes. o/n: overnight; n/a: data point not available. Conditions: 0.1M KCl, 50 mM $KHCO_3$; CO_2 purged, pH 6.7, illumination of 100 mW cm^{-2}, AM 1.5G, $\lambda > 400$ nm, 1 cm^2 active area.

The new electrode material was screened in combination with ZnSe QDs in an otherwise similar fashion as the flat electrodes in the previous section.

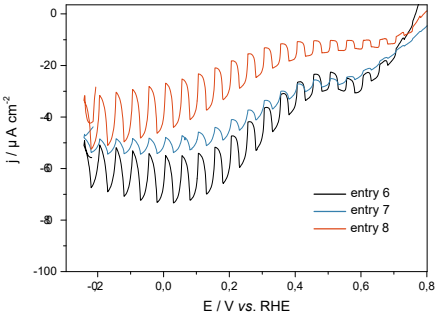

FIGURE 6.6: Linear sweep voltammetry (LSV) of $^{IO}CuCrO_2$|ZnSe photocathodes under chopped light illumination.

LSVs under chopped light illumination of the $^{IO}CuCrO_2$ | ZnSe electrodes exhibited promising photocurrents of up to 20 μA cm^{-1} (Figure 6.6). Generally, the photocurrents resemble a 'spike'-like shape which is attributed to charge accumulation at the semiconductor/electrolyte solution interface. These transient photocurrent spikes were observed in any case for the IO-electrodes and reported previously [407]. Notably, dark currents are much larger compared to the flat electrodes and there is a general drop in current at ca. 0.1 V vs. RHE which is attributed to internal Cu^I/Cu^{II} transition [407] in the $CuCrO_2$ electrode. The feature diminished in consecutive scans. The dark currents are likely more distinct on the IO-structure than on the flat electrode due to the larger surface area which leads to a higher quantity of exposed Cu sites with the electrolyte and renders the O_2 intercalation more probable.

CPPE experiments were conducted at similar conditions as previously stated (Table 6.3). First, MPA-recapped ZnSe-BF_4 QDs were dropcast onto $^{IO}CuCrO_2$ and the co-catalyst Ni(cycP) was introduced by soaking the electrode in a co-catalyst stock solution (entry 6). MPA was chosen because it was predicted that its carboxylic acid group would interact favourably with the $^{IO}CuCrO_2$ surface. An approach in the absence

Entry	Photocathode	Cat-deposition	Conditions	n (H_2) [nmol]			n (CO) [nmol]		
				1-2 h	3-4 h	o/n	1-2 h	3-4 h	o/n
6	$^{IO}CuCrO_2$|ZnSe-BF_4-MPA|Ni(cycP)	Soak	CO_2	8	8	14	-	-	3
7	$^{IO}CuCrO_2$|ZnSe-BF_4|Ni(cycP)	Preassemble	CO_2	-	n/a	5	-	n/a	3
8	$^{IO}CuCrO_2$|MPA|ZnSe-BF_4	* -	N_2	-	n/a	n/a	-	n/a	n/a

TABLE 6.3: Screening of CPPE results of (*IO*)-$CuCrO_2$|ZnSe photocathodes. Conditions: 0.1M KCl, 50mM $KHCO_3$ for CO_2 purged (pH 6.7) or 0.1M Na_2SO_4 for N_2 purged (pH 5.5); E_{app} = 0 V vs. RHE, illumination of 100 mW cm^{-2}, AM 1.5G, $\lambda > 400$ nm, 0.5 cm^2 active area. *MPA-SAM was assembled through immersion of the electrode in 2 mM MPA solution in EtOH. The electrode was rinsed, dried followed by QD deposition.

of MPA with Ni(cycP)-preassembled ZnSe-BF_4 was tested in entry 7. Both runs did not evolve any CO within 4 h, even though the photocurrents of entry 8 looked very promising. Overnight detected traces of CO are likely originating from carbonaceous residues on the delafossite electrode. Because there was barely any H_2 produced, it is doubtful at this point that the overall scheme and its charge transfer processes are feasible on the IO-structure. Another attempt therefore was purely focused on evolving H_2 (N_2 atmosphere, no co-catalyst) (entry 8). A MPA-SAM was pre-assembled on the $^{IO}CuCrO_2$ before deposition of ZnSe-BF_4 QDs through soaking of the electrode in MPA solution for 4 h. Enhanced photocurrents were recorded, however, no products could be detected.

In summary, the nanostructured IO-electrodes do not seem to be compatible with the ZnSe QDs. Surprisingly, the improved photocurrents do not translate into reaction products which implies a different pathway for the photogenerated charges such as photodegradation or internal pathways. The strong hydrophobicity of the IO-electrodes, favourable for the immobilisation of organic dyes, might be another problem for the operation of the photocathode in aqueous media as it impacts the interface of the highly charged, hydrophilic QDs and limit diffusion of the electrolyte solution into the pores. In addition, the IO-electrodes might be too thick, limiting charge transfer processes.

Further attempts to render the $CuCrO_2$ | ZnSe photocathode active for CO_2 reduction through a more 'mild' QD-deposition methodology by soaking in dilute solutions, were equally unsuccessful (details see Appendix D.1).

6.4 Conclusions

In summary, ZnSe QDs were immobilised on a p-type $CuCrO_2$ semiconductor in order to develop a QD-sensitised photocathode. The deposition methodology was optimised first by optimising photocurrents and dropcasting was found to be the most feasible

deposition method. Capping ligands did not enhance the interaction of the QDs with the electrode surface. CPPE of a $CuCrO_2$ | ZnSe photocathode was able to produce H_2 (38 ± 9 nmol H_2 after 4 h of CPPE) but attempts to reduce CO_2 remained unsuccessful. This result represents a proof-of-concept that - in principle - the sacrificial electron donor is replaceable and the ZnSe QDs can be operated in a photoelectrochemical setup. The limiting factor is likely the non-ideal interface between the $CuCrO_2$ electrode and ZnSe QDs and/or a not sufficiently reductive position of the $CuCrO_2$ valence band, which constraints fast hole quenching kinetics. Attempts to improve this interface through nano-structuring of the electrode (*inverse-opal* $CuCrO_2$) were unsuccessful. Improvements might be enabled through engineering the QD-delafossite interface by alternative assembly methods, hydrophobic linkers, and stronger anchors to enable photoelectrochemical CO_2 reduction. In particular, the dithiols introduced in section 5.2 could provide the necessary hydrophobic surface environment for a successful immobilisation on the IO-electrodes. Alternatively, varying the $CuCrO_2$ valence band (e.g. doping) might provide more driving force for the hole quenching ability of $CuCrO_2$. The photoelectrochemical activity towards CO_2 reduction might be enabled by employing the stronger anchoring molecular catalysts as presented in chapter 3.

6.5 Experimental section

The experimental procedure to prepare the flat and inverse-opal $CuCrO_2$ electrodes as well as the photoelectrochemical measurements is similar to as reported by C. E. Creissen in [319, 407].

Preparation of $^{flat}CuCrO_2$ | ZnSe electrodes.
Flat $CuCrO_2$ electrodes were prepared as reported previously [319]: $CuCrO_2$ electrodes were prepared directly on ITO-coated glass slides. First, the ITO-coated glass slides were cleaned by sonication in isopropanol, ethanol, and acetone (15 min each) and dried at 100 °C. A solution of Cu(acetate)$_2$ x H_2O (0.2 M), $Cr(NO_3)_3$ x 9 H_2O (0.2 M), and triethanolamine (0.2 M), was prepared in ethanol (absolute) and stirred for 15 h. The solution was spin-coated onto the cleaned ITO slides (*Laurell WS-650MZ* spin coater, 1500 rpm, 15 s, 3000 rpm s^{-1} acceleration, 0.4 mL volume) followed by annealing in a chamber furnace (*Carbolite Gero*) to 400 °C with a ramp rate of 10 °C min^{-1} for 45 min. The spin coating and annealing steps were repeated for a total of three layers. A tube furnace (*Carbolite Gero*, fitted with a quartz tube, end seals, and insulation plugs) was used to anneal samples to 600 °C with a 5 °C min^{-1} ramp rate for 45 min under Ar flow at 150 sccm. ZnSe QDs were immobilised by drop-casting 8 μL cm^{-2} of a stock solution (1.18 mg/mL, acetonitrile) followed by drying under N_2 atmosphere. If a co-catalyst

was used, a co-catalyst stock solution (aqueous, 5 mM) was used to cover the electrode surface after which the container was sealed and left to assemble for 3 h. The co-catalyst stock solution was removed afterwards and the electrode rinsed with MQ-water. The as-prepared $CuCrO_2$ | ZnSe photoelectrodes were directly used after preparation.

Preparation of $^{IO}CuCrO_2$ | ZnSe electrodes.
$^{IO}CuCrO_2$ electrodes were prepared as reported previously [407]: $Cu(NO_3)_2 \cdot 3\ H_2O$ (1.51 g, 6.25 mmol) and $Cr(NO_3)_3 \cdot 9\ H_2O$ (2.50 g, 6.25 mmol) were added to a vial and stirred in H_2O (70 mL, Mili-Q). NaOH (5.0 g) was added which let to a final solution pH of 13. The resulting solution was stirred for 2h (room temperature) after which 12 mL were removed by decanting into a PTFE-lined autoclave (total volume 23 mL). The autoclave was heated (240 °C, 60 h) before the resulting $CuCrO_2$ nanoparticles were removed, washed with HCl (0.1 M, 15 mL) and centrifuged (8000 rpm, 5 min). Further washing was conducted with EtOH (15 mL) followed by centrifugation. The washing steps were repeated three times in total, after which the particles were dried in a high vacuum. Finally, the dried nanoparticles were ground with a pestle/mortar and stored in vacuo before use.

Polystyrene beads (750 nm, 2.6% w/v suspension in H_2O, 0.5 mL) were centrifuged, the supernatant removed and further washed with MeOH, after which the beads were centrifuged again to yield a pellet. $CuCrO_2$ nanoparticles (as prepared above) (dispersion of 7.5 wt %, in MeOH/H_2O 1:4, 140 μL) were added to the polystyrene pellet and sonicated for 5 min at 10 °C. The solution was deposited on ITO-coated glass (0.5 cm^2, protected with parafilm) via drop-casting (4 μL) and let to dry in air for 3 h after which the parafilm was removed. The polystyrene template was removed by dissolution in toluene overnight before being rinsed with acetone and water and dried in vacuo. The electrodes were annealed under an atmosphere of Ar in a tube furnace (500 °C, 5 °C min^{-1} ramp rate, 1 h, 150 sccm flow rate) equipped with a quartz tube, end seals and insulation plugs. ZnSe QDs were immobilised by drop-casting 8 μL cm^{-2} of a stock solution (1.18 mg/mL, acetonitrile) followed by drying under N_2 atmosphere. If a co-catalyst was used, a co-catalyst stock solution (aqueous, 5 mM) was used to cover the electrode surface after which the container was sealed and left to assemble for 3 h. The co-catalyst stock solution was removed afterwards and the electrode rinsed with MQ-water. The as-prepared $CuCrO_2$ | ZnSe photoelectrodes were directly used after preparation.

Preparation of mercaptoethyl-phosphonic acid (MEPA).
Potassium thioacetate (512 mg, 4.49 mmol) was loaded into a 50 mL Schlenk flask and dried in *vacuo*. Dry acetonitrile (5-10 mL) was added and the resulting suspension was stirred for 10 min, after which bromoethylphosphonate diethylester (1.0 g, 4.08 mmol) was added. The resulting suspension was stirred overnight. The solvent was evaporated

under reduced pressure to yield mercaptoethyl-phosphonate ethyl ester.
^{1}H NMR (400 MHz, MeOD) δ (ppm) = 4.13 (m, 4H, CH_2), 3.04 (m, 2H, CH_2), 2.33 (s, 3H, CH_3), 2.10 (m, 2H, CH_2), 1.35 (t, 6H, CH_3).

Mercaptoethyl-phosphonate ethyl ester (4.08 mmol) was added to TMSBr (38 mmol, in dry DCM) and stirred overnight. The solvent was removed in *vacuo*, the residue re-dissolved in methanol and concentrated to dryness. This was repeated twice. The product was collected as yellow/orange slurry.
^{1}H NMR (400 MHz, MeOD) δ (ppm) = 3.35 (s, OH), 2.73 (m, 2H, CH_2), 2.03 (m, 2H, CH_2), 1.61 (s, SH).
MS: (m/z) calcd. for $C_2H_8O_3SP^+$: 142.9932; found 142.9928.

Synthesis of 2-mercaptoethyl-N,N,N-trimethylammonium chloride (META).
The synthesis was performed according to a modified literature procedure [408] as follows: 2-(acetothioethyl)-trimethylammonium chloride (0.73 g) was loaded into a 25 mL Schlenk-flask and hydrochloric acid (HCl,6 M, 10 mL) was added. The reaction mixture was heated to 90 °C and stirred for 1 h under an inert gas atmosphere. The solvent and volatile by-products were removed in *vacuo* to yield a white-yellow solid. The product was stored and handled under strict inert gas atmosphere only to prevent dithiol formation. No further purification was necessary.
^{1}H NMR (D_2O, 400 MHz): δ (ppm) = 2.95 (2H, m, CH_2), 3.15 (9H, s, NMe_3), 3.55 (2H, m, CH_2)
^{13}C NMR (Methanol-d4, 101 MHz) δ = 69.56, 53.64, 17.75
MS: (m/z) calcd. for $C_5H_{14}NS^+$: 120.08, found 120.08.

Photoelectrochemical Measurements.
The photoelectrochemical characterisation was performed in a one compartment three necked cell equipped with a flat borosilicate window, using an Ivium CompactStat potentiostat. A three-electrode setup was used with a $CuCrO_2$-based working electrode (1 cm^2 active area for flat electrodes, 0.5 cm^2 for inverse-opal electrodes), Ag/AgCl/KCl (sat) reference and Pt-counter electrode. The electrolyte solution consisted of aqueous Na_2SO_4 (0.1 M, pH 5.5) and was purged with N_2 for 30 minutes prior to measurements. For CO_2 reduction experiments, aqueous KCl (0.1 M) and 50 mM $KHCO_3$ was used as electrolyte solution and the cell was purged with CO_2 for 15 min, which lowered the pH to ca. 6.7. The photoelectrodes were illuminated from the front using a calibrated solar light simulator (*Newport Oriel*, 150 W, 100 mW cm^{-2}, AM 1.5G) with an IR water filter and a UQG Optics UV-Filter ($\lambda > 400$ nm). Controlled potential photoelectrolysis (CPPE) measurements were conducted at 0.0 V *vs.* RHE in an airtight two-compartment electrochemical cell equipped with Nafion membrane divider and a flat quartz window. The volume of the working compartment was 14.5 mL with a gas headspace of 5 mL

and the counter compartment contained 4 mL solution and a 3.5 mL headspace. Both compartments were purged with 2 % CH_4 in N_2 or 2 % CH_4 in CO_2 for 30 minutes prior to photo-electrolysis after which the amount of H_2 and CO was determined using gas chromatography (as described in section 4.4). The partial pressure of H_2 and CO was calculated using Henry's law to account for dissolved gas in the solution and this was added to the amount of hydrogen and CO, respectively.

Potentials were converted from the Ag/AgCl scale with the following formula:
$E_{\mathrm{RHE}} = E_{\mathrm{Ag/AgCl}} + 0.2\ V + 0.059\ V\ x\ pH.$

Scanning electron microscopy (SEM).
SEM images were recorded using a Tescan MIRA3 FEG-SEM operated by Sam Cobb. Energy-dispersive X-ray (EDX) spectra were recorded with an Oxford Instruments Aztec Energy X-maxN 80 EDX system (20 kV, 15 mm working distance).

Chapter 7

Conclusions & Outlook

This dissertation explored ZnSe QDs as a versatile platform for light-driven CO_2 reduction alongside H_2 evolution. The platform is based on benign and abundant materials which operate in fully aqueous solution. The insights are four-fold: First, a continuous-flow setup for photocatalysis was developed which combines a high sensitivity with automated in-line gas chromatography of multiple samples in parallel. Second, the QDs were interfaced with a range of molecular catalysts (QD-hybrids) including cyclam, porphyrin and quarterpyridine catalysts. Third, a novel surface modification strategy through ligand capping was introduced that enabled ZnSe-promoted CO_2 reduction even in the absence of a molecular co-catalyst based on transition-metal complexes. Lastly, a proof-of-concept demonstrated that the ZnSe QDs can be employed in a photoelectrochemical setup for H_2 evolution in combination with a $CuCrO_2$ electrode.

In Chapter 3, a continuous-flow setup for photocatalysis was successfully developed and optimised towards the detection of syngas. A high sensitivity ($1.26 \cdot 10^{-12}$ mol s^{-1}) was achieved by optimising the interplay of flow rate, sample volume and loop size in conjunction with a highly sensitive barrier discharge ionisation (BID) detector of the GC. The experimental procedure and data visualisation were exemplified with a well-understood photosystem based on ZnSe and phosphonated Ni(cyclam). The continuous-flow setup provided high-quality data on the product evolution rates with improved measurement frequency (every 4 min), while providing the added benefit of a convenient and automated approach. This method laid the foundation for the majority of light experiments conducted during this study.

Chapter 4 showed that the ZnSe QDs can drive a range of molecular co-catalysts based on earth-abundant metals under a constant flow of CO_2 in aqueous ascorbate solution. Besides H_2 evolution as side reaction, photocatalytic CO_2 reduction was achieved with a phosphonate-modified Ni(cyclam) Ni(cycP), sulfonate- and amine-modified Co

tetraphenylporphyrin Co(tppS3N1) and a Co quarterpyridine Co(qpy). The attachment of these catalysts to the QD surface was quantified and found highest for the electrostatic assembly ZnSe | Co(tppS3N1), followed by the anchored Ni(cycP), whereas Co(qpy) interacted diffusional. Benchmark activity on ZnSe QDs was accomplished with the Co(tppS3N1) catalyst which evolved up to 18.6 μmol CO, $TON_{co\text{-}cat}$ of > 600 and an EQE exceeding 1.5%. This activity is amongst the highest reported CO_2 photoreduction catalysts using QDs in aqueous solution. A remarkably long induction period was assigned to slow initial Co^{III} to Co^{II} reduction, which could be accelerated by priming the catalyst in the presence of electron donor AA. All catalyst systems were tested at lower light intensity, low CO_2 concentration and in the presence of O_2 to mimic more real-world scenarios. Lower light intensities were shown to affect the ratio of evolved H_2 vs. CO, leading to a higher CO-selectivity, in particular for the diffusional assembly of ZnSe | Co(qpy). At 20% CO_2 concentration, all hybrid assemblies exhibited greatly reduced activity. While all ZnSe QD-hybrids showed a reduced activity in the presence of O_2, the ZnSe | Co(qpy) assembly exhibited the smallest reduction in activity accompanied by a higher CO selectivity amongst the tested systems. The insights of this chapter demonstrate that the photocatalytic activity is not limited to one type of molecular catalyst and that ZnSe QDs are a particularly versatile light-absorber platform and may be used to interface many other molecular catalysts.

Chapter 5 presented a simple organic surface modification strategy to enhance photocatalytic CO_2 reduction on ZnSe QDs by immobilisation of an imidazolium group on the surface through partial ligand capping. This finding demonstrates that a molecular catalyst is not strictly required to promote CO_2 reduction on ZnSe QDs. The QD ligand interactions were first characterised quantitatively using ^{1}H-NMR spectroscopy and ITC titration which showed that only a subset of the employed ligands (12-17) interact strongly, while the rest interact in a more dynamic manner. This is the first time that those quantitative techniques have been employed in the context of colloidal photocatalysis. Furthermore, it was shown that the CO selectivity can be modulated with the imidazolium loading, yielding up to a 13-fold increase compared to the non-functionalised ZnSe-BF_4 reaching up to 20% CO selectivity. Mechanistic insights were provided through TA spectroscopy and periodic DFT calculations, which pinpoints (unpassivated) Zn atoms of the QD surface as the active sites for CO_2 reduction. It was shown that the imidazolium ligand plays a key role in stabilising the first intermediate ($^*CO_2^{\delta-}$) through a set of non-covalent interactions and thereby rationalising the improved activity. Thus, this is the first time that QDs have been rendered active towards CO_2 reduction by means of an organic surface-modification strategy and this work establishes capping ligands as a powerful tool to modify the chemical environment and therefore the product selectivity of colloidal photocatalysts. Furthermore, the

insights of assigning the non-covalent interactions advances the understanding of imidazolium groups with CO_2 reduction intermediates which is of high relevance to the electrocatalysis community. The findings also demonstrate that it is feasible to translate concepts from secondary coordination sphere effects in electrocatalysis to photocatalysis and might open up new routes in the surface design of photocatalysts without the use of precious metals or molecular co-catalysts based on transition metal complexes.

A different surface modification approach examined the influence of dithiols on ZnSe QDs and showed enhanced CO_2 reduction on the bare ZnSe surface (for a short dithiol, EDT) and in the presence of an additional transition metal molecular co-catalyst (for a longer dithiol, HexDT). The dithiol-QD interactions were studied using ^{1}H-NMR spectroscopy which quantified the number of strongly interacting ligands and additionally revealed the accumulation of dithiols within a solvation sphere strongly dominated by hydrophobic interactions. While this local hydrophobic environment may contribute towards CO_2 reduction, a series of control experiments (replacing or removing the second thiol group) implied effects beyond the hydrophobic environment. These effects were assigned to non-covalent interactions that stabilised the $^*CO_2^{\delta-}$ intermediate, as shown by DFT calculations. The findings of this chapter present dithiols as a novel class of ligands to enhance colloidal photocatalytic CO_2 reduction and have previously not been reported in the context of CO_2 reduction at all.

Finally, Chapter 6 showed that also the sacrificial electron donor is - in principle - replaceable by depositing the QDs on a p-type $CuCrO_2$ electrode forming a QD-sensitised photocathode. The deposition methodology was optimised followed by controlled potential photoelectrolysis (CPPE) which yielded up to 38 nmol of H_2 (4 h CPPE). While this performance is arguably mediocre at best, it constitutes a proof-of-concept that the QDs are able to operate in a stationary photoelectrochemical setup. Attempts to reduce CO_2 in the presence of an additional molecular catalyst remained unsuccessful. The limiting factor is likely related to a non-ideal interface between the electrode surface and the ZnSe QDs imposing kinetic constraints on hole quenching dynamics.

Overall, the results obtained in this dissertation advance the understanding of QD-facilitated photocatalysis. It is shown that ZnSe QDs provide a platform to drive molecular catalysts efficiently and that (partial) ligand capping can tailor the chemical environment of colloidal photocatalysts towards CO_2 reduction. Some techniques and insights may be transferred to other colloidal photosystems and my help to overcome some of the limitations of colloidal photocatalysis and bring the field closer towards practical applications.

Outlook

Further spectroscopic investigations can yield new insights for the understanding of the just described photosystems. *In-situ*, time resolved IR spectroscopy can potentially detect the hypothesised CO_2 reduction intermediates and further elucidate its interactions with the local chemical environment. These experiments are currently ongoing with collaborators at Uppsala University, however, are very challenging, especially on colloidal particles in aqueous solution.

This study was limited to ZnSe as a light absorber only. It would be interesting to translate the insights from this work to other photocatalytic systems, in particular the modification of the chemical environment via capping ligands to enhance CO_2 reduction. However, the material needs to be carefully selected, because intrinsically it needs to be able to reduce CO_2 without a surface modification and also allow for ligand capping.

Furthermore, there are some obvious limitations that need to be overcome for ZnSe in particular, but also for QDs more generally to be of relevance for practical applications.

First, the large band gap of ZnSe circumvents light absorption for large parts of the solar spectrum (> 420 nm), which represents a huge loss. In fact, commercial Silicon solar cells absorb at ~ 1100 nm due to their much lower bandgap of 1.11 eV [409], which allows for utilisation for larger parts of the solar spectrum. However, a semiconductor with a lower bandgap sacrifices either reductive or oxidative power for the two half reactions, which is an intrinsic limitation of single bandgap light absorbers. One solution could be Z-scheme systems: Often considered as *nature-inspired*, they utilise two different light absorbers that operate in conjunction with ideally complementary light absorption profiles. One light absorber targets the oxidative half reaction and the other one is optimised towards the reduction half reaction and the two are coupled by means of a redox mediator to transport photogenerated electrons from the one light absorber to the other. Z-scheme systems have been very successfully employed in photocatalytic water splitting [51] and to a lesser degree in CO_2 reduction [159], but are very delicate because they come with many more possible electron transfers that can short-circuit the assembly. Nevertheless, recent work demonstrates that (colloidal) Z-scheme systems can be employed for CO_2 reduction as shown with La/Rh doped $SrTiO_3$ (reduction side) coupled to Mo-doped $BiVO_4$ for water oxidation, which operated in symbiosis on a photocatalytic sheet connected through Au as a mediator. Potentially, the ZnSe QDs can operate in such a configuration which would not only enable utilisation of a larger part of the solar spectrum but also allow for a more useful oxidation reaction.

This leads to the second limitation: the use of a sacrificial electron donor. Work in the Reisner Group has demonstrated that many light absorbers are capable of useful

oxidation reaction such as oxidation of alcohols [410], oxidation of freely available waste such as biomass [57] or polymers in plastic waste [58], coupled to photocatalytic H_2 evolution. It would be intriguing to couple this process referred to as photoreforming to light-driven CO_2 reduction. In the short term, mechanistic work on the oxidation half reaction of ZnSe might lead to insights why (so far) only AA is able to supply electrons to the ZnSe VB. This could open up new routes to enable photocatalytic CO_2 reduction coupled with the oxidation of organics to value-added compounds. In the long term, coupling CO_2 reduction to water oxidation is desired. Potentially, ZnSe QDs can operate in a configuration similar to the above described photocatalyst sheet to couple it to $BiVO_4$ and allow for the use of water as the ultimate sustainable electron donor.

Lastly, the stability of the QDs needs to be improved, in particular for practical applications. Encapsulating the QDs with a passivating shell can potentially improve the robustness significantly [411]. The core/shell particles would have to be carefully engineered in a way to allow for fast charge transfer to acceptor molecules while still allowing solubility in aqueous solution and surface modification.

Looking beyond

The results presented in this thesis are part of two larger themes.

First, the mechanistic understanding of CO_2 reduction is more advanced on heterogeneous electrocatalytic surfaces [28, 287], with a range of surface sensitive *operando* spectroscopic techniques available [412]. Therefore, there is a lot of scope to translate some of the concepts and methodologies developed in electrocatalysis to photocatalysis. The imidazolium modification of the QDs can be seen as one example of this larger theme. For example, the influence of cations and anions and their effects on local pH, buffering capacity and local electric fields has not been assessed systematically for colloidal CO_2 photoreduction. Further scope lies in the use of capping ligands to fine-tune the local chemical environment with nearly endless possibilities. Potentially, carbon capture may be incorporated in close vicinity to the colloidal catalytic surface and may enable reduction of CO_2 at low substrate concentration.

Second, one grand vision in catalysis and solar fuels in particular are efforts towards synthetic enzymes and molecular machines [130]. Design principles can be drawn from enzymes because they have perfected the fine-tuning of the active site (in the classification given in Figure 1.14, electronic modification *EM*), the molecular control of their coordination environment (*NCI*) and the access/release of substrates and products (*LC-reg*). They are also able to perform at very low substrate concentrations. This characteristic (naturally) enables the enzymes to reduce CO_2 at low concentrations, which would bring CO_2 conversion a step closer towards technological implementation.

Specifically, stabilising reactive intermediates, as shown for MEMI in Chapter 5 in this work, is similar to the role of amino acids near the active site of enzymes which are not innocent and stabilise the transition state [413]. While this simple surface modification is far away from the complexity of a natural enzyme, it represents a small step towards the goal of manipulating CO_2 reduction catalysis with molecular precision. Inspiration can also be drawn from metal-organic frameworks (MOFs), which likewise allow to fine-tune the chemical environment of a catalyst and its intrinsic activity. It is envisioned that efforts and research towards these goals can help to overcome the current limitations in CO_2 conversion and move this technology towards practical applications to contribute to the transition to sustainable energy and closing the carbon cycle.

Appendix A

Appendix to chapter 3: Development of a cont. flow setup

A.1 Photocatalyst concentration dependence

The product evolution rate dependence on the photocatalyst concentration was examined. The QD concentration was tested at 0.25 μM, 0.5 μM and 1 μM in which the ratio of NiCycP to QD always remained constant (molar ratio of 20 equivalents per QD). Increasing the photocatalyst concentration from 0.25 μM to 0.5 μM likewise increased H_2 and CO formation rates, as expected (Figure A.1 A-B). At 1 μM, however, the curve shapes exhibit odd behaviour; both H_2 and CO formation fluctuate significantly over time, but not in a similar fashion, which indicates that it is not the origin of fluctuating flow rates. The real origin of this effect is somewhat elusive. It is likely related to the competition of QDs for light absorption and scattering due to the formation of agglomerates, which is more pronounced at high concentrations. In addition, it was generally found that high product evolution rates are less stable and significantly fluctuate over time, which might be related to bubble formation (in particular on the stirrer bar) which are released randomly over time.

The integrated rate curves - the total amounts of products - hide the fluctuation of the high concentration (1 μM) sample to some extent (Figure A.1 C-D). It is also noted, that CO formation is more accelerated than H_2 (1 μM sample) compared to the lower concentration samples, leading to a slightly higher CO-selectivity. Nevertheless, it was decided to proceed the following experiments throughout this dissertation at 0.5 μM photocatalyst (referring to ZnSe-BF_4 QDs) concentration (referring to ZnSe-BF_4 QDs) to avoid the fluctuating product formation rates. This has the added benefit of preserving precious materials.

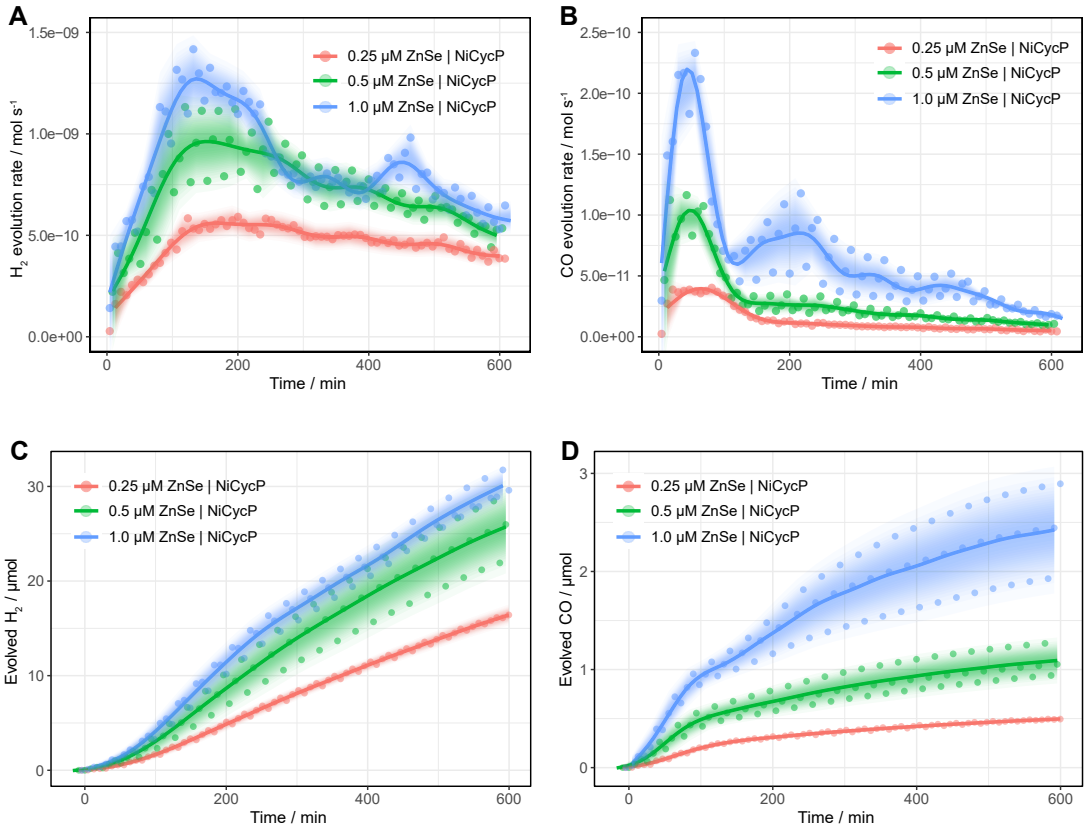

FIGURE A.1: Photocatalytic CO_2 reduction and H_2 evolution depending on the photocatalyst (ZnSe | NiCycP) concentration. (A) H_2 evolution rate. (B) CO evolution rate. (C) Evolved H_2. (D) Evolved CO. Conditions: 0.1M AA, constant molar ratio of 20 (NiCycP to QD); AM 1.5G, $\lambda \geq 400$ nm, 100 mW cm^{-2}, pH 5.5, 3.5 sccm CO_2 flow, 25 °C.

Appendix B

Appendix to chapter 4: QD-molecular catalyst hybrids

B.1 Supplementary Tables

Table B.1: Screening results. No formate was detected. (n. d.: not detected); *the high HER activity is due a different QD batch; additionally, Fe salts were found to accelerate the decomposition of AA leading to background CO (data provided by K. E. Dalle). **estimated from 24 h data point (data provided by S. Roy)

Co-catalyst	**time**	n (H_2) / μmol	n (CO) / μmol	TON_{CO}
Ni(cycH)	4	2.370	0.271	14
Ni(cycP)	4	2.646	1.645	82
Ni(terpyS)	4	0.152	0.038	2
Ni(terpyP)	4	2.334	0.071	4
Co(qpy)	4	6.089	0.752	38
Fe($tppTMA_4$)*	4	8.000	0.220	11
Co(tppS4)	4	2.206	0.942	47
Co(tppS3N1)	4	0.739	0.592	30
Co(pcTMA4)**	4	n.d	n.d	-
Co(pcS4)**	4	2.423	0.286	6
-	4	3.750	0.062	-

TABLE B.2: Tabular results of the photocatalytic CO_2 reduction experiments using ZnSe-BF_4 QDs (10 h irradiation). Standard flow conditions.

Co-catalyst	[Ccatalyst] / μM	n (H_2) $\pm$ σ / μmol	n (CO) $\pm$ σ / μmol	TON (CO) / mol CO (mol co-cat)$^{-1}$	CO selectivity / %
Ni(cycP)	10	14.5 $\pm$ 0.7	3.01 $\pm$ 0.30	100	17.2 $\pm$ 1.0
Co(qpy)	10	24.0 $\pm$ 2.2	2.06 $\pm$ 0.11	69	7.92 $\pm$ 0.4
Co(tppS3N1)	10	14.2 $\pm$ 3.1	9.78 $\pm$ 2.29	326	40.7 $\pm$ 2.0
Co(tppS4)	10	21.4 $\pm$ 1.1	5.39 $\pm$ 0.73	180	20.1 $\pm$ 1.8

TABLE B.3: Tabular results of the photocatalytic control experiments (10 h irradiation). Standard flow conditions. *conducted at pH 5.5.

Description	n (H_2) $\pm$ σ / μmol	n (CO) $\pm$ σ / μmol
ZnSe | Ni(cycP)		
standard experiment	14.5 $\pm$ 0.7	3.01 $\pm$ 0.30
no Ni(cycP)	18.7 $\pm$ 2.4	0.08 $\pm$ 0.02
no AA	not detected	not detected
no QDs	not detected	not detected
no light	not detected	not detected
ZnSe | Co(qpy)		
standard experiment	24.0 $\pm$ 2.2	2.06 $\pm$ 0.11
no Co(qpy)	18.7 $\pm$ 2.4	0.08 $\pm$ 0.02
no AA	not detected	not detected
no QDs	not detected	not detected
no light	not detected	not detected
ZnSe | Co(tppS3N1)		
standard experiment	14.2 $\pm$ 3.1	9.78 $\pm$ 2.29
no Co(tppS3N1)*	18.7 $\pm$ 2.4	0.08 $\pm$ 0.02
no AA	not detected	not detected
no QDs	not detected	not detected
no light	not detected	not detected

TABLE B.4: Quantification of co-catalyst attachment to ZnSe-BF_4 QDs.

Co-catalyst	Co-catalyst per QD employed / mol co-cat (mol QD)$^{-1}$	Co-catalyst per QD found / mol co-cat (mol QD)$^{-1}$	Attachment	Method
Ni(cycP)	20	1.57 [317]	7.9 %	ICP-OES
Co(qpy)	20	$\sim$ 0	$\sim$ 0 %	UV-vis
Co(tppS3N1)	20	16.8	84 %	UV-vis
Co(tppS4)	20	17.2	86 %	UV-vis

TABLE B.5: External quantum efficiency (EQE) determination for the photocatalytic CO_2 reduction using ZnSe | Co(tppS3N1). *Cumulative product measured in headspace. Conditions: 1.0 μM ZnSe-BF_4, 20 μM Co(tppS3N1), in 1.2 mL 0.1 M aq. AA, pH 4.5 under CO_2; I = 1.50 mW cm^{-2}, A = 0.80 cm^2, λ = 400 ± 5 nm

Time / h	n (CO) / nmol	EQE* CO / %	n (H_2) / nmol	EQE* H_2 / %
1	273	1.89	1009	6.99
2	485	1.47	2121	7.70
3	659	1.20	3169	7.25
average		1.52 ± 0.28		7.31 ± 0.29

B.2 Supplementary Figures

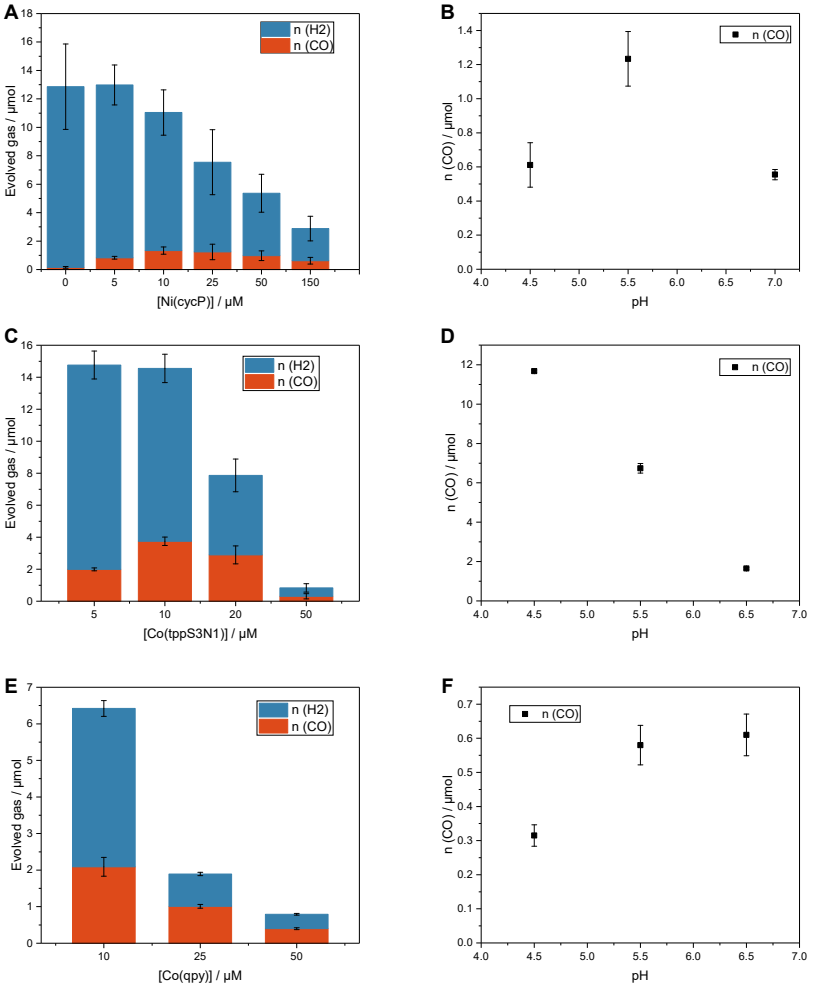

FIGURE B.1: Co-catalyst optimisation: Photocatalytic reduction of aqueous CO_2 in the presence of ZnSe | Ni(cycP) (A-B), ZnSe | Co(tppS3N1) (C-D) and ZnSe | Co(qpy) (E-F) under (non-flow) headspace accumulation conditions: (A) Dependence of the photocatalytic activity on the Ni(cycP) concentration (4 h irradiation, pH 5.5). (B) pH dependence of Ni(cycP) (4 h irradiation, 10 μM Ni(cycP)). (C) Dependence of the photocatalytic activity on the Co(tppS3N1) concentration (10 h irradiation, pH 5.5). (D) pH dependence of Co(tppS3N1) (16 h irradiation, 10 μM Co(tppS3N1)). (E) Dependence of the photocatalytic activity on the Co(qpy) concentration (4 h irradiation, pH 5.5). (F) pH dependence of Co(qpy) (4 h irradiation, 25 μM Co(qpy)). The lower activity in (F) is due to a different batch of ZnSe-QDs that was used in this experiment. Data from (A) obtained from [317]. Data from (B) obtained from [316]. Data from (F) kindly provided by Souvik Roy, single run experiment, 10% standard deviation was manually added. Unless otherwise stated, data presented from two independent experiments. General conditions: 0.1 M AA, 0.5 μM ZnSe-BF_4, AM 1.5G, $\lambda > 400$ nm, 100 mW cm^{-2}, CO_2, 25 °C.

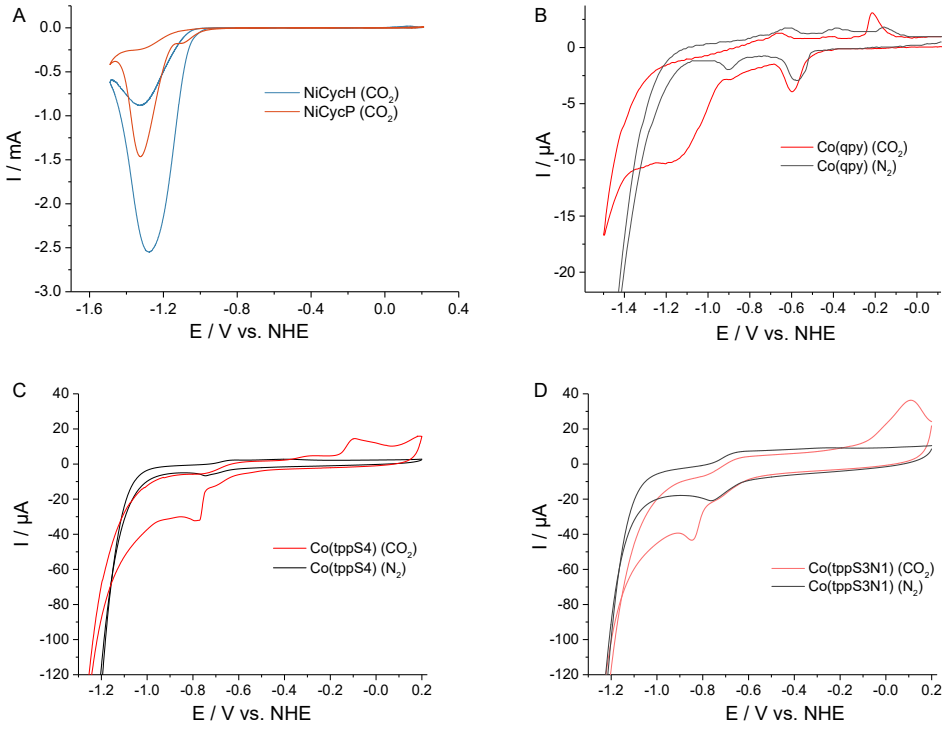

FIGURE B.2: Cyclic voltammograms of selected molecular co-catalysts employed in this section. (A) NiCycH and NiCycP (10 mM) under CO_2 on a Hg-Au amalgam working electrode. (B) Co(qpy), (C) Co(tppS4) and (D) Co(tppS3N1) (1 mM each) on a glassy carbon working electrode under either N_2 or CO_2 atmosphere. General conditions: Pt mesh counter electrode, Ag/AgCl reference electrode, scan rate 100 mVs^{-1}, 0.1 M $NaClO_4$, pH 4 (CO_2), pH 6.5 (N_2).

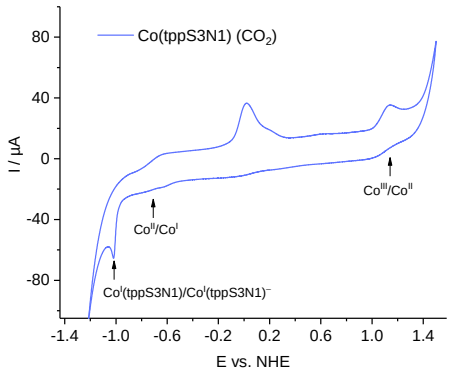

FIGURE B.3: Cyclic voltammogram of Co(tppS3N1) (1 mM) displaying also the oxidation side on a glassy carbon working electrode under CO_2 atmosphere. General conditions: Pt mesh counter electrode, Ag/AgCl reference electrode; scan rate 100 mVs^{-1}, 0.1 M $NaClO_4$, pH 4.

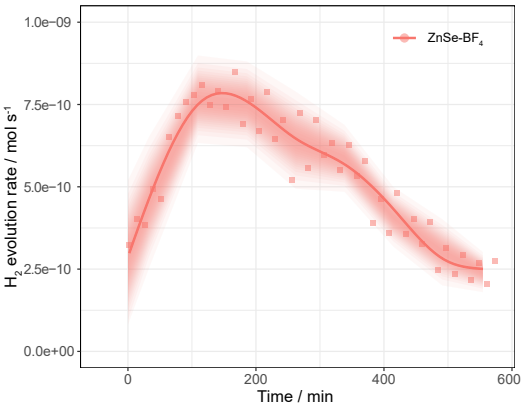

FIGURE B.4: Photocatalytic H_2 evolution using ZnSe-BF_4 in the absence of a molecular co-catalyst. Otherwise standard flow conditions.

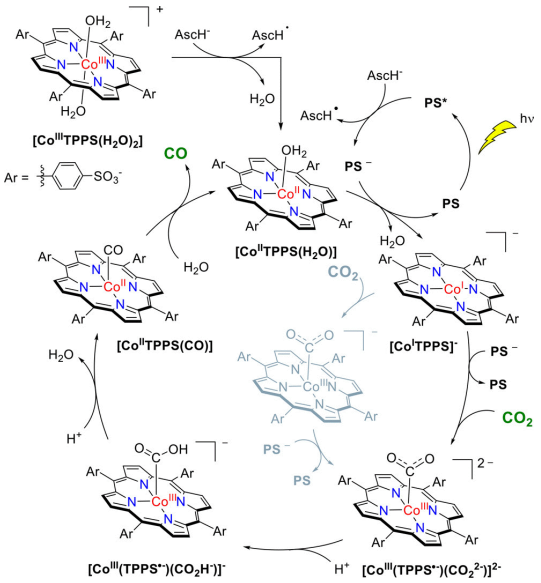

FIGURE B.5: Proposed reaction scheme for the CO_2 to CO photoconversion in the $[Ru(bpy)_3]^{2+}$/Ascorbate/Co(tppS4) system in water. Figure reprinted from [182] with permission from the *American Chemical Society*.

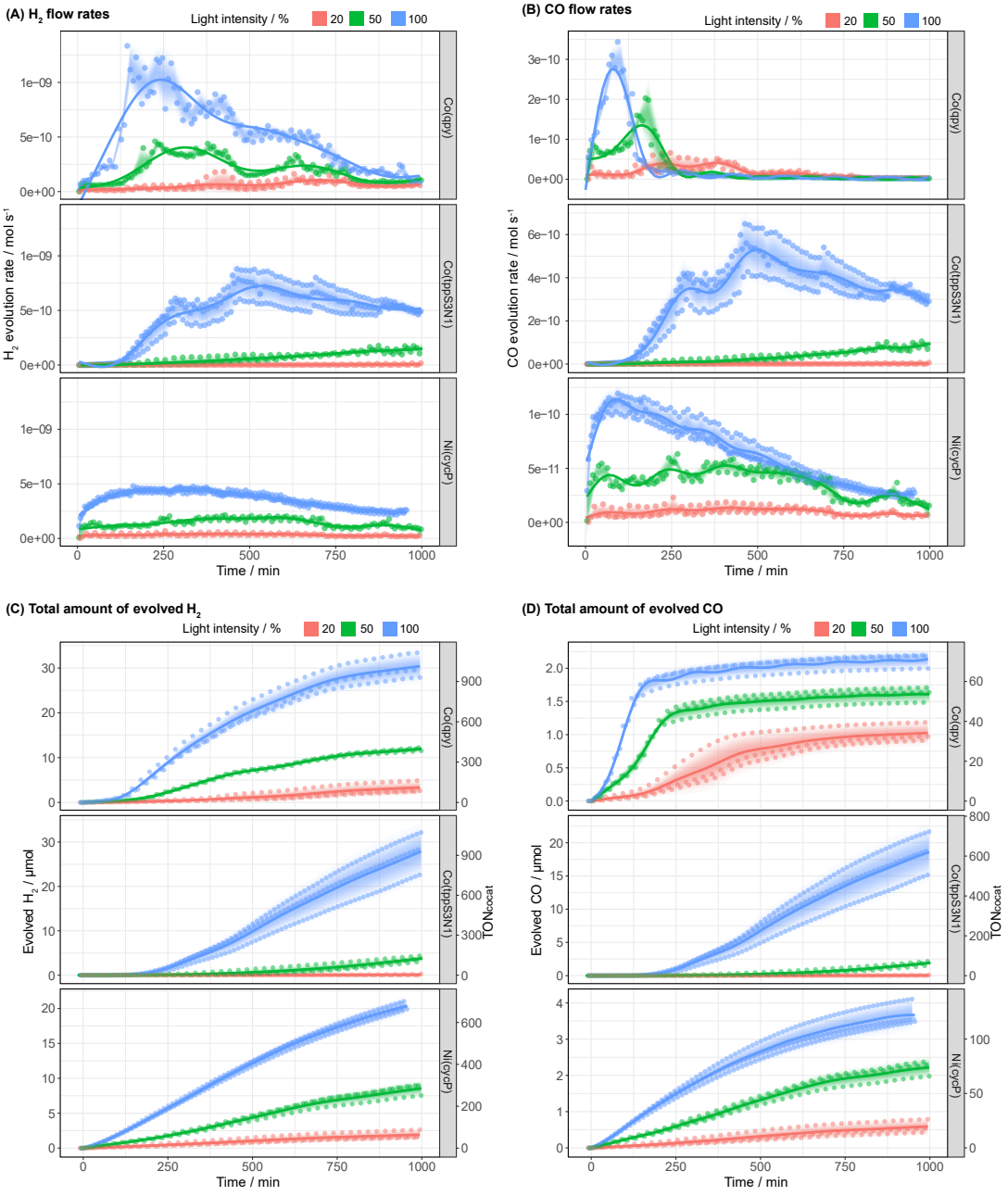

FIGURE B.6: Influence of light intensity on photocatalytic CO_2 reduction in the presence of ZnSe-BF_4 and various co-catalysts Co(qpy), Ni(cycP) and Co(tppS3N1). Standard flow conditions.

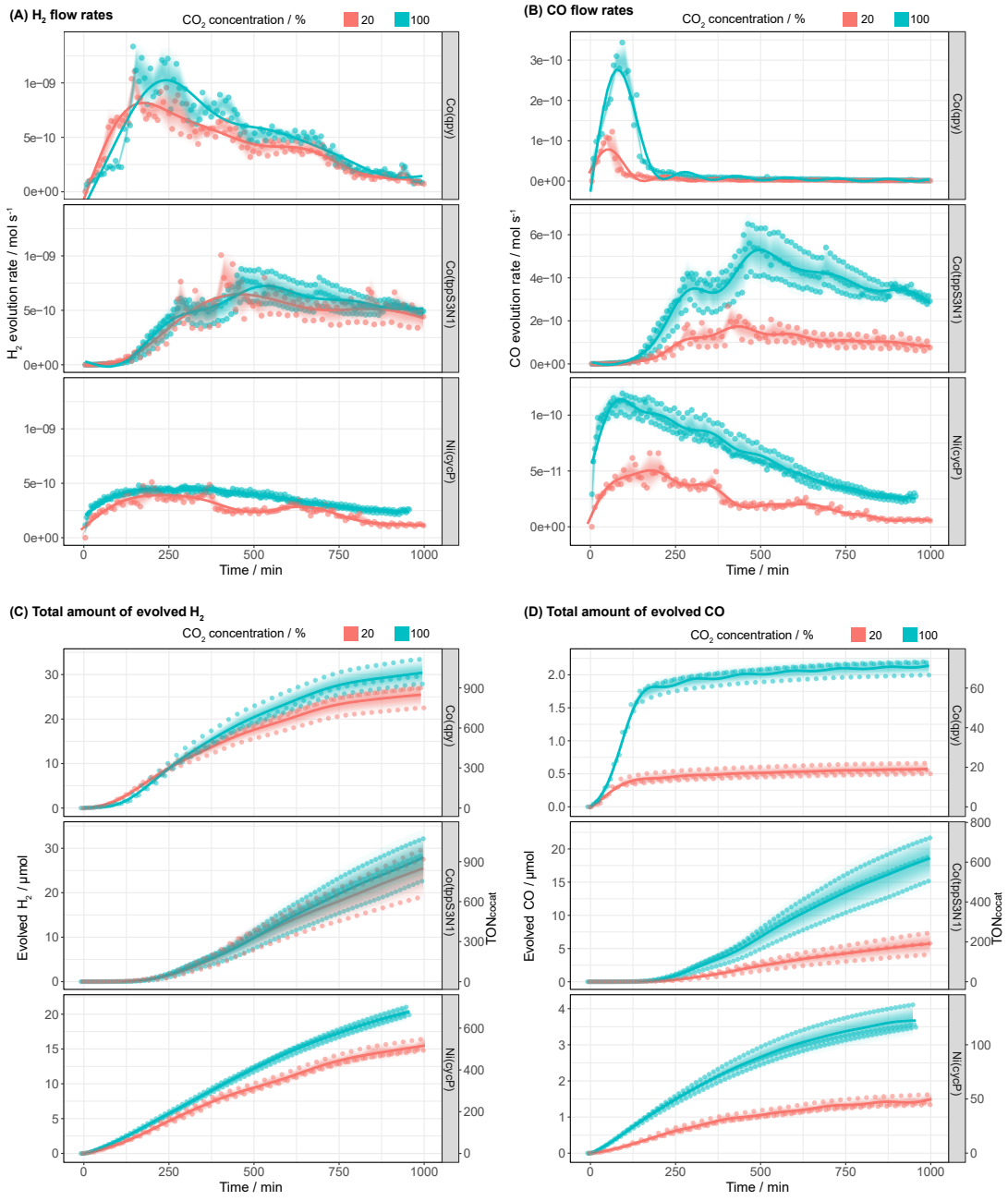

FIGURE B.7: Influence of CO_2 concentration on photocatalytic CO_2 reduction in the presence of ZnSe-BF_4 and various co-catalysts Co(qpy), Ni(cycP) and Co(tppS3N1). Standard flow conditions.

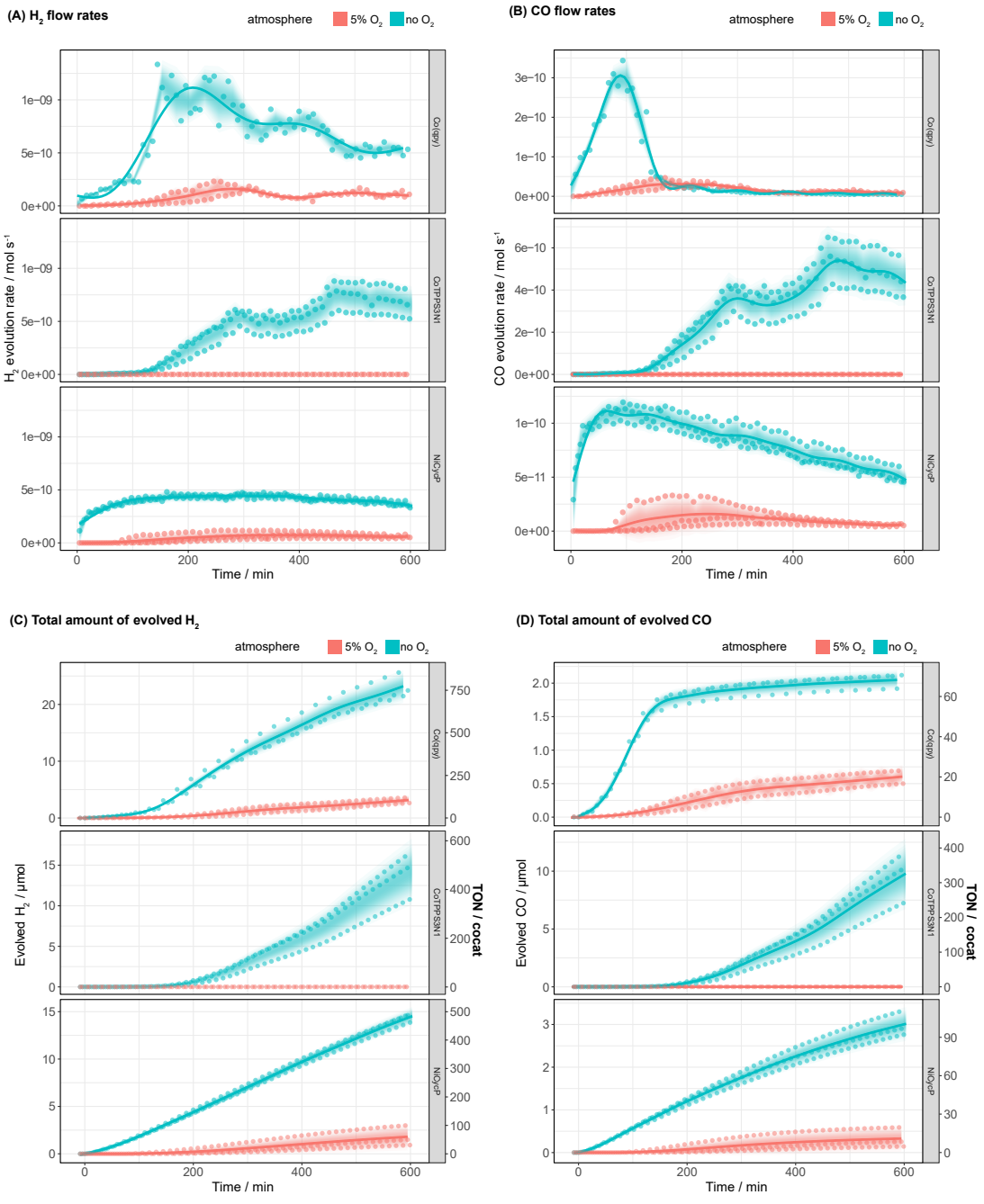

FIGURE B.8: Influence of the presence of O_2 on photocatalytic CO_2 reduction in the presence of ZnSe-BF_4 and various co-catalysts Co(qpy), Ni(cycP) and Co(tppS3N1). Standard flow conditions.

B.3 Preparation of molecular catalysts

2,2':6',2":6",2"':6"',2"'-quaterpyridine (qpy)

The following synthetic procedure was conducted by Souvik Roy and is described for completeness in the following:

A mixture of K_2CO_3 (177 mg, 1.28 mmol), $Pd(OAc)_2$ (44 mg, 0.64 mmol), NBu_4Br (208 mg, 0.64 mmol) and 6-bromobipyridine (300 mg, 1.28 mmol) in DMF (2 mL) was purged with N_2 atmosphere for 15 min followed by heating at 115 °C for 4 min. Then, isopropanol (8 mL) was added to the orange solution and the reaction mixture was stirred at 115 °C for 3.5 h. After cooling to room temperature, water (20 mL) and ether (3 x 25 mL) were added and the organic phase was extracted and dried over $MgSO_4$. The solvent was removed under vacuum and the residue was purified via chromatography (SiO_2) using NEt_3/EtOAc/hexane (1:30:69). Yield: 60 mg. ^{1}H-NMR ($CDCl_3$, 400 MHz): δ = 8.72 (m, 2H), 8.69–8.65 (m, 4H), 8.48 (dd, J = 7.8, 0.8 Hz, 2H), 8.00 (t, J = 7.8 Hz, 2H), 7.91 (td, J = 7.8, 1.8 Hz, 2H), 7.39–7.35 (ddd, J = 7.4, 4.8, 1.0 Hz, 2H).

Co(pcN4)

The following synthetic procedure was developed by Souvik Roy and is described for completeness in the following:

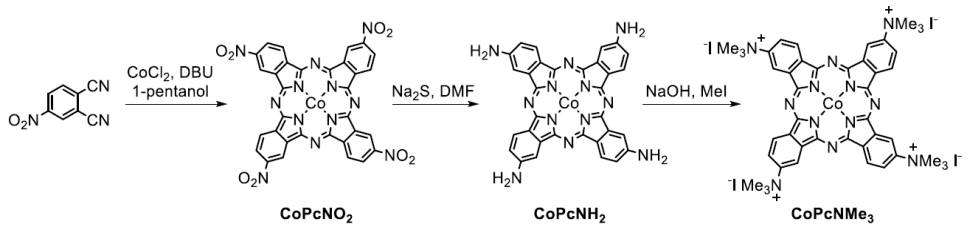

FIGURE B.9: Synthetic scheme towards Co(pcNMe$_3$) (equal to Co(pcN4)).

$CoPc(NO_2)_4$. 4-nitrophthalonitrile (4 g, 23 mmol) was suspended in 1-pentanol (25 mL) and degassed by N_2 purging for 10 min. $CoCl_2$ x 6 H_2O (2.2 g, 9.24 mmol) was added under N_2 overpressure followed by addition of diazabicycloundecene (DBU) (2 mL, 13.3 mmol). The suspension was further degassed for 15 min during which the colour turned green. The reaction mixture was heated at 150 °C for 15 h under N_2. After cooling the mixture to room temperature, methanol (50 mL) was added and the suspension was further cooled over ice. Blue/green product was collected by filtration and washed sequentially with EtOH, MeOH, water, 5% HCl solution, water, and methanol. The solid was dried under vacuum. Yield: 2 g. UV-vis (DMF): Q-band λmax 624 nm and 668 nm.

$CoPc(NH_2)_4$. The crude $CoPc(NO_2)_4$ (0.61 g, 0.82 mmol) was dissolved in DMF (10 mL) and N_2 purged for 15 min. Sodium sulfide (60 wt% Na_2S x H_2O) (2.1 g) was added to the mixture under nitrogen and dark green solution was heated at 80 °C. After cooling to room temperature, the reaction mixture was poured over 150 mL ice cold water. The green product was collected by filtration and washed with water, 20 mL EtOH, and ether. Yield: 0.5 g. UV-vis (DMF): Q-band λmax ∼640 nm and 704 nm.

$CoPc(NMe_3)_4$ (**Co(pcN4**). $CoPc(NH_2)_4$ (0.15 g, 0.24 mmol) and NaOH (0.18 g, 4.5 mmol) was dissolved in DMF (10 mL, anhydrous) and the solution was degassed by bubbling with N_2 for 15 min. Methyl iodide (2 mL, 32 mmol) was added dropwise to the mixture followed by stirring at room temperature for 3 days. The blue mixture was poured over ether (100 mL) and the precipitated solid was collected by centrifugation. The blue solid was extracted with hot water (5 x 50 mL, 70 °C). The combined aqueous fraction was evaporated to yield the product as blue solid. Yield: 90 mg. UV-vis (water): Q-band λmax ∼ 594 nm and 654 nm.

Co(tppS3N1)

The following synthetic procedure was developed by Geani M. Ucoski and is described for completeness in the following:

[5-p-amino-10,15,20–tris-p-sulfonate-phenyl-porphyrin]-tri-p-amonnium (tppS3N1) was prepared as described in the literature [414, 415].

Co(tppS3N1).

A 125 ml, three-necked flask was charged with 41.73 mg, $4.53x10^{-2}$ mmol of tppS3N1 and 10 ml of methanol. The mixture was stirred at 60 °C, under nitrogen. A solution of cobalt (II) acetate tetrahydrate (57.1 mg, 2.29 x 10^{-1} mmol) in 5 ml of methanol and 15 ml chloroform was added. The reaction was monitored by thin-layer chromatography and by UV-vis. The solution was stirred for 8 h. The solvent was removed in rotatory evaporator and the red solid resulting was purified by column chromatography on silica gel, using methanol and methanol: acetic acid (9:1) as eluent. To remove residual Co salt, the crude compound was passed through an ion exchange resin (Dowex 50W-X8, H^+ form, 50-100 mesh) followed by filtration with celite. The product was collected as red solid and dried under vacuum (yield 84%).

Appendix C

Appendix to chapter 5: The influence of capping ligands

C.1 Imidazolium modification

C.1.1 Supplementary Tables

Table C.1: Optimisation of the photocatalytic CO_2 reduction using ZnSe | MEMI. Unless otherwise stated, conditions were: 0.5 μM QD, 0.1 M AA/$NaHCO_3$, pH 6.5, 3 mL water under CO_2 flow (4 sccm); 100 mW cm^{-2}, AM 1.5G, $\lambda > 400$ nm, 25 °C.

Catalyst	Ligand loading / μM	n(H_2) $\pm$ σ / mmol $g_{ZnSe}{}^{-1}$	n(CO) $\pm$ σ / mmol $g_{ZnSe}{}^{-1}$	CO selectivity
varying the catalyst				
ZnSe	0	71.8 ± 19.7	0.64 ± 0.11	0.9% ± 0.3%
ZnSe | EMIM-BF4	50	40.2 ± 6.06	1.06 ± 0.06	2.6% ± 0.5%
ZnSe | MEMI	50	29.9 ± 8.52	1.78 ± 0.23	5.8% ± 1.1%
ZnSe | M-MEMI	50	17.3 ± 0.87	2.38 ± 0.19	12% ± 1.1%
ZnSe | BuSH	50	72.1 ± 27.6	0.69 ± 0.19	1.1% ± 0.5%
varying ligand loading				
ZnSe | MEMI	0	71.8 ± 19.7	0.64 ± 0.11	0.9% ± 0.3%
ZnSe | MEMI	12.5	46.9 ± 8.15	1.18 ± 0.22	2.5% ± 0.7%
ZnSe | MEMI	25	38.6 ± 13.0	1.41 ± 0.10	3.8% ± 1.1%
ZnSe | MEMI	37.5	26.0 ± 1.69	1.52 ± 0.14	5.5% ± 0.3%
ZnSe | MEMI	50	29.9 ± 8.52	1.78 ± 0.23	5.8% ± 1.1%

Table C.2: Control experiments for the photocatalytic CO_2 reduction using ZnSe | MEMI. Unless otherwise stated, conditions were: 0.5 μM QD, 0.1 M AA/$NaHCO_3$, pH 6.5, 3 mL water under CO_2 flow (4 sccm); 100 mW cm^{-2}, AM 1.5G, $\lambda > 400$ nm, 25 °C.

description	time / h	n(CO) $\pm$ σ / mmol $g_{ZnSe}{}^{-1}$	n(H_2) $\pm$ σ / mmol $g_{ZnSe}{}^{-1}$
std. experiment (ZnSe | MEMI)	10	1.78 ± 0.23	29.9 ± 8.52
no MEMI	10	0.64 ± 0.11	71.8 ± 19.7
no AA	16	not detected	0.05 ± 0.03
no ZnSe QDs	16	not detected	not detected
no light	10	not detected	not detected

Table C.3: Formate production. Irradiation time 4 h; The quantification of formate is complicated due to a background formation of formate, presumably from decomposition of ascorbate. In order to differentiate between formate from reduced CO_2 or decomposed ascorbate, the experiment was conducted under an atmosphere of $^{13}CO_2$ and ^{13}formate was quantified via solution ^{1}H-NMR spectroscopy and ^{13}CO via gas chromatography. Conditions were: 0.5 μM QD, 0.1 M AA/$NaHCO_3$, pH 6.5, 2 mL water under CO_2; 100 mW cm^{-2}, AM 1.5G, $\lambda > 400$ nm, 25 °C

description	n(CO) $\pm$ σ / μmol	n(formate)/ μmol	Ratio of formate vs. CO
ZnSe | MEMI	0.290 $\pm$ 0.028	0.009	2.9%

Table C.4: External quantum efficiency (EQE) determination for the photocatalytic CO_2 reduction using Zn-Se-BF4 | M-MEMI (1.0 μM ZnSe-BF_4, 100 μM M-MEMI, in 1.2 mL, 0.1 M aq. AA, pH 6.5 under CO_2; A = 0.80 cm^2, λ = 400$\pm$5 nm, rt). [a] Cumulative product measured in headspace. [b] based on two independent replicates

time / h	Intensity / mW cm^{-2}	n(CO) / nmol[a]	EQE_{CO} / %	n(H_2) / nmol[a]	EQE_{H2} / %
2	1.0	27 $\pm$ 17[b]	0.14 $\pm$ 0.09	324 $\pm$ 222[b]	1.68 $\pm$ 1.15
2	1.5	41	0.14	285	0.99
average			0.14 $\pm$ 0.06		1.45 $\pm$ 0.91

Table C.5: pH dependence of photocatalytic CO_2 reduction using ZnSe-BF_4 | MEMI. Unless otherwise stated, standard conditions were: 0.5 μM QD, 50 μM MEMI, 0.1 M AA/$NaHCO_3$, 3 mL water under CO_2 flow (4 sccm); 100 mW cm^{-2}, AM 1.5G, $\lambda > 400$ nm, 10 h irradiation, 25°C. pH determined after 10 min of purging with CO_2 after it stabilised.

Catalyst	pH	n(H_2) $\pm$ σ / mmol $g_{ZnSe}{}^{-1}$	n(CO) $\pm$ σ / mmol $g_{ZnSe}{}^{-1}$	CO selectivity
ZnSe | MEMI	4.5	62.8 $\pm$ 3.14	1.77 $\pm$ 0.15	2.7% $\pm$ 0.2%
ZnSe | MEMI	5.5	50.5 $\pm$ 5.06	1.23 $\pm$ 0.06	2.4% $\pm$ 0.3%
ZnSe | MEMI	6.5	29.9 $\pm$ 8.52	1.78 $\pm$ 0.23	5.8% $\pm$ 1.1%

Table C.6: Computed surface energies of the XRD-predominant facets for ZnSe.

Surface facet	Area of unit cell / Å^2	γ / J m^{-2}
(111)	57.083	1.00
(222)	57.083	1.00
(200)	32.975	1.33
(220)	46.608	0.49
(311)	109.305	0.93

C.1.2 Supplementary Figures

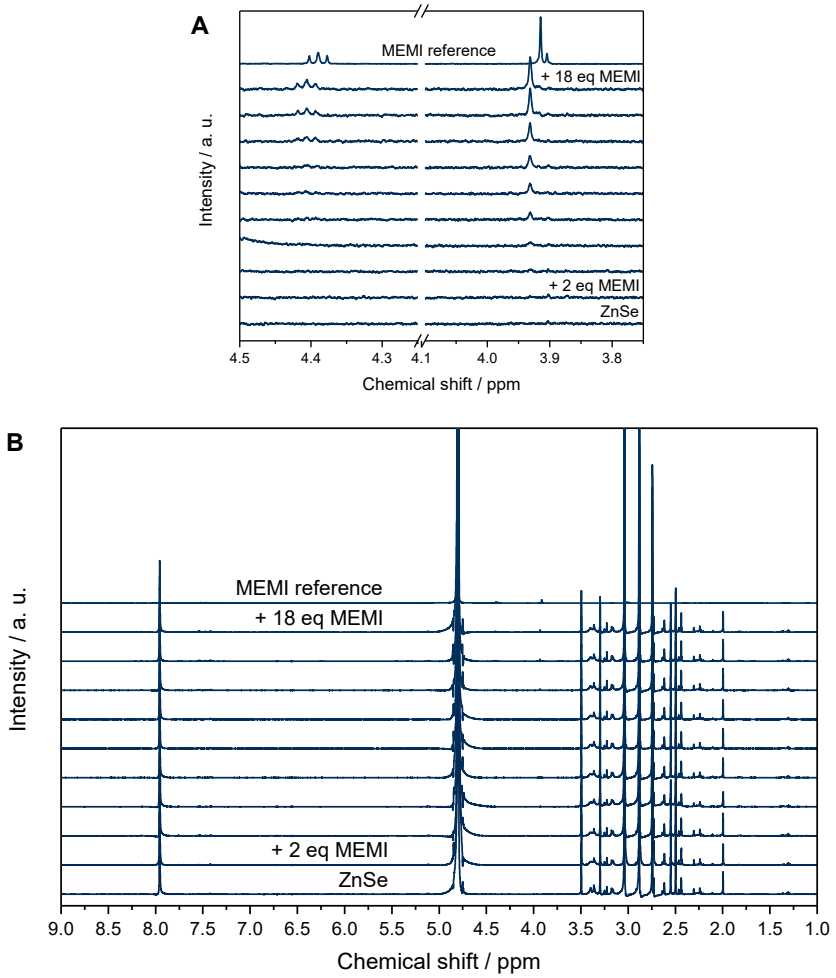

FIGURE C.1: Supplementary ^{1}H-NMR spectroscopy titration data of MEMI to ZnSe QDs (5 μM in D2O). (A) two selected peaks in comparison to a MEMI reference in the absence of QDs. (B) Overview of the full NMR spectrum. The small peak b' next the signal at 3.9 ppm represents a proton of the oxidised disulfide MEMI equiv. (due to some residual oxygen present). Aromatic protons c1 and c2 are noticeable but difficult to quantify due to an overlap with an impurity in the QD stock solution. The other CH_2 signal e (not shown) overlaps with an impurity from the QD stock solution (DMF). The acidic proton d is not visible (in D_2O) as seen before in the literature [416]. The region (1.7 to 3.5 ppm) contains residues of the solvents from the QD synthesis and purification (DMF, MeOH, BuOH, $CHCl_3$). All spectra referenced to the water peak at 4.80 ppm. The sensitivity of the NMR measurement with MEMI was determined to be 5-10 μM meaning that even the first titration (i.e. 2 equiv.) would be detectable by NMR spectroscopy.

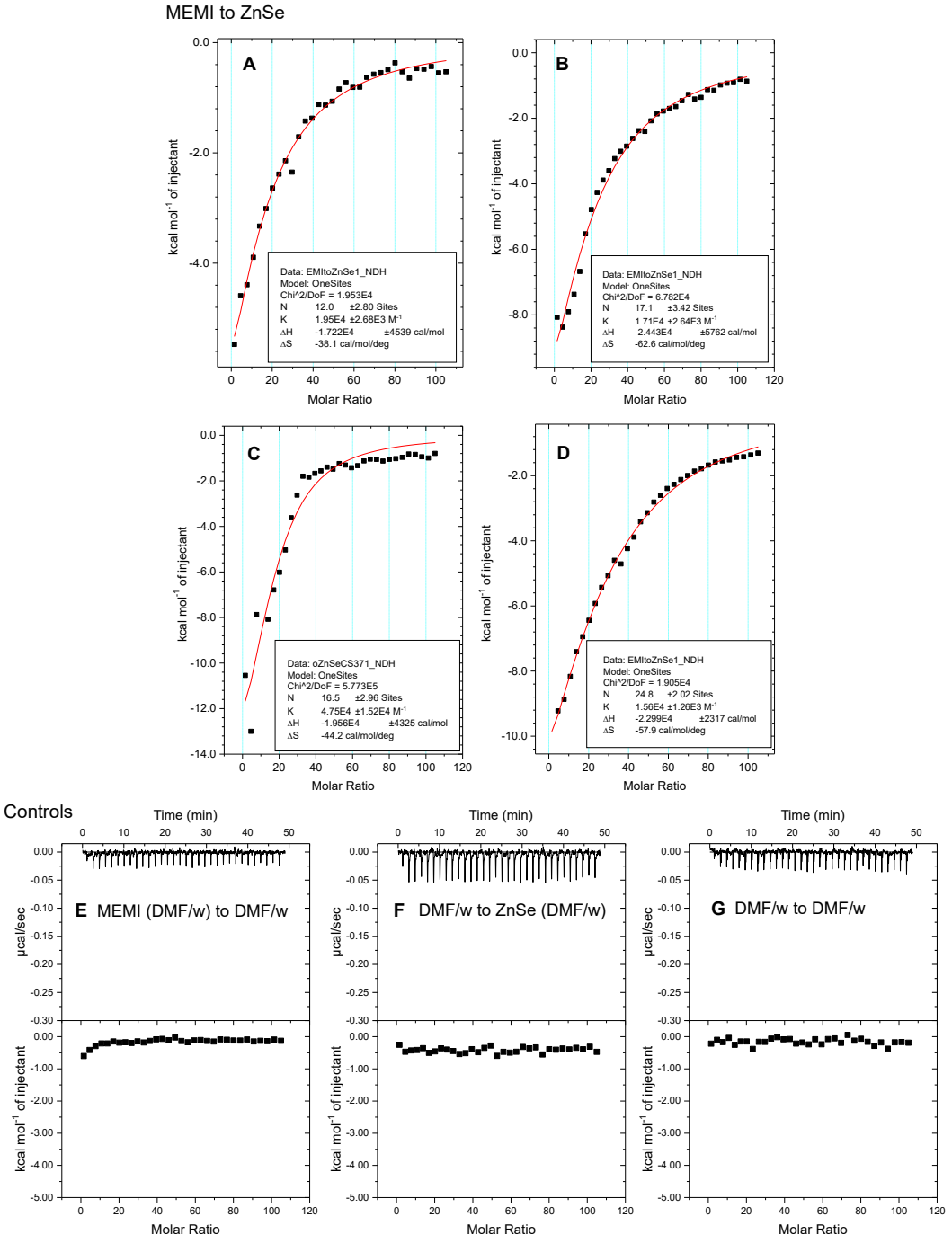

FIGURE C.2: Supplementary ITC data. (A) - (D) ITC curves and plots for replicates of four independent titrations of MEMI (in H_2O/DMF) into ZnSe-QDs (1 μM) (A), 2 μM (B, C, D) in H_2O/DMF) (black scatter) and fit using the *one set of sites* binding model to estimate the number of binding sites N (red line). (E) - (G) ITC curves and plots of control experiments: (E) titration of MEMI (0.5 mM in H_2O/DMF) into H_2O/DMF, (F) H_2O/DMF into ZnSe (1 μM in DMF/H_2O) and (G) H_2O/DMF to H_2O/DMF. The DMF concentration (3.12%, v/v) was kept constant in the cell and titrant solution in all titration experiments.

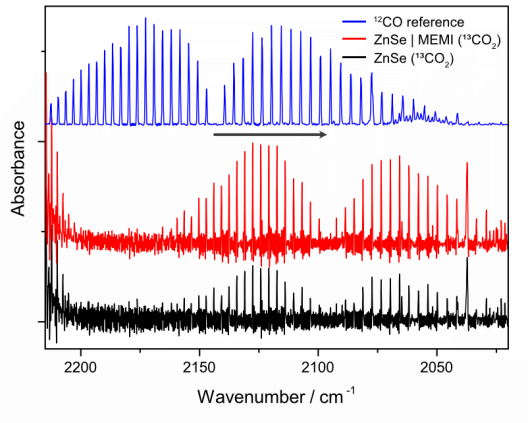

FIGURE C.3: Isotopic labelling: Gas-phase transmission IR spectra of the CO vibration depending on the employed CO_2 isotopologue. Samples ZnSe and ZnSe | MEMI under an atmosphere of $^{13}CO_2$ compared to a reference spectrum of ^{12}CO. Conditions: AM 1.5G, $\lambda > 400$ nm, 100 mW cm^{-2}, 0.5 μM ZnSe-BF_4, 50 μM MEMI, 0.1 M AA, pH 6.5, CO_2, 1000 min irradiation.

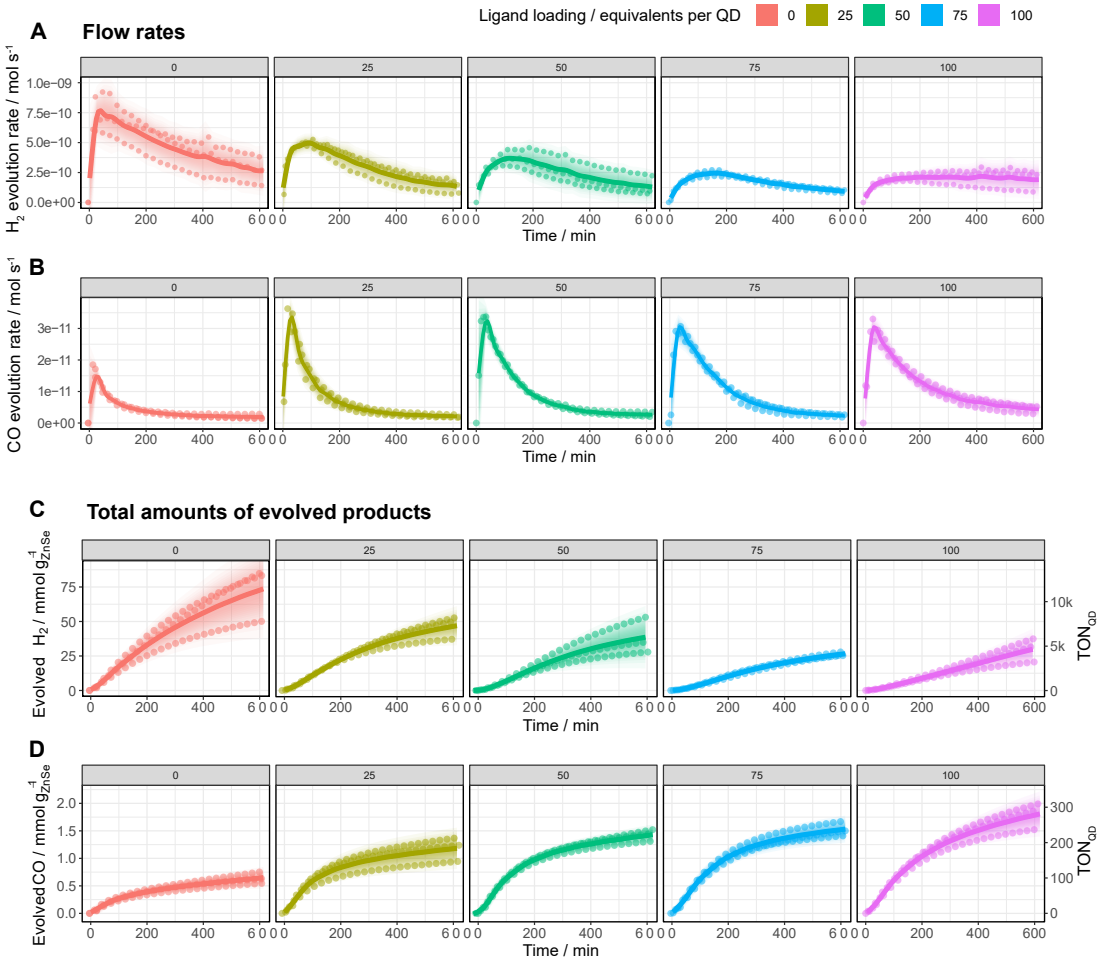

FIGURE C.4: Photocatalytic reduction of aqueous CO_2 in the presence of ZnSe | MEMI. Influence of the ligand loading (in equiv. ligand per QD) on the product distribution: (A) H_2 and (B) CO evolution rates. (C) Total amount evolved H_2 and (D) total amount evolved CO. Conditions: AM 1.5G, $\lambda > 400$ nm, 100 mW cm^{-2}, 0.5 μM ZnSe-BF_4, 0.1 M AA/$NaHCO_3$, pH 6.5, CO_2 constant flow (4 sccm).

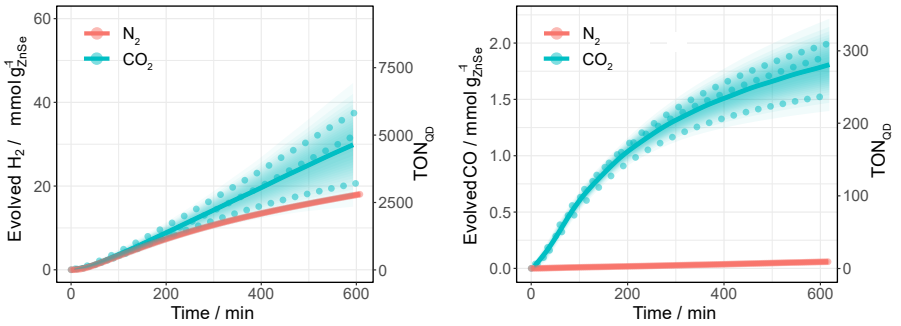

FIGURE C.5: Photocatalytic CO_2 reduction using ZnSe | MEMI under various atmospheres. Conditions: AM 1.5G, $\lambda > 400$ nm, 100 mW cm^{-2}, 0.5 μM ZnSe-BF_4, CO_2-sample: 0.1 M AA/$NaHCO_3$, CO_2, pH 6.5; N_2-sample: 0.1 M AA pH adjusted to 6.5, constant flow (4 sccm).

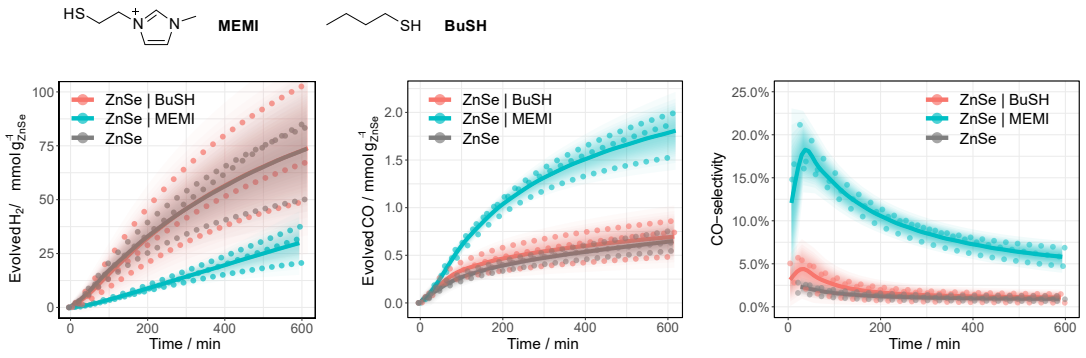

FIGURE C.6: Photocatalytic CO_2 reduction using ZnSe | MEMI in comparison to ZnSe | BuSH. Conditions: AM 1.5G, $\lambda > 400$ nm, 100 mW cm^{-2}, 0.5 μM ZnSe-BF_4, 50 μM capping ligand, 0.1 M AA/$NaHCO_3$, pH 6.5, CO_2 constant flow (4 sccm).

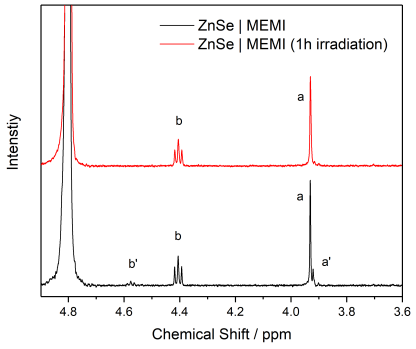

FIGURE C.7: ^{1}H-NMR spectroscopy of ZnSe | MEMI in D_2O before and after irradiation. Conditions: AM 1.5G, $\lambda > 400$ nm, 100 mW cm^{-2}, 1.0 μM ZnSe-BF_4, 50 μM MEMI, CO_2. The spectrum before irradiation (black) exhibits a mixture of MEMI and its oxidised disulfide equiv. (due to residual O_2) indicated by signals a' and b' respectively. The disulfide signals vanish after irradiation (red) suggesting the opposite reaction, a reduction of residual disulfide rather than photocatalytic thiol oxidation.

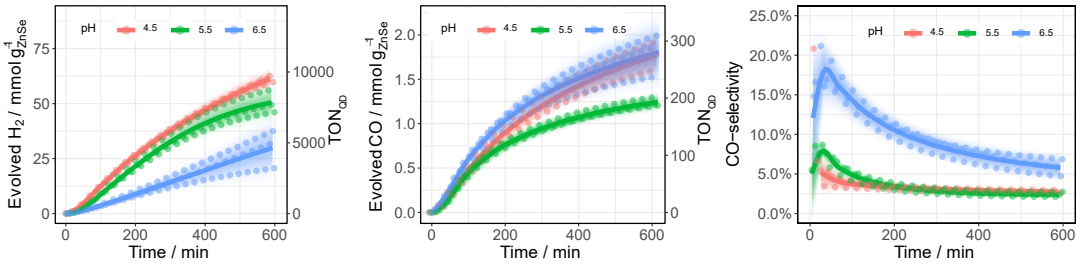

FIGURE C.8: pH dependence of the photocatalytic CO_2 reduction using ZnSe | MEMI. Conditions: AM 1.5G, $\lambda > 400$ nm, 100 mW cm^{-2}, 0.5 μM ZnSe-BF_4, 50 μM MEMI, 0.1 M AA/$NaHCO_3$, CO_2 constant flow (4 sccm).

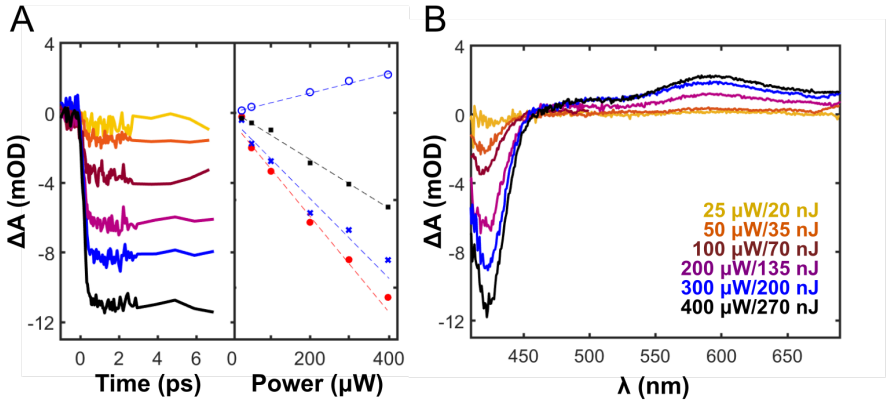

FIGURE C.9: Transient absorption (TA) optical response at varying pump pulse energies (nJ)/power (μW) for ZnSe-BF_4 quantum dots (QDs) using a 400 nm pump. **(A)** The early-time kinetics (left column) extracted at 425 nm remain unchanged within the investigated range of pump energies, see legend of corresponding color in (B). In the rightmost column, the amplitudes (mOD) were estimated by averaging over adjacent wavelengths: 412-416 nm (red circles), 416-422 (blue crosses) nm, 435-440 nm (black squares) and 585-595 nm (blue open circles). The range from 585-595 nm corresponds to the positive transient. The signal amplitudes increase linearly within the range of investigated pulse energies. **(B)** TA spectra of ZnSe QDs at varying pump pulse energies/powers. All spectra presented in the main section are recorded with pump energies of ∼70 nJ. The Figure was created by Nora Eliasson.

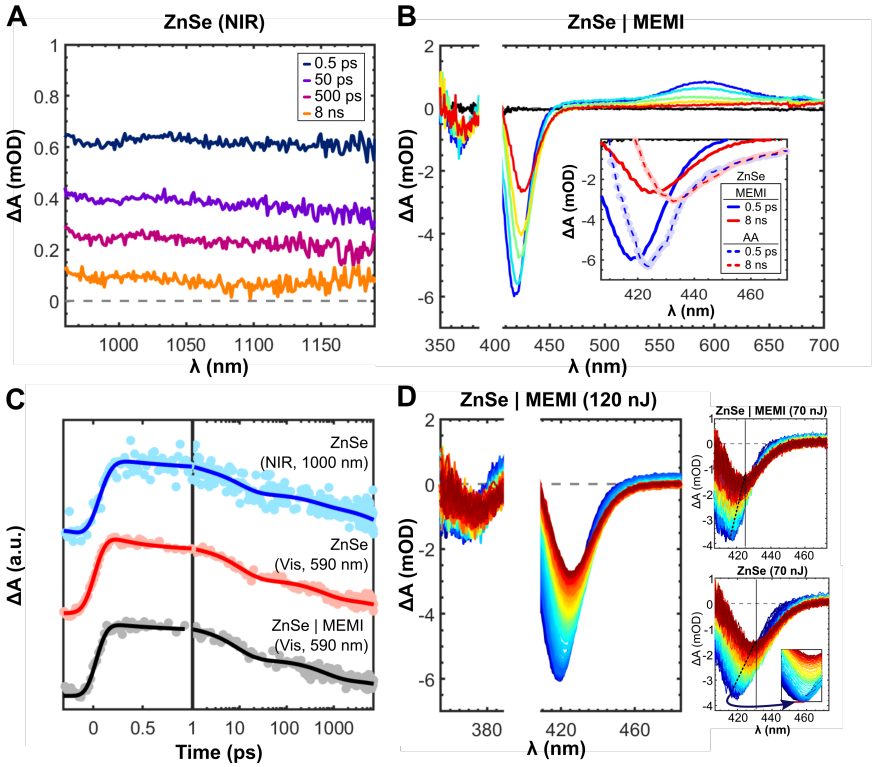

FIGURE C.10: Transient absorption (TA) experiments using a 400 nm pump. **(A)** TA-NIR spectra of ZnSe-BF_4 QDs (170 nJ/pulse). **(B)** TA spectra of ZnSe|MEMI. Inset: Close-up of ZnSe | MEMI TA spectra compared to ZnSe | AA. The ZnSe | AA spectra show an unsymmetrical bleach band with a low-energy tail that extends to energies below the ZnSe bandgap. **(C)** TA kinetics of ZnSe-BF_4 QDs (NIR: 1000 nm, blue [6 ps, A: 0.43; 850, A: 0.35; inf, A: 0.22]; Vis: 590 nm, red [8.5 ps, A: 0.43; 830 ps, A: 0.38; inf, A: 0.19]) and ZnSe | MEMI (Vis: 590 nm, black [9.5 ps, A: 0.48; 880 ps, A: 0.36; inf, A: 0.16]). These kinetics are considered equal, within sample-to-sample variances, and reflect the population of trapped holes (see main article). **(D)** Close-up of TA spectra of ZnSe | MEMI (∼120 nJ) (left), showing the spectral shift of the two bleach bands XB1 and XB2 → $XB1_T$ and XB2 $_T$. All time points between 300 fs and 8 ns are presented (blue → green → yellow → red) for the given wavelength range. Close up of TA spectra of ZnSe | MEMI at lower pump fluence (∼70 nJ, top) and ZnSe (∼70 nJ, bottom). The TA spectra of neat ZnSe (bottom) show a smaller wavelength shift with time than the spectra presented in the main section (Figure 5.8-A) but show a significantly larger shift than when MEMI is present (top). The shift magnitude is indicated by dashed lines, with a starting point at ∼416 nm corresponding to the center of the exciton bleach. In neat ZnSe (bottom) the bleach shifts with a few nanometers on the hundred of femtoseconds timescale, corresponding to a slight growth at ∼420 nm prior to recovery (see inset from spectra recorded at higher powers). The Figure was created by Nora Eliasson.

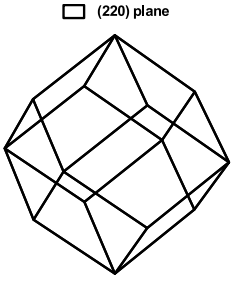

FIGURE C.11: Wulff construction representation obtained for the ZnSe-QD using the calculated surface energies (see Table C.6) of the predominant surface peaks in the experimental XRD. The Figure was created by Eric Mates-Torres.

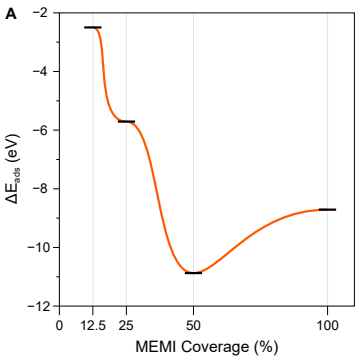

FIGURE C.12: Coverage analysis of MEMI ligands on the ZnSe | MEMI system. A coverage of 12.5 % corresponds to a $p(2\times2)$ ZnSe(220) surface with 1 of the 8 Zn surface sites occupied by a MEMI ligand; 25 % corresponds to a $p(2\times1)$ ZnSe(220) surface with 1 of the 4 sites covered; 50 %, to a $p(2\times1)$ surface with 2 of the 4 sites covered; and 100 %, to a $p(1\times1)$ surface with all of the 2 sites covered. The Figure was created by Eric Mates-Torres.

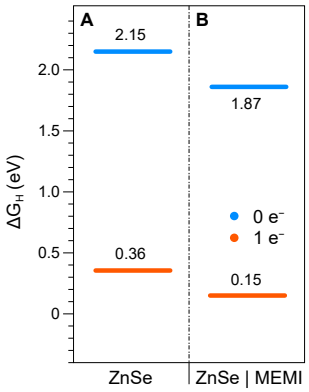

FIGURE C.13: Gibbs adsorption energies (in eV) of a H atom, ΔG_H, atop the active surface Zn sites of a (A) bare $p(2\times1)$ ZnSe(220) surface and (B) a $p(2\times1)$ ZnSe(220) surface with a 50 % MEMI coverage. For all systems, adsorption energies have been calculated without (blue trace, 0 e^-) and with the presence of a photogenerated electron (red trace, 1 e^-) by adding an additional electron in the simulation. The Figure was created by Eric Mates-Torres.

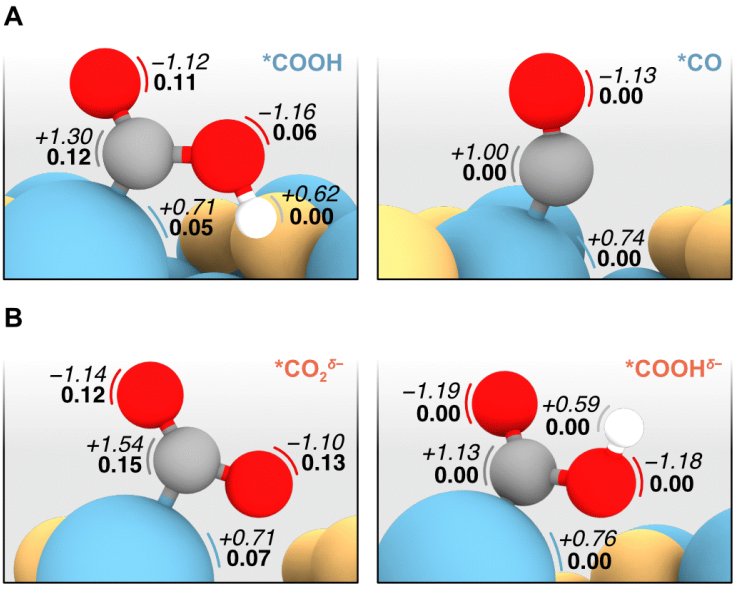

FIGURE C.14: Side view representation of the relevant intermediates along the two proposed pathways, (**A**) the conventional mechanism where CO_2 is activated in a concerted step with a PCET forming a *COOH (Path *a* in the main section), and (**B**) the proposed mechanism where CO_2 interacts with a surface photogenerated electron to form $*CO_2^{\delta-}$ (Path *b* in the main section). Atomic Bader charges (in e) are displayed in italics beside each atom, while magnetizations (in μ_B) are shown in bold. Note that neighbouring MEMI ligands have been omitted for clarity. The computational data reported in this work, including the cartesian coordinates and energies of all the modelled structures, are accessible via the following ioChem-BD online dataset, DOI: *10.19061/iochem-bd-6-36*. The Figure was created by Eric Mates-Torres.

C.2 Surface modification with dithiols

C.2.1 Supplementary Tables

TABLE C.7: Optimisation of photocatalytic CO_2 reduction using ZnSe-BF_4 and dithiols. The reason for the overall lower activity of ZnSe | Ni(cycP) towards CO (in comparison to Chapter 4) is due to QD batch-to-batch variations, presumably related to slight inconsistencies during the ligand removal process of the QD preparation procedure. To exclude that the observed effects are "one-off" of one specific batch, the experiment was repeated with a different QD batch and showed the same trends (Figure C.20). Unless otherwise stated, standard conditions were: 0.5 μM ZnSe-BF_4, 0.1 M AA/$NaHCO_3$, 3 mL water under CO_2 flow (4 sccm); 100 mW cm^{-2}, AM 1.5G, $\lambda > 400$ nm, 10 h irradiation, 25 °C

Catalyst	Ligand loading / μM	Co-catalyst loading /μM	Dithiol length / Å	n (H_2) $\pm \sigma$ / μmol	n (CO) $\pm \sigma$ / μmol	CO selectivity
ZnSe | dithiol (pH 6.5)						
ZnSe	0	0	0	16.7 ± 4.60	0.15 ± 0.02	0.9% ± 0.1%
ZnSe | EDT	50	0	4.3	5.29 ± 0.79	0.95 ± 0.19	15.1% ± 2.6%
ZnSe | BuDT	50	0	6.8	5.84 ± 0.99	0.46 ± 0.06	7.4% ± 0.4%
ZnSe | HexDT	50	0	9.3	8.18 ± 1.23	0.14 ± 0.03	1.7% ± 0.3%
ZnSe | OctDT	50	0	11.7	4.21 ± 0.63	0.27 ± 0.04	5.9% ± 0.5%
ZnSe | BenzDT	50	0	6.4	7.49 ± 0.97	0.19 ± 0.01	2.6% ± 0.3%
ZnSe | HO-EtOH	50	0	-	14.5 ± 7.89	0.56 ± 0.06	4.5% ± 2.5%
ZnSe | BuSH	50	0	-	16.8 ± 6.38	0.17 ± 0.04	1.1% ± 0.6%
ZnSe | Ni(cycP) | dithiol (pH 5.5)						
ZnSe | Ni(cycP)	0	10	0	25.7 ± 3.69	1.09 ± 0.18	4.0% ± 0.2%
ZnSe | Ni(cycP) | EDT	25	10	4.3	17.6 ± 2.64	1.21 ± 0.18	6.4% ± 0.3%
ZnSe | Ni(cycP) | BuDT	25	10	6.8	11.6 ± 1.74	3.78 ± 0.46	24.5% ± 2.0%
ZnSe | Ni(cycP) | HexDT	25	10	9.3	6.19 ± 0.93	4.05 ± 0.25	39.6% ± 1.9%
ZnSe | Ni(cycP) | OctDT	25	10	11.7	5.82 ± 0.87	2.97 ± 0.24	33.8% ± 1.8%
ZnSe | Ni(cycP) | BenzDT	25	10	6.4	11.7 ± 0.59	1.45 ± 0.07	10.9% ± 0.5%
ZnSe | Ni(cycP) | HO-HexSH	25	10	-	22.4 ± 1.51	3.10 ± 0.16	12.2% ± 0.6%
ZnSe | Ni(cycP) | HexSH	25	10	-	17.9 ± 0.89	1.15 ± 0.06	6.0% ± 0.3%

TABLE C.8: Control experiments for the photocatalytic CO_2 reduction using dithiol functionalised ZnSe-BF_4 QDs. Unless otherwise stated, conditions were: 0.5 μM ZnSe-BF_4, 0.1 M AA/$NaHCO_3$ pH 6.5 (w/o cocatalyst) or 0.1 M AA pH 5.5 (w/ co-catalyst), 3 mL under CO_2 flow (4 sccm); 100 mW cm^{-2}, AM 1.5G, $\lambda > 400$ nm, 25 °C.

description	time / h	n(CO) $\pm$ σ / μmol	n(H_2) $\pm$ σ / μmol
std. experiment (ZnSe | EDT)	10	0.95 ± 0.19	5.29 ± 0.79
no EDT	10	0.15 ± 0.2	16.7 ± 4.60
no AA	20	not detected	not detected
no ZnSe QDs	20	not detected	not detected
no light	10	not detected	not detected
std. experiment (ZnSe|Ni(cycP)|HexDT)	10	4.05 ± 0.25	6.19 ± 0.93
no Ni(cycP)	10	0.35 ± 0.08	12.07 ± 0.60
no HexDT	10	1.09 ± 0.18	25.7 ± 3.69
no AA	20	not detected	not detected
no ZnSe QDs	20	not detected	not detected
no light	20	not detected	not detected

TABLE C.9: pH controls. Unless otherwise stated, standard conditions were: 0.5 μM ZnSe-BF_4, 0.1 M AA/$NaHCO_3$, 3 mL solution under CO_2 flow (4 sccm); 100 mW cm^{-2}, AM 1.5G, $\lambda > 400$ nm, 10 h irradiation, 25 °C.

Catalyst	Ligand loading / μM	Co-catalyst loading / μM	pH	n (H_2) $\pm$ σ / μmol	n (CO) $\pm$ σ / μmol	CO selectivity
ZnSe | dithiol						
ZnSe | EDT	50	0	6.5	5.29 ± 0.79	0.95 ± 0.19	15.1% ± 2.6%
ZnSe | EDT	50	0	5.5	17.2 ± 0.86	0.68 ± 0.08	0.9% ± 0.1
ZnSe | HexDT	50	0	6.5	8.18 ± 1.23	0.14 ± 0.03	1.7% ± 0.3%
ZnSe | HexDT	50	0	5.5	8.43 ± 0.42	0.11 ± 0.01	1.3% ± 0.1
ZnSe | Ni(cycP) | dithiol						
ZnSe | Ni(cycP) | EDT	25	10	6.5	9.54 ± 1.05	0.42 ± 0.02	4.2% ± 0.6%
ZnSe | Ni(cycP) | EDT	25	10	5.5	17.6 ± 2.64	1.21 ± 0.18	6.4% ± 0.3%
ZnSe | Ni(cycP) | HexDT	25	10	6.5	7.25 ± 0.36	0.97 ± 0.22	11.8% ± 2.5%
ZnSe | Ni(cycP) | HexDT	25	10	5.5	6.19 ± 0.93	4.05 ± 0.25	39.6% ± 1.9%

C.2.2 Supplementary Figures

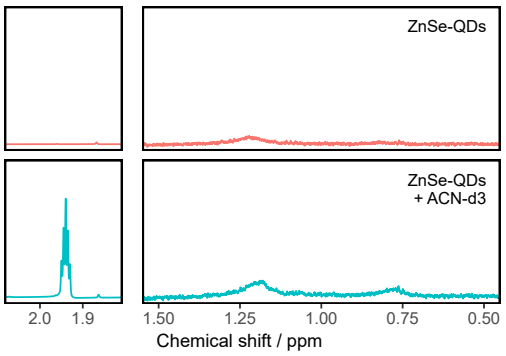

FIGURE C.15: Addition of ACN-d3 (50 μL) to a solution of ZnSe QDs (2 μM, in D_2O). The signal at 1.95 ppm is the residual solvent from ACN-d3. The broad signal at 1.20 ppm is already visible in the ZnSe QD reference and presumably originates from surface coordinated solvents (such as DMF). The signal at 0.76 ppm arises upon addition of ACN-d3 and is assigned to coordinated ACN-d3 on the QD surface. Note the right part of the spectrum is a 10x zoom compared to the left.

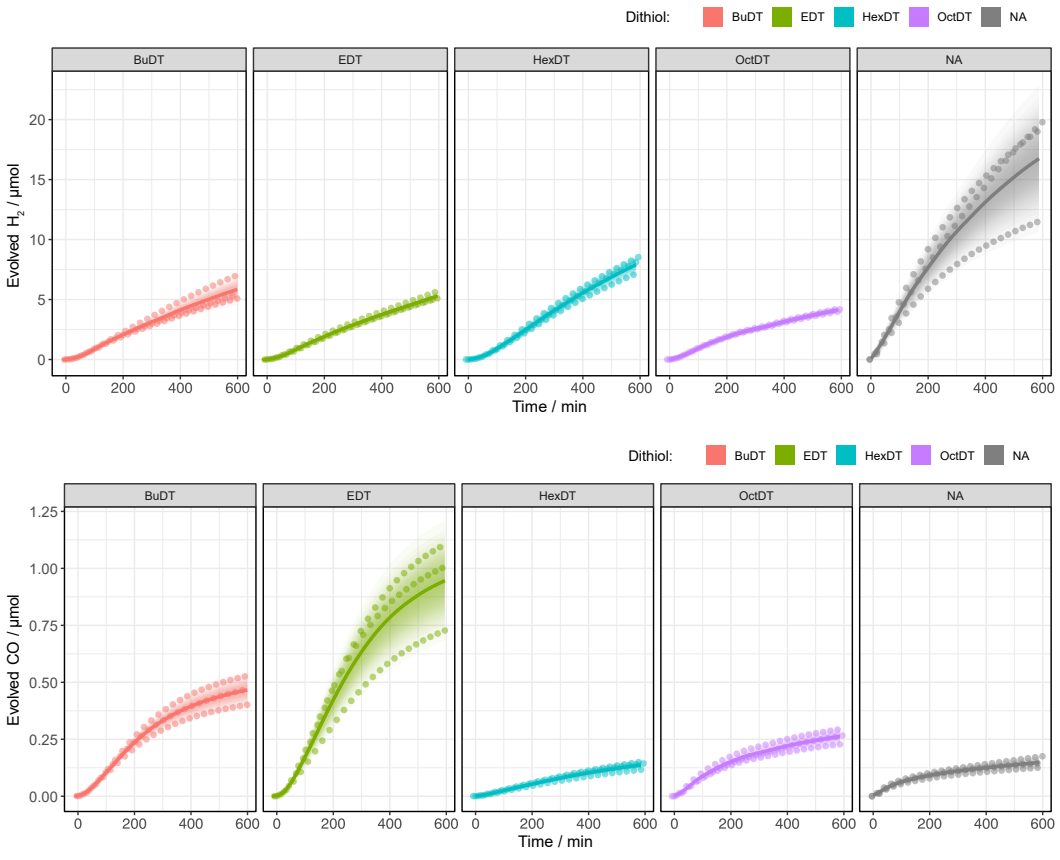

FIGURE C.16: Photocatalytic CO_2 reduction in the presence of ZnSe | dithiol: Conditions: 0.5 μM ZnSe-BF_4, 50 μM dithiol 0.1 M AA/$NaHCO_3$, pH 6.5, 3 mL under CO_2 flow (4 sccm); 100 mW cm^{-2}, AM 1.5G, $\lambda > 400$ nm, 25 °C.

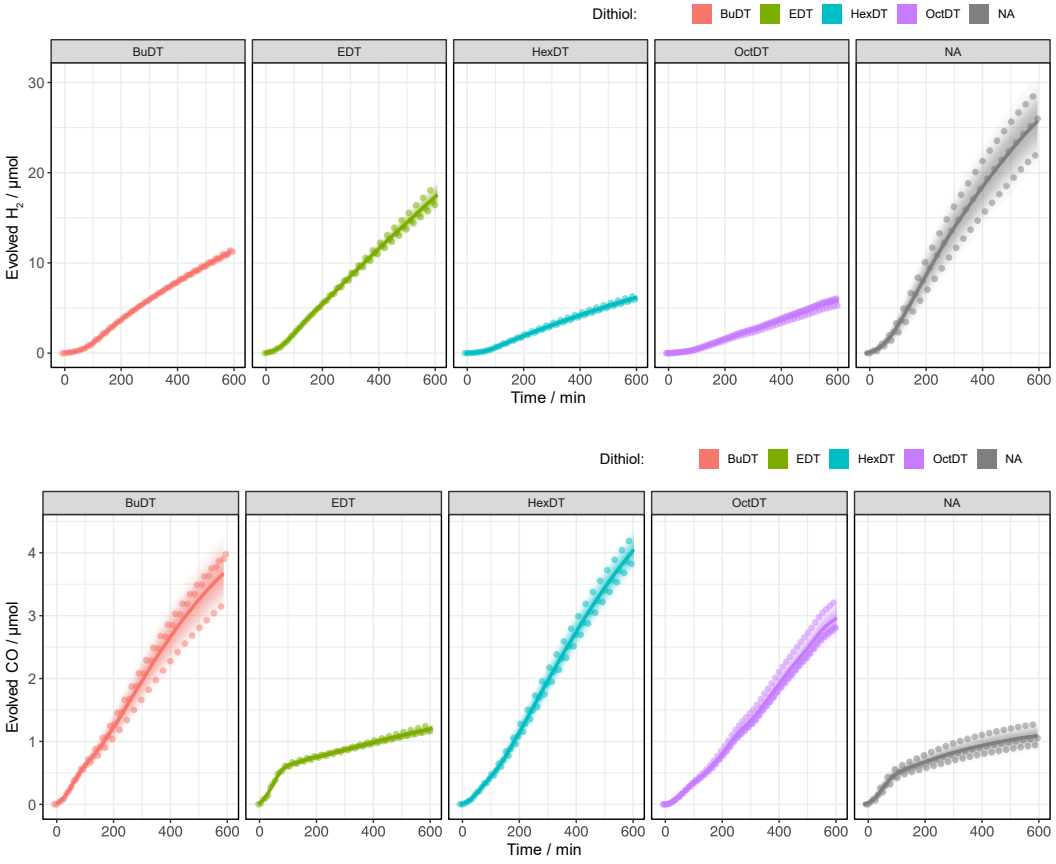

FIGURE C.17: Photocatalytic CO_2 reduction in the presence of ZnSe | Ni(cycP) | dithiol. Conditions: 0.5 μM ZnSe-BF_4, 25 μM dithiol, 10 μM Ni(cycP), 0.1 M AA, pH 5.5, 3 mL under CO_2 flow (4 sccm); 100 mW cm^{-2}, AM 1.5G, $\lambda > 400$ nm, 25 °C.

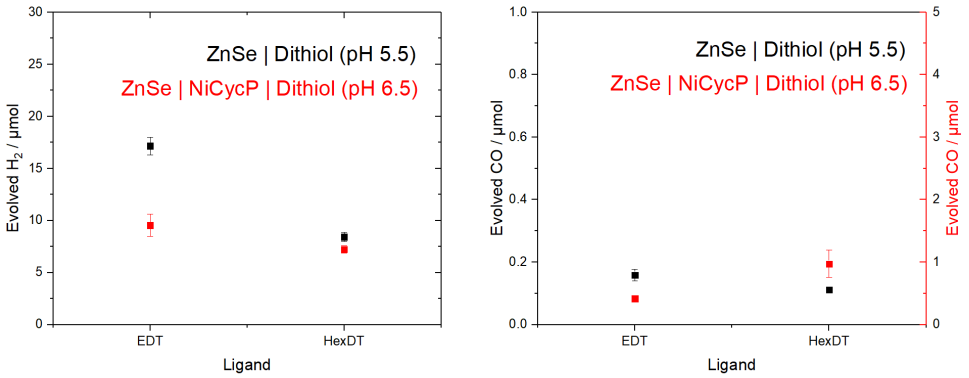

FIGURE C.18: Photocatalytic CO_2 reduction in the presence of ZnSe | dithiol: (Reverse) pH controls. Conditions: 0.5 μM ZnSe-BF_4, 0.1 M AA/$NaHCO_3$, for ZnSe | dithiol: 50 μM dithiol, for ZnSe | Ni(cycP) | dithiol: 25 μM dithiol, 10 μM Ni(cycP); 3 mL solution under CO_2 flow (4 sccm); 100 mW cm^{-2}, AM 1.5G, $\lambda > 400$ nm, 10 h irradiation, 25 °C. Based on two independent replicates.

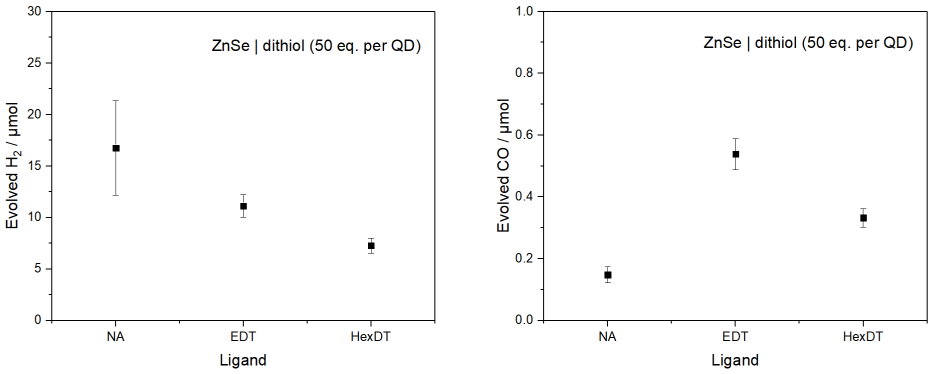

FIGURE C.19: Photocatalytic CO_2 reduction in the presence of ZnSe | dithiol: loading control. Conditions: 0.5 μM QD, 25 μM dithiol, 0.1 M AA/$NaHCO_3$, pH 6.5, 3 mL under CO_2 flow (4 sccm); 100 mW cm^{-2}, AM 1.5G, $\lambda > 400$ nm, 25 °C. Based on two independent replicates.

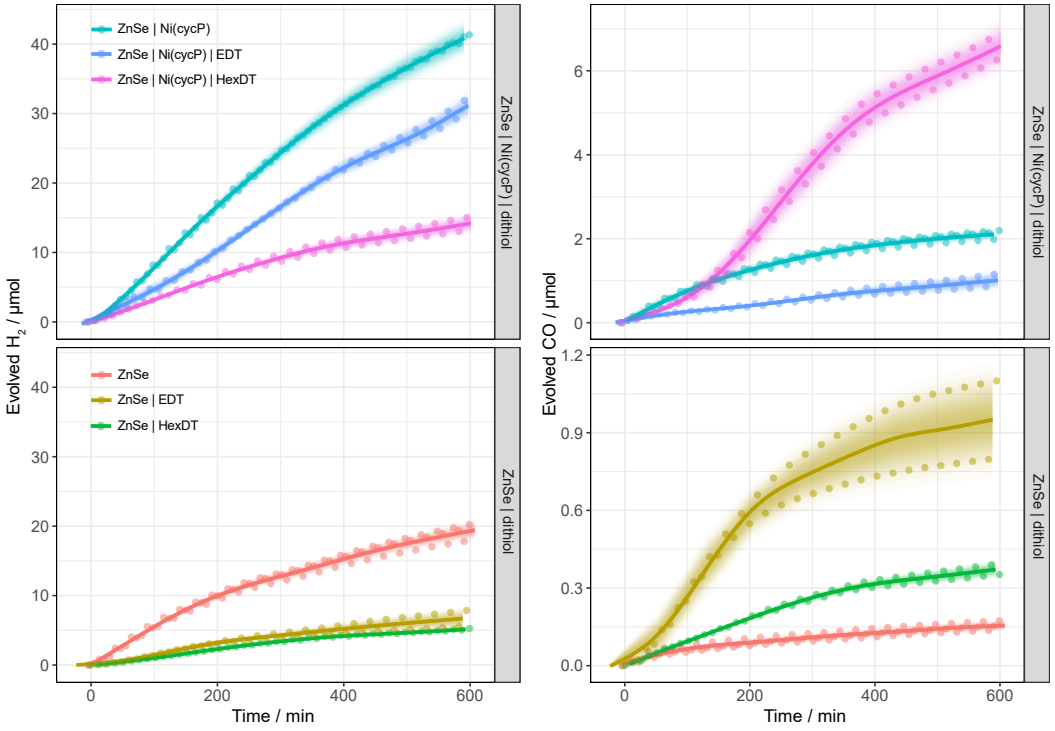

FIGURE C.20: Photocatalytic CO_2 reduction in the presence of ZnSe | dithiol: Batch control. This control experiment demonstrates that the observed trends during photocatalysis (benchmark cases ZnSe | EDT and ZnSe | Ni(cycP) | HexDT)) depending on the dithiol are reproducible and not unique to a specific QD batch. Conditions: 0.5 μM QD, 0.1 M AA/$NaHCO_3$, for ZnSe | dithiol: 50 μM dithiol, pH 6.5, for ZnSe | Ni(cycP) | dithiol: 25 μM dithiol, 10 μM Ni(cycP), pH 5.5; 3 mL under CO_2 flow (4 sccm); 100 mW cm^{-2}, AM 1.5G, $\lambda > 400$ nm, 25 °C. Based on two independent replicates.

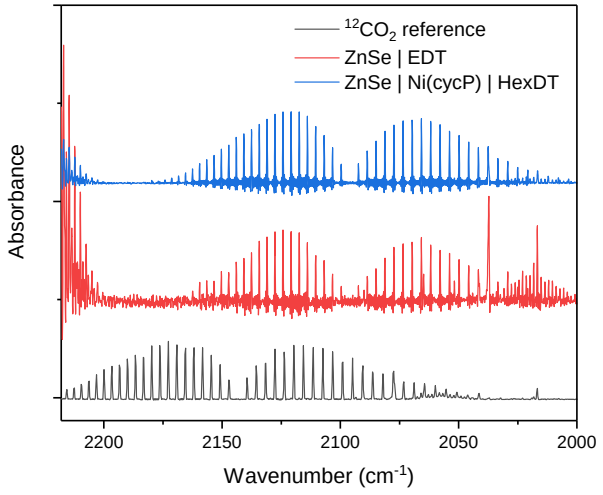

FIGURE C.21: Isotopic labelling: Gas-phase transmission IR spectra of the CO vibration depending on the employed CO_2 isotopologue. Samples ZnSe | EDT and ZnSe | Ni(CycP) | HexDT and under an atmosphere of $^{13}CO_2$ compared to a reference spectrum of ^{12}CO. Conditions: AM 1.5G, $\lambda > 400$ nm, 100 mW cm^{-2}, 0.5 μM ZnSe-BF_4, 0.1 M AA/$NaHCO_3$ pH 6.5 (w/o Ni(cycP), AA pH 5.5 (w/ Ni(cycP), CO_2, 16 h irradiation.

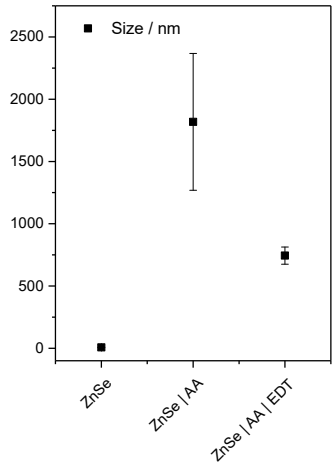

FIGURE C.22: DLS measurements of ZnSe-BF_4 QDs in water (neutral pH), in the presence of AA (0.1 M, pH 5.5) and additionally in the presence of EDT (200 equiv. per QD). Shown is the number mean.

Appendix D

Appendix to chapter 6: QD-sensitised photocathodes

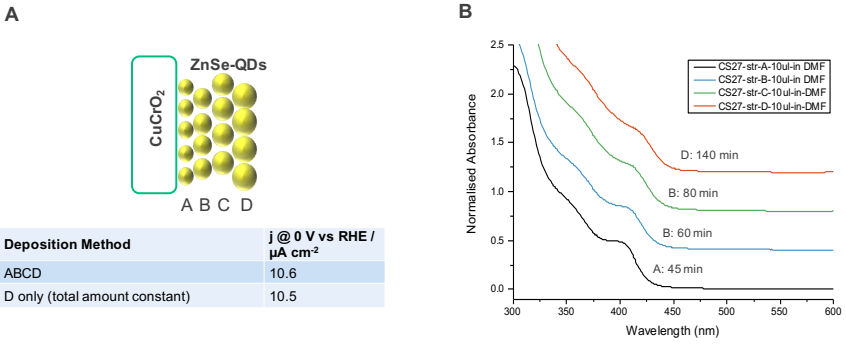

Deposition Method	j @ 0 V vs RHE / μA cm^{-2}
ABCD	10.6
D only (total amount constant)	10.5

FIGURE D.1: Outline of the proposed "rainbow" photocathode. (A) Outline and photocurrents. (B) UV-vis spectra of the four batches of QDs featuring different sizes.

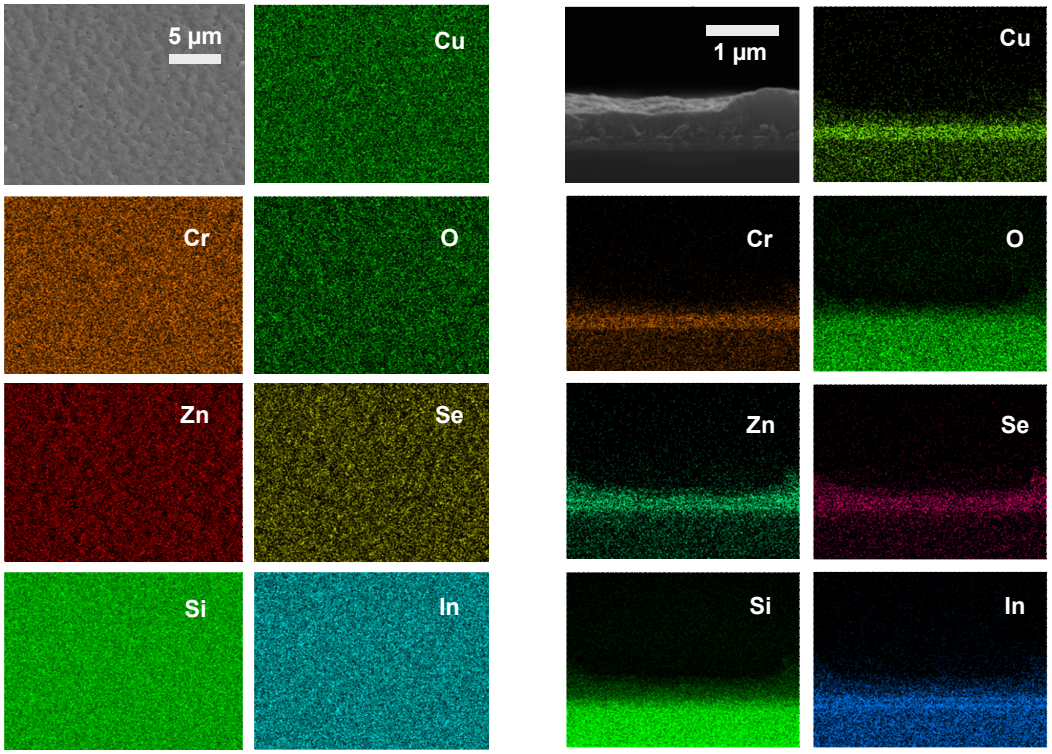

FIGURE D.2: Energy-dispersive X-ray (EDX) spectra of the $CuCrO_2$ | ZnSe photocathode. Left: Top-down view. Right: Cross-sectional view of ZnSe-modified $CuCrO_2$ areas.

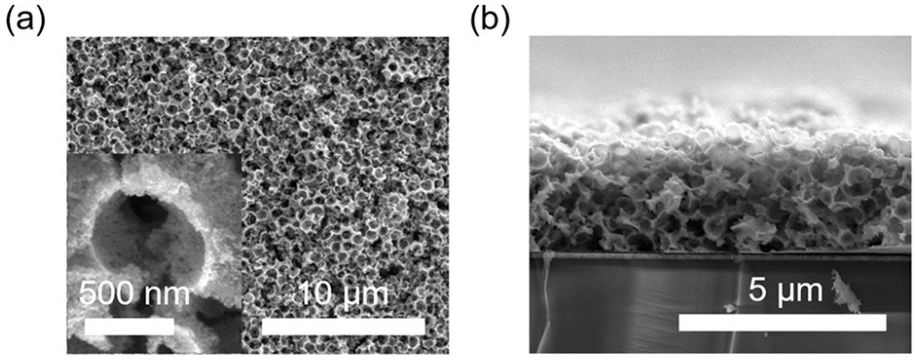

FIGURE D.3: SEM images of the IO-$CuCrO_2$ electrode. (a): Top-down view. (b): Cross-sectional. Figure reprinted from [407].

Entry	Photocathode	QD-deposition	Conditions	n (H_2) / nmol	FE / %
1	$CuCrO_2$|ZnSe-BF_4	Dropcast	N_2	44	5.2
2	$CuCrO_2$|ZnSe-BF_4	Dropcast	N_2	32	3.4
	average			38 ± 9	4.3 ± 1.3
3	$CuCrO_2$	-	N_2	6	-
4	$CuCrO_2$	-	N_2	4	-
	average	-		5 ± 1	-

TABLE D.1: CPPE of $CuCrO_2$|ZnSe photocathodes for H_2 evolution. Conditions: 0.1 M Na_2SO_4, pH 5.5, E_{app} = 0 V *vs.* RHE, illumination of 100 mW cm^{-2}, AM 1.5G, $\lambda > 400$ nm, 1 cm^2 active area.

Entry	Photocathode	Cat-deposition	Conditions	n (H2) [nmol]			n (CO) [nmol]		
				1-2 h	3-4 h	o/n	1-2 h	3-4 h	o/n
9	$^{IO}CuCrO_2$|ZnSe-BF_4	QD-soak	N_2	-	-	3	-	-	2
10	$^{flat}CuCrO_2$|ZnSe-BF_4	QD-soak	N_2	13	18	n/a	-	-	n/a
11	$^{IO}CuCrO_2$(thin)|ZnSe-BF_4	QD-soak	N_2	-	5	n/a	-	-	n/a

TABLE D.2: Screening of CPPE results of (*IO*)-$CuCrO_2$ | ZnSe photocathodes. "QD-soak" refers to a mild soaking method. Conditions: 0.1M Na_2SO_4, N_2 purged (pH 5.5); E_{app} = 0 V vs. RHE, illumination of 100 mW cm^{-2}, AM 1.5G, $\lambda > 400$ nm, 0.5 cm^2 (IO) or 1 cm^2 (flat) active area.

D.1 Further deposition optimisation

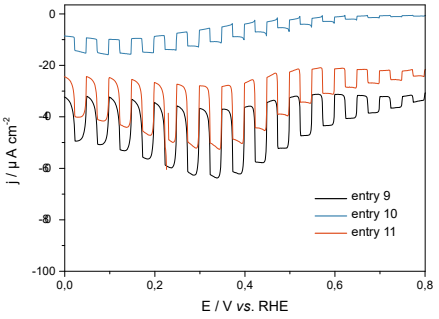

FIGURE D.4: Linear sweep voltammetry (LSV) of $CuCrO_2$|ZnSe photocathodes which have been prepared using the 'mild-soaking'technique under chopped light illumination.

As shown in the previous section, the $^{IO}CuCrO_2$ | ZnSe electrodes barely exhibited any photoelectrochemical activity. One reason for this might be related to 'overloading' of the electrode with QDs by dropcasting. Specifically in the case of the *IO*-structures, an overload of QDs might lead to poor electronic interactions and ultimately insulation. Inspired by how SAMs are assembled (immersion in very low concentration for elongated times (e.g. overnight) followed by rinsing steps), the $^{IO}CuCrO_2$ electrodes were immersed overnight in a strongly diluted (1:20 with acetonitrile) ZnSe-BF_4 solution. Electrodes were rinsed thoroughly before the CPPE experiments were conducted as described previously (Table D.2). The deposition method was tested with two IO-electrodes with various thicknesses (entry 9 and 11, the latter being a thinner version), under N_2 atmosphere aiming for H_2 evolution, however, only negligible amounts of H_2 were detected. For comparison, a flat $CuCrO_2$ was tested as well which produced 18 nmols H_2 after 3 h (entry 10), proving that the deposition method works in principle. The photocurrents were large for the *IO*-electrodes but rather low for the flat $CuCrO_2$ (see Appendix D.4); basically the opposite trend of the CPPE results. Large photocurrents clearly do not translate necessarily into product formation.

List of Figures

List of Tables

Abbreviations

E_{app}	Applied potential
E_g	Band gap energy
E_{onset}	Onset potential
AA	Ascorbic Acid
AM 1.5G	Air Mass 1.5 Global
ATR-IR	Attenuated total reflection infrared spectroscopy
ACN	Acetonitrile
BenzDT	Benzene-1,4-dithiol
bpy	bipyridine
BuDT	1,4-Butanedithiol
BuSH	1-Butanethiol
CA	Cysteamine
CB	Conduction Band
CdS-OA	Oleic acid capped CdS quantum dots
CdS-BF_4	BF_4 capped CdS quantum dots
CODH	Carbon monoxide dehydrogenase
CPE	Controlled potential electrolysis
CPPE	Controlled potential photoelectrolysis
CT	Charge transfer
CV	Cyclic Voltammetry
cyc	cyclam
DMF	N,N'-dimethylformamide
DLS	Dynamic light scattering
DTT	Dithiothreitol
EDT	1,2-Ethanedithiol
EDTA	Ethylenediaminetetraacetic acid
EDX	Energy-dispersive X-ray spectroscopy
EMIM-BF_4	1-ethyl-3-methylimidazolium tetra-fluoroborate
EQE	External Quantum Efficiency
ET	Electron transfer
FDH	Formate dehydrogenase
FE	Faradaic efficiency
FTIR	Fourier transform infrared spectoscopy

GC	Gas chromatography
HER	Hydrogen evolution reaction
HexDT	1,6-Hexanedithiol
HexSH	1-Hexanethiol
HOMO	Highest occupied molecular orbital
HO-EtSH	1,2-Mercaptoethanol
HO-HexSH	1,6-Mercaptohexanol
HRMS	High-resolution mass spectrometry
ICP-OES	Inductively Coupled Plasma-Optical Emission Spectroscopy
IL	Ionic liquid
IR	Infrared
ITO	Indium tin oxide
IO	Inverse-opal
j	Photocurrent Density
LSV	linear sweep voltammogram
LUMO	Lowest unoccupied molecular orbital
MEDA	N-(2-mercaptoethyl)dimethylamine
MEMI	3-(2-mercaptoethyl)-1-methyl-imidazolium
M-MEMI	3-(2-mercaptoethyl)-1,2-dimethyl-imidazolium
META	N-(2-mercaptoethyl)trimethylammonium
MeOH	methanol
MEPA	Mercaptoethylphosphonic acid
MFC	Mass flow controller
MP	4-Mercaptopyridine
MPA	Mercaptopropionic acid
MOF	Metal-organic Framework
NHE	Normal hydrogen electrode
NMR	Nuclear magnetic resonance
OctDT	1,8-octanedithiol
O.D.	Optical Density
ODE	Octadecene
PEC	Photoelectrochemical
PL	Photoluminescence
PV	Photovoltaic
PYET	2-(4-Pyridinyl)ethanethiol
QD	Quantum Dot
qpy	quarterpyridine
RHE	Reversible hydrogen electrode $E_{RHE} = E_{NHE} + 0.0591\ x$ pH
SAM	Self assembled monolayer
sccm	Standard cubic centimetre per minute
SED	Sacrificial electron donor
SEM	scanning electron microscopy

TAS	Transient Absorption Spectroscopy
TEOA	Triethanolamine
TEM	Transmission Electron Microscopy
terpy	terpyridine
TMA	trimethylammonium
TON	Turnover Number
TPA	Tris(2-pyridylmethyl)amine
tpp	tetraphenylporphyrin
UV	Ultraviolet
UPS	Ultraviolet photoelectron spectroscopy
VB	Valence Band
WE	Working electrode
XRD	X-ray diffraction
XPS	X-ray photoelectron spectroscopy
ZnSe-BF_4	BF_4^- Capped Zinc Selenide Quantum Dots
ZnSe-St	Stearate Capped Zinc Selenide Quantum Dots

Bibliography

[1] BP: Statistical Review of World Energy (69th edition), **2020**.

[2] Earth System Research Laboratories - Global Monitoring Laboratory, Trends in Atmospheric Carbon Dioxide (accessed April 2020).

[3] T. R. Karl, K. E. Trenberth, *Science* **2003**, *302*, 1719–1723.

[4] C. P. Morice, J. J. Kennedy, N. A. Rayner, P. D. Jones, *Journal of Geophysical Research: Atmospheres* **2012**, *117*, D08101.

[5] Intergovernmental Panel on Climate Change (IPPC), Climate Change 2013: The Physical Science Basis. Contribution of Working Group I to the Fifth Assessment Report of the Intergovernmental Panel on Climate Change, **2013**.

[6] Intergovernmental Panel on Climate Change (IPPC), Climate Change 2014: Impacts, Adaptation, and Vulnerability. Part A: Global and Sectoral Aspects. Contribution of Working Group II to the Fifth Assessment Report of the Intergovernmental Panel on Climate Change, **2014**.

[7] B. Bereiter, S. Eggleston, J. Schmitt, C. Nehrbass-Ahles, T. F. Stocker, H. Fischer, S. Kipfstuhl, J. Chappellaz, *Geophysical Research Letters* **2015**, *42*, 542–549.

[8] N. S. Lewis, D. G. Nocera, *Proceedings of the National Academy of Sciences* **2006**, *103*, 15729–15735.

[9] BP: Statistical Review of World Energy (68th edition), **2019**.

[10] International Energy Agency, Share of electricity in total final energy consumption, historical and SDS (accessed on April 2020).

[11] F. Lafond, A. Gotway, J. David, D. Rebois, R. Zadourian, P. Mcsharry, J. D. Farmer, *Technological Forecasting & Social Change* **2018**, *128*, 104–117.

[12] S. C. Roy, O. K. Varghese, M. Paulose, C. Grimes, *ACS Nano* **2010**, *4*, 1259–1278.

[13] K. E. Dalle, J. Warnan, J. J. Leung, B. Reuillard, I. S. Karmel, E. Reisner, *Chemical Reviews* **2019**, *119*, 2752–2875.

[14] R. J. Detz, J. N. H. Reek, B. C. C. van der Zwaan, *Energy & Environmental Science* **2018**, *11*, 1653–1669.

[15] B. A. Pinaud, J. D. Benck, L. C. Seitz, A. J. Forman, Z. Chen, T. G. Deutsch, B. D. James, K. N. Baum, G. N. Baum, S. Ardo, H. Wang, E. Miller, T. F. Jaramillo, *Energy & Environmental Science* **2013**, *6*, 1983.

[16] J. H. Montoya, L. C. Seitz, P. Chakthranont, A. Vojvodic, T. F. Jaramillo, J. K. Nørskov, *Nature Materials* **2017**, *16*, 70–81.

[17] J. Newman, P. G. Hoertz, C. A. Bonino, J. A. Trainham, *Journal of The Electrochemical Society* **2012**, *159*, A1722–A1729.

[18] J. K. Stolarczyk, S. Bhattacharyya, L. Polavarapu, J. Feldmann, *ACS Catalysis* **2018**, *8*, 3602–3635.

[19] M. S. Prévot, K. Sivula, *The Journal of Physical Chemistry C* **2013**, *117*, 17879–17893.

[20] M. R. Singh, E. L. Clark, A. T. Bell, *Proceedings of the National Academy of Sciences* **2015**, *112*, E6111–E6118.

[21] T. J. Jacobsson, *Energy & Environmental Science* **2018**, *11*, 1977–1979.

[22] B. Kumar, M. Llorente, J. Froehlich, T. Dang, A. Sathrum, C. P. Kubiak, *Annual Review of Physical Chemistry* **2012**, *63*, 541–569.

[23] C. D. Windle, E. Reisner, *CHIMIA International Journal for Chemistry* **2015**, *69*, 435–441.

[24] Q. Wang, T. Hisatomi, Q. Jia, H. Tokudome, M. Zhong, C. Wang, Z. Pan, T. Takata, M. Nakabayashi, N. Shibata, Y. Li, I. D. Sharp, A. Kudo, T. Yamada, K. Domen, *Nature Materials* **2016**, *15*, 611–615.

[25] E. S. Andreiadis, M. Chavarot-Kerlidou, M. Fontecave, V. Artero, *Photochemistry and Photobiology* **2011**, *87*, 946–964.

[26] Z. Wang, C. Li, K. Domen, *Chemical Society Reviews* **2019**, *48*, 2109–2125.

[27] J. Artz, T. E. Müller, K. Thenert, J. Kleinekorte, R. Meys, A. Sternberg, A. Bardow, W. Leitner, *Chemical Reviews* **2018**, *118*, 434–504.

[28] Y. Y. Birdja, E. Pérez-Gallent, M. C. Figueiredo, A. J. Göttle, F. Calle-Vallejo, M. T. M. Koper, *Nature Energy* **2019**, *4*, 732–745.

[29] M. B. Ross, P. De Luna, Y. Li, C.-T. Dinh, D. Kim, P. Yang, E. H. Sargent, *Nature Catalysis* **2019**, *2*, 648–658.

[30] Royal Society of Chemistry: Solar Fuels and Artificial Photosynthesis - Science and innovation to change our future energy options, tech. rep. January, **2012**, pp. 1–26.

[31] F. Fischer, H. Tropsch, *Brennstoff-Chemie* **1926**, *7*, 97–104.

[32] V. Sathish, A. Ramdass, P. Thanasekaran, K.-L. Lu, S. Rajagopal, *Journal of Photochemistry and Photobiology C: Photochemistry Reviews* **2015**, *23*, 25–44.

[33] IUPAC, *Compendium of Chemical Terminology 2nd ed. (the "Gold Book")* **1997**.

[34] H. Takeda, C. Cometto, O. Ishitani, M. Robert, *ACS Catalysis* **2017**, *7*, 70–88.

[35] B. Durham, J. V. Caspar, J. K. Nagle, T. J. Meyer, *Journal of the American Chemical Society* **1982**, *104*, 4803–4810.

[36] A. H. A. Tinnemans, T. P. M. Koster, D. H. M. W. Thewissen, A. Mackor, *Recueil des Travaux Chimiques des Pays-Bas* **2010**, *103*, 288–295.

[37] P. Zhang, M. Wang, Y. Na, X. Li, Y. Jiang, L. Sun, *Dalton Trans.* **2010**, *39*, 1204–1206.

[38] S. L.-F. Chan, T. L. Lam, C. Yang, S.-C. Yan, N. M. Cheng, *Chemical Communications* **2015**, *51*, 7799–7801.

[39] D. Duonghong, E. Borgarello, M. Graetzel, *Journal of the American Chemical Society* **1981**, *103*, 4685–4690.

[40] E.-G. Ha, J.-A. Chang, S.-M. Byun, C. Pac, D.-M. Jang, J. Park, S. O. Kang, *Chemical Communications* **2014**, *50*, 4462–4464.

[41] C. D. Windle, E. Pastor, A. Reynal, A. C. Whitwood, Y. Vaynzof, J. R. Durrant, R. N. Perutz, E. Reisner, *Chemistry - A European Journal* **2015**, *21*, 3746–3754.

[42] S. Sato, T. Morikawa, S. Saeki, T. Kajino, T. Motohiro, *Angewandte Chemie International Edition* **2010**, *49*, 5101–5105.

[43] T. M. Suzuki, H. Tanaka, T. Morikawa, M. Iwaki, S. Sato, S. Saeki, M. Inoue, T. Kajino, T. Motohiro, *Chemical Communications* **2011**, *47*, 8673.

[44] F. Yoshitomi, K. Sekizawa, K. Maeda, O. Ishitani, *ACS Applied Materials & Interfaces* **2015**, *7*, 13092–13097.

[45] A. Ishikawa, T. Takata, T. Matsumura, J. N. Kondo, M. Hara, H. Kobayashi, K. Domen, *Journal of Physical Chemistry B* **2004**, *35*, 2637–2642.

[46] Q. Wang, K. Domen, *Chemical Reviews* **2020**, *120*, 919–985.

[47] S. Xie, Q. Zhang, G. Liu, Y. Wang, *Chemical Communications* **2016**, *52*, 35–59.

[48] J. Willkomm, K. L. Orchard, A. Reynal, E. Pastor, J. R. Durrant, E. Reisner, *Chemical Society Reviews* **2016**, *45*, 9–23.

[49] X. Wang, K. Maeda, A. Thomas, K. Takanabe, G. Xin, J. M. Carlsson, K. Domen, M. Antonietti, *Nature Materials* **2009**, *8*, 76–80.

[50] Y. Wang, X. Wang, M. Antonietti, *Angewandte Chemie International Edition* **2012**, *51*, 68–89.

[51] K. Maeda, K. Sekizawa, O. Ishitani, *Chemical Communications* **2013**, *49*, 10127.

[52] B. C. Martindale, G. A. Hutton, C. A. Caputo, E. Reisner, *Journal of the American Chemical Society* **2015**, *137*, 6018–6025.

[53] G. A. M. Hutton, B. C. M. Martindale, E. Reisner, *Chemical Society Reviews* **2017**, *46*, 6111–6123.

[54] X.-B. Li, C.-H. Tung, L.-Z. Wu, *Nature Reviews Chemistry* **2018**, *2*, 160–173.

[55] M. B. Wilker, K. J. Schnitzenbaumer, G. Dukovic, *Israel Journal of Chemistry* **2012**, *52*, 1002–1015.

[56] Y. Pellegrin, F. Odobel, *Comptes Rendus Chimie* **2017**, *20*, 283–295.

[57] D. W. Wakerley, M. F. Kuehnel, K. L. Orchard, K. H. Ly, T. E. Rosser, E. Reisner, *Nature Energy* **2017**, *2*, 17021.

[58] T. Uekert, M. F. Kuehnel, D. W. Wakerley, E. Reisner, *Energy and Environmental Science* **2018**, *11*, 2853–2857.

[59] R. A. Marcus, *The Journal of Chemical Physics* **1956**, *24*, 966–978.

[60] R. A. Marcus, *The Journal of Chemical Physics* **1965**, *43*, 2654–2657.

[61] H. Zhu, Y. Yang, K. Wu, T. Lian, *Annual Review of Physical Chemistry* **2016**, *67*, 259–281.

[62] H. Zhu, Y. Yang, K. Hyeon-Deuk, M. Califano, N. Song, Y. Wang, W. Zhang, O. V. Prezhdo, T. Lian, *Nano Letters* **2014**, *14*, 1263–1269.

[63] J. R. Miller, L. T. Calcaterra, G. L. Closs, *Journal of the American Chemical Society* **1984**, *106*, 3047–3049.

[64] A. J. Morris-Cohen, M. D. Peterson, M. T. Frederick, J. M. Kamm, E. A. Weiss, *The Journal of Physical Chemistry Letters* **2012**, *3*, 2840–2844.

[65] M. J. Berr, A. Vaneski, C. Mauser, S. Fischbach, A. S. Susha, A. L. Rogach, F. Jäckel, J. Feldmann, *Small* **2012**, *8*, 291–297.

[66] L. Amirav, A. P. Alivisatos, *The Journal of Physical Chemistry Letters* **2010**, *1*, 1051–1054.

[67] Y. Wang, Q. Wang, X. Zhan, F. Wang, M. Safdar, J. He, *Nanoscale* **2013**, *5*, 8326.

[68] B. Zhou, B. Shi, D. Jin, X. Liu, *Nature Nanotechnology* **2015**, *10*, 924–936.

[69] B. O'Regan, M. Grätzel, *Nature* **1991**, *353*, 737–740.

[70] K. Maeda, *ACS Catalysis* **2013**, *3*, 1486–1503.

[71] M. V. Kovalenko, *Nature Nanotechnology* **2015**, *10*, 994–997.

[72] A. P. Alivisatos, *The Journal of Physical Chemistry* **1996**, *100*, 13226–13239.

[73] L. E. Brus, *The Journal of Chemical Physics* **1983**, *79*, 5566.

[74] L. E. Brus, *The Journal of Chemical Physics* **1984**, *80*, 4403.

[75] J. S. Kamal, A. Omari, K. Van Hoecke, Q. Zhao, A. Vantomme, F. Vanhaecke, R. K. Capek, Z. Hens, *The Journal of Physical Chemistry C* **2012**, *116*, 5049–5054.

[76] W. W. Yu, L. Qu, W. Guo, X. Peng, *Chemistry of Materials* **2003**, *15*, 2854–2860.

[77] F. E. Osterloh, *Chemical Society Reviews* **2013**, *42*, 2294–2320.

[78] K. Wu, H. Zhu, Z. Liu, W. Rodríguez-Córdoba, T. Lian, *Journal of the American Chemical Society* **2012**, *134*, 10337–10340.

[79] M. A. Boles, D. Ling, T. Hyeon, D. V. Talapin, *Nature Materials* **2016**, *15*, 141–153.

[80] R. Memming, *Semiconductor Electrochemistry (2nd Edition)*, WILEY-VCH Verlag GmbH, **2015**, p. 307.

[81] J. Park, J. Joo, S. G. Kwon, Y. Jang, T. Hyeon, *Angewandte Chemie International Edition* **2007**, *46*, 4630–4660.

[82] S. G. Kwon, T. Hyeon, *Small* **2011**, *7*, 2685–2702.

[83] K. J. Klabunde, R. M. Richards, *Nanoscale Materials in Chemistry, 2nd Edition*, John Wiley and Sons, **2009**.

[84] A. Heuer-Jungemann, N. Feliu, I. Bakaimi, M. Hamaly, A. Alkilany, I. Chakraborty, A. Masood, M. F. Casula, A. Kostopoulou, E. Oh, K. Susumu, M. H. Stewart, I. L. Medintz, E. Stratakis, W. J. Parak, A. G. Kanaras, *Chemical Reviews* **2019**, *119*, 4819–4880.

[85] Y. Yin, A. P. Alivisatos, *Nature* **2005**, *437*, 664–670.

[86] C. R. Bullen, P. Mulvaney, *Nano Letters* **2004**, *4*, 2303–2307.

[87] C. B. Murray, D. J. Norris, M. G. Bawendi, *Journal of the American Chemical Society* **1993**, *115*, 8706–8715.

[88] E. A. Weiss, *ACS Energy Letters* **2017**, *2*, 1005–1013.

[89] J. C. Love, L. A. Estroff, J. K. Kriebel, R. G. Nuzzo, G. M. Whitesides, *Chemical Reviews* **2005**, *105*, 1103–1170.

[90] M. S. Kodaimati, K. P. McClelland, C. He, S. Lian, Y. Jiang, Z. Zhang, E. A. Weiss, *Inorganic Chemistry* **2018**, *57*, 3659–3670.

[91] J. S. Owen, J. Park, P.-E. Trudeau, A. P. Alivisatos, *Journal of the American Chemical Society* **2008**, *130*, 12279–12281.

[92] J. Owen, *Science* **2015**, *347*, 615–616.

[93] B. Fritzinger, R. K. Capek, K. Lambert, J. C. Martins, Z. Hens, *Journal of the American Chemical Society* **2010**, *132*, 10195–10201.

[94] M. J. Hostetler, A. C. Templeton, R. W. Murray, *Langmuir* **1999**, *15*, 3782–3789.

[95] A. Nag, M. V. Kovalenko, J.-S. Lee, W. Liu, B. Spokoyny, D. V. Talapin, *Journal of the American Chemical Society* **2011**, *133*, 10612–10620.

[96] R. D. Harris, S. Bettis Homan, M. Kodaimati, C. He, A. B. Nepomnyashchii, N. K. Swenson, S. Lian, R. Calzada, E. A. Weiss, *Chemical Reviews* **2016**, *116*, 12865–12919.

[97] S. Padgaonkar, J. N. Olding, L. J. Lauhon, M. C. Hersam, E. A. Weiss, *Accounts of Chemical Research* **2020**, *53*, 763–772.

[98] A. H. Ip, S. M. Thon, S. Hoogland, O. Voznyy, D. Zhitomirsky, R. Debnath, L. Levina, L. R. Rollny, G. H. Carey, A. Fischer, K. W. Kemp, I. J. Kramer, Z. Ning, A. J. Labelle, K. W. Chou, A. Amassian, E. H. Sargent, *Nature Nanotechnology* **2012**, *7*, 577–582.

[99] J. Aldana, Y. A. Wang, X. Peng, *Journal of the American Chemical Society* **2001**, *123*, 8844–8850.

[100] S. Hohng, T. Ha, *Journal of the American Chemical Society* **2004**, *126*, 1324–1325.

[101] S. Jeong, M. Achermann, J. Nanda, S. Ivanov, V. I. Klimov, J. A. Hollingsworth, *Journal of the American Chemical Society* **2005**, *127*, 10126–10127.

[102] P. R. Brown, D. Kim, R. R. Lunt, N. Zhao, M. G. Bawendi, J. C. Grossman, V. Bulovic, *ACS Nano* **2014**, *8*, 5863–5872.

[103] M. T. Frederick, E. Weiss, *ACS Nano* **2010**, *4*, 3195–3200.

[104] M. Tagliazucchi, D. B. Tice, C. M. Sweeney, A. J. Morris-Cohen, E. A. Weiss, *ACS Nano* **2011**, *5*, 9907–9917.

[105] Z. Zhang, K. Edme, S. Lian, E. A. Weiss, *Journal of the American Chemical Society* **2017**, *139*, 4246–4249.

[106] J. Kolny, A. Kornowski, H. Weller, *Nano Letters* **2002**, *2*, 361–364.

[107] E. L. Rosen, R. Buonsanti, A. Llordes, A. M. Sawvel, D. J. Milliron, B. A. Helms, *Angewandte Chemie International Edition* **2012**, *51*, 684–689.

[108] R. M. Young, S. C. Jensen, K. Edme, Y. Wu, M. D. Krzyaniak, N. A. Vermeulen, E. J. Dale, J. F. Stoddart, E. A. Weiss, M. R. Wasielewski, D. T. Co, *Journal of the American Chemical Society* **2016**, *138*, 6163–6170.

[109] S. Lian, M. S. Kodaimati, E. A. Weiss, *ACS Nano* **2018**, *12*, 568–575.

[110] C. M. Thompson, M. Kodaimati, D. Westmoreland, R. Calzada, E. A. Weiss, *Journal of Physical Chemistry Letters* **2016**, *7*, 3954–3960.

[111] A. Perosa, M. Selva, V. Lucchini, M. Fabris, M. Noè, *International Journal of Chemical Kinetics* **2011**, *43*, 154–160.

[112] F. G. Bordwell, X.-M. Zhang, A. V. Satish, J.-P. Cheng, *Journal of the American Chemical Society* **1994**, *116*, 6605–6610.

[113] D. P. Nair, M. Podgórski, S. Chatani, T. Gong, W. Xi, C. R. Fenoli, C. N. Bowman, *Chemistry of Materials* **2014**, *26*, 724–744.

[114] K. W. E. Sy Piecco, A. M. Aboelenen, J. R. Pyle, J. R. Vicente, D. Gautam, J. Chen, *ACS Omega* **2018**, *3*, 14327–14332.

[115] R. Munday, *Free Radical Biology and Medicine* **1989**, *7*, 659–673.

[116] R. E. Hansen, J. R. Winther, *Analytical Biochemistry* **2009**, *394*, 147–158.

[117] H. O. Finklea, A. J. Bard, I. Rubinstein, *Electroanalytical Chemistry: A Series of Advances* **1996**, *19*, 109.

[118] W. Andreoni, A. Curioni, H. Grönbeck, *International Journal of Quantum Chemistry* **2000**, *80*, 598–608.

[119] C.-J. Zhong, N. T. Woods, G. Dawson, M. D. Porter, *Electrochemistry Communications* **1999**, *1*, 17–21.

[120] R. G. Nuzzo, B. R. Zegarski, L. H. Dubois, *Journal of the American Chemical Society* **1987**, *109*, 733–740.

[121] J.-G. Lee, J. Lee, J. T. Yates, *Journal of the American Chemical Society* **2004**, *126*, 440–441.

[122] M. Hasan, D. Bethell, M. Brust, *Journal of the American Chemical Society* **2002**, *124*, 1132–1133.

[123] J. Aldana, N. Lavelle, Y. Wang, X. Peng, *Journal of the American Chemical Society* **2005**, *127*, 2496–2504.

[124] B.-K. Pong, B. L. Trout, J.-Y. Lee, *Langmuir* **2008**, *24*, 5270–5276.

[125] A. R. Noble-Luginbuhl, R. G. Nuzzo, *Langmuir* **2001**, *17*, 3937–3944.

[126] X.-B. Li, Z.-J. Li, Y.-J. Gao, Q.-Y. Meng, S. Yu, R. G. Weiss, C.-H. Tung, L.-Z. Wu, *Angewandte Chemie International Edition* **2014**, *53*, 2085–2089.

[127] L.-M. Zhao, Q.-Y. Meng, X.-B. Fan, C. Ye, X.-B. Li, B. Chen, V. Ramamurthy, C.-H. Tung, L.-Z. Wu, *Angewandte Chemie International Edition* **2017**, *56*, 3020–3024.

[128] W.-B. Wu, Y.-C. Wong, Z.-K. Tan, J. Wu, *Catalysis Science & Technology* **2018**, *8*, 4257–4263.

[129] M. Berton, R. Mello, M. E. González-Núñez, *ChemSusChem* **2016**, *9*, 3397–3400.

[130] O. S. Bushuyev, P. De Luna, C. T. Dinh, L. Tao, G. Saur, J. van de Lagemaat, S. O. Kelley, E. H. Sargent, *Joule* **2018**, *2*, 825–832.

[131] S. Verma, B. Kim, H.-R. Jhong, S. Ma, P. J. A. Kenis, *ChemSusChem* **2016**, *9*, 1972–1979.

[132] S. R. Foit, I. C. Vinke, L. G. J. de Haart, R.-A. Eichel, *Angewandte Chemie International Edition* **2017**, *56*, 5402–5411.

[133] A. Wagner, C. D. Sahm, E. Reisner, *Nature Catalysis* **2020**, *3*, 775–786.

[134] A. R. Barron, *Chemistry of the Main Group Elements*, OpenStax CNX, **2014**.

[135] J. E. Huheey, E. A. Keiter, R. L. Keiter, R. Beckhaus, F. Breher, D. Johrendt, M. Kaupp, H.-J. Lunk, U. Schatzschneider, *Anorganische Chemie*, (Ed.: R. Steudel), De Gruyter, Berlin, Boston, **2012**, p. 200.

[136] W. Taifan, J.-F. Boily, J. Baltrusaitis, *Surface Science Reports* **2016**, *71*, 595–671.

[137] E. E. Benson, C. P. Kubiak, A. J. Sathrum, J. M. Smieja, *Chemical Society Reviews* **2009**, *38*, 89–99.

[138] W. Shin, S. H. Lee, J. W. Shin, S. P. Lee, Y. Kim, *Journal of the American Chemical Society* **2003**, *125*, 14688–14689.

[139] A. Bassegoda, C. Madden, D. W. Wakerley, E. Reisner, J. Hirst, *Journal of the American Chemical Society* **2014**, *136*, 15473–15476.

[140] R. Kortlever, J. Shen, K. J. P. Schouten, F. Calle-Vallejo, M. T. Koper, *Journal of Physical Chemistry Letters* **2015**, *6*, 4073–4082.

[141] J. S. Yoo, R. Christensen, T. Vegge, J. K. Nørskov, F. Studt, *ChemSusChem* **2016**, *9*, 358–363.

[142] Y. Hori, *Modern Aspects of Electrochemistry No. 42*, (Eds.: C. G. Vayenas, R. E. White, M. E. Gamboa-Aldeco), Springer New York, New York, NY, **2008**, pp. 89–182.

[143] A. J. Göttle, M. T. M. Koper, *Chemical Science* **2017**, *8*, 458–465.

[144] B. Innocent, D. Pasquier, F. Ropital, F. Hahn, J.-M. Léger, K. Kokoh, *Applied Catalysis B: Environmental* **2010**, *94*, 219–224.

[145] R. Kortlever, K. H. Tan, Y. Kwon, M. T. M. Koper, *Journal of Solid State Electrochemistry* **2013**, *17*, 1843–1849.

[146] H. A. Hansen, J. B. Varley, A. A. Peterson, J. K. Nørskov, *The Journal of Physical Chemistry Letters* **2013**, *4*, 388–392.

[147] N. Govindarajan, M. T. M. Koper, E. J. Meijer, F. Calle-Vallejo, *ACS Catalysis* **2019**, *9*, 4218–4225.

[148] B. Zhang, L. Sun, *Chemical Society Reviews* **2019**, *48*, 2216–2264.

[149] J. Hawecker, J.-M. Lehn, R. Ziessel, *Journal of the Chemical Society Chemical Communications* **1983**, 536–538.

[150] J. Hawecker, J.-M. Lehn, R. Ziessel, *Journal of the Chemical Society Chemical Communications* **1984**, *3*, 328–330.

[151] J. Hawecker, J. Lehn, R. Ziessel, *Helvetica chimica acta* **1986**, *69*, 1990–2012.

[152] H. Takeda, K. Koike, H. Inoue, O. Ishitani, *Journal of the American Chemical Society* **2008**, *130*, 2023–2031.

[153] B. Gholamkhass, H. Mametsuka, K. Koike, T. Tanabe, M. Furue, O. Ishitani, *Inorganic Chemistry* **2005**, *44*, 2326–2336.

[154] G. Sahara, H. Kumagai, K. Maeda, N. Kaeffer, V. Artero, M. Higashi, R. Abe, O. Ishitani, *Journal of the American Chemical Society* **2016**, *138*, 14152–14158.

[155] H. Ishida, H. Tanaka, K. Tanaka, T. Tanaka, *Journal of the Chemical Society Chemical Communications* **1987**, *7*, 131–132.

[156] Z. Chen, C. Chen, D. R. Weinberg, P. Kang, J. J. Concepcion, D. P. Harrison, M. S. Brookhart, T. J. Meyer, *Chemical Communications* **2011**, *47*, 12607–12609.

[157] R. Kuriki, K. Sekizawa, O. Ishitani, K. Maeda, *Angewandte Chemie International Edition* **2015**, *54*, 2406–2409.

[158] R. Kuriki, O. Ishitani, K. Maeda, *ACS Applied Materials & Interfaces* **2016**, *8*, 6011–6018.

[159] R. Kuriki, H. Matsunaga, T. Nakashima, K. Wada, A. Yamakata, O. Ishitani, K. Maeda, *Journal of the American Chemical Society* **2016**, *138*, 5159–5170.

[160] R. Kuriki, M. Yamamoto, K. Higuchi, Y. Yamamoto, M. Akatsuka, D. Lu, S. Yagi, T. Yoshida, O. Ishitani, K. Maeda, *Angewandte Chemie International Edition* **2017**, *56*, 4867–4871.

[161] D. Saito, Y. Yamazaki, Y. Tamaki, O. Ishitani, *Journal of the American Chemical Society* **2020**, *142*, 19249–19258.

[162] M. Bourrez, F. Molton, S. Chardon-Noblat, A. Deronzier, *Angewandte Chemie International Edition* **2011**, *50*, 9903–9906.

[163] H. Takeda, H. Koizumi, K. Okamoto, O. Ishitani, *Chemical Communications* **2014**, *50*, 1491–1493.

[164] P. L. Cheung, C. W. Machan, A. Y. S. Malkhasian, J. Agarwal, C. P. Kubiak, *Inorganic Chemistry* **2016**, *55*, 3192–3198.

[165] P. Govender, S. Pai, U. Schatzschneider, G. S. Smith, *Inorganic Chemistry* **2013**, *52*, 5470–5478.

[166] B. J. Fisher, R. Eisenberg, *Journal of the American Chemical Society* **1980**, *102*, 7361–7363.

[167] M. Beley, J.-P. Collin, R. Ruppert, J.-P. Sauvage, *Journal of the Chemical Society Chemical Communications* **1984**, *2*, 1315.

[168] M. Beley, J. P. Collin, R. Ruppert, J. P. Sauvage, *Journal of the American Chemical Society* **1986**, *108*, 7461–7467.

[169] J. Schneider, H. Jia, K. Kobiro, D. E. Cabelli, J. T. Muckerman, E. Fujita, *Energy & Environmental Science* **2012**, *5*, 9502.

[170] G. Neri, M. Forster, J. J. Walsh, C. M. Robertson, T. J. Whittles, P. Farràs, A. J. Cowan, *Chemical Communications* **2016**, *52*, 14200–14203.

[171] J. L. Grant, K. Goswami, L. Spreer, J. W. Otvos, M. Calvin, *Journal of the Chemical Society Dalton Transactions* **1987**, 2105–2109.

[172] C. A. Craig, L. O. Spreer, J. W. Otvos, M. Calvin, *The Journal of Physical Chemistry* **1990**, *94*, 7957–7960.

[173] E. Kimura, X. Bu, M. Shionoya, S. Wada, S. Maruyama, *Inorganic Chemistry* **1992**, *31*, 4542–4546.

[174] J. Song, E. L. Klein, F. Neese, S. Ye, *Inorganic Chemistry* **2014**, *53*, 7500–7507.

[175] M. Hammouche, D. Lexa, M. Momenteau, J. M. Savéant, *Journal of the American Chemical Society* **1991**, *113*, 8455–8466.

[176] C. Costentin, S. Drouet, M. Robert, J.-M. Savéant, *Science* **2012**, *338*, 90–94.

[177] C. Costentin, M. Robert, J.-M. Savéant, A. Tatin, *Proceedings of the National Academy of Sciences* **2015**, *112*, 6882–6886.

[178] I. Azcarate, C. Costentin, M. Robert, J.-M. Savéant, *Journal of the American Chemical Society* **2016**, *138*, 16639–16644.

[179] H. Rao, J. Bonin, M. Robert, *ChemSusChem* **2017**, *10*, 4447–4450.

[180] H. Rao, L. C. Schmidt, J. Bonin, M. Robert, *Nature* **2017**, *548*, 74–77.

[181] T. Nakazono, A. R. Parent, K. Sakai, *Chemical Communications* **2013**, *49*, 6325.

[182] A. Call, M. Cibian, K. Yamamoto, T. Nakazono, K. Yamauchi, K. Sakai, *ACS Catalysis* **2019**, *9*, 4867–4874.

[183] C. Arana, S. Yan, M. Keshavarz-K., K. T. Potts, H. D. Abruna, *Inorganic Chemistry* **1992**, *31*, 3680–3682.

[184] N. Elgrishi, M. B. Chambers, V. Artero, M. Fontecave, *Physical Chemistry Chemical Physics* **2014**, *16*, 13635–13644.

[185] N. Elgrishi, M. B. Chambers, M. Fontecave, *Chemical Science* **2015**, *6*, 2522–2531.

[186] M. F. Kuehnel, K. L. Orchard, K. E. Dalle, E. Reisner, *Journal of the American Chemical Society* **2017**, *139*, 7217–7223.

[187] J. J. Leung, J. Warnan, K. H. Ly, N. Heidary, D. H. Nam, M. F. Kuehnel, E. Reisner, *Nature Catalysis* **2019**, *2*, 354–365.

[188] Q. Wang, J. Warnan, S. Rodríguez-Jiménez, J. J. Leung, S. Kalathil, V. Andrei, K. Domen, E. Reisner, *Nature Energy* **2020**, *5*, 703–710.

[189] C. M. Lieber, N. S. Lewis, *Journal of the American Chemical Society* **1984**, *106*, 5033–5034.

[190] N. Morlanés, K. Takanabe, V. Rodionov, *ACS Catalysis* **2016**, *6*, 3092–3095.

[191] X. Zhang, Z. Wu, X. Zhang, L. Li, Y. Li, H. Xu, X. Li, X. Yu, Z. Zhang, Y. Liang, H. Wang, *Nature Communications* **2017**, *8*, 14675.

[192] N. Han, Y. Wang, L. Ma, J. Wen, J. Li, H. Zheng, K. Nie, X. Wang, F. Zhao, Y. Li, J. Fan, J. Zhong, T. Wu, D. J. Miller, J. Lu, S.-T. Lee, Y. Li, *Chem* **2017**, *3*, 652–664.

[193] S. Roy, E. Reisner, *Angewandte Chemie International Edition* **2019**, *58*, 12180–12184.

[194] K.-M. Lam, K.-Y. Wong, S.-M. Yang, C.-M. Che, *Journal of the Chemical Society Dalton Transactions* **1995**, 1103–1107.

[195] Z. Guo, S. Cheng, C. Cometto, E. Anxolabéhère-Mallart, S.-M. Ng, C.-C. Ko, G. Liu, L. Chen, M. Robert, T.-C. Lau, *Journal of the American Chemical Society* **2016**, *138*, 9413–9416.

[196] Z. Guo, F. Yu, Y. Yang, C.-F. Leung, S.-M. Ng, C.-C. Ko, C. Cometto, T.-C. Lau, M. Robert, *ChemSusChem* **2017**, *10*, 4009–4013.

[197] C. Cometto, L. Chen, P.-K. Lo, Z. Guo, K.-C. Lau, E. Anxolabéhère-Mallart, C. Fave, T.-C. Lau, M. Robert, *ACS Catalysis* **2018**, *8*, 3411–3417.

[198] C. Cometto, L. Chen, E. Anxolabéhère-Mallart, C. Fave, T.-C. Lau, M. Robert, *Organometallics* **2019**, *38*, 1280–1285.

[199] M. Wang, L. Chen, T.-C. Lau, M. Robert, *Angewandte Chemie International Edition* **2018**, *57*, 7769–7773.

[200] C. Cometto, R. Kuriki, L. Chen, K. Maeda, T.-C. Lau, O. Ishitani, M. Robert, *Journal of the American Chemical Society* **2018**, *140*, 7437–7440.

[201] B. Ma, G. Chen, C. Fave, L. Chen, R. Kuriki, K. Maeda, O. Ishitani, T.-C. Lau, J. Bonin, M. Robert, *Journal of the American Chemical Society* **2020**, *142*, 6188–6195.

[202] Z. Guo, G. Chen, C. Cometto, B. Ma, H. Zhao, T. Groizard, L. Chen, H. Fan, W.-L. Man, S.-M. Yiu, K.-C. Lau, T.-C. Lau, M. Robert, *Nature Catalysis* **2019**, *2*, 801–808.

[203] P. B. Pati, R. Wang, E. Boutin, S. Diring, S. Jobic, N. Barreau, F. Odobel, M. Robert, *Nature Communications* **2020**, *11*, 3499.

[204] K. Li, B. Peng, T. Peng, *ACS Catalysis* **2016**, *6*, 7485–7527.

[205] H.-L. Wu, X.-B. Li, C.-H. Tung, L.-Z. Wu, *Advanced Materials* **2019**, *31*, 1900709.

[206] P. Kumar, R. K. Chauhan, B. Sain, S. L. Jain, *Dalton Transactions* **2015**, *44*, 4546–4553.

[207] P. Kumar, C. Joshi, N. Labhsetwar, R. Boukherroub, S. L. Jain, *Nanoscale* **2015**, *7*, 15258–15267.

[208] F. Gonell, A. V. Puga, B. Julián-López, H. García, A. Corma, *Applied Catalysis B: Environmental* **2016**, *180*, 263–270.

[209] G. Yin, M. Nishikawa, Y. Nosaka, N. Srinivasan, D. Atarashi, E. Sakai, M. Miyauchi, *ACS Nano* **2015**, *9*, 2111–2119.

[210] Z. Wang, K. Teramura, S. Hosokawa, T. Tanaka, *Applied Catalysis B: Environmental* **2015**, *163*, 241–247.

[211] Z. Wang, K. Teramura, S. Hosokawa, T. Tanaka, *Journal of Materials Chemistry A* **2015**, *3*, 11313–11319.

[212] K. Teramura, Z. Wang, S. Hosokawa, Y. Sakata, T. Tanaka, *Chemistry - A European Journal* **2014**, *20*, 9906–9909.

[213] S. Iguchi, K. Teramura, S. Hosokawa, T. Tanaka, *Catalysis Today* **2015**, *251*, 140–144.

[214] J. Wang, T. Xia, L. Wang, X. Zheng, Z. Qi, C. Gao, J. Zhu, Z. Li, H. Xu, Y. Xiong, *Angewandte Chemie International Edition* **2018**, *57*, 16447–16451.

[215] A. Li, T. Wang, C. Li, Z. Huang, Z. Luo, J. Gong, *Angewandte Chemie International Edition* **2019**, *58*, 3804–3808.

[216] W. Xia, J. Wu, J.-C. Hu, S. Sun, M. Li, H. Liu, M. Lan, F. Wang, *ChemSusChem* **2019**, *12*, 4617–4622.

[217] H. Sheng, M. H. Oh, W. T. Osowiecki, W. Kim, A. P. Alivisatos, H. Frei, *Journal of the American Chemical Society* **2018**, *140*, 4363–4371.

[218] Q. Guo, F. Liang, X.-B. Li, Y.-J. Gao, M.-Y. Huang, Y. Wang, S.-G. Xia, X.-Y. Gao, Q.-C. Gan, Z.-S. Lin, C.-H. Tung, L.-Z. Wu, *Chem* **2019**, *5*, 2605–2616.

[219] B. Bhattacharyya, A. K. Simlandy, A. Chakraborty, G. P. Rajasekar, N. B. Aetukuri, S. Mukherjee, A. Pandey, *ACS Energy Letters* **2018**, *3*, 1508–1514.

[220] C. Wang, R. L. Thompson, P. Ohodnicki, J. Baltrus, C. Matranga, *Journal of Materials Chemistry* **2011**, *21*, 13452.

[221] H. Park, H.-H. Ou, A. J. Colussi, M. R. Hoffmann, *The Journal of Physical Chemistry A* **2015**, *119*, 4658–4666.

[222] X. An, K. Li, J. Tang, *ChemSusChem* **2014**, *7*, 1086–1093.

[223] A. Li, Q. Cao, G. Zhou, B. V. K. J. Schmidt, W. Zhu, X. Yuan, H. Huo, J. Gong, M. Antonietti, *Angewandte Chemie International Edition* **2019**, *58*, 14549–14555.

[224] Y.-F. Xu, M.-Z. Yang, B.-X. Chen, X.-D. Wang, H.-Y. Chen, D.-B. Kuang, C.-Y. Su, *Journal of the American Chemical Society* **2017**, *139*, 5660–5663.

[225] J. Hou, S. Cao, Y. Wu, Z. Gao, F. Liang, Y. Sun, Z. Lin, L. Sun, *Chemistry – A European Journal* **2017**, *23*, 9481–9485.

[226] M. Ou, W. Tu, S. Yin, W. Xing, S. Wu, H. Wang, S. Wan, Q. Zhong, R. Xu, *Angewandte Chemie International Edition* **2018**, *57*, 13570–13574.

[227] H. Zhang, J. Li, Q. Tan, L. Lu, Z. Wang, G. Wu, *Chemistry - A European Journal* **2018**, *24*, 18137–18157.

[228] Y. Chen, D. Wang, X. Deng, Z. Li, *Catalysis Science and Technology* **2017**, *7*, 4893–4904.

[229] M. Ding, R. W. Flaig, H.-L. Jiang, O. M. Yaghi, *Chemical Society Reviews* **2019**, *48*, 2783–2828.

[230] K. Sekizawa, K. Maeda, K. Domen, K. Koike, O. Ishitani, *Journal of the American Chemical Society* **2013**, *135*, 4596–4599.

[231] A. Nakada, T. Nakashima, K. Sekizawa, K. Maeda, O. Ishitani, *Chemical Science* **2016**, *7*, 4364–4371.

[232] C. D. Windle, E. Pastor, A. Reynal, A. C. Whitwood, Y. Vaynzof, J. R. Durrant, R. N. Perutz, E. Reisner, *Chemistry - A European Journal* **2015**, *21*, 3746–3754.

[233] D.-I. Won, J.-S. Lee, J.-M. Ji, W.-J. Jung, H.-J. Son, C. Pac, S. O. Kang, *Journal of the American Chemical Society* **2015**, *137*, 13679–13690.

[234] D.-I. Won, J.-S. Lee, Q. Ba, Y.-J. Cho, H.-Y. Cheong, S. Choi, C. H. Kim, H.-J. Son, C. Pac, S. O. Kang, *ACS Catalysis* **2018**, *8*, 1018–1030.

[235] T. W. Woolerton, S. Sheard, E. Reisner, E. Pierce, S. W. Ragsdale, F. A. Armstrong, *Journal of the American Chemical Society* **2010**, *132*, 2132–2133.

[236] M. Miller, W. E. Robinson, A. R. Oliveira, N. Heidary, N. Kornienko, J. Warnan, I. A. C. Pereira, E. Reisner, *Angewandte Chemie International Edition* **2019**, *58*, 4601–4605.

[237] Y. S. Chaudhary, T. W. Woolerton, C. S. Allen, J. H. Warner, E. Pierce, S. W. Ragsdale, F. A. Armstrong, *Chemical Communications* **2012**, *48*, 58–60.

[238] L. Lin, C. Hou, X. Zhang, Y. Wang, Y. Chen, T. He, *Applied Catalysis B: Environmental* **2018**, *221*, 312–319.

[239] S. Aoi, K. Mase, K. Ohkubo, S. Fukuzumi, *Chemical Communications* **2015**, *51*, 10226–10228.

[240] S. Aoi, K. Mase, K. Ohkubo, S. Fukuzumi, *Catalysis Science & Technology* **2016**, *6*, 4077–4080.

[241] J.-S. Lee, D.-I. Won, W.-J. Jung, H.-J. Son, C. Pac, S. O. Kang, *Angewandte Chemie International Edition* **2017**, *56*, 976–980.

[242] G. Neri, M. Forster, J. J. Walsh, C. M. Robertson, T. J. Whittles, P. Farràs, A. J. Cowan, *Chemical Communications* **2016**, *52*, 14200–14203.

[243] S. Lian, M. S. Kodaimati, D. S. Dolzhnikov, R. Calzada, E. A. Weiss, *Journal of the American Chemical Society* **2017**, *139*, 8931–8938.

[244] Q.-Q. Bi, J.-W. Wang, J.-X. Lv, J. Wang, W. Zhang, T.-B. Lu, *ACS Catalysis* **2018**, *8*, 11815–11821.

[245] J. Huang, M. G. Gatty, B. Xu, P. B. Pati, A. S. Etman, L. Tian, J. Sun, L. Hammarström, H. Tian, *Dalton Transactions* **2018**, *47*, 10775–10783.

[246] Y. Wu, Z. Jiang, X. Lu, Y. Liang, H. Wang, *Nature* **2019**, *575*, 639–642.

[247] K. P. Kuhl, T. Hatsukade, E. R. Cave, D. N. Abram, J. Kibsgaard, T. F. Jaramillo, *Journal of the American Chemical Society* **2014**, *136*, 14107–14113.

[248] E. R. Cave, C. Shi, K. P. Kuhl, T. Hatsukade, D. N. Abram, C. Hahn, K. Chan, T. F. Jaramillo, *ACS Catalysis* **2018**, *8*, 3035–3040.

[249] Z. P. Jovanov, H. A. Hansen, A. S. Varela, P. Malacrida, A. A. Peterson, J. K. Norskov, I. E. Stephens, I. Chorkendorff, *Journal of Catalysis* **2016**, *343*, 215–231.

[250] D. Bohra, I. Ledezma-Yanez, G. Li, W. de Jong, E. A. Pidko, W. A. Smith, *Angewandte Chemie International Edition* **2019**, *58*, 1345–1349.

[251] A. Wuttig, J. Ryu, Y. Surendranath, *chemrxiv DOI:10.26434/chemrxiv.7929038* **2019**, 1–12.

[252] A. Wuttig, M. Yaguchi, K. Motobayashi, M. Osawa, Y. Surendranath, *Proceedings of the National Academy of Sciences* **2016**, *113*, E4585–E4593.

[253] Y. Fang, J. C. Flake, *Journal of the American Chemical Society* **2017**, *139*, 3399–3405.

[254] C. Kim, H. S. Jeon, T. Eom, M. S. Jee, H. Kim, C. M. Friend, B. K. Min, Y. J. Hwang, *Journal of the American Chemical Society* **2015**, *137*, 13844–13850.

[255] F. Li, Q. Tang, *Journal of Materials Chemistry A* **2019**, *7*, 19872–19880.

[256] C. Kim, T. Eom, M. S. Jee, H. Jung, H. Kim, B. K. Min, Y. J. Hwang, *ACS Catalysis* **2017**, *7*, 779–785.

[257] M. S. Xie, B. Y. Xia, Y. Li, Y. Yan, Y. Yang, Q. Sun, S. H. Chan, A. Fisher, X. Wang, *Energy & Environmental Science* **2016**, *9*, 1687–1695.

[258] D. Wakerley, S. Lamaison, F. Ozanam, N. Menguy, D. Mercier, P. Marcus, M. Fontecave, V. Mougel, *Nature Materials* **2019**, *18*, 1222–1227.

[259] Z. Han, R. Kortlever, H.-Y. Chen, J. C. Peters, T. Agapie, *ACS Central Science* **2017**, *3*, 853–859.

[260] V. J. Ovalle, M. M. Waegele, *The Journal of Physical Chemistry C* **2019**, *123*, 24453–24460.

[261] F. Li, A. Thevenon, A. Rosas-Hernández, Z. Wang, Y. Li, C. M. Gabardo, A. Ozden, C. T. Dinh, J. Li, Y. Wang, J. P. Edwards, Y. Xu, C. McCallum, L. Tao, Z.-Q. Liang, M. Luo, X. Wang, H. Li, C. P. O'Brien, C.-S. Tan, D.-H. Nam, R. Quintero-Bermudez, T.-T. Zhuang, Y. C. Li, Z. Han, R. D. Britt, D. Sinton, T. Agapie, J. C. Peters, E. H. Sargent, *Nature* **2020**, *577*, 509–513.

[262] Z. Cao, J. S. Derrick, J. Xu, R. Gao, M. Gong, E. M. Nichols, P. T. Smith, X. Liu, X. Wen, C. Copéret, C. J. Chang, *Angewandte Chemie International Edition* **2018**, *57*, 4981–4985.

[263] Z. Cao, D. Kim, D. Hong, Y. Yu, J. Xu, S. Lin, X. Wen, E. M. Nichols, K. Jeong, J. A. Reimer, P. Yang, C. J. Chang, *Journal of the American Chemical Society* **2016**, *138*, 8120–8125.

[264] Z. Cao, S. B. Zacate, X. Sun, J. Liu, E. M. Hale, W. P. Carson, S. B. Tyndall, J. Xu, X. Liu, X. Liu, C. Song, J.-h. Luo, M.-J. Cheng, X. Wen, W. Liu, *Angewandte Chemie International Edition* **2018**, *57*, 12675–12679.

[265] J. R. Pankhurst, Y. T. Guntern, M. Mensi, R. Buonsanti, *Chemical Science* **2019**, *10*, 10356–10365.

[266] A. Wagner, K. H. Ly, N. Heidary, I. Szabó, T. Földes, K. I. Assaf, S. J. Barrow, K. Sokołowski, M. Al-Hada, N. Kornienko, M. F. Kuehnel, E. Rosta, I. Zebger, W. M. Nau, O. A. Scherman, E. Reisner, *ACS Catalysis* **2020**, *10*, 751–761.

[267] B.-J. Liu, T. Torimoto, H. Yoneyama, *Journal of Photochemistry and Photobiology A: Chemistry* **1998**, *113*, 93–97.

[268] Y. Liao, S.-W. Cao, Y. Yuan, Q. Gu, Z. Zhang, C. Xue, *Chemistry - A European Journal* **2014**, *20*, 10220–10222.

[269] Q. Huang, J. Yu, S. Cao, C. Cui, B. Cheng, *Applied Surface Science* **2015**, *358*, 350–355.

[270] K. M. Cho, K. H. Kim, K. Park, C. Kim, S. Kim, A. Al-Saggaf, I. Gereige, H.-T. Jung, *ACS Catalysis* **2017**, *7*, 7064–7069.

[271] A. Corma, H. Garcia, *Chemical Society Reviews* **2008**, *37*, 2096.

[272] L. Sun, V. Reddu, A. C. Fisher, X. Wang, *Energy & Environmental Science* **2020**, *13*, 374–403.

[273] B. Reuillard, K. H. Ly, T. E. Rosser, M. F. Kuehnel, I. Zebger, E. Reisner, *Journal of the American Chemical Society* **2017**, *139*, 14425–14435.

[274] J. J. Leung, J. A. Vigil, J. Warnan, E. Edwardes Moore, E. Reisner, *Angewandte Chemie International Edition* **2019**, *58*, 7697–7701.

[275] S. Xie, Y. Wang, Q. Zhang, W. Fan, W. Deng, Y. Wang, *Chemical Communications* **2013**, *49*, 2451.

[276] J. Hong, W. Zhang, Y. Wang, T. Zhou, R. Xu, *ChemCatChem* **2014**, *6*, 2315–2321.

[277] R. Pang, K. Teramura, H. Asakura, S. Hosokawa, T. Tanaka, *ACS Sustainable Chemistry & Engineering* **2019**, *7*, 2083–2090.

[278] B. A. Zhang, T. Ozel, J. S. Elias, C. Costentin, D. G. Nocera, *ACS Central Science* **2019**, *5*, 1097–1105.

[279] M. Moura de Salles Pupo, R. Kortlever, *ChemPhysChem* **2019**, *20*, 2926–2935.

[280] M. R. Singh, Y. Kwon, Y. Lum, J. W. Ager, A. T. Bell, *Journal of the American Chemical Society* **2016**, *138*, 13006–13012.

[281] L. Wang, S. A. Nitopi, E. Bertheussen, M. Orazov, C. G. Morales-Guio, X. Liu, D. C. Higgins, K. Chan, J. K. Nørskov, C. Hahn, T. F. Jaramillo, *ACS Catalysis* **2018**, *8*, 7445–7454.

[282] E. Pérez-Gallent, G. Marcandalli, M. C. Figueiredo, F. Calle-Vallejo, M. T. M. Koper, *Journal of the American Chemical Society* **2017**, *139*, 16412–16419.

[283] C. M. Gunathunge, V. J. Ovalle, M. M. Waegele, *Physical Chemistry Chemical Physics* **2017**, *19*, 30166–30172.

[284] L. D. Chen, M. Urushihara, K. Chan, J. K. Nørskov, *ACS Catalysis* **2016**, *6*, 7133–7139.

[285] M. L. Clark, A. Ge, P. E. Videla, B. Rudshteyn, C. J. Miller, J. Song, V. S. Batista, T. Lian, C. P. Kubiak, *Journal of the American Chemical Society* **2018**, *140*, 17643–17655.

[286] S. Ringe, E. L. Clark, J. Resasco, A. Walton, B. Seger, A. T. Bell, K. Chan, *Energy & Environmental Science* **2019**, *12*, 3001–3014.

[287] S. Nitopi, E. Bertheussen, S. B. Scott, X. Liu, A. K. Engstfeld, S. Horch, B. Seger, I. E. L. Stephens, K. Chan, C. Hahn, J. K. Nørskov, T. F. Jaramillo, I. Chorkendorff, *Chemical Reviews* **2019**, *119*, 7610–7672.

[288] J. Li, X. Li, C. M. Gunathunge, M. M. Waegele, *Proceedings of the National Academy of Sciences* **2019**, *116*, 9220–9229.

[289] Y. Hori, A. Murata, R. Takahashi, *Journal of the Chemical Society Faraday Transactions 1: Physical Chemistry in Condensed Phases* **1989**, *85*, 2309.

[290] J. Resasco, Y. Lum, E. Clark, J. Z. Zeledon, A. T. Bell, *ChemElectroChem* **2018**, *5*, 1064–1072.

[291] H. Hashiba, L.-C. Weng, Y. Chen, H. K. Sato, S. Yotsuhashi, C. Xiang, A. Z. Weber, *The Journal of Physical Chemistry C* **2018**, *122*, 3719–3726.

[292] A. Seifitokaldani, C. M. Gabardo, T. Burdyny, C.-T. Dinh, J. P. Edwards, M. G. Kibria, O. S. Bushuyev, S. O. Kelley, D. Sinton, E. H. Sargent, *Journal of the American Chemical Society* **2018**, *140*, 3833–3837.

[293] A. S. Varela, W. Ju, T. Reier, P. Strasser, *ACS Catalysis* **2016**, *6*, 2136–2144.

[294] B. A. Rosen, A. Salehi-Khojin, M. R. Thorson, W. Zhu, D. T. Whipple, P. J. A. Kenis, R. I. Masel, *Science* **2011**, *334*, 643–644.

[295] B. A. Rosen, J. L. Haan, P. Mukherjee, B. Braunschweig, W. Zhu, A. Salehi-Khojin, D. D. Dlott, R. I. Masel, *The Journal of Physical Chemistry C* **2012**, *116*, 15307–15312.

[296] Y. Wang, M. Hatakeyama, K. Ogata, M. Wakabayashi, F. Jin, S. Nakamura, *Physical Chemistry Chemical Physics* **2015**, *17*, 23521–23531.

[297] S. F. Zhao, M. Horne, A. M. Bond, J. Zhang, *Journal of Physical Chemistry C* **2016**, *120*, 23989–24001.

[298] L. Sun, G. K. Ramesha, P. V. Kamat, J. F. Brennecke, *Langmuir* **2014**, *30*, 6302–6308.

[299] G. P. S. Lau, M. Schreier, D. Vasilyev, R. Scopelliti, M. Grätzel, P. J. Dyson, *Journal of the American Chemical Society* **2016**, *138*, 7820–7823.

[300] M. Asadi, K. Kim, C. Liu, A. V. Addepalli, P. Abbasi, P. Yasaei, P. Phillips, A. Behranginia, J. M. Cerrato, R. Haasch, P. Zapol, B. Kumar, R. F. Klie, J. Abiade, L. A. Curtiss, A. Salehi-Khojin, *Science* **2016**, *353*, 467–470.

[301] H.-K. Lim, Y. Kwon, H. S. Kim, J. Jeon, Y.-H. Kim, J.-A. Lim, B.-S. Kim, J. Choi, H. Kim, *ACS Catalysis* **2018**, *8*, 2420–2427.

[302] N. García Rey, D. D. Dlott, *Physical Chemistry Chemical Physics* **2017**, *19*, 10491–10501.

[303] N. Hollingsworth, S. F. R. Taylor, M. T. Galante, J. Jacquemin, C. Longo, K. B. Holt, N. H. de Leeuw, C. Hardacre, *Angewandte Chemie International Edition* **2015**, *54*, 14164–14168.

[304] A. Atifi, D. W. Boyce, J. L. DiMeglio, J. Rosenthal, *ACS Catalysis* **2018**, *8*, 2857–2863.

[305] D. Vasilyev, E. Shirzadi, A. V. Rudnev, P. Broekmann, P. J. Dyson, *ACS Applied Energy Materials* **2018**, *1*, 5124–5128.

[306] Y. Chen, G. Ji, S. Guo, B. Yu, Y. Zhao, Y. Wu, H. Zhang, Z. Liu, B. Han, Z. Liu, *Green Chemistry* **2017**, *19*, 5777–5781.

[307] J. T. Feaster, A. L. Jongerius, X. Liu, M. Urushihara, S. A. Nitopi, C. Hahn, K. Chan, J. K. Nørskov, T. F. Jaramillo, *Langmuir* **2017**, *33*, 9464–9471.

[308] S. Banerjee, X. Han, V. S. Thoi, *ACS Catalysis* **2019**, *9*, 5631–5637.

[309] F. Quan, M. Xiong, F. Jia, L. Zhang, *Applied Surface Science* **2017**, *399*, 48–54.

[310] A. S. Hall, Y. Yoon, A. Wuttig, Y. Surendranath, *Journal of the American Chemical Society* **2015**, *137*, 14834–14837.

[311] H. Fei, M. D. Sampson, Y. Lee, C. P. Kubiak, S. M. Cohen, *Inorganic Chemistry* **2015**, *54*, 6821–6828.

[312] Mool C. Gupta, J. Ballato, *The Handbook of Photonics, Second Edition*, Taylor & Francis Ltd, London, UK, **2019**.

[313] H. Kaneko, T. Minegishi, M. Nakabayashi, N. Shibata, Y. Kuang, T. Yamada, K. Domen, *Advanced Functional Materials* **2016**, *26*, 4570–4577.

[314] Dietary Supplement Fact Sheet: Selenium, National Institutes of Health, Office of Dietary Supplements, **2016**.

[315] European Food Safety Authority, *EFSA Journal* **2012**, *10*, 2551.

[316] C. D. Sahm, Photocatalytic CO2 Reduction in Water using Zinc Selenide Quantum Dots and molecular Nickel Cyclam Catalysts (Master Thesis, ETH Zürich and University of Cambridge), **2016**.

[317] M. F. Kuehnel, C. D. Sahm, G. Neri, J. R. Lee, K. L. Orchard, A. J. Cowan, E. Reisner, *Chemical Science* **2018**, *9*, 2501–2509.

[318] M. F. Kuehnel, C. E. Creissen, C. D. Sahm, D. Wielend, A. Schlosser, K. L. Orchard, E. Reisner, *Angewandte Chemie International Edition* **2019**, *58*, 5059–5063.

[319] C. E. Creissen, J. Warnan, E. Reisner, *Chemical Science* **2018**, *9*, 1439–1447.

[320] P. Reiss, *New Journal of Chemistry* **2007**, *31*, 1843.

[321] M. Banski, M. Afzaal, M. a. Malik, A. Podhorodecki, J. Misiewicz, P. O'Brien, *Chemistry of Materials* **2015**, *27*, 3797–3800.

[322] C. M. Chang, K. L. Orchard, B. C. M. Martindale, E. Reisner, *Journal of Materials Chemistry A* **2016**, *4*, 2856–2862.

[323] S. E. Pav, Documentation for Geom_cloud function. (www.rdocumentation.org), **2020**.

[324] R Core Team: R - A language and environment for statistical computing. Vienna, Austria: R Foundation for Statistical Computing. Retrieved from https://www.R-project.org/.

[325] H. Wickham, M. Averick, J. Bryan, W. Chang, L. McGowan, R. François, G. Grolemund, A. Hayes, L. Henry, J. Hester, M. Kuhn, T. Pedersen, E. Miller, S. Bache, K. Müller, J. Ooms, D. Robinson, D. Seidel, V. Spinu, K. Takahashi, D. Vaughan, C. Wilke, K. Woo, H. Yutani, *Journal of Open Source Software* **2019**, *4*, 1686.

[326] F. E. Osterloh, *ACS Energy Letters* **2016**, *1*, 1060–1061.

[327] D. W. Keith, G. Holmes, D. St. Angelo, K. Heidel, *Joule* **2018**, *2*, 1573–1594.

[328] C.-Y. Zhu, Y.-Q. Zhang, R.-Z. Liao, W. Xia, J.-C. Hu, J. Wu, H. Liu, F. Wang, *Dalton Transactions* **2018**, *47*, 13142–13150.

[329] C. Bozal-Ginesta, C. A. Mesa, A. Eisenschmidt, L. Francàs, R. B. Shankar, D. Antón-García, J. Warnan, J. Willkomm, A. Reynal, E. Reisner, J. R. Durrant, *Chemical Science* **2021**, *12*, 946–959.

[330] B. M. Giuliano, R. M. Escribano, R. Martín-Doménech, E. Dartois, G. M. Muñoz Caro, *Astronomy & Astrophysics* **2014**, *565*, A108.

[331] P. Koehler, T. Lawson, J. Neises, J. Willkomm, B. C. M. Martindale, G. A. M. Hutton, D. Antón-García, A. Lage, A. S. Gentleman, M. H. Frosz, P. S. Russell, E. Reisner, T. G. Euser, *Analytical Chemistry* **2021**, *93*, 895–901.

[332] H. Kisch, *Semiconductor Photocatalysis*, (Ed.: H. Kisch), Wiley-VCH Verlag, Weinheim, Germany, **2014**.

[333] H. Al-Ekabi, P. De Mayo, *The Journal of Physical Chemistry* **1985**, *89*, 5815–5821.

[334] T. Nakajima, Y. Tamaki, K. Ueno, E. Kato, T. Nishikawa, K. Ohkubo, Y. Yamazaki, T. Morimoto, O. Ishitani, *Journal of the American Chemical Society* **2016**, *138*, 13818–13821.

[335] D. W. Wakerley, K. H. Ly, N. Kornienko, K. L. Orchard, M. F. Kuehnel, E. Reisner, *Chemistry – A European Journal* **2018**, *24*, 18385–18388.

[336] J.-P. Yuan, F. Chen, *Journal of Agricultural and Food Chemistry* **1998**, *46*, 5078–5082.

[337] M. Szultka, M. Buszewska-Forajta, R. Kaliszan, B. Buszewski, *Electrophoresis* **2014**, *35*, 585–592.

[338] E. Kimoto, H. Tanaka, T. Ohmoto, M. Choami, *Analytical Biochemistry* **1993**, *214*, 38–44.

[339] Y.-C. Yang, R. J. Ward, R. P. Seiders, *Inorganic Chemistry* **1985**, *24*, 1765–1769.

[340] W. Xia, J. Wu, J. C. Hu, S. Sun, M. D. Li, H. Liu, M. Lan, F. Wang, *ChemSusChem* **2019**, *12*, 4617–4622.

[341] D. Faggion, W. D. G. Gonçalves, J. Dupont, *Frontiers in Chemistry* **2019**, *7*, 102.

[342] Y. Chen, T. Mu, *Green Chemistry* **2019**, *21*, 2544–2574.

[343] J. Tamura, A. Ono, Y. Sugano, C. Huang, H. Nishizawa, S. Mikoshiba, *Physical Chemistry Chemical Physics* **2015**, *17*, 26072–26078.

[344] X. Wang, J. Zhuang, Q. Peng, Y. Li, *Nature* **2005**, *437*, 121–124.

[345] P. Tamilarasan, S. Ramaprabhu, *RSC Advances* **2015**, *5*, 24864–24871.

[346] J. Lin, Z. Ding, Y. Hou, X. Wang, *Scientific Reports* **2013**, *3*, 1056.

[347] Z. Hens, J. C. Martins, *Chemistry of Materials* **2013**, *25*, 1211–1221.

[348] A. M. Cieślak, E.-R. Janeček, K. Sokołowski, T. Ratajczyk, M. K. Leszczyński, O. A. Scherman, J. Lewiński, *Nanoscale* **2017**, *9*, 16128–16132.

[349] M. G. Berrettini, G. Braun, J. G. Hu, G. F. Strouse, *Journal of the American Chemical Society* **2004**, *126*, 7063–7070.

[350] M. Tomaselli, J. L. Yarger, M. Bruchez, R. H. Havlin, D. DeGraw, A. Pines, A. P. Alivisatos, *The Journal of Chemical Physics* **1999**, *110*, 8861–8864.

[351] Z. Huang, X. Chen, G. Wu, P. Metrangolo, D. Whitaker, J. A. McCune, O. A. Scherman, *Journal of the American Chemical Society* **2020**, *142*, 7356–7361.

[352] F. Biedermann, O. A. Scherman, *The Journal of Physical Chemistry B* **2012**, *116*, 2842–2849.

[353] S. Lin, C. S. Diercks, Y.-B. Zhang, N. Kornienko, E. M. Nichols, Y. Zhao, A. R. Paris, D. Kim, P. Yang, O. M. Yaghi, C. J. Chang, *Science* **2015**, *349*, 1208–1213.

[354] V. Ravi, J. M. Binz, R. M. Rioux, *Nano Letters* **2013**, *13*, 4442–4448.

[355] Y. Shen, R. Tan, M. Y. Gee, A. B. Greytak, *ACS Nano* **2015**, *9*, 3345–3359.

[356] E. Freire, O. L. Mayorga, M. Straume, *Analytical Chemistry* **1990**, *62*, 950A–959A.

[357] E. S. Williams, K. J. Major, A. Tobias, D. Woodall, V. Morales, C. Lippincott, P. J. Moyer, M. Jones, *The Journal of Physical Chemistry C* **2013**, *117*, 4227–4237.

[358] B. C. M. Martindale, E. Joliat, C. Bachmann, R. Alberto, E. Reisner, *Angewandte Chemie International Edition* **2016**, *55*, 9402–9406.

[359] C. Bachmann, B. Probst, M. Guttentag, R. Alberto, *Chem. Commun.* **2014**, *50*, 6737–6739.

[360] M. Abdellah, S. Zhang, M. Wang, L. Hammarström, *ACS Energy Letters* **2017**, *2*, 2576–2580.

[361] F. E. Gostev, I. V. Shelaev, A. V. Aibush, A. N. Kostrov, A. A. Titov, S. Y. Kochev, Y. A. Kabachii, M. S. Mekhata, V. A. Nadtochenko, *High Energy Chemistry* **2018**, *52*, 283–288.

[362] V. I. Klimov, D. W. McBranch, C. A. Leatherdale, M. G. Bawendi, *Physical Review B* **1999**, *60*, 13740–13749.

[363] K. Wu, Q. Li, Y. Du, Z. Chen, T. Lian, *Chemical Science* **2015**, *6*, 1049–1054.

[364] M. Lomascolo, A. Cretı, G. Leo, L. Vasanelli, L. Manna, *Applied Physics Letters* **2003**, *82*, 418–420.

[365] A. L. Weaver, D. R. Gamelin, *Journal of the American Chemical Society* **2012**, *134*, 6819–6825.

[366] V. V. Matylitsky, A. Shavel, N. Gaponik, A. Eychmüller, J. Wachtveitl, *Journal of Physical Chemistry C* **2008**, *112*, 2703–2710.

[367] L. Tian, L. di Mario, V. Zannier, D. Catone, S. Colonna, P. O'Keeffe, S. Turchini, N. Zema, S. Rubini, F. Martelli, *Physical Review B* **2016**, *94*, 165442.

[368] V. Babentsov, F. Sizov, *Opto-Electronics Review* **2008**, *16*, 208–225.

[369] I. V. Chernyshova, P. Somasundaran, S. Ponnurangam, *Proceedings of the National Academy of Sciences* **2018**, *115*, E9261–E9270.

[370] A. S. Barnard, C. A. Feigl, S. P. Russo, *Nanoscale* **2010**, *2*, 2294.

[371] J. Contreras-García, R. A. Boto, F. Izquierdo-Ruiz, I. Reva, T. Woller, M. Alonso, *Theoretical Chemistry Accounts* **2016**, *135*, 242.

[372] A. Otero-de-la-Roza, E. R. Johnson, V. Luaña, *Computer Physics Communications* **2014**, *185*, 1007–1018.

[373] V. A. Kuznetsova, E. Mates-Torres, N. Prochukhan, M. Marcastel, F. Purcell-Milton, J. O'Brien, A. K. Visheratina, M. Martinez-Carmona, Y. Gromova, M. Garcia-Melchor, Y. K. Gun'ko, *ACS Nano* **2019**, *13*, 13560–13572.

[374] A. J. Göttle, M. T. M. Koper, *Chemical Science* **2017**, *8*, 458–465.

[375] L. D. Field, B. A. Messerle, K. Q. Vuong, P. Turner, *Organometallics* **2005**, *24*, 4241–4250.

[376] G. I. Matiello, A. Pazini, K. I. da Silva, R. G. da Costa, G. Ebeling, J. Dupont, J. Limberger, J. D. Scholten, *Tetrahedron Letters* **2019**, *60*, 780–784.

[377] D. Yuan, H. V. Huynh, *Dalton Transactions* **2011**, *40*, 11698.

[378] J. P. Perdew, K. Burke, M. Ernzerhof, *Physical Review Letters* **1996**, *77*, 3865–3868.

[379] P. E. Blöchl, *Physical Review B* **1994**, *50*, 17953–17979.

[380] S. Grimme, S. Ehrlich, L. Goerigk, *Journal of Computational Chemistry* **2011**, *32*, 1456–1465.

[381] A. Jain, S. P. Ong, G. Hautier, W. Chen, W. D. Richards, S. Dacek, S. Cholia, D. Gunter, D. Skinner, G. Ceder, K. A. Persson, *APL Materials* **2013**, *1*, 011002.

[382] R. Tran, Z. Xu, B. Radhakrishnan, D. Winston, W. Sun, K. A. Persson, S. P. Ong, *Scientific Data* **2016**, *3*, 160080.

[383] J. K. Nørskov, J. Rossmeisl, A. Logadottir, L. Lindqvist, J. R. Kitchin, T. Bligaard, H. Jónsson, *The Journal of Physical Chemistry B* **2004**, *108*, 17886–17892.

[384] J. K. Nørskov, T. Bligaard, A. Logadottir, J. R. Kitchin, J. G. Chen, S. Pandelov, U. Stimming, *Journal of The Electrochemical Society* **2005**, *152*, J23.

[385] B. C. Mei, K. Susumu, I. L. Medintz, H. Mattoussi, *Nature Protocols* **2009**, *4*, 412–423.

[386] M. H. Stewart, K. Susumu, B. C. Mei, I. L. Medintz, J. B. Delehanty, J. B. Blanco-Canosa, P. E. Dawson, H. Mattoussi, *Journal of the American Chemical Society* **2010**, *132*, 9804–9813.

[387] R. Koole, B. Luigjes, M. Tachiya, R. Pool, T. J. H. Vlugt, C. de Mello Donegá, A. Meijerink, D. Vanmaekelbergh, *The Journal of Physical Chemistry C* **2007**, *111*, 11208–11215.

[388] B. Kundu, S. Chakrabarti, A. J. Pal, *Chemistry of Materials* **2014**, *26*, 5506–5513.

[389] T. Nakanishi, B. Ohtani, K. Uosaki, *The Journal of Physical Chemistry B* **1998**, *102*, 1571–1577.

[390] T. Løver, W. Henderson, G. A. Bowmaker, J. M. Seakins, R. P. Cooney, *Chemistry of Materials* **1997**, *9*, 1878–1886.

[391] S. Volk, N. Yazdani, E. Sanusoglu, O. Yarema, M. Yarema, V. Wood, *The Journal of Physical Chemistry Letters* **2018**, *9*, 1384–1392.

[392] M. Bonomo, D. Dini, F. Decker, *Frontiers in Chemistry* **2018**, *6*, 601.

[393] J. He, H. Lindström, A. Hagfeldt, S.-E. Lindquist, *The Journal of Physical Chemistry B* **1999**, *103*, 8940–8943.

[394] L. Li, L. Duan, F. Wen, C. Li, M. Wang, A. Hagfeldt, L. Sun, *Chemical Communications* **2012**, *48*, 988–990.

[395] L. D'Amario, J. Föhlinger, G. Boschloo, L. Hammarström, *Chemical Science* **2018**, *9*, 223–230.

[396] P. Xu, N. S. McCool, T. E. Mallouk, *Nano Today* **2017**, *14*, 42–58.

[397] M. Borgström, E. Blart, G. Boschloo, E. Mukhtar, A. Hagfeldt, L. Hammarström, F. Odobel, *The Journal of Physical Chemistry B* **2005**, *109*, 22928–22934.

[398] H. Cho, W. D. Kim, K. Lee, S. Lee, G. S. Kang, H. I. Joh, D. C. Lee, *Applied Surface Science* **2018**, *429*, 2–8.

[399] D. Guzmán, M. Isaacs, I. Osorio-Román, M. García, J. Astudillo, M. Ohlbaum, *ACS Applied Materials & Interfaces* **2015**, *7*, 19865–19869.

[400] D. Guzmán, M. Isaacs, T. Tsukuda, S. Yamazoe, R. Takahata, R. Schrebler, A. Burgos, I. Osorio-Román, F. Castillo, *Applied Surface Science* **2020**, *509*, 145386.

[401] R. Nie, W. Ma, Y. Dong, Y. Xu, J. Wang, J. Wang, H. Jing, *ChemCatChem* **2018**, *10*, 3342–3350.

[402] Q. Wang, L. Tao, X. Jiang, M. Wang, Y. Shen, *Applied Surface Science* **2019**, *465*, 607–613.

[403] J. Huang, B. Xu, L. Tian, P. B. Pati, A. S. Etman, J. Sun, L. Hammarström, H. Tian, *Chemical Communications* **2019**, *55*, 7918–7921.

[404] H. Lv, C. Wang, G. Li, R. Burke, T. D. Krauss, Y. Gao, R. Eisenberg, *Proceedings of the National Academy of Sciences* **2017**, *114*, 11297–11302.

[405] W. Ketir, A. Bouguelia, M. Trari, *Desalination* **2009**, *244*, 144–152.

[406] C. D. Windle, J. Massin, M. Chavarot-Kerlidou, V. Artero, *Dalton Transactions* **2018**, *47*, 10509–10516.

[407] C. E. Creissen, J. Warnan, D. Antón-García, Y. Farré, F. Odobel, E. Reisner, *ACS Catalysis* **2019**, *9*, 9530–9538.

[408] J. M. Chalker, L. Lercher, N. R. Rose, C. J. Schofield, B. G. Davis, *Angewandte Chemie International Edition* **2012**, *51*, 1835–1839.

[409] C. Kittel, *Introduction to Solid State Physics, 6th Ed.* John Wiley and Sons, New York, **1986**.

[410] H. Kasap, C. A. Caputo, B. C. M. Martindale, R. Godin, V. W.-h. Lau, B. V. Lotsch, J. R. Durrant, E. Reisner, *Journal of the American Chemical Society* **2016**, *138*, 9183–9192.

[411] P. Reiss, M. Protière, L. Li, *Small* **2009**, *5*, 154–168.

[412] A. D. Handoko, F. Wei, Jenndy, B. S. Yeo, Z. W. Seh, *Nature Catalysis* **2018**, *1*, 922–934.

[413] J.-H. Jeoung, H. Dobbek, *Science* **2007**, *318*, 1461–1464.

[414] R. Luguya, L. Jaquinod, F. R. Fronczek, M. H. Vicente, K. M. Smith, *Tetrahedron* **2004**, *60*, 2757–2763.

[415] E. Sansiaume, R. Ricoux, D. Gori, J.-P. Mahy, *Tetrahedron: Asymmetry* **2010**, *21*, 1593–1600.

[416] K. I. Assaf, H. Abed alfattah, A. F. Eftaiha, S. K. Bardaweel, M. A. Alnajjar, F. A. Alsoubani, A. K. Qaroush, M. I. El-Barghouthi, W. M. Nau, *Organic & Biomolecular Chemistry* **2020**, *18*, 2120–2128.